



PhD Thesis

Atmospheric Re-entry Analysis of Space Objects

Department of Mechanical and Aerospace Engineering (MAE)

Aerospace Centre of Excellence

University of Strathclyde, Glasgow

Alessandro Falchi

February 17, 2020

Declaration of author's rights

This thesis is the result of the author's original research. It has been composed by the author and has not been previously submitted for examination which has led to the award of a degree.

The copyright of this thesis belongs to the author under the terms of the United Kingdom Copyright Acts as qualified by University of Strathclyde Regulation 3.50. Due acknowledgement must always be made of the use of any material contained in, or derived from, this thesis.

Alessandro Falchi
February 17, 2020

Abstract

This Ph.D. work focuses on the investigation of numerical methods for estimating the aerodynamics and aerothermodynamics of space objects re-entering the Earth atmosphere. The well-known simplified panel methods applicable to hypersonic aerothermodynamics within continuum and rarefied flow regimes have been implemented in a numerical framework in order to assess different methods and techniques aiming at increasing their accuracy on arbitrarily shaped objects and assemblies. The main tested methods and techniques comprise: the use of a combination of panels visibility detection algorithms, the application of a local radius computation and smoothing algorithm, the introduction of high fidelity-based correction factors, and the definition of general rarefied transitional regime bridging functions for both aerodynamic and aerothermodynamics.

Various re-entry scenarios, experimental tests, and literature references have been simulated with the proposed methods in order to understand their accuracy. A preliminary validation of the aerodynamics and aerothermodynamics was performed on different test cases: Space Shuttle Orbiter, Orion Crew Exploration Vehicle, Mars Microprobe, Stardust Sample Return Capsule, VEGA payload fairing, and various other test cases such as spheres, and blunted cones. A particular effort was made to define and apply the methods for allowing the simulation of complete atmospheric re-entry scenarios, in order to simulate and study controlled and uncontrolled re-entres of simple and complex objects assemblies. In order to evaluate the applicability of the proposed methodologies, different re-entry scenarios have been simulated, such as: Stardust SRC (focusing on the thermal protection system ablation and temperature), and the Intermediate Experimental Vehicle (estimating the wall temperature over the re-entry).

The last application which has been studied was the estimation of the re-entry human casualty risk as expressed by the space debris mitigation guidelines. For such application, a toy satellite was built and simulated using a statistical approach based on the use of surrogate models and Monte Carlo technique aiming at providing a statistical impact ground footprint along with the human casualty risk distribution for a set of uncertain parameters given as input.

"The ancients considered Mechanics in a twofold respect; as rational, which proceeds accurately by demonstration, and practical. To practical Mechanics all the manual arts belong, from which Mechanics took its name. But as artificers do not work with perfect accuracy, it comes to pass that Mechanics is so distinguished from Geometry, that what is perfectly accurate is called Geometrical, what is less so is called Mechanical.

But the errors are not in the art, but in the artificers",

Philosophiæ Naturalis Principia Mathematica (1687)

- Sir Isaac Newton (Scientist and Natural Philosopher, 1643-1727)

Acknowledgements

First and foremost, I would like to thank my advisor Dr. Edmondo Minisci for his guidance and support over the last four years. Edmondo has been always keen to provide thoughtful and valuable insights, actively contributing to the continuous improvement and development of my professional capabilities. He always granted me the chance to explore and identify potential ideas toward the progression of my PhD project, providing me the opportunity to develop the confidence to independently pursue my own vision as a researcher.

I would like to thank also Dr. Thomas Scanlon and Dr. Vincent Casseau for sharing their knowledge and expertise in the DSMC method and their support with the use of OpenFoam; their valuable know-how has been paramount for achieving many of the results obtained during my PhD project.

A special thanks goes to Dr. Martin Kubicek who was always keen to collaborate and share his experience and knowledge on statistical and mathematical methods. Many of the projects I have successfully accomplished today carry also your sign. You have been an amazing colleague and a great friend, thanks for your support and invaluable advice.

My immense gratitude goes to all my wonderful colleagues and friends from the Mechanical and Aerospace Department, all the visiting students whom I had the chance to share a limited but valuable time with, and all the persons that made my PhD experience in Glasgow fantastic. Thanks for all the wonderful experiences we had the opportunity to share inside and outside the office; thanks for sharing your own culture and points of view; thanks for being along with me during tough and joyful times; thanks for allowing me to smile while remembering those wonderful times in Glasgow.

Last but not least, I would like to thank my family and old friends for always supporting and motivating me for giving my best. Even from miles and miles away, you have been always been ready to support me in every way you could, never letting me forget my roots. Thanks for having always believed in me.

Contents

Abstract	ii
Acknowledgements	iv
Introduction	28
1.1 Motivation	29
1.2 Thesis outline	31
1.3 Atmospheric Reentry Aerodynamics and Aerothermodynamics	33
1.3.1 Knudsen Number	36
1.3.2 Free Molecular Flow Regime	39
1.3.3 Continuum Regime	47
1.4 Space Debris and Spacecraft Atmospheric Reentry Simulations	60
1.4.1 DAS	62
1.4.2 ORSAT	63
1.4.3 SCARAB	65
1.4.4 Theoretical Analysis of SCARAB Aerothermal Model	67
1.4.5 DRAMA/SESAM	73
1.4.6 PAMPERO	75
1.4.7 DEBRISK	76
1.4.8 SAM	77
1.4.9 SPEAD	78
1.4.10 Re-entry Software Summary	79
Integrated Modelling approach	82
2.1 Previous Work	83
2.2 Aerodynamics and Aerothermodynamics Methodology: Overview	84
2.3 Mesh Handler	92
2.3.1 Mesh Initialization	92
2.3.2 Adaptive Mesh Refinement Algorithm	94
2.3.3 Local Radius Algorithm	101

Contents

2.4	Panels Visibility Detection method	115
Aerodynamics Computation Methodology		127
3.1	Aerodynamic Bridging Function	128
3.2	Aerodynamic Module Validations	132
3.2.1	Mesh Convergence Validation	132
3.2.2	Sphere	139
3.2.3	Space Shuttle Orbiter	140
3.2.4	Orion Crew Exploration Vehicle	141
3.2.5	Mars Microprobe	143
3.3	Free Molecular Regime Correction Factors	145
3.3.1	Methodology	148
3.3.2	Cylinder and Parallelepiped Correction Factor Tests	152
3.3.3	GOCE Drag Coefficient test case	154
Aerothermodynamics Computation Methodology		157
4.1	General description	157
4.2	Aerothermodynamics Bridging functions	162
4.3	Aero-thermodynamics Module Validations	167
4.3.1	Preliminary Smoothing Algorithm Validation Cases	168
4.3.2	Space Shuttle Orbiter	172
4.3.3	Stardust Sample Return Capsule	176
4.3.4	Blunted Cone	179
4.3.5	Launcher Vehicle Payload Fairing	181
Coupled Aero-thermodynamics Applications		187
5.1	IXV Atmospheric Re-entry	187
5.1.1	Ablative Response Code	188
5.1.2	Problem Description and Results	189
5.2	Stardust TPS Ablation Modelling	194
5.3	VEGA PLF and payload temperature estimation	200
5.3.1	Dummy payload temperature estimation	203
5.4	Re-entry Casualty Risk Statistical Modelling	206
5.4.1	Initial Testing of 1D ablation modelling	207
5.4.2	Lumped Mass Approach (0D), required modules, and assumptions	210
5.4.3	HDMR-based Sensitivity Analysis of Re-entry Survivability of an Aluminum Cube	214
5.4.4	Demise altitude of a Sphere	222
5.4.5	Toy Satellite Statistical Re-entry Casualty Risk Modelling	225

Contents

Conclusions	242
6.1 Future Works	246
Bibliography	246

List of Figures

1.1	Titanium tank surviving the atmospheric re-entry (available at https://orbitaldebris.jsc.nasa.gov/gallery - ©Space Research Institute, King Abdulaziz City for Science and Technology, Riyadh, Saudi Arabia, last accessed 31 May 2020)	30
1.2	Speed of Sound over atmospheric altitude (using a reference NRLM-SISE00 atmospheric model [Picone et al., 2002])	33
1.3	Typical velocity profile for a ballistic reentry from a circular orbit	34
1.4	Knudsen Number over altitude, computed with different models: the Hard Sphere model with Maxwellian molecular velocity distribution (λ_{HS} eq. 1.3), the Variable Hard Sphere model (λ_{VHS} , eq. 1.4), and using the viscosity approach with Sutherland’s and Chapman-Enskog’s models ($\lambda_{\mu,Su}$, $\lambda_{\mu,CE}$, eq. 1.5 with the respective viscosity models eq. 1.7 and 1.8)	38
1.5	Viscosity computed with the NRLMSISE00 Atmospheric model, for altitudes from 0 to 500km, and the different relationships: Sutherland’s (μ_{Su} , 1.7), Chapman-Enskog with VHS diameter (μ_{VHS} , 1.8), power law (μ_{pl} , 1.9), plotted against λ (equivalent to Kn for $L = 1$); Temperature and Altitudes plotted on the right axis	39
1.6	Viscosity bridging function for the transitional regime computed with the for altitudes from 0 to 500km, based on Sutherland’s in the continuum regime (μ_{Su} , 1.7), and Chapman-Enskog with VHS diameter in the FM regime (μ_{VHS} , 1.8)	40
1.7	Example for specular and diffusive reflection models	41
1.8	Flat plate in a free molecular flow	42
1.9	Normal Pressure coefficient distribution of a sphere in the free molecular regime. <i>On the left:</i> pressure distribution of a sphere computed with the developed software. <i>On the right:</i> numerical implementation of eq.1.18 and 1.32 at different conditions	47

List of Figures

1.10	Heat transfer coefficient distribution of a sphere in the free molecular regime. <i>On the left:</i> heat transfer distribution computed with the developed software. <i>On the right:</i> numerical implementation of eq.1.23 and 1.27 with a $S_R = 12$	48
1.11	Flat plate in a free molecular flow: a) impact and tangential motion, b) flux of particles characteristic.	49
1.12	Schematics for 3D Newtonian theory.	50
1.13	Maximum pressure coefficient variation w.r.t. M_∞ and γ	52
1.14	Left: C_p distribution on the surface of a sphere (post processed with FOSTRAD) for $\gamma = 1.4$ and $M_\infty = 24$. Right: comparison of modified Newtonian and standard Newtonian C_p on the windward surface	52
1.15	Variation of specific heat ratio (γ) over altitude for a US 1976 atmospheric model.	53
1.16	Schematic of an atmospheric re-entry	54
1.17	Lees laminar heat transfer distribution 1.51 over a hemisphere for different M_∞ and $\gamma = 1.4$	55
1.18	Heat transfer coefficient as defined in eq. 1.56 over the atoms recombination rate for a fully catalytic and a non-catalytic wall [Fay, 1957]. . . .	57
1.19	Typical break-up scenario (available at http://www.spacesafetymagazine.com/wp-content/uploads/2014/07/satellite-reentry-footprint.jpg - ©Andrea Gini on July 9, 2014, last accessed 31 May 2020)	61
1.20	Comparison of the different aerothermal heat flux models in the continuum regime, showing SCARAB overestimation.	68
1.21	<i>Left:</i> Normalized atmospheric properties (normalization computed as: $x/\min(x)$, where x is the considered property). <i>Right:</i> normalized $\Gamma(H, \omega)$ function obtained for $\omega = [0.70, 0.72, 0.76]$	70
1.22	Wall Enthalpy term analysis for estimating the error introduced by the cold wall assumption for the simplified approximations of Kemp and Riddell [Kemp, 1956], and the DKR model [Detra, 1957].	70
1.23	SCARAB aerothermal heating overestimation sensitivity analysis w.r.t. to the original Detra, Kemp, Riddell approximation [Detra, 1957], the analysis shows a lower boundary (i.e.: cold wall assumption).	72
1.24	SCARAB aerothermal heating overestimation sensitivity analysis w.r.t. to the original Kemp and Riddell approximation [Kemp, 1956], the analysis shows a lower boundary (i.e.: cold wall assumption).	73
2.1	FOSTRAD block and work-flow diagram (overview).	85
2.2	Atmospheric and Environmental properties detailed work-flow.	87

List of Figures

2.3	Mesh Handler block work-flow.	89
2.4	Inputs/outputs of aerodynamics and aerothermodynamics blocks.	91
2.5	Stardust Sample Return Capsule .stl mesh example.	92
2.6	Normals (shown with a quiver plot) on faces for a non-coherent (left) and a coherent (right) vertexes winding direction. The arrows representing the facets normal directions pointing outside the object surface (as in the right figure) show a correct vertex winding direction.	93
2.7	GOCE initial mesh (on the left) and refined mesh.	94
2.8	GOCE coarse and fine mesh, seen from the flow perspective, i.e.: taking into account of the attitude angles $\alpha = 35\text{deg}$ and $\beta = 45\text{deg}$	95
2.9	Visualization of the error introduce by a coarse mesh, due to the complete visibility associated to the partially shadowed panels. On the left the original mesh with 750 facets, and on the right a refined mesh with 10'000 facets.	96
2.10	Triangular mesh refinement step example.	97
2.11	Iterative loop for the side length-based refinement.	99
2.12	Iterative loop for the side area-based refinement.	100
2.13	Fully refined mesh, obtained with 300 iterations, starting from the initial mesh which had approximately 1300 facets to $\approx 30\text{k}$ panels.	101
2.14	Heat transfer distribution on a cube (0.25m), DSMC simulation performed at 90km altitude ($\text{Kn} \approx 0.1$) in a transitional regime.	102
2.15	Comparison of a LPI application on Kemp [Kemp et al., 1959] shock tube data, on the left: constant nose radius, on the right: local radius formulation (computed with the local radius algorithm presented in this paragraph).	103
2.16	Curvature algorithm applied on a complex geometry, showing the sharp variation of the local radius. Left: local radius of the refined triangulated mesh generated with snappyHexMesh starting from the original STL surface. right: local radius computed on the original STL surface .	105
2.17	Curvature algorithm applied on the Space Shuttle geometry, showing the mesh glitches. Left: local radius of the refined triangulated mesh generated with snappyHexMesh starting from the original STL surface. right: local radius computed on the original STL surface.	106
2.18	Left: Bogus Bennu Asteroid STL geometry representation. right: Erroneous local radius computed on the non-pre-processed surface.	108
2.19	Bogus Bennu after the cleaning preprocessing phase. Left: local radius distribution on the snappyHexMesh STL geometry. Right: local radius distribution computed on the cleaned original STL.	108

List of Figures

2.20 **Left:** simplified 2D meshing procedure for a circle with two different resolutions **right:** representation of flat surfaces recognition when meshing an STL with snappyHexMesh using a resolution higher than the original STL. 110

2.21 Smoothing algorithm block diagram 110

2.24 Flat Edge parameter effect on a complex geometry. 112

2.32 Ellipsoid local radius estimation. The non-smoothed and sigmoid-smoothed local radius shown respectively on the left and right. It is worth notice that the smoothed local radius give a better representation of the “true” surface curvature distribution. 115

2.33 Back-face culling application example. 116

2.36 Visibility panels detection algorithm computational cost and accuracy for a cube with a fixed attitude (small angle of attack and side-slip). . . 118

2.37 Visibility panels detection algorithm computational cost and accuracy for a cylinder with a fixed attitude. 118

2.38 Rasterization error on the occlusion culling, the black panels should be shadowed but have been misidentified, the back-face filtering avoid this kind of error. 119

2.39 Occlusion culling dependence on the attitude and pixel resolution for the GOCE study case. 119

2.22 *N. smooth* parameter (number of closest values taken for the average) comparison on a complex geometry. 120

2.23 Non-weighted smoothing local radius algorithm block diagram. 121

2.25 Weighted smoothing local radius algorithm block diagram. 122

2.26 *Linear* and *Sigmoid* Flat faces weighting functions 123

2.27 Local radius estimation of GOCE high resolution mesh. **left:** non-smoothed local radius. **right:** sigmoid-smoothed local radius. 123

2.28 Local radius estimation of IXV high resolution mesh. Comparison of the different flat-faces weighted smoothing options: linear weighted (left), sigmoid weighted (right). 124

2.29 Difference of local radius estimation sigmoid-linear smoothing mapped on the surface, directly taken from Figure 2.28. The relative differences are computed as $\frac{(R_{i,\text{sigmoid}}-R_{i,\text{linear}})}{R_{i,\text{sigmoid}}}\%$, the sigmoid smoothing shows lower radii at the corners and higher values close to the flat faces. 124

List of Figures

2.30 Cube local radius estimation, respectively from the left to the right: the non-smoothed, linear-smoothed, and sigmoid-smoothed. Noteworthy comparison with the thermal mapping shown in Figure 2.14. It can be observed that the sigmoid smoothing better approximate the relative magnitude distribution in the corners. In addition, since a high number of points is being averaged, the flat-non-flat faces ratio at the corners is always >0.5 , therefore, the sigmoid smoothing computes a higher radius at the corners. 125

2.31 Flat Cylinder ($R = 0.8m$) local radius estimation. The non-smoothed and sigmoid-smoothed local radius shown respectively on the left and right. It may be observed that the sigmoid smoothing can give a better representation than the non-smoothed of a possible surface thermal heating distribution for a head-on flow condition within the transitional and continuum regime. 125

2.34 Occlusion culling, random color IDs assignment and windward direction rotated object. 126

2.35 Occlusion culling, occluded panels red colored with black border. 126

3.1 GOCE model automatic cross sectional reference computation. 128

3.2 Aerodynamic computation methodology detailed work-flow. 129

3.3 left: Standard Error function ($Erf(x)$), right: auxiliary function corrective function. 130

3.4 Left: general shape of the aerodynamic bridging function. Right: bridging function fitted on the aerodynamic references ($A = 1e-6$, $B = 0.150$, $Kn_{c,ref} = 1.0e - 4$ and $Kn_{fm,ref} = 1e2$) 131

3.5 Mars Microprobe C_D (left y-axis) convergence wrt to the number of mesh panels (x-axis log scale). On the right y-axis the absolute error wrt the reference value from [Moss et al., 1997] is reported. 135

3.6 STS-orbiter C_D (left y-axis) convergence wrt to the number of mesh panels (x-axis log scale). On the right y-axis the absolute error wrt the reference value from [Rault, 1994] is reported. 135

3.7 GOCE C_D (left y-axis) reported against the side-slip angle for a fixed number of panels (20'000). On the right y-axis is reported the relative error wrt the correspondent reference values computed with dsmcFoam from [Benedetti et al., 2018]. 136

List of Figures

3.8	GOCE C_D convergence test (left y-axis) reported against the number of panels for three different side-slip angles: -4deg (top), -7deg (middle), and -10deg (bottom). On the right y-axis is reported the relative error wrt the reference correspondent values computed with dsmcFoam from [Benedetti et al., 2018].	137
3.9	Overview of the mesh convergence analyses wrt to the number of panels normalized on the averaged pixel resolution (eq. 3.117). The pictures shows the drag coefficient convergence for complex and simple geometries at different condition.	139
3.10	Sphere C_D free molecular, transitional and continuum regime validation [Dogra et al., 1992].	140
3.11	Space Shuttle Orbiter Mesh.	141
3.12	Left: C_D and C_L comparison. Right: L/D ratio for a wider set of literature data [Rault, 1994], UB and LB represents the flight data upper and lower boundaries respectively. On the right y-axis the relative error wrt to DSMC data is reported for the L/D ratio.	141
3.13	Orion CEV C_D comparison, $V_\infty = 7600\text{m/s}$, $\text{AofA} = -26\text{deg}$, $S_{\text{ref}} = 19.865\text{m}^2$ [Moss et al., 2006a]. The relative error has been computed in accordance to the flight regime validity of the reported references (i.e.: continuum or transitional rarefied regime).	142
3.14	Lift to Drag ratio comparison for Orion CEV. <u>Left</u> : [Moss et al., 2006a], <u>right</u> : simulations performed with STRATH-A.. The discrepancies for angles higher than $\pm 75\text{deg}$ are due to the afterbody geometric differences	143
3.15	Pitching moment coefficient, center of rotation on the nose, ref. length = 5.0292m. left: [Moss et al., 2006a], right: simulations performed with STRATH-A.	143
3.16	Left: Mars Microprobe geometry. Right: Microprobe Martian atmospheric C_D , $S_{\text{ref}} = 0.0962$ V_∞ from 6900 to 6100m/s, $\text{AofA} = 0\text{deg}$ [Moss et al., 2006a]. On the right y-axis the relative error wrt reference data is reported.	144
3.17	Iterative AD-HDMR process flow chart and DSMC coupling scheme: (1) The AD-HDMR starts decomposing the input domains. (2i) Selects the important sub-domains according to the latest results. (3i) Performs the adaptive sampling and requests a new DSMC simulation. (4i) Evaluates the function with respect to the sampled inputs. (5i) Adaptively selects an interpolation method. Performs the steps from 2i to 5i till the process has reached a statistical convergence.	148

List of Figures

3.18	parallelepiped parameterization based on the A_{ratio}	150
3.19	cylindrical geometry C_F surrogate model.	150
3.20	Parallelepiped C_F surrogate models for two different constant side-slip angles 0deg (on the left) and 90deg (on the right). It is possible to notice the strong interaction between all different variables taken into consideration.	151
3.21	Monte Carlo analysis results on the drag C_F , representative of the average random tumbling discrepancy between FOSTRAD and the DSMC code. The parallelepiped and cylinder are shown on the left and the right respectively.	152
3.22	FOSTRAD-DSMC C_D comparisons for parallelepipeds (on the left) and cylinders (on the right).	153
3.23	FOSTRAD-DSMC C_L comparisons for parallelepipeds (on the left) and cylinders (on the right). No correction has been applied to the C_L	153
3.24	FOSTRAD-DSMC $C_{M,z}$ comparisons for parallelepipeds (on the left) and cylinders (on the right). The same drag C_F has been applied to the moments, the corrected models show a very accurate agreement.	154
3.25	On the left: GOCE triangulated mesh used for FOSTRAD simulations. On the right: Monte Carlo probability distribution (4500samples) of a DSMC predefined SM and FOSTRAD with and without C_F	156
4.1	Aerothermodynamics block work-flow description	158
4.2	Local nose radius quality depending on the mesh resolution, left: 3100 faces, right: 24000 faces	159
4.3	Qualitative comparison of the atmospheric re-entry of a cube with the classical approach and the local nose radius approach.	160
4.4	Left: C_H mapping of a cube for a head-on flow at 60km showing the diagonal sampling points. Right: Heat transfer distribution on the diagonal for different altitudes. The centre of the front face is taken as the origin, and the panels with a black edge are the ones reported on the right.	160
4.5	Shuttle local radius distribution. The flat faces are assigned a reference hydraulic radius for the equivalent cross-section.	161
4.6	Comparison of the heat flux distribution for a reference nose radius (on the left), and the local nose radius Fay-Riddell heat-flux estimation for the STS Orbiter. The two different colorbar scales highlight the differences due to the local radius approach.	162

List of Figures

4.7	Heat transfer coefficients for different re-entry scenarios and objects characterized by a different nose radius; Mars Pathfinder [Milos et al., 1999], Mars Microprobe [Mitcheltree et al., 1999], 1.6m diameter sphere [Dogra et al., 1992], and Orion CEV [Mehta et al., 2015b].	163
4.8	Normalized bridging functions for different space objects and scenarios, characterizing the geometries with different nose radius. Based on the normalization of data reported in Figure 4.7	164
4.9	Transitional regime normalized bridging model as a function of the local radius and Knudsen number.	165
4.10	Transitional regime normalized variation of the C_H w.r.t. to the local panel radius and inclination angle. Data extracted from the STS-orbiter validation case, reported in page 174.	166
4.11	STRATH-A relative heat-flux distribution computed with the smoothed-local radius formulation, compared to the experimental data reported in [Kemp et al., 1959].	168
4.12	STRATH-A relative heat-flux distribution comparison of CNR and LNR approach. <u>On the left:</u> the comparison of the relative error on the raw experimental data [Kemp et al., 1959]. <u>On the right:</u> comparative analysis of interpolated data aiming at evaluating an averaged relative error for the CNR and LNR.	169
4.13	STRATH-A relative heat-flux distribution: hypersonic continuum regime with local radius formulation.	170
4.14	Relative heat transfer coefficient distribution comparison of CFD, DSMC and STRATH-A data on the IXV model. Sensitivity analysis on the number of local radius smoothing points.	171
4.15	Relative heat transfer coefficient distribution simulated with a classical constant radius approach.	172
4.16	Shuttle Heat Tranfer comparison of flight data with STRATH-A using different models.	173
4.17	Shuttle heat transfer distribution over the surface at 80km computed with STRATH-A using the KRd model and the LNR approach.	173
4.18	Shuttle heat transfer distribution at different altitude on the centerline. The simulations have been performed using STRATH-A with a KRd aerothermal model and Local Radius approach.	174
4.19	Shuttle heat transfer coefficient at the nose for different altitudes.	175
4.20	Validation of the different aerothermal models tested in FOSTRAD and also implemented STRATH-A.	177

List of Figures

4.21	Preliminary validation of FOSTRAD heat-flux surface distribution on Stardust SRC geometry [Falchi et al., 2017c].	177
4.22	Geometrical differences between the Stardust SRC simulated in the present study (bottom) and the one simulated by Trumble [Trumble et al., 2010] on the top.	178
4.23	Mesh and Geometry used for the blunted cone test case.	179
4.24	Blunted code heat transfer coefficient over Knudsen Number.	180
4.25	Blunted code heat transfer coefficient over Knudsen Number. On the right y-axis the relative error is reported wrt to literature data.	180
4.26	Comparison between the C_H distribution on the blunted cone spherical cap. Left: reference data from Moss [Moss and Simmonds, 1987]. Right: simulation results obtained with STRATH-A.	181
4.27	Left: Comparison between the C_H distribution on the entire geometry between the DSMC data and STRATH-A results. Right: comparison between the use of a Local Radius approach and the constant reference nose radius approach.	182
4.28	Payload Fairing and 3rd stage solid rocket motor geometry.	182
4.29	Sensitivity of the local heat transfer distribution to the reference length in the transition rarefied regime.	184
4.30	Payload Fairing and Z9 SRM simplified geometric model simulated at 105km, the particles velocity distribution and the surface heat transfer are reported in the two displayed color scales	184
4.31	Payload fairing Heat transfer distribution comparison between STRATH-A and dsmcFoam+ at 105km (on the left), and 107km (on the right)	185
4.32	Payload fairing Heat transfer distribution comparison between STRATH-A and dsmcFoam+ at 115km (on the left), and 130km (on the right)	185
4.33	Comparison of the PLF nose heat transfer coefficient for a nominal VEGA trajectory.	186
5.1	IXV mesh used for simulating the atmospheric re-entry via STRATH-A. In the mesh are also shown the points later used for reporting the wall temperature distribution over the surface.	188
5.2	IXV Trajectory optimization: angle of attack optimal control law.	190
5.3	IXV atmospheric re-entry: heat-flux optimized trajectory.	191
5.4	IXV atmospheric re-entry: surface temperature distribution computed by STRATH-A and the coupled thermal code.	192
5.5	IXV wall temperature distribution for the re-entry simulated with STRATH-A on the main body centerline.	193

List of Figures

5.6	IXV wall temperature distribution for the re-entry simulated with STRATH-A over the flaps.	193
5.7	Stardust atmospheric re-entry simulated with STRATH-A using 3DOF, highlighting different representative points: final altitude and velocity, drogue trigger timer activation, and maximum heat flux.	195
5.8	Stardust SRC atmospheric re-entry simulation: recession and temperature distribution at the heat-flux peak. The gray mesh is the initial geometry.	196
5.9	Stardust SRC atmospheric re-entry simulation: final time(before the hypersonic drogue opening triggers).	197
5.10	Comparison of Stardust re-entry maximum and averaged wall temperature over altitude, computed with STRATH-A and observed with the SLIT telescope [Winter and Trumble, 2010]. <u>On the left:</u> nominal re-entry trajectory. <u>On the right:</u> re-entry trajectory considering an offset of +6km on the results.	198
5.11	Stardust SRC wall temperature estimation comparison between the re-entry simulated with STRATH-A and ARC against the CFD simulations reported in [Olynick et al., 1999].	198
5.12	Stardust SRC predicted recession distribution at the hypersonic drogue opening time.	199
5.13	Stardust SRC wall recession estimation on the forebody starting from the stagnation point (i.e.: arc length = 0); comparison between the re-entry simulated with STRATH-A and ARC against the CFD simulations reported in [Olynick et al., 1999] for a re-entry time of 80s.	200
5.14	Payload fairing thermal model used to simulate the ascent trajectory, TPS and sandwich thermal capacities are based on typical values found in the literature	201
5.15	On the left - PLF heat transfer for the nominal ascent trajectory simulated with STRATH-A for AofA = 0deg. On the right - enveloping surface heat transfer for AofA = 10deg	202
5.16	On the left - PLF averaged external TPS layer estimated wall temperature. On the right - PLF back-wall estimated temperature	202
5.17	On the left - PLF internally emitted infrared radiation assuming $\epsilon = 0.85$ for the different averaged longitudinal stations. On the right - maximum radiative heat flux absorbed by the payload assuming an unitary view factor and four different infrared emissivity values	203
5.18	Z9 plume radiative heat fluxes as defined in VEGA user manual [Arianespace, 2014]	204

List of Figures

5.19	Dummy payload external wall averaged temperature predictions for different PLF separation times at different reference stations; on the left $T_{\text{PLF,sep}} = 200\text{s}$ and $T_{\text{PLF,sep}} = 215\text{s}$ on the right	205
5.20	Dummy payload external wall averaged temperature predictions for different PLF separation times at different reference stations at the nominal $T_{\text{PLF,sep}} = 231\text{s}$	205
5.21	Dummy payload potential external aerothermal convective fluxes and maximum PLF emitted radiative heat fluxes comparison at various reference stations	206
5.22	Local ablation of a cubic shell made possible by using a 1D thermal-ablation approach.	209
5.23	Voxelization example of complex objects. On the left: full body voxelization of GOCE, on the right: shell voxelization of a complex model of Orion CEV (only a slice has been shown).	212
5.24	Toy satellite initial 3D .stl model assembly (left) and mesh (right) with center of gravities of each singular part (red dots).	213
5.25	Surviving mass probability histogram obtained with the Monte Carlo sampling in the defined interval with the HDMR approach.	217
5.26	Left: Distribution of the flight path angle increment function (i.e.: surviving mass w.r.t. to the central value). Right: surrogate model used for building the increment function distribution.	219
5.27	Left: Distribution of the rotational velocity increment function. Right: surrogate model used for building the increment function distribution.	219
5.28	Left: Distribution of the initial re-entry velocity increment function. Right: surrogate model used for building the increment function distribution.	220
5.29	Left: Distribution of the initial re-entry velocity increment function. Right: surrogate model used for building the increment function distribution.	221
5.30	Aluminum cube angular rotational factor analysis for different initial flight path angles.	222
5.31	Aluminum temperature dependent specific heat and emissivity factor.	223
5.32	Aluminum and copper sphere terminal velocity and correspondent kinetic energy at sea level.	224
5.33	Sphere demise comparison between SCARAB [Koppenwallner et al., 2005] and STRATH-A.	224

List of Figures

5.34	Re-entry scenario simulation block diagram and work-flow for a single break-up event and using a step-by-step aero-aerothermodynamic integration.	228
5.35	Gridded population density of the world, original resolution (0.0417deg) reported in a base-10 log scale.	230
5.36	Gridded population density of the world, reduced resolution (0.5deg) reported in a base-10 log scale.	230
5.37	Cloud of ground impact points for all the 64 simulated re-entry scenarios.	231
5.38	Work-flow diagram for the computation of scenario-averaged statistical casualty risk using surrogate models.	233
5.39	Monte Carlo sampling of the Casualty Risk surrogate model (high resolution grid: 0.0417deg).	234
5.40	Monte Carlo sampling of the Casualty Risk surrogate model (low resolution grid: 0.5deg).	234
5.41	Monte Carlo sampling of the averaged population density casualty risk surrogate model	235
5.42	Work-flow diagram for the computation of object-specific statistical casualty risk using multiple surrogate models for latitude, longitude, and casualty cross section of each spacecraft component.	236
5.43	Discretized ground footprint probability for the first object (BodyID: 1 - one of the two solar panels).	237
5.44	Casualty Area mapped distribution (averaged per bin) for the solar panel.	238
5.45	Casualty area standard deviation distribution for the solar panel. . . .	239
5.46	Probabilistic ground footprint for cubic shell (left), and for the electronic box (right).	239
5.47	Probabilistic casualty risk distribution for one solar panel (left), and for the main body (right).	240
5.48	Total casualty risk distribution computed for the average casualty area.	240
5.49	Total casualty risk histogram computed for the average casualty area, neglecting the non-null casualty risk of the footprint.	241

List of Tables

1.1	Viscosity models coefficients [Bird, 1976, White and Corfield, 2006, Cowling and Chapman, 1970]	36
1.2	Taxonomy for re-entry software currently used [1/2].	80
1.3	Taxonomy for re-entry software currently used [2/2].	81
3.1	GOCE test case inputs for the comparison wrt to [Benedetti et al., 2018]	138
3.2	Configurations evaluated for the C_F	151
4.1	DSMC atmospheric properties: altitude, temperature, mass density, and molecular density	183
4.2	PLF stagnation point heat transfer coefficient comparison between dsmcFoam+ and STRATH-A	186
5.1	Sensitivity analysis results of the surviving mass computed with the AD-HDMR.	217
5.2	Geometric dimensions and mass information for the toy satellite.	226

Nomenclature

Acronyms

ARC Ablative Response Code

CFD Computational Fluid Dynamics

CNR Constant Nose Radius

D4D Design for Demise

DKR Detra-Kemp-Rose aerothermal model

DRAMA Debris Risk Assessment and Mitigation Analysis

DSMC Direct Simulation Monte Carlo

ESA European Space Agency

FM Free Molecular

FMF Free Molecular Flow

FOSTRAD Free and Open Source Tool for Re-entry Analysis of Asteroids and Space Debris

FPA Flight Path Angle [deg]

GOCE Gravity Field and Steady-State Ocean Circulation Explorer satellite

GPW Gridded Population of the World

GSI Gas-Surface Interaction

HDMR High Dimensional Model Representation

HPC High Performance Computer

HS Hard Sphere

Nomenclature

IXV	Intermediate eXperimental Vehicle
LEO	Low Earth Orbit
LHS	Latin Hypercube Sampling
LNR	Local Nose Radius
LPI	Local Panel Inclination
LV	Launcher Vehicle
MF	Multi-Fidelity approach
MFP	Mean Free Path λ
MPMS	Most Probable Molecular Speed
NASA	National Aeronautics and Space Administration
PL	Payload
PLF	Payload Fairing
QK	Quantum Kinetic
SF	Single-Fidelity approach
SM	Surrogate Model
SRC	Stardust Sample Return Capsule
STRATH-A	Spacecraft Tool for Re-entry and Aerothermal Analysis
TPS	Thermal Protection System
UQ	Uncertainty Quantification
VHS	Variable Hard Sphere

Subscripts

∞	Free flow condition
c, cont	continuum regime
fm	free molecular regime
max	maximum reference value

Nomenclature

min	minimum reference value
ref	reference value
s	stagnation point
w	wall

Symbols

α	Side-slip angle [deg]
δ	Atomic diameter [m]
\dot{q}_c	Continuum regime heat transfer [W/m ²]
\dot{q}_{fm}	Free molecular heat transfer [W/m ²]
γ	Specific Heat Ratio $\gamma = \frac{c_p}{c_v}$
λ	Mean free path [m]
μ	Dynamic viscosity [Pa s]
μ_{CE}	Dynamic Viscosity Chapman-Enskog's model [Pa.s]
μ_{pl}	Dynamic Viscosity power-law model [Pa.s]
μ_{Su}	Dynamic viscosity for Sutherland's model [Pa.s]
ω	Viscosity coefficient temperature exponent
\vec{n}	Geometric surface normal vector
ϕ	Angle between surface normal and flow direction [deg]
ρ	Mass density $\left[\frac{\text{kg}}{\text{m}^3} \right]$
ρ_∞	Free flow mass density $\left[\frac{\text{kg}}{\text{m}^3} \right]$
σ_d	collisional cross section [m ²]
σ_{diff}	Diffusive energy accommodation coefficient
τ_{fm}	Free molecular shear stress [Pa]
θ	Angle between surface tangent and flow direction [deg]
ΔT	DSMC simulation time-step [s]

Nomenclature

ΔT_{av}	DSMC averaging time-step [s]
\mathbf{a}	speed of sound [m/s]
A_{ref}	Reference Aerodynamic cross-section [m ²]
C_D	Drag coefficient
C_H	Heat transfer coefficient
C_L	Lift coefficient
C_p	Aerodynamic pressure coefficient
c_p	Constant pressure specific heat [J/kgK]
c_v	Constant volume specific heat [J/kgK]
$C_{M,z}$	Pitching moment coefficient
D_A	Debris casualty Area m ²
E_k	Casualty Risk Estimate
$E_{i,r,w}$	Energy of incident, reflected, and wall temperature, molecules [J]
F_D	Drag force [N]
f_n, f_t	Normal and Tangential accommodation coefficient
$F_{Derr\%}$	Maximum drag force convergence residual
H	Altitude [km]
h_w	Enthalpy at the wall [m]
H_{break}	Break-up altitude [km]
k_b	Boltzmann constant $k_b = 1.3806 \cdot 10^{-23} \text{m}^2\text{kg}/\text{s}^2\text{K}$
Kn	Knudsen number
L_{ref}	Reference length [m]
lat	Latitude [deg]
lon	Longitude [deg]
m	Atomic mass [kg]

Nomenclature

M_∞	Free flow Mach Number
n	Atomic density $[\frac{1}{m^3}]$
$N_{O_2, O, N_2, Ar}$	Atomic density $[\frac{1}{m^3}]$
Nu	Nusselt number
p	Pressure [Pa]
p_∞	Free flow pressure [Pa]
P_D	Population Density $[1/m^2]$
p_{fm}	Free molecular pressure [Pa]
Pr	Prandtl number
q_∞	Dynamic pressure $q_\infty = \frac{1}{2}\rho_\infty V_\infty^2$ [J/kg]
q_{rad}	Radiative heat transfer rate $[W/m^2]$
q_s	Wall heat transfer rate at the stagnation point $[W/m^2]$
q_w	Wall heat transfer rate $[W/m^2]$
R	Specific gas constant $[\frac{J}{kgK}]$
R_N	Nose radius [m]
Re	Reynolds number
$Rot_{y,\alpha}$	side-slip rotation matrix
S_R	Molecular speed ratio $[\frac{V}{MPMS}]$
S_t	Stanton number
S_u	Sutherland's effective temperature [K]
S_{u1}	Sutherland's coefficients
T_0	Reference temperature [K]
T_w	Wall temperature [K]
T_∞	Free stream temperature [K]
T_{ratio}	Temperature ratio $\frac{T_w}{T_\infty}$

Nomenclature

T_w Wall temperature [K]

V Satellite velocity [$\frac{m}{s}$]

V_∞ Free stream velocity [$\frac{m}{s}$]

Publications

1. Falchi, A., Minisci, E., Vasile, M., and Kubicek, M. (2017). Aero-thermal re-entry sensitivity analysis using dsmc and a high dimensional model representation-based approach. In 7th European Conference on Space Debris.
2. Falchi, A., Minisci, E., Vasile, M., Rastelli, D., and Bellini, N. (2017). Dsmc-based correction factor for low-fidelity hypersonic aerodynamics of re-entering objects and space debris. In 7th European Conference for Aeronautics and Space Sciences, pages 1-15.
3. Falchi, A., Renato, V., Minisci, E., and Vasile, M. (2017). Fostrad: An advanced open source tool for re-entry analysis. In 15th Reinventing Space Conference.
4. Falchi, A., Minisci, E., Kubicek, M., Vasile, M., and Lemmens, S. (2018). Hdmr-based sensitivity analysis and uncertainty quantification of goce aerodynamics using dsmc. In Stardust Final Conference, pages 301-323. Springer.
5. Falchi, A., Gentile, L., Minisci, E., Tirelli, M., and Perugini, P. (2019). Launcher vehicle aerothermodynamics and fairing separation altitude effects on payload temperature. In 8th European Conference for Aeronautics and Space Sciences, pages 1-16.
6. Benedetti, G., Viola, N., Minisci, E., Falchi, A., and Vasile, M. (2018). Low-fidelity modelling for aerodynamic characteristics of re-entry objects. In Stardust Final Conference, pages 247-264. Springer.

Introduction

1.1 Motivation

In the latest decades the number of space objects orbiting around Earth has always been increasing, although, just a minor fraction are active satellites. Most of the orbiting objects may be considered space debris, which are inactive satellites, fragments generated due to collisions between different active or inactive, natural or artificial space debris, or fragments generated after explosions of satellites or space accidents. Independently from their origin, space debris range through a wide variety of dimensions and shapes, and they pose a threat to other active objects. As it was forecast by Kessler in the 1978 [Kessler and Cour-Palais, 1978], the number of orbiting space debris, if no corrective action is taken, may be expected to exponentially increase. This is due to a cascade collision effect, where each new collision will generate more space debris which leads to an always increasing probability of new collisions up to a point where the natural occurring cleansing of the Earth orbits will not be enough to maintain usable orbits. In order to prevent this run-away scenario, where any human remediation attempt would be futile, it has been deemed as paramount to actively reduce the number of newly generated space debris, and reduce the time inactive satellites remain orbiting around the Earth.

Since the always growing number of space debris is posing a threat to the usage of sensible strategic orbits, and to any space operation or mission. A number of initiatives with the aim of reducing the impact of any new space mission to the current catalogue of space debris has been planned by ESA and NASA. Different strategies range from the active debris removal [Liou et al., 2010, Bonnal et al., 2013] to the establishment of guidelines with the scope of limiting the end-of-life satellite de-orbiting time, or defining the graveyard orbits where the satellite should be at its end-of-life. Many different concepts have been proposed for active debris removal strategies: drag augmentation devices, de-orbiting propulsion systems, on-orbit capture devices. Their applicability highly depends on the orbital regime, mass removal efficiency, and associated risks [Klinkrad and Johnson, 2009]. In LEO, one of the feasible methods is reducing the post end-of-life orbital time taking advantage of the aerodynamic drag, and causing the satellite to slowly de-orbit toward the Earth.

During the atmospheric re-entry, thanks to the harsh environment, characterized by a hypersonic velocity, extremely high structural and heating loads, can cause the complete destruction and ablation of the satellite and its internal component. Although, the components made of heat resistant materials (e.g.: titanium fig. 1.1) having a high melting temperature, or a low area-to-mass ratio, may survive the re-entry, posing a

threat to the human population. In the latest years, the concept of Design for Demise (D4D) has found its place among the design drivers, aiming at reducing the probability of a re-entering satellite to survive, and generally reducing the risk associated with its re-entry.

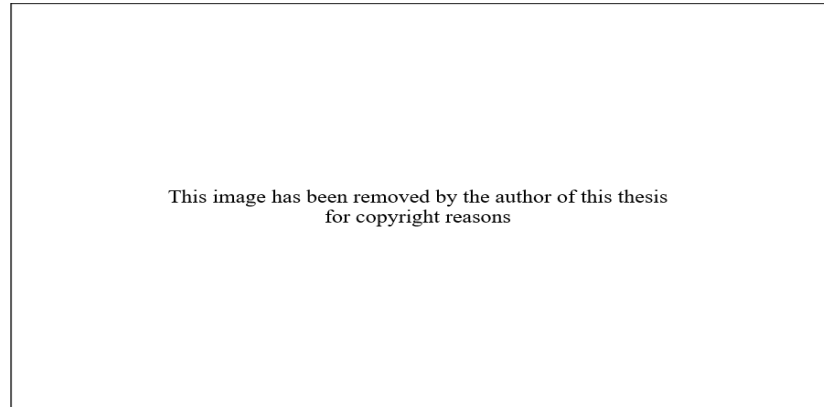


Figure 1.1: Titanium tank surviving the atmospheric re-entry (available at <https://orbitaldebris.jsc.nasa.gov/photo-gallery> - ©Space Research Institute, King Abdulaziz City for Science and Technology, Riyadh, Saudi Arabia, last accessed 31 May 2020)

The work described in this thesis focuses on the development of a low-fidelity simulation suite aiming at studying re-entry scenarios from different perspectives: uncontrolled space debris re-entries to evaluate their surviving probabilities and a statistical impact footprint, and controlled spacecraft re-entries providing the capability to evaluate their optimal trajectories, maximum heat loads, designing and optimizing their thermal protection systems. Such a tool would allow the detailed study of D4D techniques and approaches, and statistically study the impact of each change in the casualty risk, surviving mass, and impact footprint. The software, being conceived as open source and low-fidelity, would allow the user to arbitrarily implement his own D4D solutions during a preliminary design phase, investigating a wide range of solutions. Indeed, as it has been illustrated in the previous years [Kelley, 2012, Waswa and Hoffman, 2012], a variety of solutions to reduce the survivability may be identified, from the system level, to the material, shape and layout change. In the latest years, a material change on most critical components has been tested in different instances [Grassi et al., , Riley et al., 2016]. Sometimes simulations with high-fidelity CFD- or DSMC-based tools are required to gain a better understanding of different phenomena, although, running simulations with such software may often require several days and weeks to test few design points, while a low fidelity approach will provide the opportunity of investigating a wider range of solutions and include a statistical uncertainty quantification approach.

During this research work, many fellow researchers from a wide range of institutes, universities, and industrial companies have expressed the need for having a comprehensive tool for facilitating and enabling their research in the field of re-entry and ascent of space objects. A low-fidelity methodology may allow the rapid characterization and preliminary estimation of aerodynamic coefficients, aerothermal heating, preliminary design of LEO trajectories, characterization of thermal protection systems, preliminary sizing of thermal shields, assessment of re-entry footprint and many other applications. Having identified such a need from the scientific community, this thesis has the aim of summarizing and providing a comprehensive analysis of low-fidelity methods for hypersonic aerodynamics and aerothermodynamics potential applications and assess their level of confidence and range of error. In addition, the implementation of the aggregation of required methods is thoroughly described and explained, introducing some innovative concepts allowing a better accuracy from the aerodynamics and aerothermodynamics point of view. The actual implementation in a reference software called STRATH-A (Spacecraft Tool for Re-entry and Aerothermal Analysis) is presented, the Open-Source nature of the programmed tool will allow the scientific community to take advantage from this thesis theoretically and practically by providing the direct access to the developed tool.

1.2 Thesis outline

The structure of this work is defined to allow the reader a smooth escalation from the theory behind the atmospheric Re-entry of spacecraft to their practical application, explaining the techniques and methods developed during this research for performing complete atmospheric re-entry analysis.

In the first chapter the simplified hypersonic formulation for aerodynamics and aerothermodynamics, focusing on the Local Panel Inclination methods, describing the different formulation that have been proposed over the years. In the second part of chapter 1, a brief description of the commonly used re-entry software at different space agencies, research centers, and companies is presented; highlighting the differences between all the different available (and not) software.

In the second chapter, the investigated methodology implemented in the Free and Open Source Tool for Re-entry Analysis of Asteroids and Space Debris (FOSTRAD) and the later developed STRATH-A is described. Introducing the methodologies and the innovative content of the thesis; then the required steps for performing a complete re-entry analysis are described; the application of graphical rendering technique for using the local panel methods is presented; different methods for increasing the accuracy of aerodynamic and aerothermal heating estimation are highlighted, the necessary steps

Chapter 1. Introduction

to manipulate the geometrical mesh for applying the local panel inclination methods are reported.

In the third chapter, the aerodynamic methodology as implemented in STRATH-A is validated with respect to various literature cases such as: a sphere, the Space Shuttle Orbiter, Orion Crew Exploration Vehicle and Mars Microprobe. Drag, lift, and moment coefficients are compared against experimental and computational fluid dynamics data in order to assess the error range to be expected among the different rarefaction regimes (i.e.: continuum, transitional, and free molecular). The mesh convergence is validated against the Gravity Field and Steady-State Ocean Circulation Explorer satellite.

In the fourth chapter, the aerothermodynamics are investigated providing a general description of the LPI application, a set of generalized bridging functions for different geometries are provided. The chapter follows with validation study cases aiming at assessing the heat transfer distribution of simple and complex objects: the Space Shuttle Orbiter, Stardust Sample Return Capsule, a blunted cone, and the VEGA launcher vehicle Payload Fairing.

In the fifth chapter, the application of the developed framework to different study cases is presented: the controlled gliding atmospheric re-entry of the ESA Intermediate Experimental Vehicle (IXV), the simulation of the uncontrolled ballistic re-entry of Stardust Sample Return Capsule (SRC) with the coupled thermal protection system ablation, the VEGA Payload Fairing temperature estimation during the ascent phase, and last but not least a mock satellite uncontrolled re-entry break-up analysis for estimating the impact footprint and assessment of a break-up strategy implementation.

The thesis ends with the sixth chapter containing the concluding remarks, future developments and possible areas of improvement.

1.3 Atmospheric Reentry Aerodynamics and Aerothermodynamics

Atmospheric reentries are generally assumed to begin at the entry interface at 120km. At this altitude the orbiting spacecraft has a velocity of approximately 7800m/s (circular orbit approximation). It is immediate to imagine that for a significant part of the reentry the object will be subjected to a hypersonic flow. The velocity regime is generally characterized by the Mach Number (M_∞), defined as the ratio between the relative velocity between the undisturbed flow and the space object (V_∞) and its speed of sound (a):

$$M_\infty = \frac{V_\infty}{a} \quad (1.1)$$

The velocity regimes are usually characterized as it follows [Anderson Jr, 2000]:

- Subsonic (incompressible) $M_\infty \leq 0.3$
- Subsonic (compressible) $0.3 \geq M_\infty \geq 0.8$
- Transonic $0.8 \geq M_\infty \geq 1.2$
- Supersonic $1.2 \geq M_\infty \geq 5$
- Hypersonic $5 \geq M_\infty$

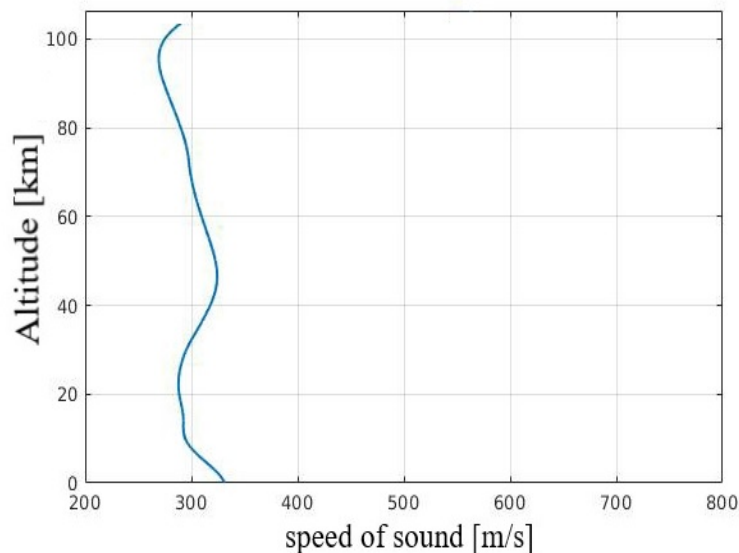


Figure 1.2: Speed of Sound over atmospheric altitude (using a reference NRLMSISE00 atmospheric model [Picone et al., 2002])

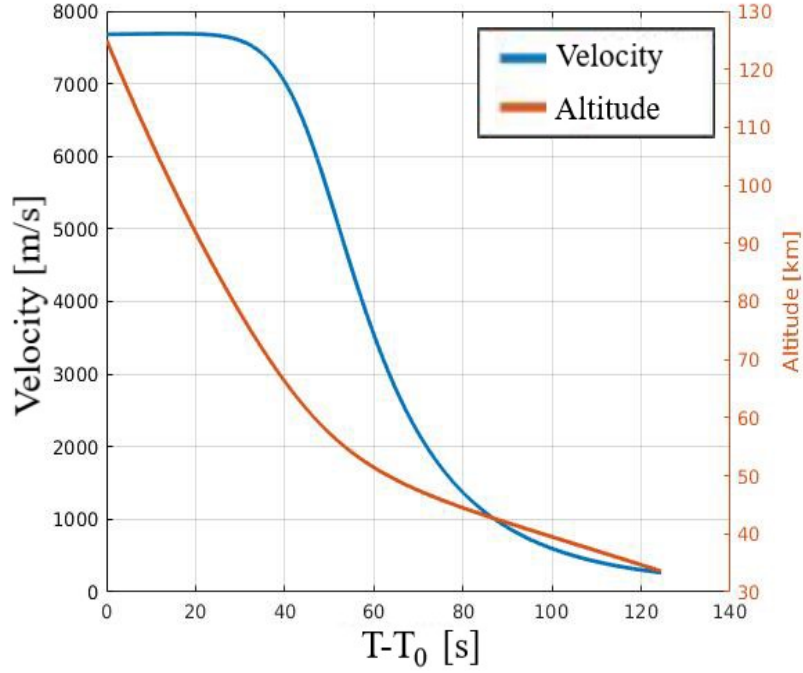


Figure 1.3: Typical velocity profile for a ballistic reentry from a circular orbit

The speed of sound computed as ($a = \sqrt{\gamma RT_\infty}$, for a typical NRLMSISE00 atmospheric database [Picone et al., 2002]) over the atmospheric altitude has the profile shown in fig. 1.2, while a typical ballistic reentry can be generally characterized by the velocity profile shown in fig. 1.3. For such reentries, which are typical of space debris, it is immediate observing how the object will be characterized by a hypersonic Mach Number till 40~50 km, the gradually slowing to the hypersonic, transonic and then subsonic regime. It becomes intuitive that for simulating the complete reentry of a space debris or a spacecraft, the software should be able to model all the different velocity regimes.

Another challenging aspect for reentry simulation are the different rarefaction regimes encountered by the spacecraft. In fact, at the reentry interface the atmosphere is highly rarefied, and then it becomes gradually thicker. The Knudsen Number (Kn) is commonly used to define the degree of rarefaction:

$$\text{Kn} = \frac{\lambda}{L_{\text{ref}}} \quad (1.2)$$

Where λ is the *Mean Free Path* (MFP), and L_{ref} is the reference scale of the considered system.

Assuming that the gas has a uniform Maxwellian velocity distribution, the mean

free path can be defined as [Cowling and Chapman, 1970]:

$$\lambda_{\text{HS}} = \frac{1}{\sqrt{2n}\sigma_d} \quad (1.3)$$

where n is the atomic density [atoms/m³], and σ_d is the collisional cross section [m²], which for a Hard sphere (HS) model (which assumes a constant molecular diameter, δ) $\sigma_d = \pi\delta^2$.

If a Variable Hard Sphere (VHS) molecular model is assumed, the mean free path for a rarefied gas [Bird, 1983] can be defined as:

$$\lambda_{\text{VHS}} = \left(\frac{2\mu}{15\rho_\infty} \right) (7 - 2\omega) (5 - 2\omega) \frac{1}{\sqrt{2\pi R T_\infty}} \quad (1.4)$$

Where μ is the dynamic viscosity, ρ_∞ is the density, ω is the viscosity temperature exponent, T_∞ is the atmospheric temperature, and R is the specific gas constant.

Another common way of defining the mean free path without knowing the molecular diameter is:

$$\lambda_\mu = \frac{\mu}{p} \sqrt{\frac{\pi k_B T_\infty}{2m}} \quad (1.5)$$

where p is the pressure, k_B is the Boltzmann constant, and m is the atomic mass. This estimation method assumes a Hard Sphere model, but it is highly dependent on the model used for the viscosity, which can be computed with the general Sutherland dynamic viscosity relationship [Sutherland, 1893]:

$$\mu_{S_u} = \mu_0 \left(\frac{T_\infty}{T_0} \right)^{3/2} \frac{T_0 + S_u}{T_\infty + S_u} \quad (1.6)$$

or

$$\mu_{S_u} = S_{u1} \frac{T^{3/2}}{T_\infty + S_u} \quad (1.7)$$

where μ_{S_u} is the viscosity computed with Sutherland's model, μ_0 is the viscosity at a reference temperature (T_0), and S_u is the Sutherland's effective temperature, while S_{u1} is the Sutherland coefficient [White and Corfield, 2006]. Sutherland's model is valid for a temperature below 555K [Smits and Dussauge, 2006], which implies that it should not be used for atmospheric altitudes where the translational temperature is above that limit. For rarefied gas the viscosity can be computed with the Chapman-Enskog model [Hirschfelder et al., 1954]:

$$\mu_{\text{CE}} = \frac{5m}{16\pi\delta^2} \sqrt{\pi R T_\infty} \quad (1.8)$$

Table 1.1: Viscosity models coefficients [Bird, 1976, White and Corfield, 2006, Cowling and Chapman, 1970]

Species	ω	δ_{HS} [m $\times 10^{-10}$]	δ_{VHS} [m $\times 10^{-10}$]	S_u [K]	S_{u1} [m $\times 10^{-6}$]
O	0.80*	3.0*	3.0*	127	1.693
N ₂	0.74	3.784	4.17	111	1.407
O ₂	0.77	3.636	4.07	127	1.6934
Ar	0.81	3.659	4.17	144	21.25
N	0.8*	3.0*	3.0*	111	1.407
He	0.66	2.33	2.33	79.4	1.484
H	0.8*	3.0*	3.0*	72	0.636

* Reference values

Another common way but less accurate [Sutherland, 1893] to define the viscosity is using the power-law defined as:

$$\mu_{pl} = \mu_0 \left(\frac{T}{T_0} \right)^\omega \quad (1.9)$$

where ω is the previously cited (eq. 1.4) viscosity temperature exponent.

In Table 1.1 are reported typical coefficients required for computing the viscosity for different atomic species. The atmospheric models such as the US 1976, or the NRLMSISE00 [Picone et al., 2002] provide the atomic density for each atomic species, allowing to determine molecular averaged properties.

1.3.1 Knudsen Number

The Knudsen number is generally used for defining a flow rarefaction degree, which determines the methods that can be used for resolving the flow field and flow-structure interactions. The following regimes are generally assumed:

- $Kn \geq 10$ - free molecular regime (methods: collision-less Boltzmann equation, Test Particle Monte Carlo, Direct Simulation Monte Carlo)
- $0.1 \leq Kn \leq 10$ - transitional regime (methods: Boltzmann equation, Direct Simulation Monte Carlo)
- $0.001 \leq Kn \leq 0.1$ - slip regime (method: Navier-Stokes-Fourier equations with velocity slip)
- $Kn \leq 0.001$ - continuum flow regime (method: Navier-Stokes-Fourier)

Using the equations from 1.2 to 1.5, in combination with the different viscosity models (eq. 1.7, 1.8, 1.9), and the NRLMSISE atmospheric model for obtaining the

various atmospheric properties, it is possible to investigate the influence of each model on the determination of the flow regime. Determining in which atmospheric regime is paramount to define which methodology can be used to assess the aerothermodynamic properties during the atmospheric reentry. The mean free path for the different models is reported in Figure 1.4; if the system reference scale is 1m λ is equal to Kn, thus the same analyses can be extended to Kn.

Using eq. 1.5, λ_μ can be computed without knowing the average molecular diameter by assuming that the hard sphere molecules have the same viscosity as the one computed with either Sutherland models ($\lambda_{\mu, Su}$, eq. 1.7) or the viscosity power law ($\lambda_{\mu, pl}$, eq. 1.9). Although, Sutherland's model should not be used for temperature above 555K, therefore, it requires to check the atmospheric temperature across the altitude range (reported in the right axis of fig. 1.5), the results show that Sutherland's model should be used up to 125km. If the average molecular diameter is known, it is possible to use Chapman-Enskog model according to Bird's definition, which is based on the VHS model and should provide more realistic results [Bird, 1983] ($\lambda_{\mu, VHS}$, eq. 1.4). Another option would be using the Hard Sphere model assuming the Maxwellian probabilistic velocity distribution (λ_{HS} eq. 1.3), or using eq. 1.5 in combination with Chapman-Enskog model ($\lambda_{\mu, CE}$). Although, it must be reminded that the Chapman-Enskog model is valid for diluted gases, thus it should not be used below transitional regime (i.e.: an altitude from 100km to 125km). The results would suggest the use a combination of Sutherland in the continuum and slip-flow regime and Bird's VHS model, or the more simple model λ_{HS} whose results lay between $\lambda_{\mu, VHS}$ and $\lambda_{\mu, Su}$.

The viscosity does not influence only the Knudsen number, but also many of the different aerothermodynamic properties computed during the various stages of a reentry at different altitudes. In this paragraph it is reported an analysis of the different models previously explained. Assuming the Kn (or λ) defined with the HS model (λ_{HS} eq. 1.3), an analysis showing the viscosity over Kn, all the atmospheric properties have been computed with a reference NRLMSISE00 atmospheric model for an altitude ranging from 0 to 500km is reported in Figure 1.5, showing how the different models lead to a significant difference in the viscosity estimation. Sutherland's model (μ_{Su} , 1.7) and the viscosity computed with the power law match quite well within the limit for Sutherland's model validity ($T_\infty < 555K$). Chapman-Enskog model with the molecular diameter defined via the VHS model is sensibly lower than the other two models, and the estimation in the continuum regime is inaccurate, while the other two models are overestimating the viscosity in the transitional and free molecular regime.

The proposed solution, which in order to obtain a model which is valid throughout all regimes, is to use the Sutherland's model in the continuum regime and Chapman-Enskog with the VHS molecular diameter for the free molecular regime. While a bridging

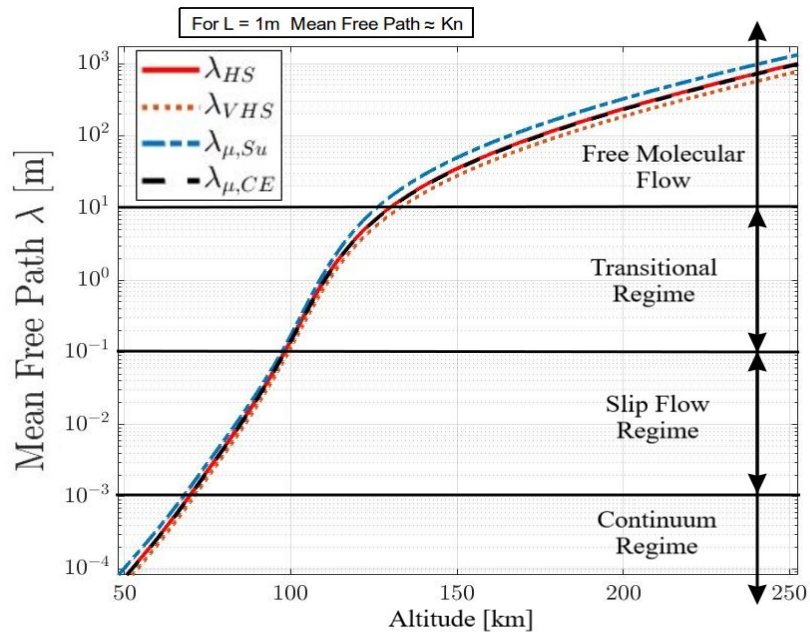


Figure 1.4: Knudsen Number over altitude, computed with different models: the Hard Sphere model with Maxwellian molecular velocity distribution (λ_{HS} eq. 1.3), the Variable Hard Sphere model (λ_{VHS} , eq. 1.4), and using the viscosity approach with Sutherland's and Chapman-Enskog's models ($\lambda_{\mu,Su}$, $\lambda_{\mu,CE}$, eq. 1.5 with the respective viscosity models eq. 1.7 and 1.8)

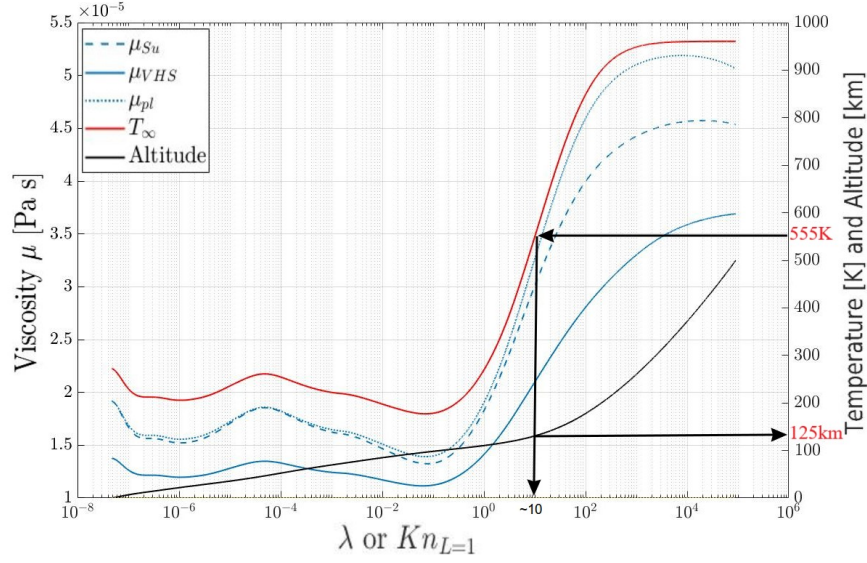


Figure 1.5: Viscosity computed with the NRLMSISE00 Atmospheric model, for altitudes from 0 to 500km, and the different relationships: Sutherland’s (μ_{Su} , 1.7), Chapman-Enskog with VHS diameter (μ_{VHS} , 1.8), power law (μ_{pl} , 1.9), plotted against λ (equivalent to Kn for $L = 1$); Temperature and Altitudes plotted on the right axis

function between the free molecular and continuum regime may be used. In order to avoid discontinuities, a Kn -based Surrogate Model may be used:

$$\mathbb{M} = f(\mu_{Su}, \mu_{VHS}, Kn) \quad (1.10)$$

In order to obtain a smooth transition for the viscosity a Piecewise Cubic Hermitian interpolation [Fritsch and Carlson, 1980] can be used; selecting the viscosity values between the lower and upper boundaries of the transitional regime ($Kn = 0.1$ and $Kn = 10$ respectively) the two models will be within their validity limits. An explicative result is shown in Figure 1.6.

1.3.2 Free Molecular Flow Regime

At the very beginning of an atmospheric re-entry, the spacecraft is more likely be within the free molecular flow (FMF) regime. At the entry interface (usually assumed at 125km), the free flow around a space object is characterized by a $\lambda \approx 10m$ (as shown in Fig. 1.5), this value is highly dependent on the atmospheric conditions and it will change throughout the year [Hedin, 1991] (e.g.: the density sensibly change depending on the solar activity). When simulating a satellite re-entry, the initial state vector could also be defined from a higher altitude, meaning that the simulation will most

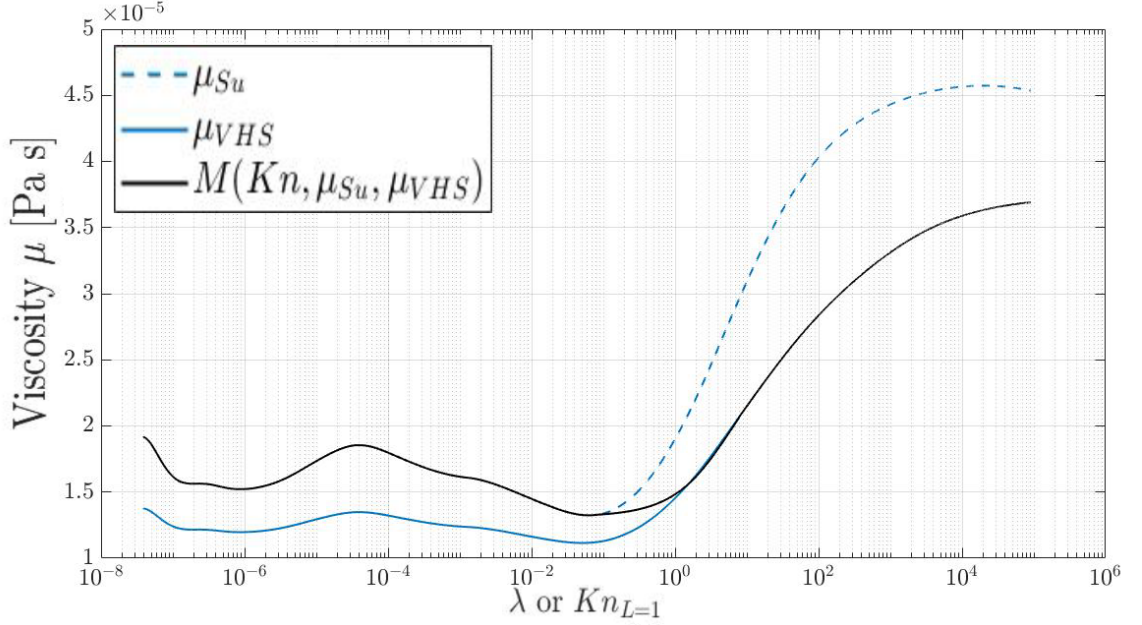


Figure 1.6: Viscosity bridging function for the transitional regime computed with the for altitudes from 0 to 500km, based on Sutherland's in the continuum regime (μ_{Su} , 1.7), and Chapman-Enskog with VHS diameter in the FM regime (μ_{VHS} , 1.8)

likely start from a FMF regime. In such regime, the collisions among the molecules are so rare that it can also be defined as "collisionless". When the particles impact onto the spacecraft surface, their remittance and scatter will not disturb the free flow, meaning that alteration of the free flow properties due to the presence of the body is negligible. In the FMF the velocity may be assumed by its Maxwellian distribution superimposed to the spacecraft velocity, and when a molecular impact the body surface it will have a negligible probability of impacting the body a second time. Thanks to this assumption the flow of incident molecules and re-emitted molecules can be considered separately. Although, when the molecules impact the body, there is a exchange of energy and momentum between the two, and the velocity of the re-emitted molecules depends on the amount of energy that has been exchanged. In this energy transfer phenomena an important role is played by the wall temperature, and is generally described by the energy accommodation coefficient [Moe et al., 1998], defined as:

$$\sigma_{\text{diff}} = \frac{E_i - E_r}{E_i - E_w} \quad (1.11)$$

where σ_{diff} is the energy accommodation coefficient (the subscript "diff" means diffusive, since it is also a measure of how the particles are re-emitted reflectively or diffu-

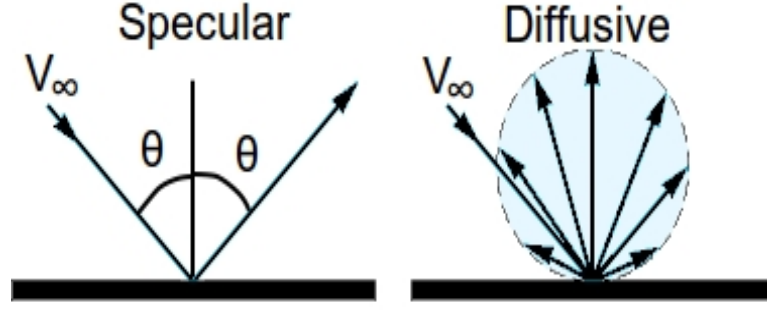


Figure 1.7: Example for specular and diffusive reflection models

sively). E_i and E_r are the energy per unit area per second of the incident and re-emitted molecules respectively, and E_w is the energy that the stream of molecules would have if they were re-emitted with a Maxwellian velocity probability distribution correspondent at the body surface temperature (T_w). The two extreme scenarios are defined by a complete accommodation ($\sigma_{diff} = 1$) and a complete reflection of the stream ($\sigma_{diff} = 0$). This two possible condition are identified with the diffusive and specular reflection respectively (Figure 1.7), the specular reflection was firstly considered by Newton, where the molecules impacting a surface were reflected with a tangent velocity with unaffected velocity, but in the reality such a condition is rarely found. As was later assumed by Maxwell, the molecules impinging a surface were trapped and then re-emitted with a velocity probability distribution close to the one determined by the surface temperature. This behavior may be explained considering that in the micro-scale surfaces cannot be considered smooth. Although, as it was later reported by Schaaf [Schaaf, 1953], using a single coefficient for describing the gas-surface interaction was not accurate, and two different coefficient for respectively the tangential and normal accommodation were defined:

$$f_n = \frac{p_i - p_r}{p_i - p_w} \quad (1.12)$$

$$f_t = \frac{\tau_i - \tau_r}{\tau_i} \quad (1.13)$$

where f_t is the tangential accommodation coefficient, while f_n refers to the normal accommodation coefficient, and the subscripts i , r , and w represents the incident, reflected, and wall normal/tangential momentum.

Even though theoretical distinction should be made to discern the different reflection modes, Estermann [Estermann, 1955] has highlighted that the tangential coefficient values lie between 0.8 and 1, and all experimental evidences have shown that the reflection is mainly diffusive, meaning that also the normal accommodation coefficient should be

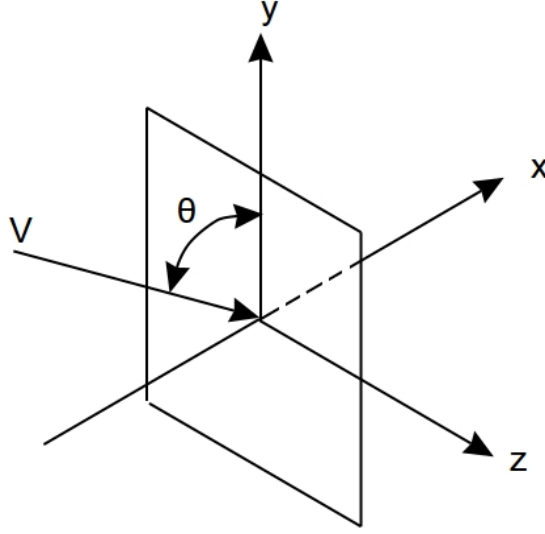


Figure 1.8: Flat plate in a free molecular flow

close to 1. Tests on different materials have shown that for air under static conditions the accommodation coefficient vary between 0.87 and 0.97 [Wiedmann, 1946], and it is influenced by adsorption phenomena by the surface material [Goodman, 1980]. Additionally, also the surface temperature and surface inclination influences the energy accommodation coefficient [Wachman, 1962].

In the specific application of satellite aerodynamics and aerothermodynamics, the diffusive accommodation coefficient is generally assumed to be equal to 0.93 [Cook, 1965, Moe et al., 1998], and no distinction is made between tangential and normal components.

By definition, in a free molecular flow, the object has little or no influence on the flow field. Thus, to derive the aerodynamic and aerothermodynamic properties of an object in this regime it is possible to consider the problem reduced to a flat plate immersed in a flow of molecules having a Maxwellian velocity distribution dependent on the temperature and a superimposed mean velocity (Figure 1.8), which is given by [Kennard et al., 1938]:

$$\mathbb{F}(c_x, c_y, c_z) = \frac{n_\infty}{(2\pi RT_\infty)^{3/2}} \exp \left[-\frac{(c_x - \bar{V} \sin \theta)^2 + (c_y + \bar{V} \cos \theta)^2 + c_z^2}{2RT_\infty} \right] \quad (1.14)$$

where \mathbb{F} is the atomic density in a probabilistic velocity interval, n_∞ is the total atomic density, R is the specific gas constant for a perfect gas, \bar{V} is the mean superimposed

velocity (i.e.: V_∞), θ is the incidence angle defined as in Figure 1.8, $c_{x,y,z}$ are the molecular velocity defined in such a way that $f(\mathbf{dc}_x, \mathbf{dc}_y, \mathbf{dc}_z)$ will determine the atomic density of molecules having a velocity between c_x and $c_x + \mathbf{dc}_x$, c_y and $c_y + \mathbf{dc}_y$, and c_z and $c_z + \mathbf{dc}_z$. Observing the geometry of the problem, the molecule flux can be defined as:

$$N_i = \int_{-\infty}^{\infty} \int_{-\infty}^{\infty} \int_0^{\infty} c_x \mathbb{F} \, \mathbf{dc}_x \mathbf{dc}_y \mathbf{dc}_z \quad (1.15)$$

Considering the two above defined equations, and defining the ratio of the mean velocity and the average Maxwellian molecular velocity as the *Molecular Speed Ratio*:

$$S_R = \frac{V_\infty}{\sqrt{2RT_\infty}} \quad (1.16)$$

or as a function of M_∞ :

$$S_R = M_\infty \sqrt{\frac{\gamma}{2}} \quad (1.17)$$

taking into account the definition of the tangential and normal accommodation coefficients, along with the momentum conservation on particle flux impacting on the flat plate as thoroughly described in [Hayes, 1959], it is possible to obtain the pressure acting on the surface:

$$p_{fm} = \frac{\rho_\infty V_\infty^2}{2S_R^2} \left\{ \left[\frac{(2-f_n)}{\sqrt{\pi}} (S_R \sin \theta) + \frac{f_n}{2} \sqrt{\frac{T_w}{T_\infty}} \right] e^{-(S_R \sin \theta)^2} + \left[(2-f_n) \left(S_R^2 \sin^2 \theta + \frac{1}{2} \right) + \frac{f_n}{2} (S_R \sin \theta) \sqrt{\frac{\pi T_w}{T_\infty}} [1 + \operatorname{erf}(S_R \sin \theta)] \right] \right\} \quad (1.18)$$

while the tangential shear component is:

$$\tau_{fm} = \frac{f_t \rho_\infty V_\infty^2 \cos \theta}{2S_R \sqrt{\pi}} \left\{ e^{-(S_R \sin \theta)^2} + \sqrt{\pi} (S_R \sin \theta) [1 + \operatorname{erf}(S_R \sin \theta)] \right\} \quad (1.19)$$

Observing the two momentum transfer equation, it is evident that the inclination angle θ has a significant influence on the overall pressure and shear distribution, while the velocity V_∞ (or in the form of S_R , as defined in eq. 1.17) along with the surface temperature ratio $\frac{T_w}{T_\infty}$ determine the maximum momentum transfer. In the above equations, $\operatorname{erf}(x)$ is the error function, defined as:

$$\operatorname{erf}(x) = \frac{2}{\sqrt{\pi}} \int_0^x e^{-t^2} dt \quad (1.20)$$

The equations 1.71-1.72 can be further simplified by considering that the term $\frac{\rho V_\infty^2}{2}$ is

the dynamic pressure, and so deriving the same form reported by Schaaf and Chambre [Chambre and Schaaf, 1961] as in eq. 1.71-1.72.

It is now essential to estimate the energy transfer to the flat plate, which referring to eq. 1.11 can be defined as:

$$\dot{q}_{fm} = \sigma_{diff}(E_i - E_w) \quad (1.21)$$

where E_i is the energy of the molecules impacting the surface, and E_w is the energy of molecules re-emitted from the surface, which depends on the wall surface temperature (T_w), while the coefficient σ_{diff} defines the amount of reflected molecules, which have an unchanged internal energy. The energy of the molecules can be broken down down to the contribution of the internal energy ($E_{i,int}$) and translational kinetic energy ($E_{i,tr}$). Assuming the following:

- Steady state: number of impinging and re-emitted molecules is the same
- Re-emitted molecules leave the surface with a Maxwellian velocity distribution, according to T_w
- perfect gas: internal degrees of freedom $j_{int} = (5 - 3\gamma)/(\gamma - 1)$ (where γ is the specific heat ratio)

it is possible to determine the heat transfer flux as [Hayes, 1959]:

$$\dot{q}_{fm} = \sigma_{diff} p_{\infty} \sqrt{\frac{RT_{\infty}}{2\pi}} \left\{ \left[S_R^2 + \frac{\gamma}{\gamma-1} - \frac{\gamma+1}{2(\gamma-1)} \frac{T_w}{T_{\infty}} \right] \left[e^{-(S_R \sin \theta)^2} + \sqrt{\pi} (S_R \sin \theta) [1 + \operatorname{erf}(S_R \sin \theta)] \right] - \frac{1}{2} e^{-(S_R \sin \theta)^2} \right\} \quad (1.22)$$

By considering the eq. 1.17 and the perfect gas law, This equation can also be derived in the form of:

$$\dot{q}_{fm} = \frac{\sigma_{diff} \rho_{\infty} V_{\infty}^3}{4S_R^3 \sqrt{\pi}} \left\{ \left[S_R^2 + \frac{\gamma}{\gamma-1} - \frac{\gamma+1}{2(\gamma-1)} \frac{T_w}{T_{\infty}} \right] \left[e^{-(S_R \sin \theta)^2} + \sqrt{\pi} (S_R \sin \theta) [1 + \operatorname{erf}(S_R \sin \theta)] \right] - \frac{1}{2} e^{-(S_R \sin \theta)^2} \right\} \quad (1.23)$$

Using the equations 1.18, 1.19, and 1.23 it is possible to estimate the normal and shear forces along with the heat transfer of flat plate in a free molecular flow. Since in this specific regime the assumption is that the body presence does not significantly influence the surrounding flow field, and the particle flow impacting the body surface is at a steady state, an arbitrary body shape can be discretized using a sufficiently high number of panels, which are representative of flat plates. Integrating the contribution

of each panel provides an estimate of the total forces, moments and heat transfer on the body surface. This approach is generally known as Local Panel Inclination method [Anderson Jr, 2000].

With the specific application of an atmospheric re-entry, and in order to understand which are the boundaries of the previously defined equations, it is interesting to assume the scenario with the following assumptions:

- A sufficiently high velocity ($S_R \rightarrow \infty$)
- A body which is not too slender (i.e.: on the average the term $S_{R,i} \sin \theta_i \gg 1$)
- A complete diffusive accommodation (i.e.: $\sigma_{\text{diff}} = f_t = f_n = 1$)
- A cold wall condition (i.e.: $T_\infty \gg T_w$)

it is possible to simplify and estimate the eq. 1.18, 1.19, and 1.23 obtaining the following conditions:

$$p_{fm} = \rho_\infty V_\infty^2 \sin^2 \theta \quad (1.24)$$

$$\tau_{fm} = \rho_\infty V_\infty^2 \sin \theta \cos \theta \quad (1.25)$$

$$\dot{q}_{fm} = \frac{1}{2} \rho_\infty V_\infty^3 \sin \theta \quad (1.26)$$

Assuming a flat plate in the low earth orbit, with a circular orbit velocity ($V_\infty \approx 7600\text{m/s}$, which leads to a $S_R \geq 20$), the above mentioned conditions are verified, and assuming a flow normal to the flat plate (i.e.: $\theta = 90\text{deg}$), the maximum heat flux is $\frac{1}{2} \rho_\infty V_\infty^3$. While in a flow reference frame the maximum drag per unit unit area is $\rho_\infty V_\infty^2$, which can be used for estimating the maximum energy dissipation rate by multiplying for the velocity, thus obtaining: $\rho_\infty V_\infty^3$, where the maximum heat flux absorbed by the body is 50% of the maximum energy dissipation rate. The maximum heat flux can also be used to define the heat transfer coefficient:

$$C_H = \frac{2\dot{q}}{\rho_\infty V_\infty^3} \quad (1.27)$$

where \dot{q} is the total heat transfer rate. It is interesting noting the similarity with the Stanton Number (S_t), commonly defined as the ratio of heat transferred to a fluid and the fluid thermal capacity, or in terms of Nusselt (Nu), Reynolds (Re), and Prandtl numbers Pr :

$$S_t = \frac{H_c}{\rho_\infty V_\infty c_p} = \frac{Nu}{Re Pr} \quad (1.28)$$

where H_c is the convection heat transfer coefficient. In order to find a similarity with eq. 1.27, multiplying both members by $(T_s - T_w)$ (stagnation and wall temperature,

respectively):

$$S_t(T_s - T_w) = \frac{H_c(T_s - T_w)}{\rho_\infty V_\infty c_p} \quad (1.29)$$

which can be written as:

$$S_t = \frac{q_c}{\rho_\infty V_\infty (h_s - h_w)} \quad (1.30)$$

where h_s and h_w are the stagnation and wall enthalpy respectively and the subscript c indicates the convective heat transfer rate. If we assume a complete accommodation, and a hypersonic flow, the wall enthalpy may be neglected (i.e.: $c_p T_s \gg c_p T_w$), thus the stagnation enthalpy may be approximated with the total enthalpy (i.e.: $h_s \approx \frac{1}{2} V_\infty^2$):

$$S_t = \frac{2q_c}{\rho_\infty V_\infty^3} \quad (1.31)$$

which is exactly in the same form of the heat transfer coefficient.

The Free molecular pressure defined in eq. 1.18 should be treated as a relative pressure w.r.t. to the free flow condition, in this way a generic pressure coefficient can be defined as:

$$C_p = \frac{p - p_\infty}{\frac{1}{2} \rho_\infty V_\infty^2} = \frac{p_{fm}}{\frac{1}{2} \rho_\infty V_\infty^2} \quad (1.32)$$

Combining eq. 1.25 and 1.71, which are valid for a $S_R \gg 1$ and a cold wall ($T_w/T_\infty \rightarrow 0$) the pressure coefficient can be estimated as:

$$C_p = 2 \sin^2 \theta \quad (1.33)$$

which allows the estimation of pressure coefficient only having the surface inclination and represents the exact same conclusion reached by the Newtonian theory for the continuum hypersonic regime, which defines the famous *Newtonian sine-squared law*.

It is now possible to defined the drag coefficient in terms of the free molecular pressure due to the particles impacting the surface (eq. 1.33), and taking into account the drag coefficient definition, according to the diagram in Fig. 1.8:

$$C_D = \frac{F_D}{\frac{1}{2} A_{ref} \rho_\infty V_\infty^2} = \frac{p_{fm} A \sin \theta}{\frac{1}{2} A_{ref} \rho_\infty V_\infty^2} \quad (1.34)$$

where C_D is the drag coefficient, F_D is the drag, and A_{ref} is the cross section reference area, and A is the flat plate area. Which substituting with eq. 1.71-1.33) becomes:

$$C_D = \frac{C_p \frac{1}{2} A \rho_\infty V_\infty^2 A \sin \theta}{\frac{1}{2} A_{ref} \rho_\infty V_\infty^2} = \frac{C_p A \sin \theta}{A_{ref}} = \frac{2A \sin^3 \theta}{A_{ref}} \quad (1.35)$$

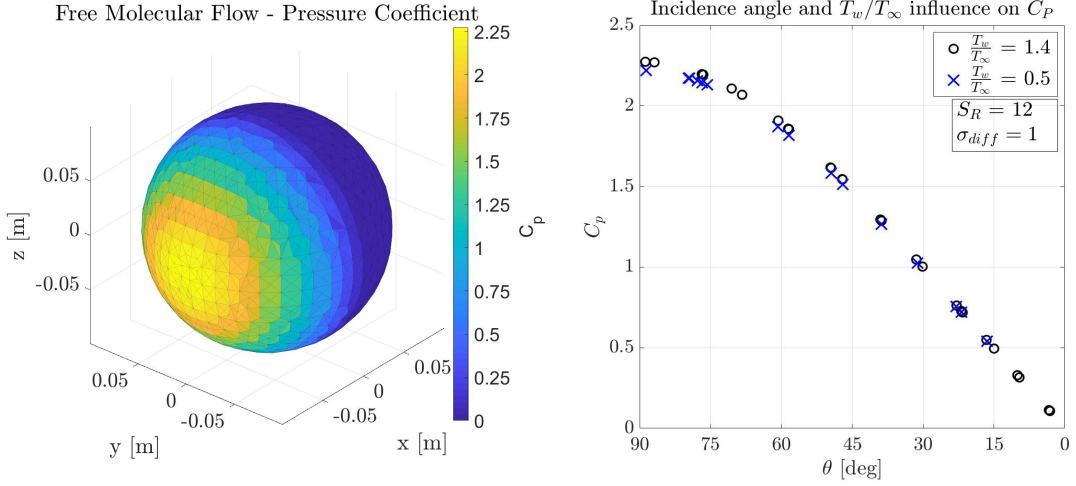


Figure 1.9: Normal Pressure coefficient distribution of a sphere in the free molecular regime. *On the left:* pressure distribution of a sphere computed with the developed software. *On the right:* numerical implementation of eq.1.18 and 1.32 at different conditions

It is clear that for a flat plate normal to the flow (with $\theta = 90\text{deg}$ and $A = A_{\text{ref}}$) with the fore mentioned assumptions (i.e.: $S_R \rightarrow \infty$ and $T_w/T_\infty \rightarrow 0$), the drag coefficient is 2.0, but such result is underestimated when compared to common literature values of 2.2 [Sentman, 1961], mainly due to the influence of T_w/T_∞ and the completely diffusive accommodation coefficient, which both help to increase the drag force acting on the surface.

An example of the application of eq. 1.18, 1.19, and 1.23 for studying the aerothermodynamics properties of a sphere is shown in the following figures. The sphere was simulated assuming typical atmospheric characteristic of a low earth circular orbit. The normal pressure coefficient distribution and the dependence w.r.t. to inclination angle and T_w/T_∞ is shown in Figure 1.9; while the distribution of the heat transfer coefficient is reported in Figure 1.10, where it is possible to notice that due to the finite speed ratio at the test conditions ($S_R = 12$) the C_H is not equal to the theoretical maximum (i.e.: 1). Integrating over the entire surface the complete aerodynamic characterization of the object can be obtained (i.e.: forces and moments aerodynamic coefficients).

1.3.3 Continuum Regime

The hypersonic aerodynamics represent significant challenges from both aerodynamic and aero-thermodynamic perspective. In the continuum regime the flow field will be significantly disturbed by the presence of the object, in contrast to what could be as-

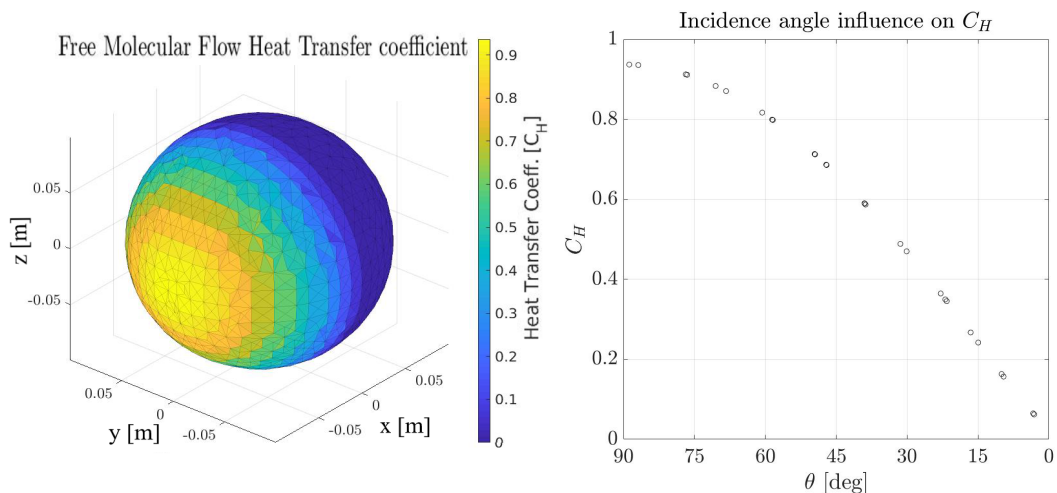


Figure 1.10: Heat transfer coefficient distribution of a sphere in the free molecular regime. *On the left:* heat transfer distribution computed with the developed software. *On the right:* numerical implementation of eq.1.23 and 1.27 with a $S_R = 12$.

sumed in the free molecular regime. This fluid-structure interaction is dominated by non linear phenomena, and the characterization of pressure and heat transfer, considering the high energy involved during an atmospheric reentry aspects such as the chemical reactions, viscous interactions, high temperature, and shock waves interactions cannot be neglected. The high-fidelity characterization of flow-structure interaction was out the scope of this project, and a more simplified approach was sought. The local surface inclination methods can describe with a reasonable accuracy and very computationally efficiently the local pressure and heat-transfer of a body in a hypersonic flow. In the following paragraphs, the different models for studying the aerodynamics and aero-thermodynamics in the hypersonic continuum regime will be briefly described.

Aerodynamics: Newtonian Theory

The basic theory for performing simplified aerodynamic analysis within the continuum regime at a hypersonic speed is the well known Newtonian theory, which was originally thought for applications of low-speed fluid dynamics. Although being conceived for the low-speed regime, the theory was proven to be extremely efficient for characterizing the pressure distribution of a body in a hypersonic flow. The Newtonian theory models the flow as a stream of particles, very similarly to what was described for the free molecular flow, but as the particles impact the surface, instead of being reflected (or diffused) they would move tangentially to the surface (Figure 1.11).

The picture show a stream of particles impacting a surface with a velocity (V_∞) and

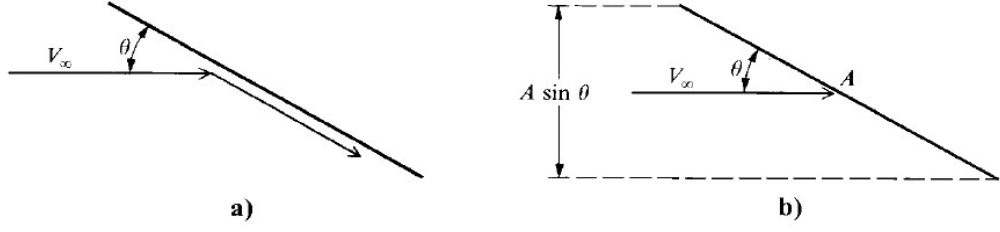


Figure 1.11: Flat plate in a free molecular flow: a) impact and tangential motion, b) flux of particles characteristic.

an inclination θ without any loss of momentum. The mass flux incident on the surface can be defined as:

$$\dot{m} = \rho_{\infty} V_{\infty} A \sin \theta \quad (1.36)$$

where A is the flat plate area, and θ is the deflection angle. The change on the normal velocity is:

$$\Delta V_n = V_{\infty} \sin \theta \quad (1.37)$$

Thus, the rate of change of momentum is:

$$\dot{m} \Delta V_n = \rho_{\infty} V_{\infty}^2 A \sin^2 \theta \quad (1.38)$$

Which, by Newton's second law, is equal to the force exerted on the surface:

$$\frac{F}{A} = \rho_{\infty} V_{\infty}^2 \sin^2 \theta \quad (1.39)$$

When Newton firstly introduced this theory, the random motion of particles was not known, and the contribution computed in this way only considers the rectilinear motion of the stream of particles. Thus, this force must be interpreted as a differential pressure, w.r.t. the ambient (or static) pressure:

$$\frac{F}{A} = p - p_{\infty} \quad (1.40)$$

which substituting becomes:

$$\rho_{\infty} V_{\infty}^2 \sin^2 \theta = p - p_{\infty} \quad (1.41)$$

and considering the dynamic pressure, defined as:

$$q_{\infty} = \frac{1}{2} \rho_{\infty} V_{\infty}^2 \quad (1.42)$$

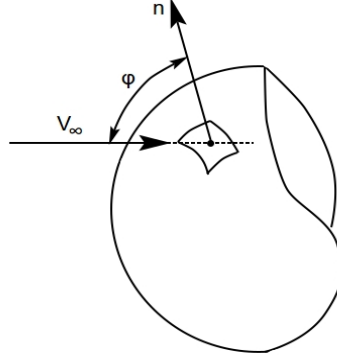


Figure 1.12: Schematics for 3D Newtonian theory.

which can be expressed in terms of the pressure coefficient:

$$C_p = \frac{p - p_\infty}{q_\infty} = 2 \sin^2 \theta \quad (1.43)$$

which is the well known *Newtonian sine-squared law* for pressure coefficient. Interestingly, even though it has been obtained with different assumptions, Newtonian pressure coefficient is the same as the one obtained for the free molecular flow regime with an infinite molecular speed ratio (eg. 1.33).

This is a local inclination method, as the pressure distribution depends solely on the local surface inclination. The relation which has been obtained for a 2D case, can be easily extended for estimating pressure distribution over 3D shapes. In a 3D case, the angle must be defined considering the inclination between the surface normal and flow direction, as shown in Figure 1.12.

Defining the angle ϕ as the angle between the surface normal (\vec{n}) and the flow direction:

$$V_\infty \cdot \vec{n} = |V_\infty| \cos \phi = |V_\infty| \sin \left(\frac{\pi}{2} - \phi \right) \quad (1.44)$$

θ (defined as the angle between the surface tangent and the flow direction) can be obtained via a simple geometric relationship:

$$\sin \theta = \frac{V_\infty}{|V_\infty|} \cdot \vec{n} \quad (1.45)$$

The Newtonian theory assumes that in the shadowed region (which for a simple shape is the defined where the cross product between the surface normal and the flow direction is negative) the pressure is equal to the ambient pressure, as the theory assumes that no particle directly hit the shadowed region. Thus for a leeward region $C_p = 0$, such

assumption will be valid as long as the flow regime is at a hypersonic regime. Indeed, considering as an airfoil in the subsonic regime as example, the pressure distribution on the leeward (or shadowed) region will be highly dependent on the angle of attack and will more likely be negative (i.e.: generating lift).

Modified Newtonian

In 1955 Lester Lees [Lees, 1955] proposed a modification of the Newtonian theory, which could take into account the normal shock wave theory and the stagnation point pressure:

$$C_p = C_{p,\max} \sin^2 \theta \quad (1.46)$$

where $C_{p,\max}$ is the maximum value of the pressure coefficient, evaluated behind the shock wave:

$$C_{p,\max} = \frac{p_{02} - p_\infty}{\frac{1}{2}\rho_\infty V_\infty^2} \quad (1.47)$$

from the normal shock wave theory the pressure after the shock can be evaluated as:

$$\frac{p_{02}}{p_\infty} = \left[\frac{(\gamma + 1)^2 M_\infty^2}{4\gamma M_\infty^2 - 2(\gamma - 1)} \right]^{\frac{\gamma}{\gamma-1}} \left[\frac{1 - \gamma + 2\gamma M_\infty^2}{\gamma + 1} \right] \quad (1.48)$$

and observing that the dynamic pressure can be defined as:

$$\frac{1}{2}\rho_\infty V_\infty^2 = \frac{\gamma}{2} p_\infty M_\infty^2 \quad (1.49)$$

then the pressure coefficient is:

$$C_{p,\max} = \frac{2}{\gamma M_\infty^2} \left[\frac{p_{02}}{p_\infty} - 1 \right] \quad (1.50)$$

The modified Newtonian pressure coefficient proposed by Lees has been proven to be very accurate in describing pressure distribution over blunt bodies [Hayes, 1959]. The variation of $C_{p,\max}$ w.r.t. M_∞ and γ is shown in Figure 1.13. If the reader can observe that as the velocity increases and when the specific heat gas ratio equal to 1, the relationship proposed by Lees (eq. 1.47) becomes equal to the Newtonian theory (eq. 1.43), A comparison between the two methods is shown in Figure 1.14.

Centrifugal Correction

The Newtonian and Modified Newtonian approach were derived considering the particles flow impacting a flat surface, but when the surface is not flat the particles are subjected to a centrifugal force. For this reason, Busemann [BusEMANN, 1933] inves-

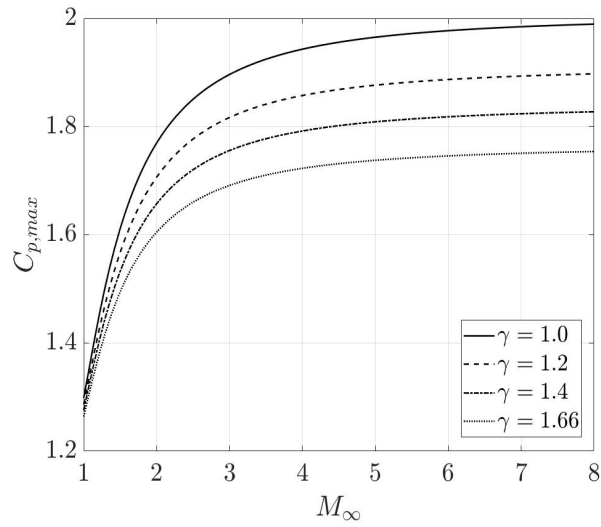


Figure 1.13: Maximum pressure coefficient variation w.r.t. M_∞ and γ

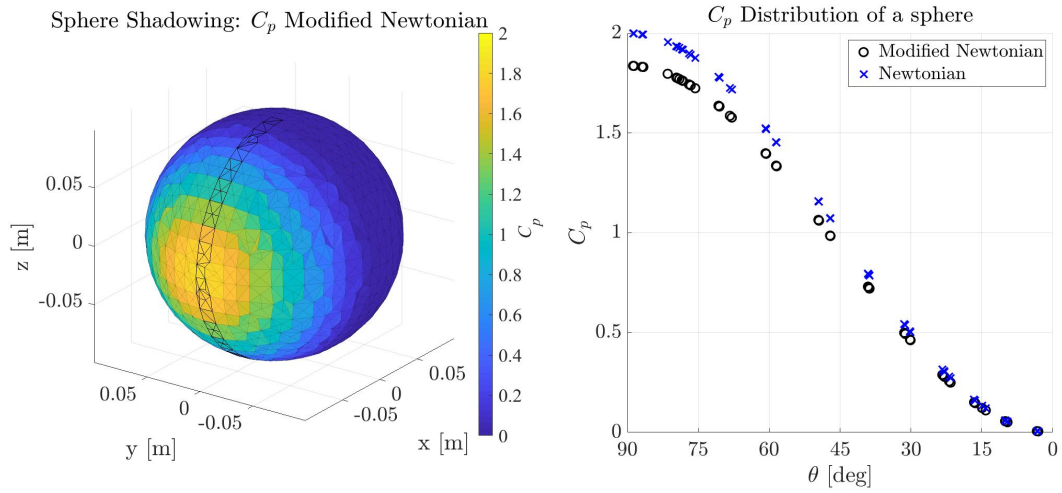


Figure 1.14: Left: C_p distribution on the surface of a sphere (post processed with FOSTRAD) for $\gamma = 1.4$ and $M_\infty = 24$. Right: comparison of modified Newtonian and standard Newtonian C_p on the windward surface

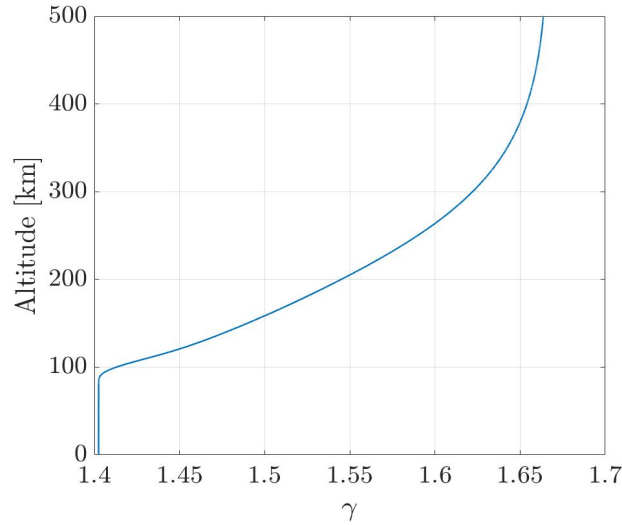


Figure 1.15: Variation of specific heat ratio (γ) over altitude for a US 1976 atmospheric model.

tigated the use of a centrifugal correction to the Newtonian theory. Later in the 1957, Eggers [EGGERS et al., 1956] studied the application of the centrifugal correction in a similar way, the approach was found to provide accurate results for slender bodies at very high Mach numbers $M_\infty \rightarrow \infty$ and $\gamma \rightarrow 1$. Although from the fluid mechanics point of view the centrifugal correction is correct, for blunt bodies and different γ was proven to provide results which were qualitatively and quantitatively worse than both standard and modified Newtonian theory, results for circular cylinder at the condition of $\gamma = 1.4$ and $M_\infty \rightarrow \infty$ were reported by Van Dyke [Dyke, 1958]. Additionally cases where investigated for biconvex airfoils at $\gamma = 1.4$ and $M_\infty \rightarrow \infty$ and the same conclusions were drawn: the practical application of the Busemann centrifugal correction provides worse results for standard air conditions [Cox and Crabtree, 1965, Chernyi, 1961, Eggers et al., 1953]. In the specific study of spacecraft atmospheric reentry and for a standard atmospheric model, γ has the profile shown in Figure 1.15; therefore the use of a centrifugal correction for C_p estimation would most likely provide worse results than the Modified Newtonian theory.

When the geometry of the object has sharp angles, other methods such as the *Tangent-Wedge* and *Tangent-Cone* would most likely provide most accurate results, this methods require the detection of specific geometry and their application is not generalized on arbitrary geometries, a thorough description and the calibration coefficients for the use of this theory may be found in: [Kopal, 1947, Probstein and Bray, 1954, Sims, 1964, Hayes, 1959].

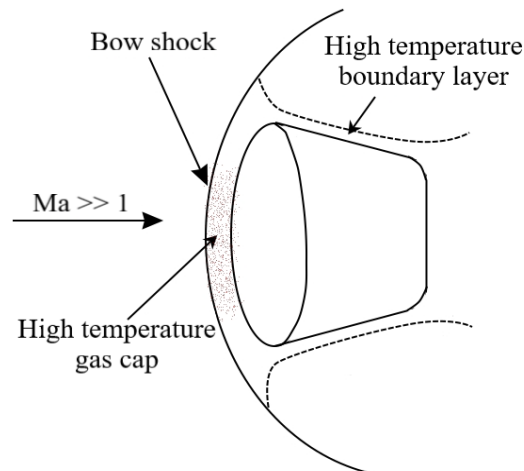


Figure 1.16: Schematic of an atmospheric re-entry

Aerothermodynamics

Whenever a spacecraft is expected to re-enter the atmosphere the aerothermodynamics must be investigated. One of the most famous example is the re-entry of the apollo 11 from the first manned flight to the moon. The re-entry vehicle reached a velocity approximately of 11.2km/s causing extremely high temperature ($\approx 12,000\text{K}$) to be reached during the atmospheric re-entry. Calculating the heat-flux for the correct design of the thermal protection system has always been a challenge, and many theories and formulation have been proposed for the purpose. The difficulties raised by the hypersonic velocities re-entries for the heat-flux estimation are many: the high temperature reached in the shock layer cause the dissociation and ionization of the atomic species, highlighting the importance of considering the chemical reactions in the flow. A typical schematic of a re-entering body is reported in Figure 1.16.

In 1956, Lester Lees [Lees, 1956] studied the heat transfer over a blunt-nosed body for a typical hypersonic atmospheric re-entry scenario, analyzing the two limiting cases of a thermodynamic equilibrium where the chemical reaction rates are very fast w.r.t. to the diffusion rates across the streamlines and the case where the diffusion rates within the boundary layer are very slow compared to the diffusion rates across the streamlines outside the boundary layer. In both scenarios the density within the boundary layer is much higher compared to the density outside the boundary layer, which makes the stagnation enthalpy less sensitive to pressure gradient, allowing the use of a zero-gradient approach for estimating the surface heat distribution, which in the case of a hemisphere,

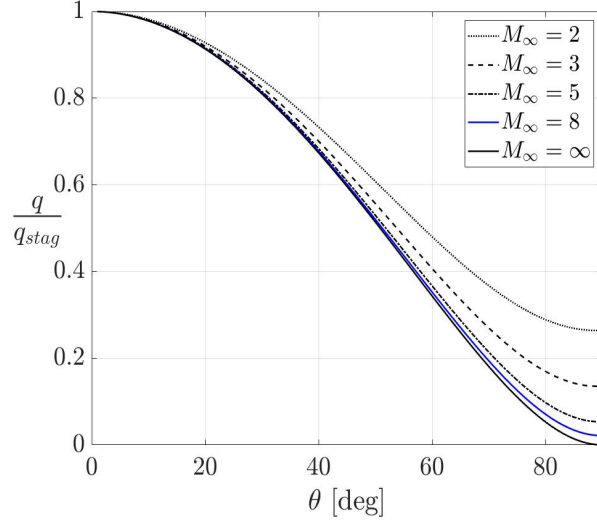


Figure 1.17: Lees laminar heat transfer distribution 1.51 over a hemisphere for different M_∞ and $\gamma = 1.4$.

and using the Modified Newtonian pressure distribution Lees defines as:

$$\frac{\dot{q}_w}{\dot{q}_{w,s}} = \frac{2\theta \sin \theta \left\{ \left[1 - \frac{1}{(\gamma_\infty M_\infty^2)} \right] \cos^2 \theta + \frac{1}{(\gamma_\infty M_\infty^2)} \right\}}{\sqrt{D(\theta)}} \quad (1.51)$$

where \dot{q}_w and $\dot{q}_{w,s}$ are the heat local and stagnation point transfer rate respectively, and $D(\theta)$ is a polynomial function whose first terms are:

$$D(\theta) = \left(1 - \frac{1}{\gamma_\infty M_\infty^2} \right) \left(\theta^2 - \frac{\theta \sin 4\theta}{2} + \frac{1 - \cos 4\theta}{8} \right) + \frac{4}{\gamma_\infty M_\infty^2} \left(\theta^2 - \theta \sin 2\theta + \frac{1 - \cos 2\theta}{2} \right) + \dots \quad (1.52)$$

The equations determine the heat transfer distribution reported in Figure 1.17.

In the end of 1956, Kemp and Riddell presented an investigation of the application of the previous formulation specifically for spacecraft re-entering the atmosphere in [Kemp, 1956] defining general approximations for estimating the heat transfer at the stagnation point, which in the free molecular flow is:

$$q_{s, \text{fm}} = 2.69 \times 10^7 \sigma_{\text{diff}} \frac{\rho_\infty}{\rho_{\text{SL}}} \left(\frac{V_\infty}{V_{\text{circ}}} \right)^3 \quad \left[\frac{\text{Btu}}{\text{ft}^2 \text{s}} \right] \quad (1.53)$$

where V_{circ} is the circular orbit velocity at the specific altitude, and ρ_{SL} is the density

at sea level. Whereas in the continuum regime the approximation is defined as:

$$q_s = \frac{20800}{\sqrt{R_N}} \sqrt{\frac{\rho_\infty}{\rho_{SL}}} \left(\frac{V_\infty}{V_{\text{circ}}} \right)^{3.25} \left(1 - \frac{h_w}{h_s} \right) \quad \left[\frac{\text{Btu}}{\text{ft}^2 \text{s}} \right] \quad (1.54)$$

where R_N is the nose radius, the subscripts w and s refers to the wall and stagnation points respectively, and h is the enthalpy.

Later in 1957, Fay and Riddell investigated the heat transfer at the stagnation point taking into account the effects of diffusion and atoms recombination [Fay, 1957]. By considering the sum of conductive and diffusive transport phenomena at the stagnation point, the local heat transfer can be defined as:

$$q_s = (\text{Nu}/\sqrt{\text{Re}}) \sqrt{\rho_w \mu_w} \left(\frac{du_e}{dx} \right)_s [(h_s - h_w)/\text{Pr}] \quad (1.55)$$

where Pr is Prandtl number, while the $(\text{Nu}/\sqrt{\text{Re}})$ is a heat transfer parameter defined as a function of the Nusselt and Reynolds number, which was solved by Fay and Riddell for the case of a hypersonic flow with a velocity between 5800ft/s (1760m/s) and 22800ft/s (7000m/s) and a wall temperature between 300K and 3000K, and a Lewis Number $\text{Le} = 1$:

$$(\text{Nu}/\sqrt{\text{Re}})_{\text{Le}=1} = 0.67 \left(\frac{\rho_s \mu_s}{\rho_w \mu_w} \right)^{0.4} \quad (1.56)$$

when Le is not equal to unity, values of the heat transfer coefficient are defined as:

$$\frac{\text{Nu}/\sqrt{\text{Re}}}{(\text{Nu}/\sqrt{\text{Re}})_{\text{Le}=1}} = 1 + (\text{Le}^{0.52} - 1)(h_D/h_s) \quad (1.57)$$

where h_D is the dissociation enthalpy per unit mass in the undisturbed flow. Combining the previous equations, and assuming $\text{Pr} = 0.71$, the heat flux at the stagnation point can be defined as:

$$q_s = 0.76 \text{Pr}^{-0.6} (\rho_w \mu_w)^{0.1} (\rho_s \mu_s)^{0.4} [1 + (\text{Le}^\alpha - 1)(h_D/h_s)] (h_s - h_w) \sqrt{\left(\frac{du_e}{dx} \right)_s} \quad (1.58)$$

where for Pr equal to 0.71 the term $(0.76 \text{Pr}^{-0.6})$ is usually replaced with 0.94, and α may have different values dependent on the wall boundary conditions:

- $\alpha = 0.52$ for a thermodynamic equilibrium in the boundary layer
- $\alpha = 0.63$ for a frozen boundary layer and a fully catalytic wall
- $\alpha = -\infty$ for a frozen boundary layer and a non-catalytic wall

For a Earth atmospheric re-entry the Lewis number is estimated as $\text{Le} = 1.4$, but

assuming $Le = 1$ the heat flux can be further simplified as:

$$\dot{q}_s = 0.94(\rho_w \mu_w)^{0.1} (\rho_s \mu_s)^{0.4} (h_s - h_w) \sqrt{(du_e/dx)_s} \quad (1.59)$$

where the term $\sqrt{(du_e/dx)_s}$ is the velocity gradient over the curvilinear abscissa at the stagnation point, which is defined as in the Modified Newtonian Theory [Lees, 1955]:

$$\left(\frac{du_e}{dx}\right)_s = \frac{1}{R_N} \sqrt{\frac{2(p_s - p_\infty)}{\rho_s}} \quad (1.60)$$

Fay and Riddell performed several analyses on different assumption in order to determine the influence of a catalytic or non-catalytic wall. They concluded that if Lewis number is close to the unity, the heat transfer will not be affected by non equilibrium state at the boundary layer, and the eq. 1.59 could be used to estimated the heat transfer rate at the stagnation point. A diagram indicating the influence of wall catalicity on the heat transfer coefficient w.r.t. to the recombination rate is reported in Figure 1.18. The extremes of recombination rate are representative of a frozen wall ($C_1 \rightarrow 0$) and thermal equilibrium ($C_1 \rightarrow \infty$). Assuming a perfect gas and $Le = 1$, the heat transfer estimated is close to the one computed considering a real gas and recombination effects with $Le = 1.4$ and a thermal equilibrium (or a fully catalytic frozen wall); although, the same approximation does not stand for a non-catalytic frozen wall, which may cause a sensible ($\sim 40\%$) reduced heat-flux.

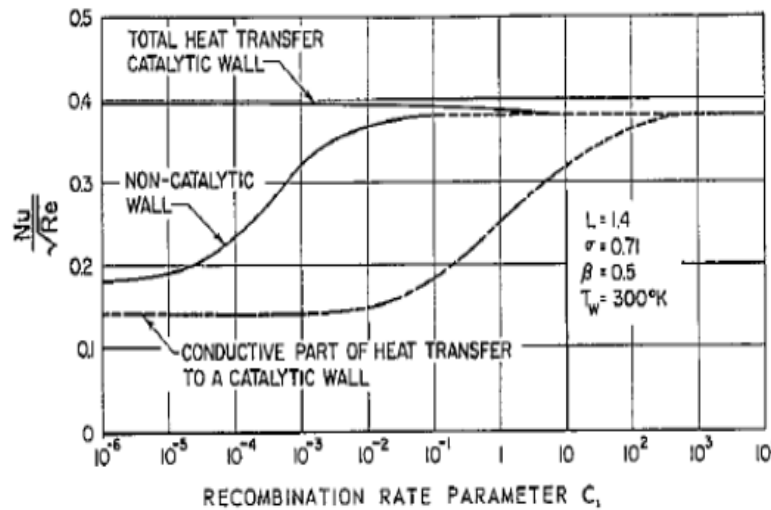


Figure 1.18: Heat transfer coefficient as defined in eq. 1.56 over the atoms recombination rate for a fully catalytic and a non-catalytic wall [Fay, 1957].

In light of the research carried out by Fay and Riddell [Fay, 1957], Detra, Kemp and Riddell published an addendum [Detra, 1957] to their previous article ([Kemp, 1956]), proposing a modification to the earlier proposed approximation for the continuum regime (eq. 1.54). Highlighting more accurate empirical correlations, the approximation was corrected as:

$$q_s = \frac{17600}{\sqrt{R_N}} \sqrt{\frac{\rho_\infty}{\rho_{SL}}} \left(\frac{V_\infty}{V_{circ}} \right)^{3.15} \left(\frac{h_s - h_w}{h_s - h_{w,300}} \right) \left[\frac{Btu}{ft^2s} \right] \quad (1.61)$$

where the term $h_{w,300}$ is the enthalpy for a wall at 300K. It must be noted that the correlation is valid (with an error within $\pm 10\%$ of the experimental observation) in the range of altitudes between sea level and 76km (250000ft), and velocities between 2000m/s(7000fps) and 7600m/s(25000fps).

In 1959, following the work of Fay and Riddell, a further development of laminar heat transfer theory was published by Kemp, Rose and Detra [Kemp et al., 1959]. Their approach was based on the local similarity concept (which was firstly introduced by Lees), and they extended the ideas proposed by Fay and Riddell, finding an exact solution to the constitutive equation for the heat transfer of a highly cooled wall in a dissociated flow. The complete formulation is described with:

$$\begin{aligned} \dot{q}_s = & 0.76Pr^{-0.6}(\rho_w\mu_w)^{0.1}(\rho_s\mu_s)^{0.4}h_s(1 - g_{ws}) \\ & [1 + (Le^\alpha - 1)(h_D/h_s)](h_s - h_w)\sqrt{\left(\frac{du_e}{dx}\right)_s} \end{aligned} \quad (1.62)$$

where $\alpha = 0.52$ for the thermodynamic equilibrium, $\alpha = 0.63$ for a fully catalytic frozen wall, and $\alpha = -\infty$ for a frozen non-catalytic wall, while the term $h_s(1 - g_{ws})$ is representative for the atoms dissociation, where g_{ws} is numerical correlation described in [Kemp et al., 1959] as function of the local expansion ratio. Although, the formulation is not of an immediate use, and the approximation proposed by Fay and Riddell is often preferred for a practical use. Based on their experimental analyses, the relative stagnation point heating distribution of a hemispherical cylinder that can be approximated as:

$$\frac{q}{q_s} = \cos\left(\frac{\theta}{2}\right)^{5.27} \quad (1.63)$$

In 1960 Detra and Hidalgo [Detra and Hidalgo, 1960] published a research based on all the previously reported investigation on the laminar, turbulent and radiative heat transfer in dissociated air, proposing a set of approximated formulations for estimating the heat transfer for a blunt-nosed body during an Earth's atmospheric re-entry. In fact, Fay and Riddell, as well as Kemp, Rose, and Detra, investigated the effects of laminar

heat transfer. While, Detra and Hidalgo, extended the studies on the turbulent regime by taking into account the investigations performed by Rose and Probstain [Rose et al., 1958], which dealt with the turbulent heat transfer for blunt bodies. As thoroughly described in [Detra and Hidalgo, 1960], the heat transfer in a turbulent flow can be simplified assuming the following:

- Sutherland's law for viscosity
- Prandtl Number = 0.71
- Highly Cooled wall ($T_w = 300\text{K}$)
- constant ratio of specific heats $\gamma = 1.2$
- Neglecting the recombination effects (dissociation enthalpies)
- Neglecting the form factor (representative of the blunt body geometry)

Such assumption leads to the following formulation of estimating the convective heat-flux in a turbulent flow:

$$q_x^{0.2} = 1.346 \times 10^4 \left(\frac{\rho_\infty}{\rho_{SL}} \right)^{0.8} \left(\frac{V_\infty}{10^4} \right)^{3.18} \Phi \quad \left[\frac{\text{Btu}}{\text{ft}^2\text{s}} \right] \quad (1.64)$$

where x is the running length from the stagnation point (it must be noted that x and V_∞ are expressed in ft and fps respectively), and Φ is a function of the local pressure ratio, defined as:

$$\Phi = \left(\frac{p}{p_s} \right)^{\frac{4.1}{6}} \left[1 - \left(\frac{p}{p_s} \right)^{\frac{1}{6}} \right]^{0.4} \quad (1.65)$$

where p and p_s are the local and stagnation pressure respectively. Detra and Hidalgo defined also an approximation for the radiative heat transfer, defined as:

$$q_{\text{rad}} = R_N \times 10^2 \left(\frac{V_\infty}{10^4} \right)^{8.5} \left(\frac{\rho_\infty}{\rho_{SL}} \right)^{1.6} \quad \left[\frac{\text{Btu}}{\text{ft}^2\text{s}} \right] \quad (1.66)$$

observing the equation is clear that the radiative heat-flux becomes significant as the body nose radius increases, which is representative of a higher influence of the high-temperature gas cap at the body's stagnation point, and for very high re-entry velocities.

The different formulation that have been presented in this paragraph represent a wide variety of engineering models that can be used for a preliminary evaluation of heat transfer for blunt bodies during an atmospheric re-entry scenario. Depending on the specific application different models may be better suitable (e.g.: a fully catalytic model could be used as a conservative approach for a thermal protection system preliminary design). Therefore, the use of these models must be properly selected according to the performed analysis, and taking into account the different simplification degrees used for each formulation.

1.4 Space Debris and Spacecraft Atmospheric Reentry Simulations

Even though the purpose of simulating spacecraft and space debris atmospheric re-entries is completely different, the environment conditions are very similar. During an atmospheric re-entry, different velocities (supersonic, transonic and subsonic regimes) are experienced by the spacecraft. These conditions are faced in various phases of the re-entry as the space object goes through increasing atmospheric densities regimes, commonly defined by the Knudsen number regime (Kn). As the spacecraft (or the debris) reach a dense layer of the atmosphere, the supersonic velocity in combination with the increasing density causes a steep increase in the heat-flux absorbed by the object. In addition, the aerodynamic forces at supersonic velocity cause a strong deceleration, usually identified as the G-load. The combination of the two effects poses a challenge for the vehicle safe re-entry, and allows the complete or partial burn-up of the space debris. Aerodynamic and aerothermodynamic simulations of the two categories are often required for different purposes. The re-entry vehicle or capsule is required to survive the harsh environment, structural integrity analyses must be performed to ensure the design can withstand the G-loads, while thermal simulations are required to correctly design the vehicle thermal protection system. Simulations of space debris re-entries, is usually required for other purposes: determining the possible impact footprint, estimating the casualty risk, and evaluating design for demise solutions. Satellites are designed to withstand the G-load during the launch, but during the re-entry the high G-load in combination with the extreme temperatures will cause a break-up and the subsequent ablation of the internal and external components (fig. 1.19).

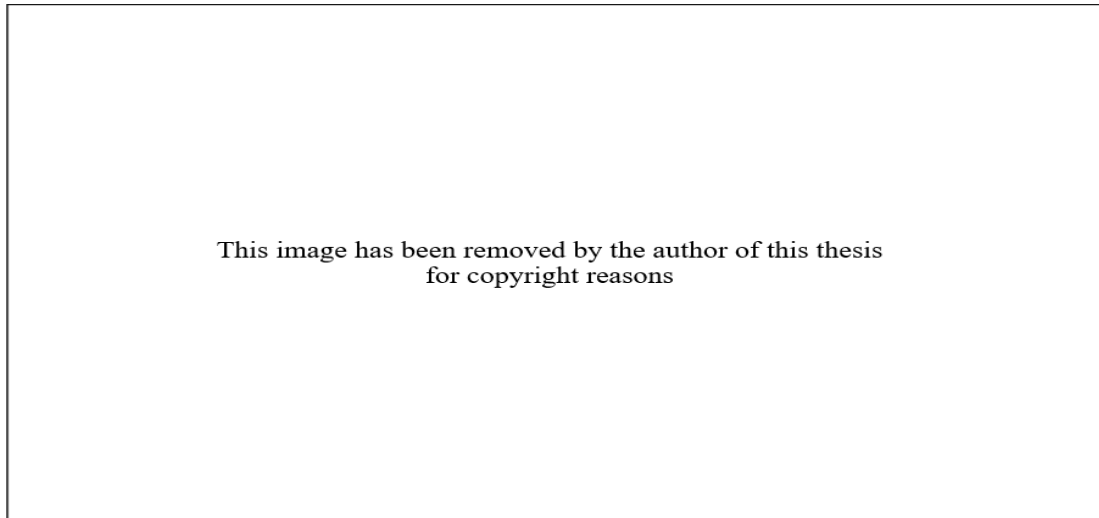


Figure 1.19: Typical break-up scenario (available at <http://www.spacesafetymagazine.com/wp-content/uploads/2014/07/satellite-reentry-footprint.jpg> - ©Andrea Gini on July 9, 2014, last accessed 31 May 2020)

The break-up is one of the main challenges for simulating re-entry of space debris. In fact, while it is relatively simple to simulate a single geometry using high-fidelity methods based on a computational fluid dynamics approach on a set of predefined re-entry trajectory points and conditions, it is not trivial to do the same for each fragment generated during a break-up. Indeed, each fragment would have its own trajectory, and the sensible change in the shape due to the progressive ablation would require the use of a dynamic mesh, able to properly capture the change in the shape required by the ablation processes. In addition, the particular re-entry conditions (i.e.: supersonic velocity and rarefied atmosphere) require to use accurate simulation parameters and different methods at different altitudes, making the use of high fidelity computational simulation very computational expensive and often unfeasible for this purpose.

Re-entry simulations usually involve also a high degree of uncertainty, which should be taken into account when performing the trajectory propagation, aerodynamic estimation, thermal and heat-flux computation, and material and object ablation. In fact, identifying the probabilistic fragments footprints is largely dependent on the aerodynamic parameters computation and atmospheric parameters estimation. Although, most known tools which perform aerodynamic simulations are deterministic, and do not take into account the uncertainty associated with the provided inputs. Additionally, performing statistically significant analyses, will require to simulate large set of data points, making of using high fidelity approaches unfeasible. Other examples of uncertain parameters may be the following: the attitude and in some specific case

also the geometry (or its evolution), material properties (e.g.: thermal and structural properties), uncertainties in the physical and mathematical models, numerical errors in thermal and trajectory propagations, some coefficients employed by the methods, which are usually treated as conventional constants, are affected by epistemic uncertainties. The uncertainty in the inputs, coefficients, and parameters, propagates directly into the resulting analyses. Thus, It is paramount to identify the most significant sources of uncertainty to be taken into account; performing a proper uncertainty quantification (UQ) will provide information regarding boundaries and confidence intervals for the propagated quantities,.

The framework developed during this work includes different modules: aerodynamic and aerothermodynamic computation employing the simplified local panel inclination method, a mesh module used to handle complex geometries and assemblies, a material and thermal response module for computing the temperature propagation and the ablation at the surface, an uncertainty quantification module for studying statistical distributions of the different properties, and a trajectory propagator used to simulate controlled and uncontrolled re-entry scenarios. The software may be used for simulating both gliding and ballistic re-entries, and with the proper adjustments, it can also be interfaced with a trajectory optimization for solving optimal control problems.

Focusing on controlled and uncontrolled re-entries of space debris and satellites, the following sub-sections will provide a brief overview currently existing software capable of assessing re-entry risk and simulate re-entry scenarios.

1.4.1 DAS

The Debris Assessment Software [Opiela et al., 2007] (DAS) is a tool developed maintained by NASA for studying the compliance of space mission to the NASA Technical Standard 8719.14 (Process for Limiting Orbital Debris). DAS can be used to assess the compliance uncontrolled re-entries of spacecraft and satellites as well as jettisoned components. Focusing on the re-entry casualty risk, if the satellite is compliant with the requirements of the STD 8719.14 no further analyses have to be performed. If the analyses show noncompliance, further analyses may be performed with ORSAT (Object Reentry Survival Analysis Tool, the higher fidelity tool developed by NASA). DAS is a fast evaluation tool able to provide conservative results, it has been classified as an object oriented code [Lips and Fritsche, 2005]. In DAS the spacecraft is modeled as a set of simple geometries and shapes (spheres, boxes, cylinders and plates). Each object is associated with a mass, geometric dimension and material. The objects may be solid or hollow with a finite thickness, the first ones are modeled with a lumped mass approach (the temperature is assumed to be uniform in the whole body), while the hollow objects

are modeled using an effective density. The object is considered to be demised only if the absorbed heat is above the heat of ablation, no partial melting is considered. Additionally, DAS takes into account a radiative cooling according to Stefan-Boltzmann law using an emissivity equal to 1.0. In DAS 2.0, multiple parent-children nested levels can be modeled. The first level of children objects is considered to be exposed to the aero-heating at 78km. If the nested objects have additional children, they will be released once their immediate parent object demises, providing a progressive break-up modeling capability. DAS neglects any pre-heating of nested objects, and their temperature is assumed to be 300K at their release.

1.4.2 ORSAT

The Orbital Debris Object Reentry Survival Analysis Tool is the higher fidelity analyses code used by NASA for predicting the survivability of atmospheric re-entries of satellite and launch vehicle upper stages and assessing the human casualty risk associated with the events. ORSAT is generally used when a space mission cannot be proven to be compliant running the initial analyses with DAS. Indeed, as DAS is very conservative, further analyses with a higher fidelity tool may provide additional information on the effective casualty risk. ORSAT can perform a complete re-entry analyses using integrated trajectory, aerodynamic, aerothermodynamic, atmospheric, material and ablation models [Rochelle et al., 1999]. The trajectory propagation is performed using a 3-DOF approach with different motions (combinations of spinning and random tumbling). The trajectory propagation is performed using 6 scalar equations to solve the time derivatives of velocity, flight path angle, altitude, longitude, latitude and heading angle. In the latest version of the tool the aerodynamic, gravitational, and atmospheric forces can result in a lift coefficient. The aerodynamics of the objects are computed according to the different regimes; free molecular, rarefied transitional, and hypersonic (or subsonic) continuum flow. For each of the different regimes the drag coefficient is computed according to the shape and the type of motion. In the transitional regime a Knudsen number-dependent bridging functions are used:

$$C_{D_{\text{trans}}} = C_{D_{\text{cont}}} + (C_{D_{\text{cont}}} - C_{D_{\text{fm}}})[\sin(\pi(0.5 + 0.25 \lg Kn))]^3 \quad (1.67)$$

The aero-heating is computed using an averaged shape- and motion-dependent heat-flux. The heat-flux is computed according to the different regimes, in the free molecular regime it is used the energy accommodation coefficient and kinetic energy dependent function

$$\dot{q}_{\text{st}_{\text{fm}}} = \frac{\alpha \rho_{\infty} V_{\infty}^3}{2} \quad (1.68)$$

whereas in the hypersonic continuum regime, the Detra, Kemp, and Riddell approximation [Detra, 1957] can be used:

$$\dot{q}_{\text{st}_{\text{cont}}} = \frac{110,285}{\sqrt{R_{N,\text{eff}}}} \left(\frac{\rho_{\infty}}{\rho_{\text{sl}}} \right) \left(\frac{V_{\infty}}{V_{\text{circ}}} \right)^{3.15} \quad (1.69)$$

In the latest version of ORSAT, it has been implemented also the Fay-Riddell model [Fay, 1957], which takes into account real gas effects. In the rarefied transitional regime, different bridging function for the different geometries are used. The shape are simulated assuming an effective curvature radius, and motion dependent averaging factors are used for simulating the different rotating scenario. ORSAT provides the option of simulating different break-up altitude, and distinguish the aerodynamic mass from the thermal mass. The aerodynamic mass is used to propagate the trajectory taking into account the total mass of parents and nested children objects, while the thermal mass is considered to be only the parent object, allowing the nested children objects to be released when the ablation of the parent object occurs. ORSAT computes also the radiative heat exchange between parent and children objects. The thermal conductive models can either use a lumped mass approach, 1D models for boxes and flat plates, and 2D models for spheres and cylinders.

For hypervelocity reentries ORSAT computes also the gas cap radiative heating as defined in [Hamilton et al., 1991]:

$$\log_{10} \dot{q}_{\text{rad}} = 0.3542 + 0.5646V_{\infty} + (0.306 + 0.066V_{\infty}) [\log_{10}(\rho_{\infty} R_{N,\text{eff}})] \quad (1.70)$$

The gas cap radiative heating has a major impact for high velocity reentries and object with a significant effective nose radius [Dobarco-Otero et al., 2005]. ORSAT models the melting of metallic materials using a standard heat of fusion and melting temperature approach. For non metallic ablators the recession rate is modeled using a exponential correlation based approach, dependent on the cold wall heat-flux and the material response experimental data.

For some particular cases the failure is not thermally induced, for example objects as solar arrays and high area-to-mass ratio will fail due to mechanical stresses. ORSAT computes the bending moment caused by aerodynamic forces to determine when the mechanical failure happens. Another failure scenario considered by ORSAT is the tank bursting, which happens when the internal pressure of the tank exceeds the maximum tensile stress. The internal pressure is computed according to the ideal gas law.

1.4.3 SCARAB

The Spacecraft Atmospheric Re-entry and Aerothermal Break-Up (SCARAB) is the first spacecraft oriented code and allows the simulation of spacecraft reentries using a local panel inclination method approach [Fritsche et al., 2000, Lips et al., 2004]. In the latest decades SCARAB has been used for assessing the reentry scenario of many different space missions, and its modern developments have been driven by practical modeling problems. SCARAB has an embedded FEM modeling system, ensuring the capability of recreating realistic spacecraft models. The material database comprises all the different properties required during the simulation phase: melting temperature, heat of melting, specific heat capacity, thermal conductivity, emissivity, and different structural properties such as: elasticity module and ultimate tensile strength. The objects are built by panels with a finite volume which in combination with the material properties may provide the inertia tensors which are required by the 6-DOF trajectory propagation. The volumetric panels are built with internal layers, allowing the in-depth heat conduction. In addition, the panels are connected via a neighboring relationship allowing the 2D heat conduction. The fragmentation process may be triggered by the temperature or the structural load. SCARAB can model also the bursting of tanks, using a temperature-dependent burst pressure.

SCARAB uses local panel inclination methods for hypersonic aerodynamics and aerothermodynamics analysis, as described in [Lips and Fritsche, 2005, Koppellwallner et al., 2005]. The trajectory is initially propagated with a 6-DOF approach, where the external forces are gravitational and aerodynamic. After the end of the ablation phase the surviving fragments are propagated with 3-DOF. The Aerodynamics for the free molecular flow regime are defined by the Schaaf and Chambre model [Chambre and Schaaf, 1961]:

$$C_{p,fm} = \frac{1}{S_R^2} \left[(2 - \sigma_N) \Pi(S_{R,\delta}) + \frac{\sigma_N}{2} \sqrt{\frac{\pi T_w}{T_\infty}} \chi(S_{R,\delta}) \right] \quad (1.71)$$

$$C_{t,fm} = \frac{\sigma_T \sin \delta}{S_R} \chi(S_{R,\delta}) \quad (1.72)$$

where:

$$S_{R,\delta} = S_R \cos \delta \quad (1.73)$$

$$\Pi(x) = \frac{1}{\sqrt{\pi}} \left[x \exp(-x^2) + \frac{\sqrt{\pi}}{2} (1 + 2x^2)(1 + \operatorname{erf} x) \right] \quad (1.74)$$

$$\chi(x) = \frac{1}{\sqrt{\pi}} \left[\exp(-x^2) + \sqrt{\pi} x (1 + \operatorname{erf} x) \right] \quad (1.75)$$

S_R is the molecular speed ratio, and *erf* is the error function. In the continuum regime the aerodynamics are based on the modified Newtonian theory, even though no specific formulation has been reported in the literature [Klinkrad et al., 2001, Koppenwallner et al., 2005]. In the transitional regime the aerodynamics are computed according to the reference values from the continuum and free molecular regime, interpolated with a Knudsen number-based bridging function. In the subsonic and transonic regime a cross-flow approximation is employed.

The aerothermal heating is computed depending on the flow regime. In the free molecular regime the local heat transfer is calculated using a custom formulation based on the velocity, attitude, and atmospheric conditions. In the continuum regime, a simplified formulation based on the Detra, Kemp, and Riddell model [Kemp et al., 1959] with the local panel inclination distribution term defined as in [Lees, 1956]:

$$St_c = \frac{2.1}{\sqrt{Re_{\infty,s}}} (0.1 + 0.9 \cos \theta) \quad (1.76)$$

where:

$$Re_{\infty,s} = \frac{\rho_{\infty} V_{\infty} R_N}{\mu(T_s)} \quad (1.77)$$

by defining $\mu(T_s)$ as:

$$\mu(T_0) = \mu(T_{\infty}) \left(\frac{T_s}{T_{\infty}} \right)^{\omega} \quad \text{with} \quad \omega = 0.72 \quad (1.78)$$

While in the transitional rarefied regime a bridging function is used:

$$St = \frac{St_c}{\sqrt{1 + (St_c/St_{fm})}} \quad (1.79)$$

Where St is the Stanton Number, the subscript s represents the stagnation point, and R_N is the effective nose radius, which in the literature [Koppenwallner et al., 2005, Klinkrad et al., 2001] is not described how it is computed for complex shapes. The heat transfer in the continuum regime can be computed by using the equations 1.31 and 1.76. SCARAB computes the aerodynamics and aerothermal heating only on the visible panels, the internal ones are considered as shadowed, and the self shadowing (attitude dependent) is also considered.

Once the heat-flux has been computed for each panel, the thermal module calculates the energy balance. Each panel has a heat loss computed according the Stephan-Boltzmann law. Depending on the size of the panel and the rate of heating, the panel

may be subdivided into several layers for computing the in-depth heat conduction. If the melting temperature is reached, the panel start melting, it is assumed that the molten mass is blown away by the external flow. This is the standard assumption for metallic materials, however, it has been recently proven that the ablation of CFRP materials used for overwrapping aluminum fuel tanks may not be simulated with typical metallic materials model [Masuda et al., 2015, Lips et al., 2017]. SCARAB can model CFRP ablation, taking into account pyrolysis, oxidation and sublimation, a full description of the model may be found in [Fritsche, 2013].

At each simulation step a structural analyses is evaluated, and the differential load, which are due to the aerodynamic and inertia forces, are computed. The differential load cause internal stresses which are assimilated to an equivalent stress, and the structural break-up occurs if the following condition is met:

$$\sigma_{eq} = \sqrt{\sigma + 3\tau^2} \geq \sigma_{ult}(T) \quad (1.80)$$

where the $\sigma_{ult}(T)$ is the temperature-dependent ultimate tensile strength.

1.4.4 Theoretical Analysis of SCARAB Aerothermal Model

SCARAB approximation for computing the Stanton Number in the continuum regime, and the subsequent heat transfer, was already found overestimate the aerothermal heating of 30% to 40% [Merrifield et al., 2015a]. During the preliminary analyses of all the different models used in the literature, and a research recently published [Benedetti et al., 2018] the authors reached the same conclusion. SCARAB model should be a direct simplification of Detra, Kemp, and Riddell approximation (DKR, [Detra, 1957], eq. 1.61) and such a discrepancy should not be expected. Therefore, some analyses have been performed using a reference velocity of 7600m/s, a reference atmospheric model (NRLMSISE-00), in the altitude range between 45km and 65km, a reference nose radius of 1.24m was used, and only the stagnation point with a normal inclination (i.e.: $\theta = 0deg$) was chosen. Additionally, further analyses were performed using also Fay-Ridell model (eq. 1.58 which is a more accurate version of the DKR approximation), and the Van Driest model (which represents a lower boundary, as the model is non-catalytic for the recombination). The comparisons are reported in Figure 1.20.

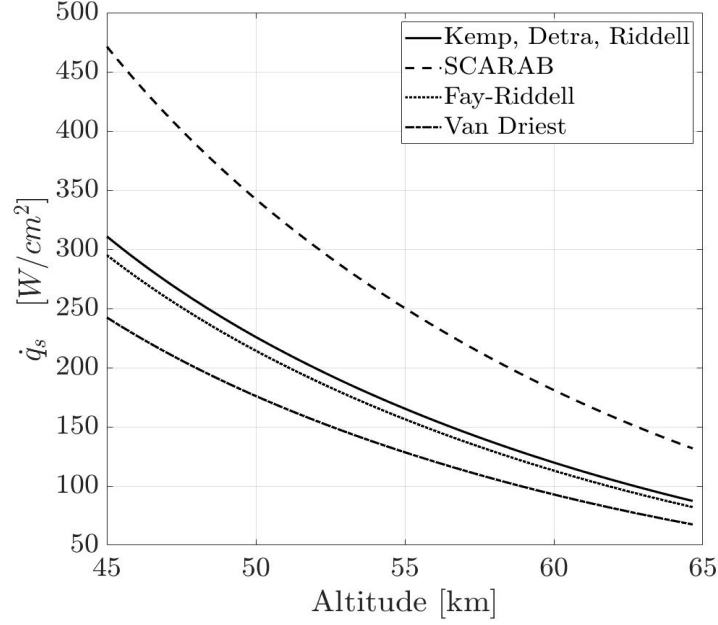


Figure 1.20: Comparison of the different aerothermal heat flux models in the continuum regime, showing SCARAB overestimation.

Fay-Riddell and DKR formulations compare very well, indeed, only a minor difference due to the fully catalytic (DKR) and partial catalytic wall (FR) was shown. In fact, the Fay-Riddell implementation used for the comparison was for a partial catalytic condition (i.e.: approximated with $Le = 1$, which cannot be representative of the non-catalytic condition, but neither of a fully catalytic condition), Van Driest model is sensibly lower, due to the non-catalytic wall condition, and this model represents the lower boundary. Even though SCARAB should be a fully catalytic model as well as the DKR model, the discrepancies are clearly too significant to be neglected, indeed the comparative figure shows roughly a 45% overestimation. Therefore, in order to investigate which was the possible origin of the discrepancy, a theoretical comparison of the two models was performed. SCARAB formulation from eq. 1.76 to eq. 1.78, may be written as:

$$St_{sc} = \frac{2.1\sqrt{\mu_{\infty}} \left(\frac{T_s}{T_{\infty}}\right)^{\frac{\omega}{2}}}{\sqrt{R_N V_{\infty} \rho_{\infty}}} \quad (1.81)$$

where the temperature ratio, for a hypersonic flow (i.e.: $h_s \gg h_{\infty}$) can be written as:

$$\frac{T_s}{T_{\infty}} = 1 + \frac{V_{\infty}^2}{2cpT_{\infty}} \approx \frac{V_{\infty}^2}{2cpT_{\infty}} \quad (1.82)$$

and substituting in eq. 1.81:

$$\text{St}_{\text{sc}} = \frac{2.1 \sqrt{\mu_{\infty}} \left(\frac{V_{\infty}^2}{2cpT_{\infty}} \right)^{\frac{\omega}{2}}}{\sqrt{R_N V_{\infty} \rho_{\infty}}} \quad (1.83)$$

which can be simplified as:

$$\text{St}_{\text{sc}} = \frac{2.1 V_{\infty}^{(\omega-0.5)} \sqrt{\mu_{\infty}}}{\sqrt{R_N \rho_{\infty}} (2cpT_{\infty})^{\frac{\omega}{2}}} \quad (1.84)$$

where the terms μ_{∞} , cp , and T_{∞} are variable w.r.t. the altitude and the atmospheric model, and can be normalized (in order to better appreciate their variability within the investigated atmospheric range) and are reported in Fig. 1.21; by observing the figure it can be concluded that the variation of cp is negligible. The ratio of the atmospheric properties may be defined as:

$$\Gamma(H, \omega) = \frac{\sqrt{\mu_{\infty}}}{(2cpT_{\infty})^{\frac{\omega}{2}}} \quad (1.85)$$

where $\Gamma(H, \omega)$ is the investigated ratio as a function of the atmospheric altitude, and the viscosity exponent coefficient (ω). Only the variability of this function is of interest, thus it can be normalized obtaining the function shown in Fig. 1.21 on the right (obtained for different values of ω , which may vary from 0.70 to 0.80, as shown in Table 1.1. The results show a minor variation over the investigated altitude range (less than 1%), thus its variation can be neglected, and the average values for the viscosity, temperature, and the constant pressure specific heat can be used.

The previous analysis can be used to further reducing the SCARAB model as:

$$\text{St}_{\text{sc}} = \bar{\Gamma}_0 \frac{2.1 V_{\infty}^{(\omega-0.5)}}{\sqrt{R_N \rho_{\infty}}} \quad (1.86)$$

where $\bar{\Gamma}_0$ is the mean value over the altitude range and for $\omega = 0.72$ (as in SCARAB), $\bar{\Gamma}_0 = 0.3745 \times 10^{-4}$. Leading to the definition of St_{sc} as a function of R_N , ρ_{∞} , V_{∞} and ω . This form is directly comparable with the approximation defined by Detra, Kemp, and Riddell in eq. 1.61, which for the sake of readability is reported below (in metric units):

$$q_{s,\text{DKR}} = \frac{110.30 \times 10^6}{\sqrt{R_N}} \sqrt{\frac{\rho_{\infty}}{\rho_{\text{SL}}}} \left(\frac{V_{\infty}}{V_{\text{circ}}} \right)^{3.15} \left(\frac{h_s - h_w}{h_s - h_{w,300}} \right) \left[\frac{W}{m^2 s} \right] \quad (1.87)$$

Assuming a cold wall condition (i.e.: $h_w = h_{w,300}$), the enthalpy term is unitary, but

Chapter 1. Introduction

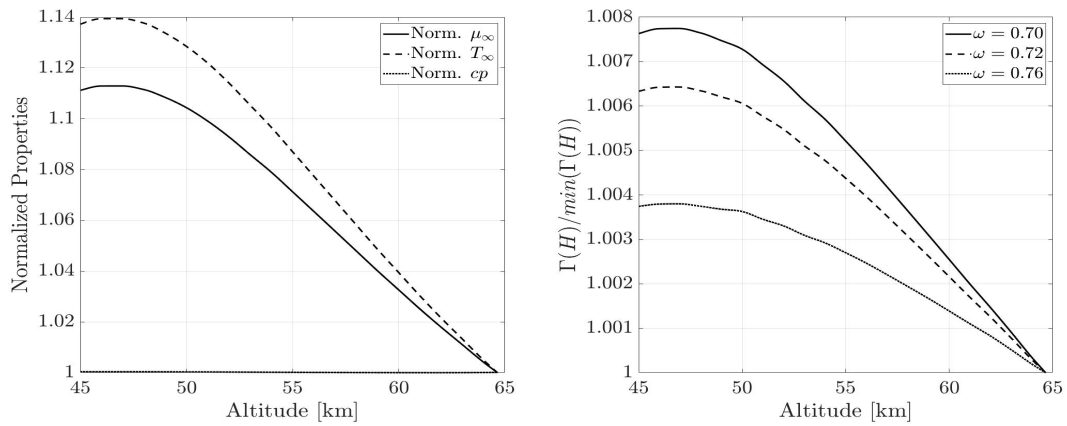


Figure 1.21: *Left*: Normalized atmospheric properties (normalization computed as: $x/\min(x)$, where x is the considered property). *Right*: normalized $\Gamma(H, \omega)$ function obtained for $\omega = [0.70, 0.72, 0.76]$.

even without this assumption, for a hypersonic flow the term $(h_s - h_w)/(h_s - h_{w,300})$ lays in the range between 0.9 and 1. The analysis of the error introduced with the cold wall assumption for the approximation of Kemp and Riddell (eq. 1.54) and the updated form (DKR, eq. 1.87), is reported in Figure 1.22.

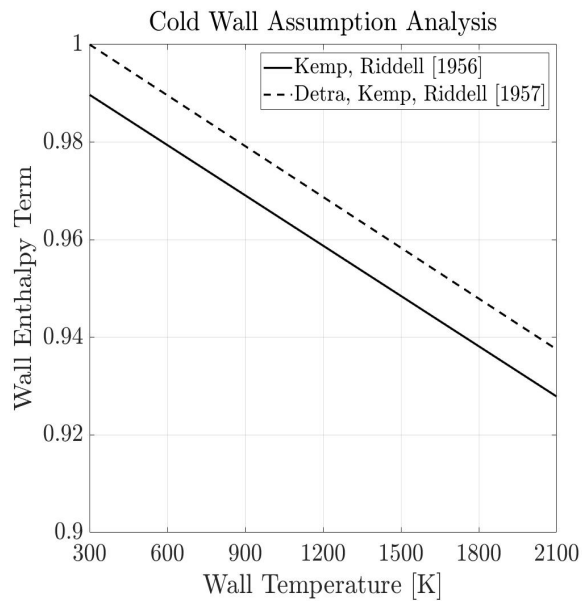


Figure 1.22: Wall Enthalpy term analysis for estimating the error introduced by the cold wall assumption for the simplified approximations of Kemp and Riddell [Kemp, 1956], and the DKR model [Detra, 1957].

Referring to the simplified form of the Stanton number (in the form of eq. 1.31), St_{DKR} can be defined as:

$$St_{DKR} = \frac{2 q_{s,DKR}}{\rho_{\infty} V_{\infty}^3} \quad (1.88)$$

which taking into account the simplifications becomes:

$$St_{DKR} = \frac{110.30 \times 10^6}{\sqrt{R_N}} \sqrt{\frac{\rho_{\infty}}{\rho_{SL}}} \left(\frac{V_{\infty}}{V_{circ}} \right)^{3.15} \left(\frac{2}{\rho_{\infty} V_{\infty}^3} \right) \quad (1.89)$$

which simplifying and re-arranging the terms becomes:

$$St_{DKR} = \left(\frac{2 \cdot 110.30 \times 10^6}{V_{circ}^{3.15} \sqrt{\rho_{SL}}} \right) \left(\frac{V_{\infty}^{0.15}}{\sqrt{R_N \rho_{\infty}}} \right) \quad (1.90)$$

where the first term is a constant, where $V_{circ} \approx 7915\text{m/s}$ is the circular orbit velocity, $\rho_{SL} = 1.2250\text{kg/m}^3$ is the sea level density, and the second term is representative of the atmospheric variables, expressed in an analogous form of eq. 1.86. The St_{DKR} equation can be further simplified as:

$$St_{DKR} = 1.046 \times 10^{-4} \left(\frac{V_{\infty}^{0.15}}{\sqrt{R_N \rho_{\infty}}} \right) \quad (1.91)$$

which can be directly compared with St_{sc} (eq. 1.86) rewritten as:

$$St_{sc} = 0.786 \times 10^{-4} \left(\frac{V_{\infty}^{(\omega-0.5)}}{\sqrt{R_N \rho_{\infty}}} \right) \quad (1.92)$$

Using $\omega = 0.72$, it appears evident that SCARAB formulation will overestimate the aerothermal heating, indeed the ratio between SCARAB and DKR approximations is:

$$\frac{St_{sc}}{St_{DKR}} = \frac{0.786}{1.046} V_{\infty}^{(\omega-0.65)} \quad (1.93)$$

which is representative of the discrepancy which was initially described. A sensitivity analysis of such overestimation is shown in figure 1.23. It must be noted that the simplification (i.e.: cold wall assumption) applied to DKR model tend to increase the aerothermal heating estimated, thus reducing the discrepancy. Additionally, the comparison was performed also with the first approximation proposed by Kemp and Riddell (eq. 1.54, [Kemp, 1956]), for which the ratio (after the proper elaborations) may be written as:

$$\frac{St_{sc}}{St_{KR}} = \frac{0.786}{0.504} V_{\infty}^{(\omega-0.75)} \quad (1.94)$$

It is worth noting the opposite effect of an increased velocity for this model, shown

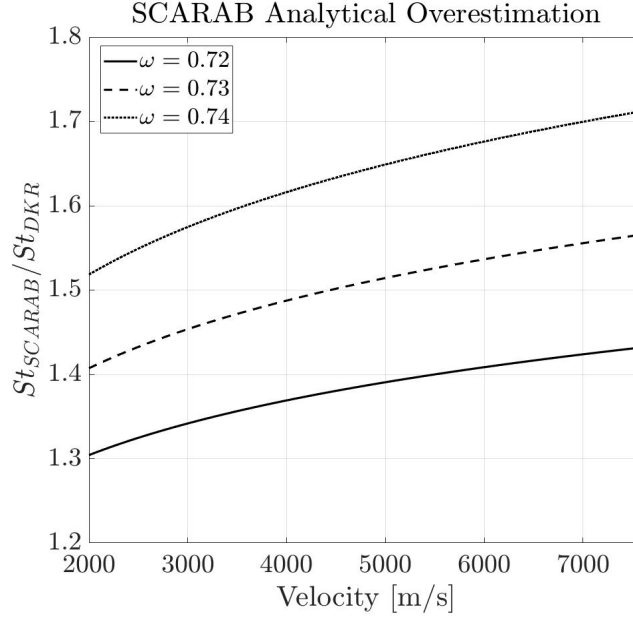


Figure 1.23: SCARAB aerothermal heating overestimation sensitivity analysis w.r.t. to the original Detra, Kemp, Riddell approximation [Detra, 1957], the analysis shows a lower boundary (i.e.: cold wall assumption).

in Figure 1.24. In this ratio, the velocity causes an underestimation of the heat transfer. In addition, the viscosity exponential coefficient used in SCARAB is closer to the value of the negative exponent of the velocity (-0.75), which causes the lesser sensitivity of the ratios to the velocity variation. Although, SCARAB constant coefficients is yet 56% higher than the Kemp-Riddell model, which leads to the overall overestimation for SCARAB aerothermal heating. As a final consideration, the aerothermal heating ratio between the original Kemp-Riddell and the DKR models can be derived from eq. 1.93 and eq. 1.94 as:

$$\frac{St_{DKR}}{St_{KR}} = \frac{1.046}{0.504} V_{\infty}^{(-0.10)} \quad (1.95)$$

This model shows that the DKR model, (which is a correction of the KR model, taking into account the findings of Fay and Riddell [Fay, 1957] and a wider set of experimental data [Kemp, 1956]), decreases the estimated heat flux which was earlier predicted with the KR approximation. Analyzing eq. 1.95, a reduction ranging from -4% at 2000m/s to -18% at 7600m/s may be observed, making the use of DKR model not only more accurate but also more conservative for performing re-entry survivability analysis.

Even though this analysis shows an analytical relationship of the discrepancies between the different models, it is still unclear which assumptions have been used for defining the SCARAB model as an equivalent form [Koppenwallner et al., 2005] of

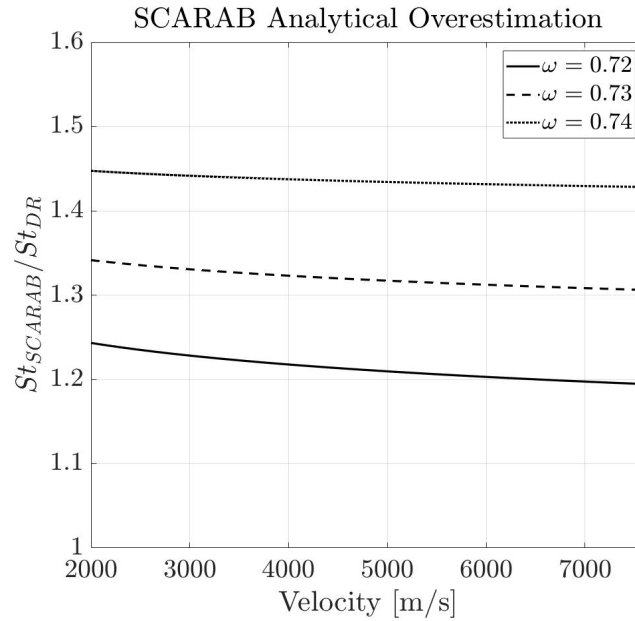


Figure 1.24: SCARAB aerothermal heating overestimation sensitivity analysis w.r.t. to the original Kemp and Riddell approximation [Kemp, 1956], the analysis shows a lower boundary (i.e.: cold wall assumption).

Detra-Kemp-Riddell model, as it appears evident that at equal conditions SCARAB model computes an overestimated heat-flux ranging from 30% to 45% higher. In this analysis it has not been considered the radiative heat-flux, which has been estimated in the order of 5% to 10% at the maximum velocity (7600m/s) and for the reference nose radius (1.24m). In light of the performed analysis, using SCARAB model for the aerothermal heating is not recommended, especially if the purpose of the re-entry simulation is to estimate the survivability risk, as this simplification would lead to an increased mass ablation, and lower estimated risk, which for the purpose is not conservative. Although, SCARAB model could be used for designing thermal protection systems, and the model could be considered as an upper boundary for the aerothermal heating estimation, representative of a super-catalytic model.

1.4.5 DRAMA/SESAM

The Debris Risk Assessment and Mitigation Analysis suite had been commissioned by the ESA's Space Debris Office to provide a tool for verifying the compliance of space mission to the Space Debris Mitigation Compliance Verification Guidelines [ESA, 2015]. DRAMA is a suite that provides different capabilities such as: prediction of debris and meteoroid flux, determination of penetration for different shielding design, prediction

of required avoidance maneuvers for operational satellites and spacecrafts, prediction of orbital lifetime and de-orbiting procedures, object oriented atmospheric reentry and casualty risk analyses. SARA is the designated module for performing the "Survival and Risk Analysis", which comprises the two modules: the Spacecraft Entry Survival Analysis Module (SESAM) and the Spacecraft Entry Risk Analysis Module (SERAM). SESAM simulates the atmospheric survivability of the reentering spacecraft and its fragments, then SERAM computes the casualty risk assessment based on the ground impact location. SESAM is an object oriented tool, it is very similar to ORSAT and the aerothermodynamics and aerodynamics formulations are almost a direct implementation of what has been already described for ORSAT.

DRAMA allows to simulate the reentry of spacecraft represented by assemblies of simple-shaped objects, such as sphere, cones, boxes and flat plates. The objects may be connected with the relationship of "connected-to" and "included-in", whereas the first one represents the connection between two objects and the second one implies the relationship of parent/children objects. These relationships are broken according to a thermal criterion, which means that two objects will separate when one of the two objects' melting temperature is reached. In addition, SESAM takes into account the shadowing effects in order to redistribute the aero-thermodynamic properties (i.e.: heat flux and drag coefficient) weighted with a computed visibility factor (according to a voxelator-based approach [Mehta et al., 2016a]). The aerothermodynamics are computed based on the environment properties obtained as a combination of three atmospheric models: the US Standard Atmosphere 1976, the NRLMSISE00, and the Horizontal Wind Model 2014.

The computation of aerodynamic and aerothermodynamic parameters of several different combinations of primitives, which are not predictable a priori, are computed in order to obtain averaged aerodynamic and aerothermodynamic coefficients. In SESAM it is used a linear combination of pre-computed averaged properties on the selected primitives assuming that they were in a free stream. The databases are Mach and Knudsen number -dependent. The weights of the linear combination is assumed to be the visibility factor ratio computed as the visible surface of each primitive w.r.t. the total object surface. If the primitive is completely hidden the visibility ratio (thus also its aerothermodynamic contribution) will be null. A basic assumption is that the surface or the shape of each primitive does not change with the progressive ablation, and only the breaking of connection bounds of the different primitives and the relative shadowing interaction may cause a variation of the computed aerothermodynamics properties. The aerodynamics are modeled depending on the flow regime (FMF, continuum, or rarefied transitional) and the Mach number. In the subsonic regime, the drag coefficient is reduced by 50%. The aerodynamic coefficients (lift, drag and side force) are computed as

a linear combination of the visibility ratio of each primitive. The heat-flux is computed as an averaged, shape dependent, stagnation point correlation, using an equivalent effective nose radius, employing the same equation as in ORSAT for the different regimes [1.68-1.69]. The heat-flux for each primitive is then multiplied to an averaging factor dependent on the shape, dimension, and attitude. Afterwards, the shading factors are applied to take into account the self-shadowing effects which are attitude dependent.

The structural thermal and ablation models assume that two connected primitives exchange heat depending on two parameters: thermal conduction and connection area. Two different ablative models are used for metallic materials and CFRP materials. The metallic materials are assumed to initiate the ablation when the melting temperature is reached and the ablation rate is dependent on the incoming heat (computed by the aerothermodynamics module), the radiative cooling, and the specific heat of melting. The CFRP materials ablation is modeled through a multi-layered approach, according to epoxy pyrolysis and oxidation of the charred carbon fibers. The thermal properties are modeled as temperature independent. The thermal and trajectory propagator are coupled, thus the mass change and size change which occurs during the ablation will affect the dynamics of the fragments. Also the In SESAM it is possible to model explosion events, which have been modeled according to NASA's EVOLVE 4.0 [Johnson and Stansbery, 2010].

The breakup and the trajectory propagation is performed with a 3-DOF approach. Different attitude motion may be assumed: random tumbling, tumbling around a given axis and a fixed attitude. When the breakup occurs, the fragment will either inherit the attitude from its parent or assume a random tumbling motion.

1.4.6 PAMPERO

PAMPERO [Annaloro et al., 2014] is a spacecraft oriented tool recently developed by the CNES (Centre National d'Etudes Spatiales). PAMPERO simulates objects using a complex 3D mesh which allows a more accurate modeling capabilities for structural and thermal analysis. The reentry trajectory is simulated via a 6-DOF approach. At each time-step the viewing factors are computed for determining windward elements. Surface elements are also used to compute the local curvature radius, which is then employed by the convective heat-flux estimation algorithm. The aerodynamics are computed according to the local panel inclination; in the continuum regime the Modified Newtonian Theory [Lees, 1955] is used:

$$C_p = C_{p,stag} \sin^2 \theta \quad (1.96)$$

where the C_p is the pressure coefficient for each i th panel, dependent on the maximum C_p which is computed for the stagnation point and the panel inclination θ . The

computation in the free molecular regime are based on the analytical law proposed by Bird [Bird, 1976], while in the transitional rarefied regime a typical Knudsen-dependent bridging function is employed.

The aerothermal heating is estimated according to empirical and numerical correlations of convective heat flux (the radiative heating is not considered). The aerothermal heating depends on the stagnation point heating which is redistributed according to a function dependent on the local pressure and local nose radius. These functions have been calibrated based on DSMC (for the free molecular regime) and CFD results (in the continuum regime). PAMPERO structural thermal module allows the detection of the ablation of a tetrahedron, which is assumed to happen when the melting temperature is reached [Annaloro et al., 2014]. After the ablation the mesh is updated and the tetrahedron is deactivated, requiring the update of the local nose radius and viewing factors.

Over the last years, PAMPERO has been compared to different CFD, DSMC, and experimental cases [Annaloro et al., 2017a]. The validations have shown a good agreement also with SCARAB [Annaloro et al., 2017b].

1.4.7 DEBRISK

DEBRISK is the object oriented reentry analysis tool developed by CNES. The tool firstly introduced in [Omaly and Dieudonne, 2010] is based on a 3-DOF trajectory propagation. The aerodynamics are based on a set of curves defined for the subsonic, transonic and supersonic regimes. The drag coefficients of different primitives [Omaly and Spel, 2012] is referred to the same models used in ORSAT [Dobarco-Otero et al., 2005]. The aerothermal heating is based on the different terms: convective, oxidation heat transfer (as in [Dobarco-Otero et al., 2005]), and radiative cooling (the radiative heat flux due to the hot gas cap is neglected). The convective heating is based on the experimental correlations defined with the shape factors by Klett [Klett, 1964]. The temperature of the object is defined with the lumped mass approach, where the object temperature is assumed to be uniform. When the melting temperature is reached, the thermal energy is used to initiate the melting of the object, where the molten mass is assumed to be blown out by the external flow. In [Omaly et al., 2013, Omaly et al., 2015] Debrisk has been validated and tested against ORSAT and other CFD and experimental analyses, highlighting that there are no significant discrepancies between the two object oriented tools, but the aerothermal heat flux is generally overestimated when compared to experiments and CFD tools.

1.4.8 SAM

The Spacecraft Aerothermal Model has been developed with the aim of thoroughly investigating the influence of trajectory propagation, aerothermal modeling, fragmentation and material thermal response models. An initial description of the software along with some validation and comparison test case has been reported by Merrifield et al. in [Merrifield et al., 2015b]. SAM performs a trajectory propagation with 6-DOF before the main breakup, and a 3-DOF propagation on the fragments. The aerodynamic and aerothermal estimation is based on the local panel inclination methods with some specific adjustments. The continuum aerodynamic coefficients are computed with the Modified Newtonian Theory [Lees, 1955], while the Schaaf and Chambre [Chambre and Schaaf, 1961] flat plate model is used for the rarefied regime; even though not clearly stated, it can be assumed that a bridging function is used in the transitional rarefied regime. In [Merrifield et al., 2015a] Merrifield et al. compared the commonly used models for estimating the aerothermal heat flux, proposing a combination of the Detra and Hidalgo [Detra and Hidalgo, 1960] model with a running length and a flat face shape-dependent correction. The running length correlation has been tested on the HB2 geometry and on an end-on cylinder, and it is defined in the general form of:

$$\frac{Q}{Q_{\text{stag}}} = \frac{f(\theta)}{\sqrt{x}} \quad (1.97)$$

where x represents the running length from the nearest edge of the geometry measured on the flow direction, and $f(\theta)$ is a function dependent on the inclination angle.

When the object is characterized by flat faces (e.g.: flat cylinder in an end-on configuration) the correlation proposed by Klett [Klett, 1964] taken into account for the flat face heat distribution:

$$\frac{Q}{Q_{\text{stag}}} = 1 + 0.6 \left(\frac{x}{r} \right)^{3.3} \quad (1.98)$$

where x is the distance from the center of the face and r is the radius of the circular face (in the case of a box, it could be assumed to use the half-diagonal instead of r). In SAM it is used a combination of eq.1.97-1.98 and the Detra Hidalgo aerothermal model. Such combination has been tested on different geometries (cube [Merrifield et al., 2015b], open cylinders, flat cylinders and the HB2 probe [?]), the results have shown significant improvements w.r.t. standard inclination methodologies, with particular attention to flat faces and sharp corner relative heat flux distributions.

In SAM, the material thermal response is modeled with mainly two approaches: for metallic materials the recession rate is estimated according to simple conduction and ablation models, while for insulators it has been developed a simplified Heat Balance

Integral model, which has been proven to provide more accurate results when compared to standard metal bulk heating and ablation models [Beck and Merrifield, 2015]. In [Beck et al., 2015] SAM has been verified on the DELTA II reentry, highlighting the importance of employing 6-DOF trajectory propagation due to complex object self-shadowing impact on the aerothermal estimation.

Considering the overall approach on the reentry problem, the capability of modeling complex geometries, the local aerothermal modeling approach, the material-based thermal response modeling and the 6-DOF trajectory propagation, SAM may be considered to be in between spacecraft and object oriented codes.

1.4.9 SPEAD

The Simulation for Prediction of Entry Article Demise (SPEAD) is a software used to perform spacecraft break-up and burn-up analyses [Ling, 2015] developed by NASA. The tool has been used for performing off-nominal re-entries, risk assessments, and modeling debris impact footprints. Although the software was mainly thought for evaluating contingency plan in case of failure during a nominal ascent/reentry, its capabilities are considered comparable to the previously described reentry software. The tool is able to perform both 3- and 6-DOF trajectory propagation, integrating translational and rotational motion using a 4th order Runge-Kutta. The dynamics are computed according to gravitational, aerodynamics, control and actuation forces and moments. The atmospheric properties are provided with the use of tables and are planet-dependent. The G-load is computed using non-gravitational accelerations. The aerodynamics are computed using linear interpolation on table data. During the trajectory propagation, mass change due to node ablation and fuel depletion is considered. The footprint estimation is dependent on all the considered variables and the winds, which may be taken into account for considering downrange and crossrange distances. The statistical footprint is generated to bound the debris' impact points location due to uncertainties in the considered variables: environment, winds intensity and direction, vehicle properties and configuration. Monte Carlo analyses may be performed using uniform or normal distribution on the inputs. The thermal models uses a free molecular to continuum convective heating transition, the lower values for the two are taken as references. The spacecraft is modeled through the use of thermal nodes represented by simple shapes (i.e.: sphere, cylinders, cubes...), once the nodes reach the melting temperature, the ablation is initiated. The heat flux at each node is computed in accordance with its orientation and an exposure factor, computed in accordance to the node visibility. Geometries and nodes heat fluxes are influence by a "heating factor" and a convective area. The radiative heating is considered for high velocity reentries (velocity greater

than 9km/s), and the radiative cooling is computed according to Stefan-Boltzman law. The nodes temperature is computed with a lumped mass approach, whereas the adjacent nodes conductive heating is approximated with the 1D Fourier's law. The ablation rate is considered dependent on the incoming heat-flux to the node and its heat of fusion. The ablation decreases the convective, radiative and reference areas, thus decreasing the total incoming heat-flux; not considering this effect would result in a underestimated surviving mass and fragments. The material properties are stored in a built-in database, solid and liquids (propellants) properties are modeled as constants. The software allows the node failure evaluation due to different strategies: material melting temperature and structural break-up due to g-load and/or differential force along the direction of deceleration on two different objects connected by a support. The tanks have three different mode of failure: through the reaching of the melting temperature, when the liquid propellant reaches the boiling point, and due to increasing of internal pressure and the consequent structural failure.

In SPEAD several different phenomena are taken into account; it provides the capabilities for propagating trajectories, modeling thermal analyses and evaluating failure scenarios. The coupled burn-up and impact footprint estimation allows the analyses of a sequence of break-up events and progressive demise on the thermal nodes. Although, the aerodynamics and aerothermodynamics are modelled with a very simplified approach, most likely causing a decrease of the overall accuracy. Although, this is taken into account by coupling a Monte Carlo approach on the impact footprint and surviving debris estimation.

1.4.10 Re-entry Software Summary

Following the brief description of the software currently used for performing atmospheric re-entry analysis, a taxonomy highlighting the major differences and similarities is presented in table 1.2 and 1.3. A critical information that is missing in the description of almost every software is whether the shape evolution due to the ablation is coupled with the trajectory propagation or not, and how the shape is assumed to evolve during the ablation (i.e.: shape preserving, based on the aspect ratio, etc...). Such assumption is deemed to have a great influence on both the aerodynamics and on the total aerothermal heating absorption, as it is also highlighted in [Ling, 2015]. Software using 3D volumetric meshes may allow a better representation of the space debris evolution during the re-entry, mitigating the influence of this potential source of uncertainty.

Table 1.2: Taxonomy for re-entry software currently used [1/2].

	Aero-thermal model	Aerodynamics	Flight dynamics	Breakup model
DAS	Convective Radiative (cooling)	Shape based Averaged	3DOF No lift	Fixed altitude parent-children
ORSAT	Convective Radiative Conductive Shape/motion-based	Shape-based Motion-based	3DOF Lift Motion-based	Thermal Structural Tank bursting
SCARAB	Convective Radiative Conductive LPI	LPI Shadowing	6DOF 3DOF (surviving fragments)	Thermal Structural (FEM) Tank bursting
DRAMA (SESAM)	Convective Radiative Conductive View Factors	Shape-based View factors (Voxelator)	3DOF Viewing factor Motion based	Fixed altitude connections breakup
DEBRISK	Convective Radiative (cooling)	Shape-based	3DOF Lift (?)	Fixed altitude
PAMPERO	Convective Radiative Conductive LPI (Local Radius)	View Factors	6DOF	(?)
SAM	Convective Radiative Conduction LPI	LPI	6DOF 3DOF	Fixed altitude Critical points
SPEAD	Convective Radiative conductive Heating/viewing Factors	Shape-based View Factors	6DOF 3DOF	Node failure (thermal/structural) Tank bursting

Table 1.3: Taxonomy for re-entry software currently used [2/2].

	Uncertainty treatment	Geometry accuracy	Modelling fidelity	Materials
DAS	No (?)	Simple shapes	Low fidelity Lumped-mass Coupled (?)	Metals
ORSAT	No (?)	Simple shapes	Ablation, thermal 1D/2D Coupled (?)	Metals Non-metallic Ablators Liquids
SCARAB	Monte Carlo	Complex geometries 3D Mesh	Ablation, pyrolysis..., thermal 1D/2D Coupled	Metals CFRP Non-metallic Liquids
DRAMA (SESAM)	Monte Carlo (?)	Simple shapes (with connections)	Low-fidelity, Lumped mass Coupled (?)	Metallic CFRP
DEBRISK	No (?)	Simple shapes	Low-fidelity Lumped mass Coupled (?)	Metals (?)
PAMPERO	No (?)	Complex 3D Mesh	Thermal 3D	Metals (?)
SAM	Monte Carlo (?)	Complex geometries	Lumped mass 1D conduction HBI (ablaters) Coupled (?)	Metals Non-metallic CFRP
SPEAD	Monte Carlo (integrated)	Simple shapes	Lumped mass Coupled	Metals Non-metallic Liquids

Integrated Modelling approach

The software initially presented as the Free and Open Source Tool for Re-entry Analysis of Asteroids and Debris (FOSTRAD) was initially developed to allow the probabilistic assessments of survivability of asteroids and space debris in the event of an atmospheric reentry [Mehta et al., 2015b]; the objects were modeled with a low-fidelity and computationally efficient approach. FOSTRAD was tested on different geometries, such as the STS orbiter, CFASTT-1 space-plane and the Gravity field and steady-state Ocean Circulation Explorer satellite aerodynamics [Benedetti et al., 2018] (GOCE). FOSTRAD's aerodynamics module showed an acceptable accuracy with experimental data when studying blunt-shaped bodies [Mehta et al., 2015c], but when applied to flat-shaped bodies like parallelepiped and flat cylinders the accuracy decreased. The software was progressively improved to allow a better aerodynamics and aerothermodynamics characterization of complex objects and spacecrafts. One of the most significant improvements was the introduction of a local radius-based approach on the standard LPI algorithm, which significantly increased the accuracy of the aerothermal heating estimation on complex objects [Falchi et al., 2017c]. Another significant update was the introduction of a coupling between the convective aerothermodynamics with a structural thermal and ablation code. Due to the shift in the application field, the software was later renamed as Spacecraft Tool for Re-entry and Aerothermal Analysis (STRATH-A). The upgraded software was tested on the Intermediate Experimental Vehicle (IXV), the Stardust Sample Return Capsule (Stardust SRC), and VEGA launcher vehicle payload fairing initial ascent phase [Falchi et al., 2019]; the analyses had shown a good approximation of high-fidelity aerothermal heat-fluxes distributions and provided a good match with both high fidelity simulations and experimental observations. A validation campaign of the aerodynamic and aerothermodynamic modules of the developed tool was performed and has been reported in the 3rd and 4th chapter of this thesis. In this chapter, the early developments of the software are described in the first section, which is followed by the developments and improvements performed as a part of this Ph.D. project.

2.1 Previous Work

FOSTRAD was firstly presented in [Mehta et al., 2015b], where the initial validation of the aerodynamic and aerothermodynamics modules of the software was performed against literature, CFD and DSMC data. The modeling was based on the Local Panel Inclination methods (as described in the first chapter). In the continuum regime the aerodynamic model was based on the Modified Newtonian theory (eq. 1.43), while in the continuum regime the Schaaf and Chambre flat plate theory was used (eq. 1.71). Initially, a shape-dependent sigmoid bridging function was used in the transitional regime. In the aerothermal heating estimation different models were available: Fay-Riddell formulation (eq. 1.56), Kemp-Detra-Riddell approximation (eq. 1.69), and Van Driest model [Van Driest, 1956], simplified as:

$$q_s = 0.94(\rho_s \mu_s)^{0.5} (h_s - h_w) \sqrt{\left(\frac{du_e}{dx}\right)_s} \quad (2.99)$$

where the subscript s refers to the stagnation point, and the boundary layer velocity gradient can be estimated with the Modified Newtonian formulation (eq. 1.43). In the free molecular regime the Schaaf and Chambre formulation was used, whereas in the transitional regime the bridging function defined by Legge was used:

$$Q_{s,\text{trans}} = \frac{Q_{s,\text{cont}}}{\sqrt{1 + \left(\frac{Q_{s,\text{cont}}}{Q_{s,\text{fm}}}\right)}} \quad (2.100)$$

In [Mehta et al., 2016b] Kubicek et al., presented an interesting application of FOSTRAD aerodynamic module for the uncertainty treatment of atmospheric reentries using a High Dimensional Model Representation (HDMR) approach. A spherical object of a constant mass (ablation is not considered) is simulated for an atmospheric re-entry using a 3DOF trajectory propagator with a planar reentry assumption, where the drag was the only aerodynamic force acting on the debris. The uncertainty quantification took into account 16 parameters, including flight path angle, reentry velocity, object mass, and direction angle, along with atmospheric variables. The research highlighted the necessity of using a probabilistic modeling approach for simulating atmospheric reentries.

A recent publication [Benedetti et al., 2018] focusing on FOSTRAD aerodynamic module highlighted the application of the methodology on different study cases: a sphere, IXV, STS orbiter, Orion capsule and GOCE. The research describes the techniques used

for applying the local panel inclination method to complex geometries and proposed general bridging functions for the accurate estimation of aerodynamic coefficients in the transitional regime. The paper explained a underestimation in the drag coefficient for shapes with a high lateral to front surface area ratio at small angle of attack (or side-slip), caused by the misidentification of visible facets, which lead to the underestimation of viscous forces on the lateral surfaces.

2.2 Aerodynamics and Aerothermodynamics Methodology: Overview

FOSTRAD has been thought for performing aerodynamics and aerothermodynamics simulations of space debris (having arbitrary and complex geometries) reentering the earth atmosphere; before performing a complete reentry simulation and elaborating on the destruction of these objects, the software has to compute the aerodynamics and estimate a reliable aerothermal heating in all the different regimes (at different altitudes and velocities). Therefore, an initial and simplified problem statement, can be formalized as it follows:

Determining the aerodynamic forces and moments along with the aerothermal heating rate and its distribution for an arbitrary shape reentering the atmosphere at a fixed velocity hypersonic (V_∞), with an arbitrary attitude (α, β), at a fixed altitude (H).

Which can be written as:

$$(C_{D,L,S}, C_{M_{x,y,z}}, q_{dyn}, C_H) = \Theta(H, V_\infty, \alpha, \beta, stl, \Phi_{atm}) \quad (2.101)$$

where the outputs $C_{D,L,S}$ and $C_{M_{x,y,z}}$ are the aerodynamic forces and moments coefficients, q_{dyn} is the dynamic pressure (defined as: $q_{dyn} = \frac{1}{2}\rho_\infty V_\infty^2$), C_H is the heat transfer coefficient (defined as: $C_H = \dot{q}/(\frac{1}{2}\rho_\infty V_\infty^3)$); and as for the inputs H is the atmospheric altitude, V_∞ is the undisturbed flow velocity, α and β are the attitude-defining parameters: angle of attack and side-slip respectively (also a roll angle could be included), the term "stl" is refers to the stereolithographic geometrical model (the .stl is a specific superficial mesh file extension), and the function Φ_{atm} represents the specific atmospheric model used for determining the altitude dependent atmospheric properties (for example the NRLMSISE00 or the U.S. Standard Atmosphere 1976 may be used). In order to solve such model, various techniques and formulation must be applied, and FOSTRAD has been thought to provide a solution for the defined problem statement. In Figure 2.1, the block diagram and the work flow of FOSTRAD has been reproduced, and a brief description of each module follows.

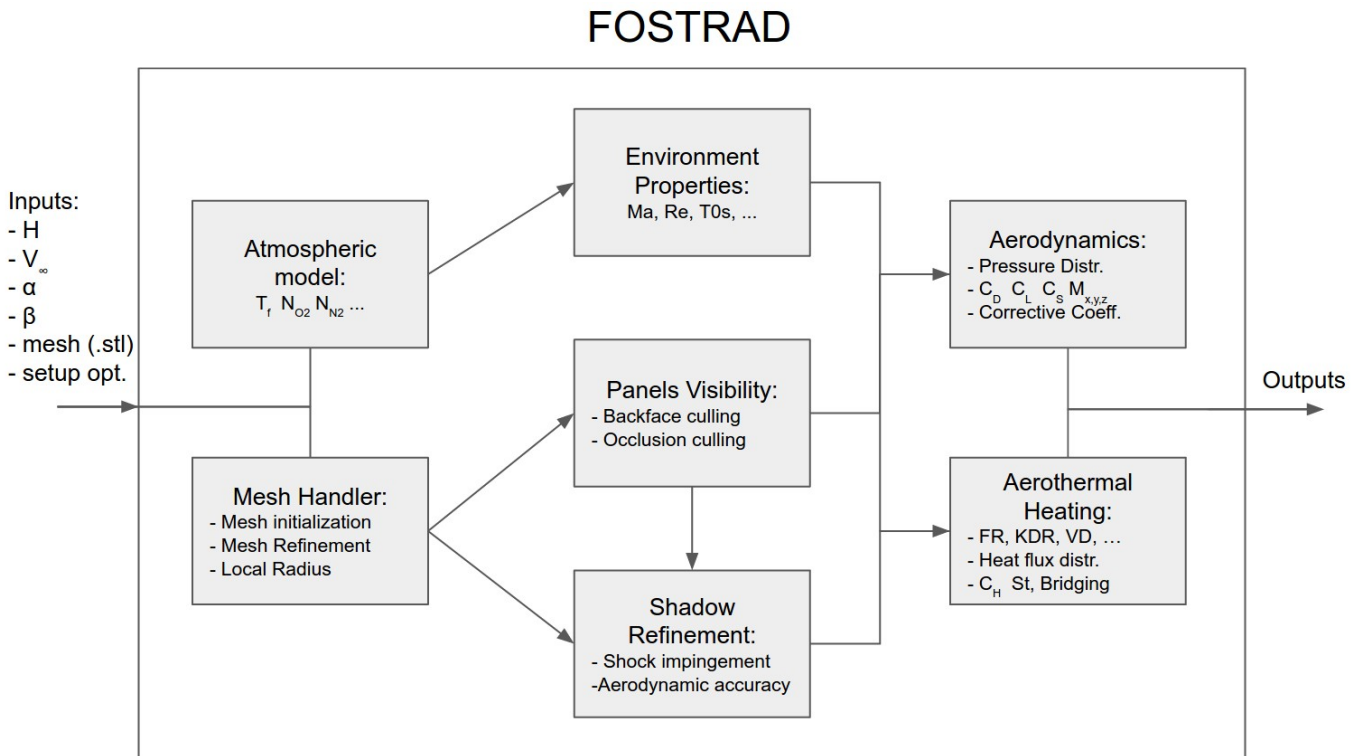


Figure 2.1: FOSTRAD block and work-flow diagram (overview).

Atmospheric Model and Environmental Properties

The atmospheric model is required in order to obtain the atmospheric properties per each possible altitude. This block has to provide the reference values for the atomic species densities (O, O₂, N₂, He, Ar, H, N), in alternative, the mass densities per species may be used to compute the atomic densities. The models will usually provide also the total mass density and the atmospheric temperature. This values are generally subjected to uncertainty, highly dependent on the solar activity which causes the expansion and contraction of the atmosphere. At the same altitude the atmospheric properties may have different values depending on the solar activity. The effect of the uncertainty may be reduced knowing an accurate value of the magnetic index, which is usually taken into account into the NRLMSISE00 atmospheric model.

In order to compute the aerodynamics and aerothermodynamics, the average properties of a gas mixture can be computed starting from an initial atmospheric database containing the atomic densities and temperature as a function of the altitude. The required equations have been thoroughly described in the atmospheric re-entry introduction (paragraph 1.3). The work-flow for computing the averaged gas mixture properties

and the environmental properties (including the required dimensionless numbers) is reported in Figure 2.2, where the detailed inputs and outputs from the atmospheric model and environmental properties blocks (from Figure 2.1) have been shown. In order to compute the averaged mixture properties, it is necessary to have all the information on the atmospheric species provided by the employed model, and then it is possible to compute the weighted average properties. For example for computing the mixture-averaged specific gas constant:

$$R_{\text{mix}} = \frac{\sum_{i=1}^m N_i R_i}{\sum_{i=1}^m N_i} \quad (2.102)$$

where R_{mix} is the average mixture specific gas constant, m is the number of atomic species considered, N_i and R_i are the i -th atomic species density [atoms/m³] and specific gas constant respectively.

Observing Figure 2.2, the reader may notice that it is necessary to swipe through a range of different altitudes to identify the altitude corresponding to the reference continuum and free molecular Knudsen numbers ($Kn_{c,\text{ref}}$ and $Kn_{fm,\text{ref}}$ respectively) of the specific object. Indeed, within the transition from the continuum to free molecular regime, it is necessary to use a bridging function to compute the flow viscosity (eq. 1.10). As it will be better explained in the aerodynamics and aerothermodynamics chapters (3 and 4 respectively), the altitude corresponding to the reference continuum and free molecular regime are of utmost importance for the accurate computation of aerodynamic and heat transfer coefficients.

The environmental properties computed from these blocks will be provided directly to the aerodynamics and aerothermodynamics blocks, which can further elaborate the properties taking into account the inputs provided by the mesh handler and the panel visibility blocks. The required environmental properties are the following:

- p - pressure [Pa]
- ρ_{mix} mixture density [kg/m³]
- $c_{p,\text{mix}}$ - mixture specific heat at constant pressure [J/kgK]
- R_{mix} - mixture gas constant [J/kgK]
- γ_{mix} - mixture specific heat ratio
- μ_{mix} - dynamic viscosity for Sutherland's and Enskog-Chapman models [Pa s]
- ω_{mix} - viscosity temperature exponent
- m_{mix} - mixture-averaged molecular mass
- Ma_{∞} - Mach Number
- Re_{∞} - Reynolds Number
- S_R - molecular speed ratio
- Kn - Knudsen Number

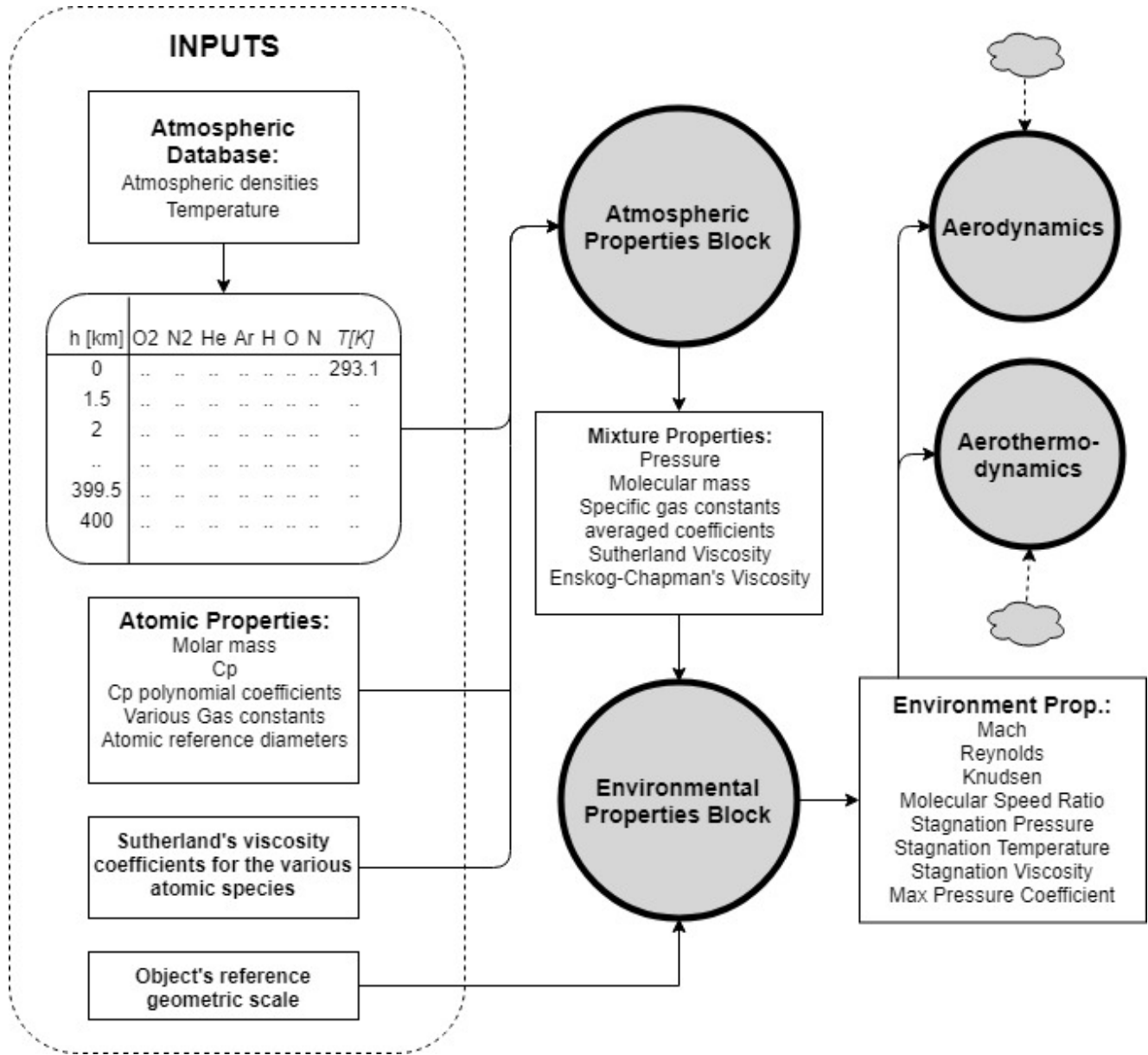


Figure 2.2: Atmospheric and Environmental properties detailed work-flow.

- Pr - Prandtl Number
- P_{02} - hypersonic continuum stagnation point pressure (after the bow-shock) [Pa]
- T_{0s} - stagnation point temperature (after the bow-shock) [K]
- ρ_s - stagnation point density (after the bow-shock) [kg/m³]
- h_s - stagnation point enthalpy [J/kg]
- $C_{p,max}$ continuum maximum pressure coefficient (Mod. Newtonian Theory)

Mesh Handler

The Mesh Handler block is required in order to perform all the necessary operation on the geometric model. Indeed, as the software is based on the local panel inclination method, the properties of each panel must be computed, some of the most important properties are:

- Inclination angle (θ_i)
- Panel area (A_i)
- Panel barycenter coordinate (w.r.t. the entire body barycenter)

In this block two main functions are performed: the mesh refinement and the local radius computation. The first one is required to increase the global accuracy of both aerodynamic and aerothermodynamics modules. The second one is required to allow the use of a local radius during the aero-thermal heating estimation. Both functions will be thoroughly described in the following paragraphs. A detailed work-flow of this block is shown in Figure 2.3.

In the first step, the .STL geometries are loaded and cleaned, and a triangular mesh matrix is obtained. Afterwards, the mesh must be refined according to the number of panels (analogous of a FEM cell size parameter). In this way, a sensitivity analysis of the required number of panels for obtaining a good accuracy may be performed. Once the mesh has been properly defined, it can be used for computing the panels properties (e.g.: barycenter, area, inclination w.r.t. a reference direction) and the local radius distribution may be computed in accordance with the algorithm setup parameters. The geometry voxelization may be required to compute some volumetric properties, such as inertia tensors, and mass distribution. All the computed properties must be used to perform aerodynamic, aerothermodynamic, and re-entry analyses.

Depending on the problem, it may be necessary to estimate different properties directly related to the geometry. For example, a complex space object such as a satellite, should be simulated with many different simple geometries, which could be approximated having a uniform density. Some parts could be approximated with full objects,

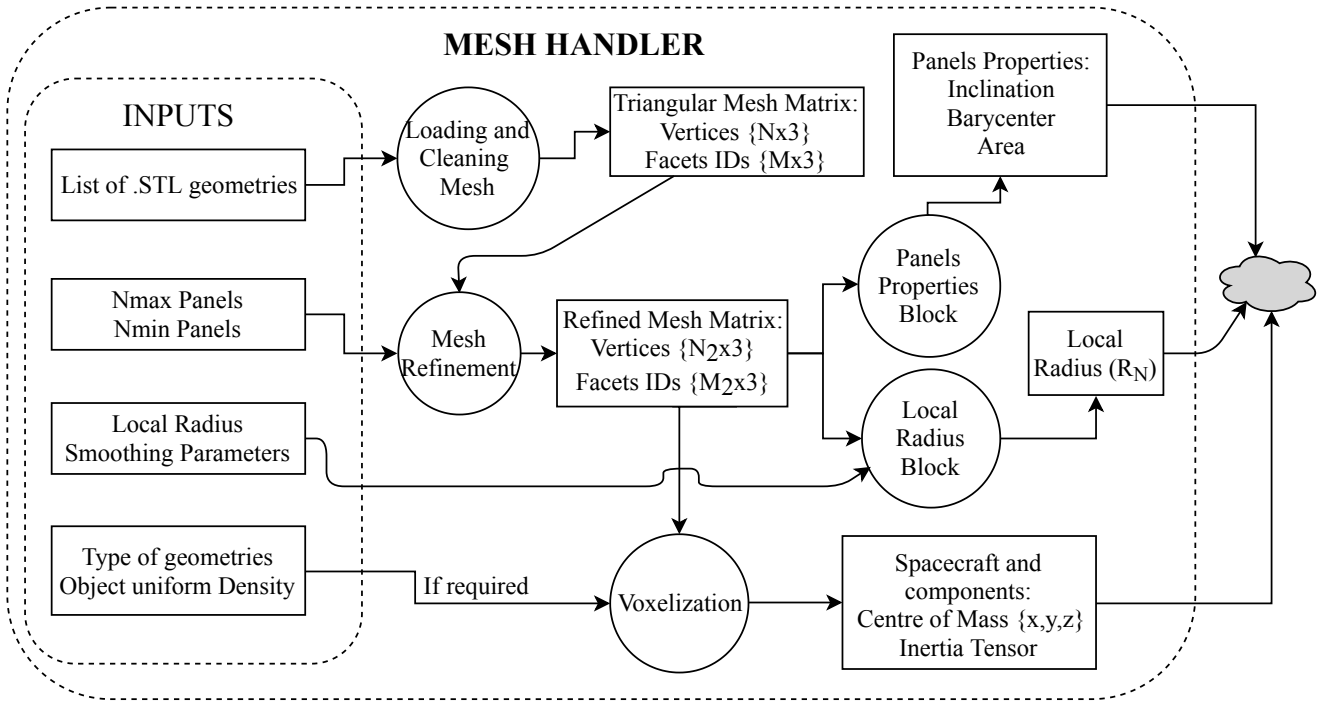


Figure 2.3: Mesh Handler block work-flow.

shells, or thin plates. The different components should be simulated with a consistent panel size, in fact the entire spacecraft has to go through the panel visibility check using a fixed imaging resolution. Using a very different panel sizing for the different objects, may cause visibility detection problems due to the imaging resolution and the rasterization errors, thus decreasing the aerodynamics and aerothermodynamics results accuracy (details on the panel visibility detection phase will be provided in the following paragraphs).

Panels Visibility

This block is fundamental for determining which panels are windward or leeward. The first ones contribute to the aerodynamics and aerothermodynamics of the object, while the leeward have a negligible contribution. Additionally, for complex objects it is necessary to detect the self-shadowing, which are assumed to have a minor contribution. The visibility detection is performed using the combination of two techniques: the back-face culling, and the occlusion culling. The first one filters the leeward panels, while the second one detects the panels which are shaded by other parts of the geometry (self shadowing). A detailed description of this block will be provided in the following paragraphs.

Shadow Refinement

This block allows the iterative refinement of the edges of the shadow detected with the occlusion culling technique; this approach allows the accurate computation of aerodynamic coefficients for coarse meshes. The same approach can be used for detecting the surface of an object which may be subjected to shock impingement, determining which panels should have an increased heat-flux due to this phenomenon.

Aerodynamics and Aerothermodynamics

All the necessary models for computing the aerodynamic forces and moments acting on the body in the free molecular, rarefied transitional and continuum regime are contained in the aerodynamics block. The pressure coefficient is computed for each panel, and then the integration all over the surface is performed in order to obtain the complete geometry characterization. The same description applies on the aerothermodynamics block, where different formulation may be used for the appropriate reentry scenario (i.e.: survivability risk assessment or thermal protection system studies). With the inputs provided by the upstream blocks, the aerothermodynamics block may be used to apply a stagnation point-based formulation (with an equivalent effective nose radius) or the local radius formulation. The work-flow using the input from the previous blocks is shown in Figure 2.4. The computation in the rarefied transitional regime is performed with general bridging models, which have been built within this Ph.D. project.

Work Flow description

The aero-thermodynamic simulation can be described in different steps:

1. Mesh initialization: the mesh file is checked, and the geometrical properties are computed and stored.
2. Atmospheric model: the atmospheric model is loaded, and the environmental and flow properties are computed and the free molecular, transitional, and continuum regime are identified.
3. The panels visibility for the requested attitude is performed. If the shadow-edge refinement is active the iterative mesh refinement is carried out.
4. The aerodynamics and aerothermodynamics of the object are computed for each of the visible panel, and the surface integration is performed, determining the object aero-thermodynamic characteristics.

Following this work flow it is possible to characterize the aerodynamics and aerothermodynamics of the object. The characterization for a range of altitudes with a constant attitude can be performed simultaneously; whereas, only a single attitude can be computed per simulation (due to the visibility identification phase).

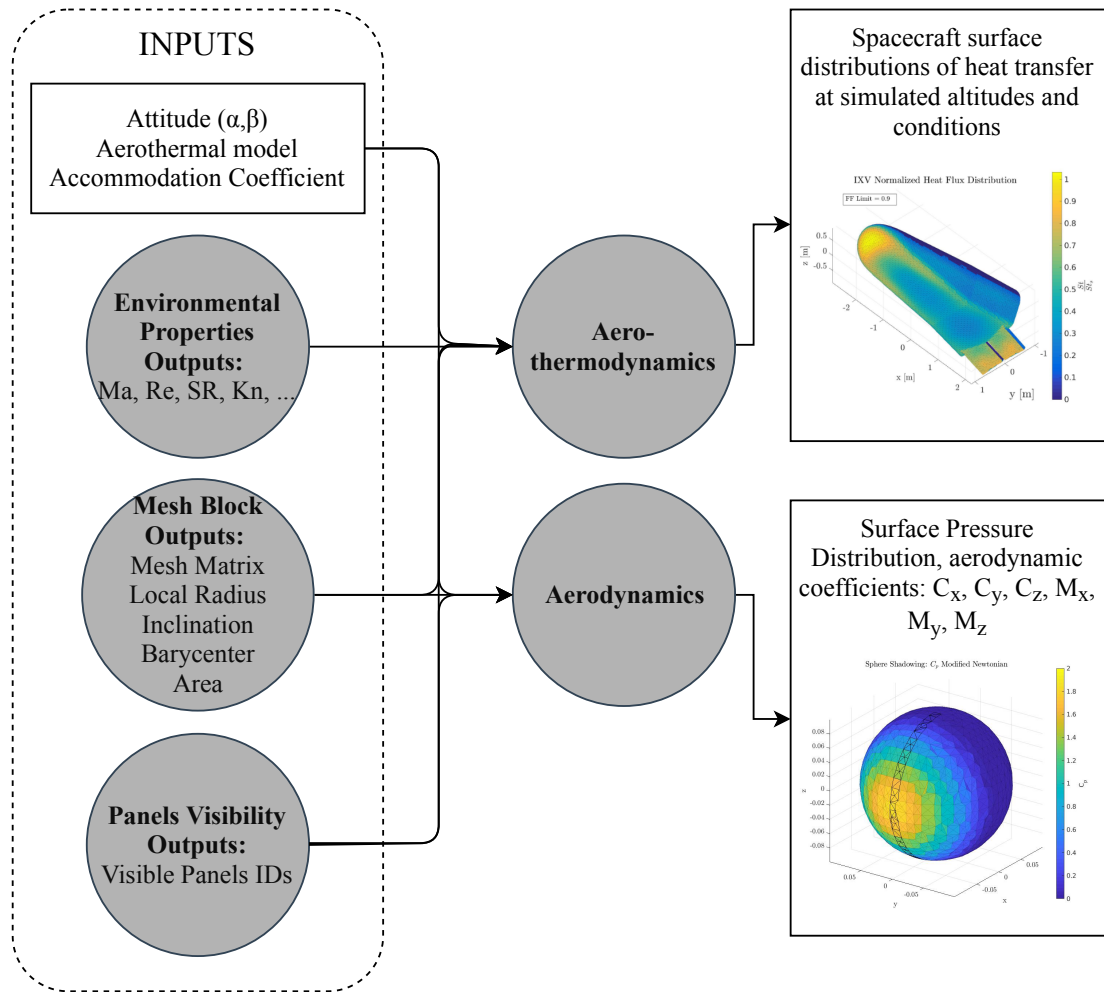


Figure 2.4: Inputs/outputs of aerodynamics and aerothermodynamics blocks.

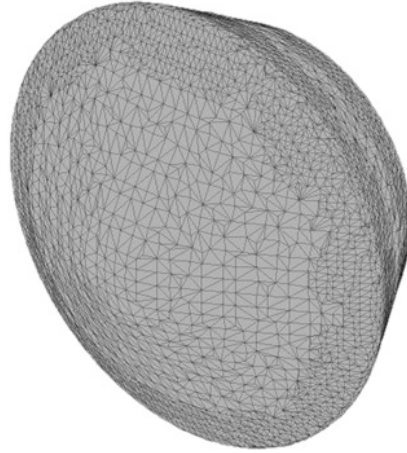


Figure 2.5: Stardust Sample Return Capsule .stl mesh example.

2.3 Mesh Handler

In this paragraph, the methodology for the meshing process and the different operations required for performing accurate reentry simulations are described.

2.3.1 Mesh Initialization

The mesh has to be provided in a standard stereolithographic format (.stl, example in Figure 2.5), which defines a surface by triangular facets (vertexes coordinates and connections). The .stl mesh format provides also the normals computed for each facet, but a common problem of the mesh is having a non-coherent winding direction. The winding direction represents the orientation order of the vertexes, which could be either clockwise or counterclockwise. Such problem causes the incorrect simulation of the object, and it must be corrected. Indeed, a non-coherent winding direction will result in a wrong identification of the visible facets, and a wrong computation of aerodynamics.

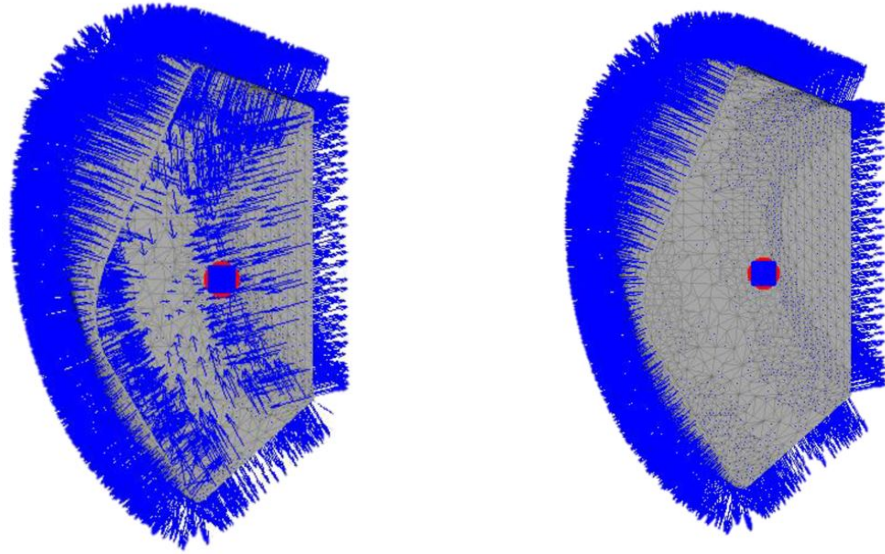
The normals of a i -th triangular panel can be computed as:

$$\vec{N}_i = \vec{e}_{12} \times \vec{e}_{13} \quad (2.103)$$

where \vec{e}_{12} is the position vector from the vertex 1 to the vertex 2, e.g.:

$$\vec{e}_{12} = \vec{P}_2(x, y, z) - \vec{P}_1(x, y, z) \quad (2.104)$$

In Figure 2.6 an example for a non-coherent (on the left), and a coherent winding direction (on the right) is shown. For simple geometries the correction of non-coherent



(a) Non-consistent .stl winding direction

(b) Consistent .stl winding direction

Figure 2.6: Normals (shown with a quiver plot) on faces for a non-coherent (left) and a coherent (right) vertexes winding direction. The arrows representing the facets normal directions pointing outside the object surface (as in the right figure) show a correct vertex winding direction.

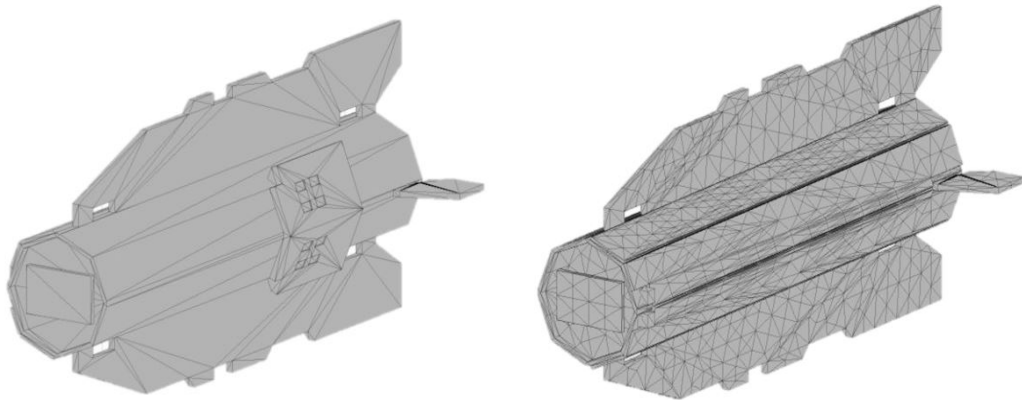
winding vertexes is fairly simple. If we define a *simple geometry* as an object whose the dot product of all the facets normals and the facets barycenter is positive, then the correction may be applied by reversing the winding order of the vertexes of those facets whose dot product is negative. Formally the condition may be expressed as:

$$\text{all}(\vec{N}_i \cdot \vec{F}_{b,i} > 0) \quad (2.105)$$

where $\vec{F}_{b,i}$ is the barycenter of the i -th facet, computed on the local reference system of the object centered on the geometric barycenter. If the geometry is not simple, the vertexes winding direction may be performed using ad-hoc algorithms, but the computation becomes more computationally expensive, and it may be best to correct the winding direction with a common mesh elaboration software.

Sometimes the mesh may have a coherent winding, but opposite to the one assumed for computing the normals. Indeed, eq. 2.103 assumes a specific winding, and reversing the order of the vertexes will cause the reversal on the verse of the normals; this will practically cause the normals to be inward-pointing.

The simplified aero-thermodynamics require the computation of the local panel inclination, which depends on the normal vector; if the normals are reversed, the panel



(a) GOCE raw .stl mesh

(b) GOCE refined .stl mesh

Figure 2.7: GOCE initial mesh (on the left) and refined mesh.

inclination angle will be rotated of 180deg, resulting in a completely wrong aerothermodynamic characterization. For this reasons, the mesh initialization phase is of utmost importance, and several checks must be performed before running the actual reentry simulation.

During the initialization phase the area of each triangle must be computed, and given the coordinates of the vertexes it may be computed using the well known Heron's formula. Using the triangles area, it is possible to compute of the geometric barycenter of the object as the weighted average of the face barycenter coordinates; if the object has a uniform density, the geometric barycenter coincides with the center of gravity.

2.3.2 Adaptive Mesh Refinement Algorithm

The mesh refinement level is an important parameter for performing an accurate aerodynamic and aerothermodynamic characterization. In fact, due to the nature of the surface inclination methodology, if the mesh refinement is coarse some panels may be identified as visible, even though they should be shaded, causing an overestimation of the aerodynamic coefficients. This type of error is highly dependent on the complexity of the geometry. A short example is presented using the geometric model of the Gravity field and steady-state Ocean Circulation Explorer (GOCE). A standard mesh created using the 3D model is shown in figure 2.7 (on the left). The same model refined with the algorithm developed and later described in this paragraph, is reported on the right.

If a coarse mesh is simulated, the visibility detection algorithm will identify the facets partially shadowed as if they are completely visible; thus the entire area of the panel

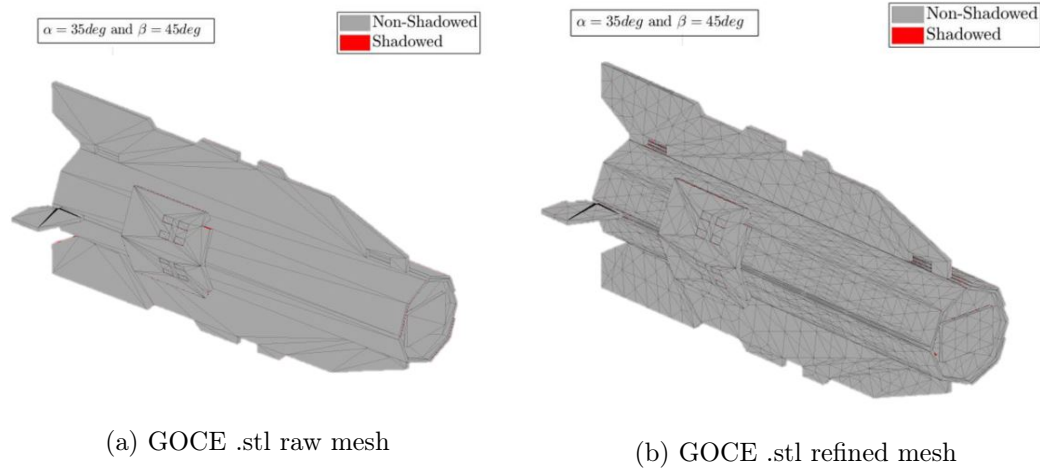


Figure 2.8: GOCE coarse and fine mesh, seen from the flow perspective, i.e.: taking into account of the attitude angles $\alpha = 35\text{deg}$ and $\beta = 45\text{deg}$.

will be virtually exposed to the flow, causing the overestimation on the aerodynamic coefficients. Such error can be reduced increasing the refinement of the mesh. An example for this typical error is shown in the following figures. In Figure 2.8, the two different mesh have been rotated in representation of the assumed flow direction ($\alpha = 35\text{deg}$ and $\beta = 45\text{deg}$), no shadowed panel is visible as we are currently looking at the figure from the same direction as the flow velocity. In Figure 2.9 the mesh were rotated to show a visible representation of the visibility error for a coarse mesh.

It is immediate to think that a higher number of facets causes an increased computational cost. Although, thanks to the preliminary mesh initialization and storage phase, if the geometry of the object is constant (i.e.: no ablation), only the first trajectory propagation step has a higher computational cost, as all the other operation performed by the software are almost insensitive to the number of panels.

The progressive mesh refinement algorithm developed for this application, can be used with two different approach: the first one is based on the refinement based on the maximum length of the triangle side, and the second one is based on the area of the triangles; also a combination of the two may be used. In order to achieve a proper refinement, the algorithm has to be iterative, and at each loop, a number of triangles has to be refined. The algorithm takes as inputs the following:

1. Mesh Structure (Facets IDs, Vertexes coordinates)
2. Refinement type (area/length/both)
3. Minimum Area/length (or both)
4. number of maximum facets

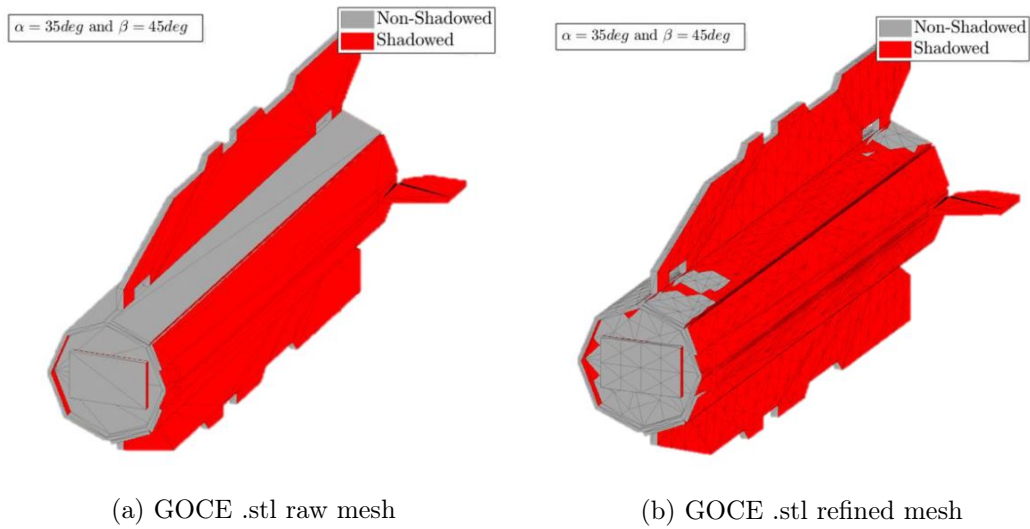


Figure 2.9: Visualization of the error introduced by a coarse mesh, due to the complete visibility associated to the partially shadowed panels. On the left the original mesh with 750 facets, and on the right a refined mesh with 10'000 facets.

5. number of maximum iteration
6. Non-adaptive mode: provide the facets index to be refined

These parameters are thought to allow the flexibility to generate a uniform refined mesh, with a balanced area and aspect ratio. The adaptive refinement follows a simple rule: the triangular facets with the biggest area (or side length) are the first to be refined. The refinement of a triangular mesh may be performed in different ways; in this algorithm the longest side of the triangle is halved, creating an auxiliary vertex, which is going to be a common vertex for the two following triangles (e.g.: Figure 2.10). In the figure we can also see the difference between an area-based refinement or a length-based refinement. Assuming that the panels 1 and 2 have a similar area, the algorithm will select the one with the biggest area for the refinement. Even though, with the purpose of obtaining a uniform mesh, it would be best to refine the triangle n. 2. The probability of misidentifying the triangle n. 2 as *visible* highly depends on its aspect ratio, thus affecting the accuracy of the aerodynamic properties of an object. At the same time, the area of the triangles needs to be controlled; in fact, if the triangle becomes too small, the probability of misidentifying the triangle as hidden increases (due to the limited pixel resolution that can be used by the visibility algorithm, which will be explained in the next paragraphs). Therefore, the best compromise comes from using both an area-based and a length-based iterative refinement. The parameters of minimum length and area, must be provided according to the desired refinement (in combination with

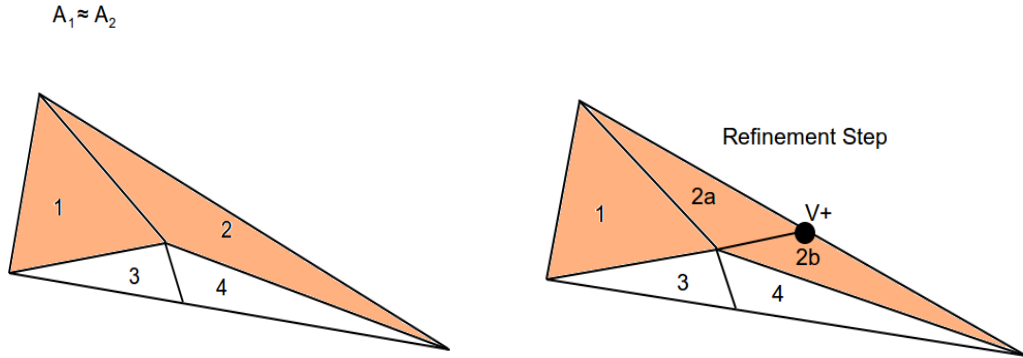


Figure 2.10: Triangular mesh refinement step example.

the maximum number of triangles).

The iterative refinement is necessary to have a step-by-step refinement of bigger triangles into smaller triangles. In fact, a single refinement step can only halve the biggest side of a triangle. The number of refinement steps increases the computational time, but increases the uniformity of the mesh. The number of triangles refined at each refinement step is defined as:

$$N_{t,i} = \frac{N_{t,max} - N_{t,0}}{N_{iter}} \quad (2.106)$$

where $N_{t,i}$ is the number of triangles refined per step, $N_{t,max}$ is the Maximum number of triangles (which is enforced in a weak way by the algorithm), $N_{t,0}$ is the initial number of triangles, and N_{iter} is the number of iteration steps. It is clear that $N_{t,i}$ must be an integer ≥ 1 . The iterative loop stops when the maximum number of triangles has been exceeded or when the minimum length (and/or area) is below the requested limits. Two examples of the iterative loop with the side length-based and area-based refinement are respectively reported in the Figures 2.11 and 2.12. The number of facets refined per iteration has been kept constant for the two methods, the results show that for the same number of iterations the area-based method is able to reach a more uniform mesh. Using the area-based method usually provides a better quality mesh, the downside is that it is difficult to automatically estimate the size of the minimum area to be used for the refinement, while for the side length a fraction of the simulated object's reference length could be used. The mixed area-length-based refinement has been programmed for prioritizing the refinement based on the area; therefore, using a combination of an

overestimated minimum area, and an underestimated minimum length, may provides a more uniform mesh in the first iterations, which is then further refined by the side length; this approach may allow the generation of a very fine mesh controlled by the number of triangles and the minimum triangle side length.

An example of a very fine mesh obtained with the use of the mixed area-length-based refinement is shown in Figure 2.13, the result has been achieved in 300 iterations, with 48 facets refined per iteration. The computational cost of the mesh refinement operation is relatively efficient, the example reported here required ≈ 1 s; since the mesh refinement is performed only in the first initialization phase, the computational cost does not influence the computational time of a complete reentry trajectory propagation, or an aerodynamic attitude-based sensitivity analysis.

The number of panels along with their size have an impact on the accuracy of aerodynamic and aerothermodynamics properties estimation. A dedicated study with the aim of identifying a suitable parameter to perform accurate aerodynamic analysis has been carried out and is presented in section 3.2.1.

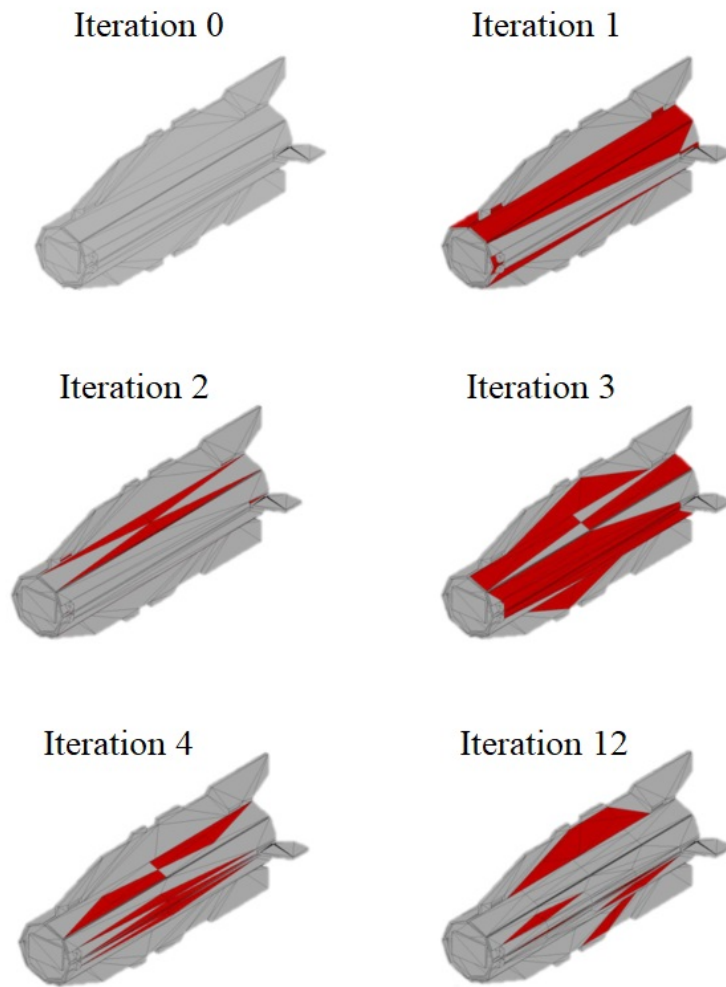


Figure 2.11: Iterative loop for the side length-based refinement.

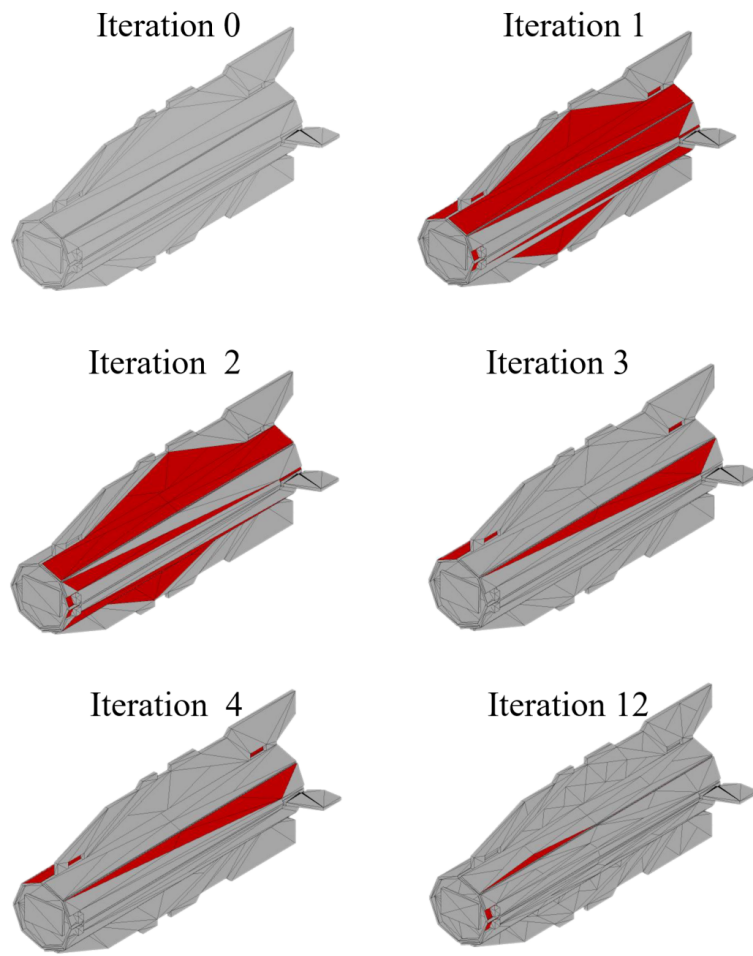


Figure 2.12: Iterative loop for the side area-based refinement.

Iteration 301 - N. faces 29583

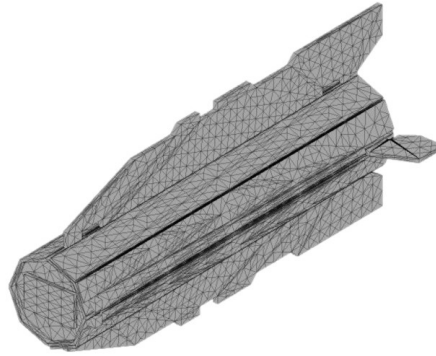


Figure 2.13: Fully refined mesh, obtained with 300 iterations, starting from the initial mesh which had approximately 1300 facets to $\approx 30k$ panels.

2.3.3 Local Radius Algorithm

The local panel inclination method becomes problematic when used to compute the heat transfer for a non-hemispheric object. Indeed, all the methodology assumptions are based on hemispheric objects such as; hemisphere, cylinder with a hemispheric end, and hemispheric cone. As shown by [Lees, 1956] for an hemisphere and a blunted cone, the laminar heat transfer depends on several factors, and other than the parameters that must be computed by the atmospheric properties, the relative flow velocity and the hemispheric surface radius are the most influencing on the stagnation point heat transfer. Therefore, when the object is not hemispheric, the choice of the *reference radius* becomes of utmost importance. In addition, the local panel inclination method, express the Q_i/Q_{stag} ratio as function of theta (which is the inclination of the local panel with respect to the flow) or the equivalent distance from the stagnation point. For a hemispheric geometry, the LPI methods generally provide a good approximation for the convective heat transfer over the surface, but when the object is not hemispheric e.g.: a flat cylinder, the heat transfer distribution at the corners presents a high error. In fact for a cube, a reference curvature radius could be hypothetically assumed, this could provide an acceptable approximation for the Q_{stag} , but as the LPI computes the local heat transfer based on the inclination θ_i , the frontal flat surface would show a constant heat transfer, which is far from accurate. In fact, the cube should present an increasing heat transfer as the considered point moves from the center to the corners or edges, e.g.: Figure 2.14, a DSMC simulation performed in the lower transitional regime,

where the heat transfer distribution cannot be properly characterized by a formulation solely based on the local panel inclination.

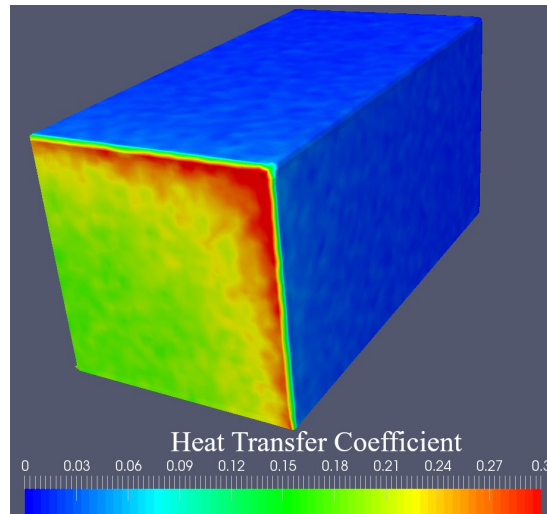


Figure 2.14: Heat transfer distribution on a cube (0.25m), DSMC simulation performed at 90km altitude ($Kn \approx 0.1$) in a transitional regime.

Another representative investigation is reported by [Kemp et al., 1959], where Lees' work is further developed and applied to a flat cylinder with rounded edges and a round cylinder. In Kemp's research, Q/Q_{stag} for flat round-edged cylinder is reported to increase as the point reaches the rounded edge. If the rounding is too small, A standard LPI method employing a constant reference curvature radius would not be able to capture the increase of the local Q_i/Q_{stag} nearby the edge. In addition, since a LPI algorithm operates using the facet inclination, chances are that the facets close to the rounded edge change their inclination, and therefore, instead of being characterized by a higher thermal flux, this would result in the opposite effect. In the analysis reported by Kemp et al., it is evident that the formulation itself is thought to be used with a local radius approach, which in most of the reviewed software based on the LPI method is completely neglected (Figure 2.15). More recently, the implementation of a local radius formulation was also tested and compared in various instances by Annaloro [Annaloro et al., 2014, Annaloro et al., 2017b], and the results show better performance than the more classic reference-radius approach (as the one used in SCARAB, DRAMA, DAS, and other codes).

The definition of a local curvature radius is expected to provide a better approximation for flat surfaces and complex objects having different curvatures all over the surfaces. In fact, each local panel, would be characterized not only by the inclination with the free stream flow but also by a local curvature radius. In this way, taking as

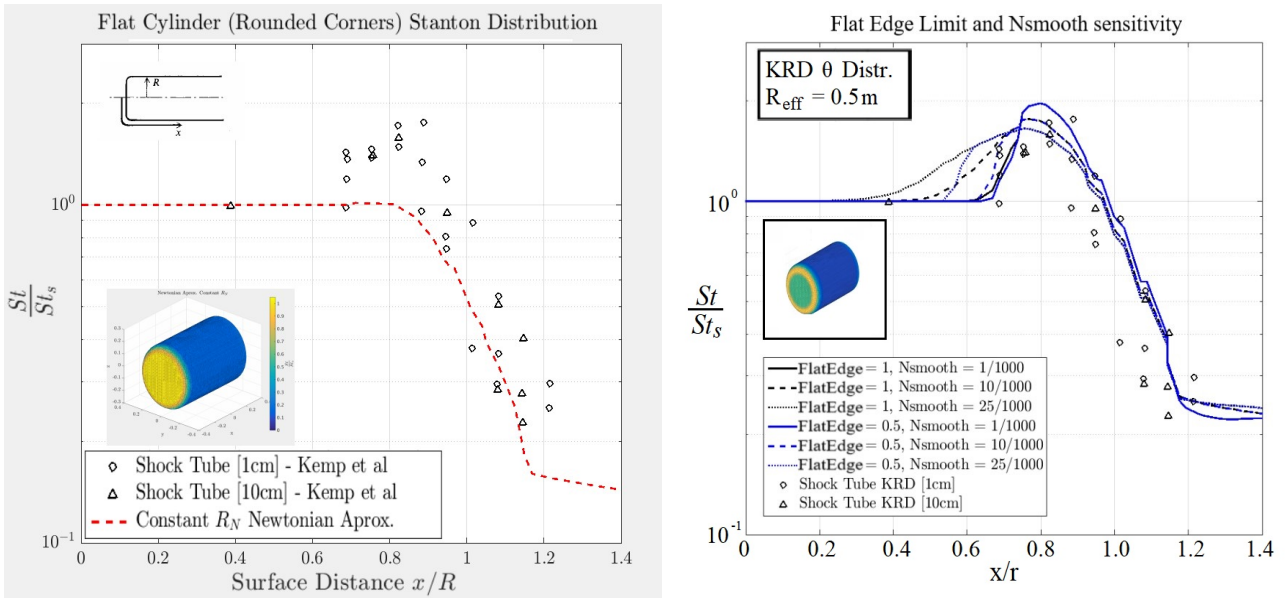


Figure 2.15: Comparison of a LPI application on Kemp [Kemp et al., 1959] shock tube data, on the left: constant nose radius, on the right: local radius formulation (computed with the local radius algorithm presented in this paragraph).

an example the flat cylinder with rounded edges, would provide a better approximation on the corners. Indeed, the local radius would decrease as the point moves from the flat face toward the rounded edge. In addition, using a local curvature radius it would be possible to take into account sharp variations of the surface, which would be more exposed to the flow, thus presenting a higher heat transfer.

In this paragraph, the point of view focuses also on the possible coupled application of the dsmcFoam code, developed on the openFoam platform, which operates on the mesh via the snappyHexMesh tool, and the FOSTRAD code. Therefore, the surface curvature estimation, will be analyzed also on the geometric models generated via the snappyHexMesh tool and the consequent mesh triangularization.

Surface Curvature Estimation methodology

The algorithm that has been implemented has been specifically studied for FOSTRAD, although its general implementation is possible within any LPI-based software. Indeed, the curvature computation is performed on a stereolithography (STL) model, which is a simplified triangulated surface. The STL file contains all the information to build an unstructured triangular mesh; points coordinates, points connections for each facet, and also the normals of each facet. FOSTRAD requires the geometry to be given as a triangulated STL mesh. The local radius computation module is based on the curva-

ture estimation algorithm proposed by [Rusinkiewicz, 2004] that has been developed on MATLAB. The curvature algorithm computes the estimated principal Gaussian curvatures for each vertex of the STL mesh. The curvatures are estimated locally on each different facet. The estimation is based on the change of the normals from a face to their neighbors. The triangulated mesh allows the computation of the facet normals, from these, it is possible to average neighbors facets normals and obtain the per-vertex normals. The normals averaging is computed according to the method proposed by [Max, 1999].

The local curvature radius is then defined by the general Gaussian principal curvatures relation:

$$R_i = \frac{1}{\sqrt{\kappa_{1,i}\kappa_{2,i}}} \quad (2.107)$$

where R_i is the i -th vertex average local radius, κ_1 and κ_2 are the principal Gaussian curvatures. In its form, the algorithm allows the computation of the curvature just by taking a ring of neighbors around each vertex, this leads to local vertex or face radii that will present very steep variations for complex objects. In addition, the radius for a flat surface is obviously infinite, therefore, a fixed reference local radius is applied on the “flat” vertexes or facets.

In Figure 2.16 it is shown an example of the raw algorithm applied on a Space suit, the original STL mesh (on the right) is characterized by more than 36k vertexes, the model has then been elaborated on openFOAM via snappyHexMesh in order to create the solid mesh representing the field around the object, which is the procedure needed for a DSMC simulation. Afterwards, the patch representing the object on openFOAM has been converted into a STL surface. Then, it has been computed the local radius on the new SnappyHexMesh triangulated space suit with more than 110k vertexes, shown on the left of Figure 2.16. This procedure, has been tested for the evaluation of integrating the snappyHexMesh feature as a preprocessing phase of FOSTRAD.

In the previous paragraph, an iterative mesh refinement algorithm has been proposed, although, the ability of producing an uniformly distributed triangular mesh (i.e.: having good quality aspect ratio distribution) is highly dependent on the initial STL mesh quality. Some of the most common CAD tools allow to convert a solid mesh file into an STL one, although the triangulated mesh quality depends on the geometrical feature of the object. In this case, further post-processing with different meshing software should be performed to increase the mesh quality.

Independently from the preprocessing meshing tool used, it is paramount that the provided mesh is properly elaborated for having a good quality triangular aspect ratio distribution. Some of the problems that may arise from a poor quality mesh are highlighted hereafter.

SnappyHexMesh tool, independently from the initial aspect ratio quality of the provided STL mesh, is generally able to create a solid hexahedral mesh, which can then be converted into an STL one. Indeed, in this way it is possible to have a good quality and highly refined triangulated surface, granting a higher accuracy for the aerothermodynamics simulations. Even though, by applying the curvature algorithm on the same geometry with the two different refinements the local radius distribution is greatly affected. The most evident problems are:

1. Sharp edges are identified with a very low local radius $R_i \rightarrow 0$
2. Non-flat facets are misidentified as flat (e.g.: the helmet)
3. The implicit surfaces cannot be recognized
4. The radius distribution is highly dependent on the mesh

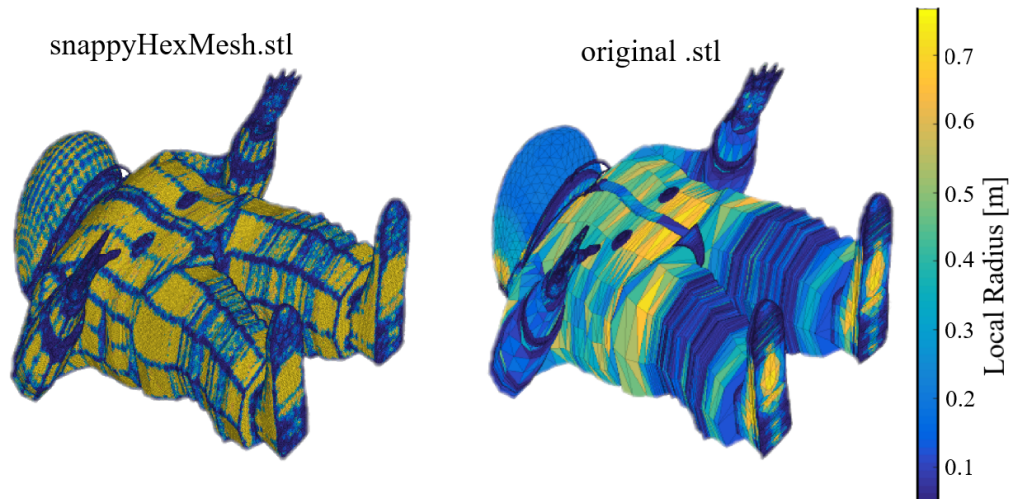


Figure 2.16: Curvature algorithm applied on a complex geometry, showing the sharp variation of the local radius. **Left:** local radius of the refined triangulated mesh generated with snappyHexMesh starting from the original STL surface. **right:** local radius computed on the original STL surface

Such problems and results are not suitable for the studied application. In fact, the software is expected to compute the aero-thermodynamic simulations of arbitrary and complex geometries and the local radius is required to show a smooth and continuous variation. Therefore, before the integration on the tool, the curvature algorithm had to be thoroughly tested and properly adapted in order to guarantee the expected improvements. Numerous tests have been performed and the needed corrections have been applied and are hereby presented. Another example of the geometrical glitches and

mesh dependencies are highlighted in Figure 2.17. It would be desirable to have a local radius distribution robust to mesh tessellation irregularities. In this work different solutions have been defined and will be tested directly on the aero-thermal flux estimation for spacecraft and objects re-entry.

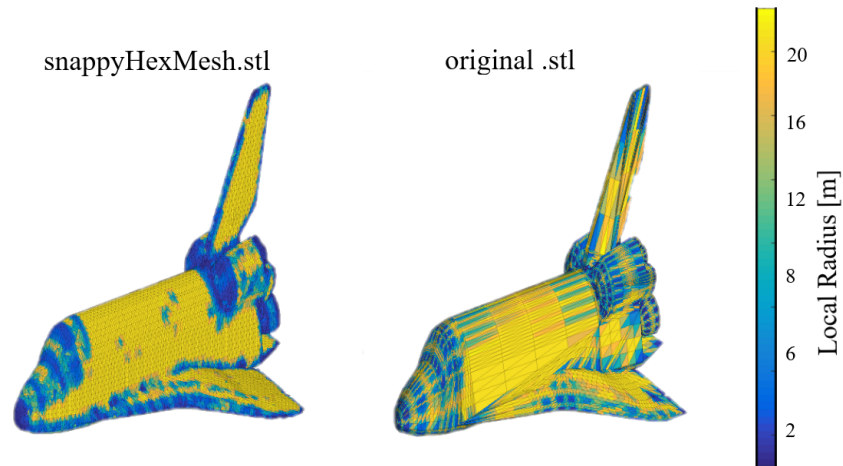


Figure 2.17: Curvature algorithm applied on the Space Shuttle geometry, showing the mesh glitches. **Left:** local radius of the refined triangulated mesh generated with snappyHexMesh starting from the original STL surface. **right:** local radius computed on the original STL surface.

Triangulated Mesh Preprocessing

The curvature computation algorithm performs well when the initial STL mesh has a regular tessellation, it provides smooth and clean curvature distribution. Although, if the initial mesh presents tessellation distortions or the triangles are not well defined e.g.: some triangles are collinear or some vertexes with different indexes are coincident (duplicate vertexes), the algorithm fails to compute the curvature properly (e.g.: Figure 2.18). For the specific object, a smoothing on the original mesh geometry was required. The problem was that the vertexes which defined the surface were sharp, defining a radius tending to zero.

Another STL mesh definition problem was related to collapsing or duplicated triangles vertexes. The first problem occurs when the two vertexes of the same triangle are very close, and their edge length tends to zero. This will cause a problem on the definition of the triangles local coordinate systems, which leads to the impossibility of solving the least square problem used for the interpolation of vertexes normals.

The cited issues have been fixed with a built-in preprocessing phase called “Mesh cleaning and Reordering”, by cleaning the mesh from collapsing and duplicated edges,

and re-ordering the mesh vertexes and faces according to the X-Y-Z coordinates. Even though, a very sharp defined mesh could still cause problems at this point. The results of the preprocessing cleaning phase are illustrated in Figure 2.19. It is still possible to observe a difference in the radius distributions due to the irregular tessellation of the snappyHexMesh-generated STL. This is caused by the very way the meshing tool works, indeed, the triangulated surface mesh is obtained from the hexahedral solid mesh, which usually presents some irregularities on hemispherical geometries.

Flat Faces Detection glitch

After the first preprocessing phase that allows the regular computation of the radius distribution, it is still necessary to fix the problems previously reported. The most problematic one is definitely the recognition of flat faces and implicit hemispherical surfaces. The issue is strictly connected to the use of the snappyHexMesh tool. Indeed, depending on the initial resolution of the STL mesh, it is possible that the object surfaces are not well identified.

To better outline the problem an example is hereby described; considering for simplicity a bi-dimensional case of a circle, the STL generation process first defines the vertexes laying on the circle edge, and then establish the connection among the vertexes. The STL mesh is a triangulated surface, in a bi-dimensional case it would be represented by a polygon inscribed in the circle. Increasing the STL resolution would mean inscribing a polygon with a higher number of edges. In figure 2.20 on the left, it is shown the simplified STL meshing concept. Assume that the circle is defined by a “2D STL” composed of 7 vertexes, which is equal to inscribing an hexagon within the circle. Assuming that it were possible to mesh the polygon via snappyHexMesh in order to build the mesh around the polygon via 2D triangles (instead of the equivalent tetrahedrons in the 3D case), if the imposed snappyHexMesh resolution were to be higher than the one used for building the original polygon, the tool would not be able to properly generate the implicit circle.

Precisely, as shown on the right of figure 2.20, where there are shown the normals, which are used for estimating the local curvature of each “edge” or “triangle”, it is possible to notice the nature of the geometrical glitch. In fact, Imagine to build a snappyHexMesh model by using a refinement 3 times higher then the starting hexagon (the 7 vertexes polygon). The snappyHexMesh model would be built on the same hexagon, for simplicity assume that it would be defined as the hexagon edges divided in 3. The model defined in this way, is representative of the 3D mesh generated by snappyHexMesh when it resolves the original STL with a higher refinement. This object will be characterized by the “inner vertexes” normals which will be parallel, such as the ones in blue of points

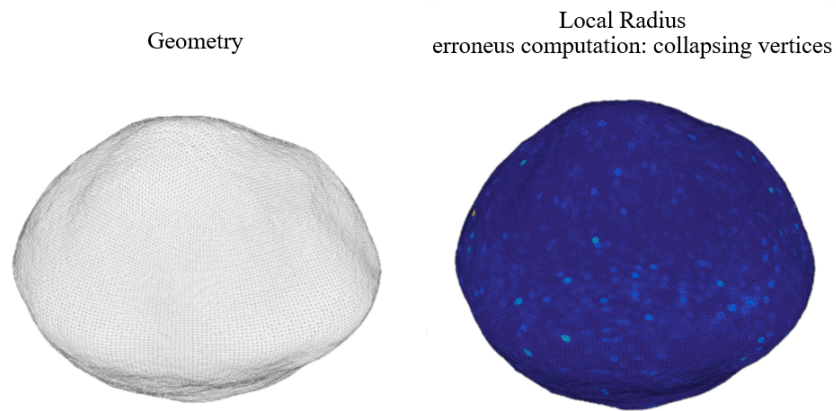


Figure 2.18: **Left:** Bogus Bennu Asteroid STL geometry representation. **right:** Erroneous local radius computed on the non-pre-processed surface.

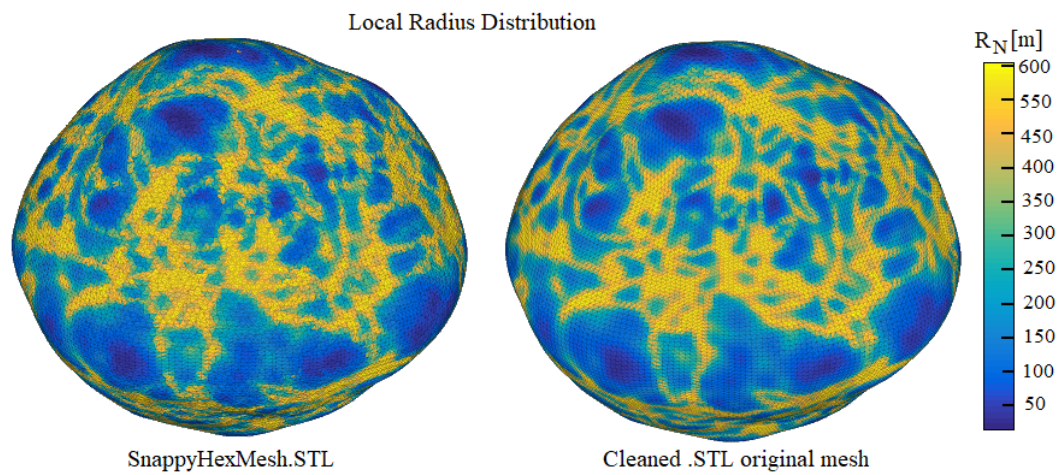


Figure 2.19: Bogus Bennu after the cleaning preprocessing phase. **Left:** local radius distribution on the snappyHexMesh STL geometry. **Right:** local radius distribution computed on the cleaned original STL.

P₃ and P₄. In the simplified 2D conceptualization, the algorithm would detect the surface between two points having parallel normals as “flat surfaces”, characterized by a zero-curvature, and therefore an infinite radius. The described problems appears only when snappyHexMesh refines the mesh with a resolution higher then the starting STL geometry. In fact, a correct representation of the geometry could be obtainable by using an STL defined with the 19-vertexes polygon shown on the left of Figure 2.20. In this case, snappyHexMesh would be able to correctly capture the geometry, preventing the “Flat surfaces” glitch. In light of what has been shown for a simplified 2D conceptualization, if an STL mesh is to be used in openFOAM, its resolution (intended as vertexes per surface area), must be higher the the maximum resolution expected defined by the snappyHexMesh tool.

Another solution dealing with a flat faces detection and weighing has been investigated, and it has been included within the radius smoothing algorithm. Such solution may also be used to obtain a smooth transition from a flat surface to a rounded one, allowing a better accuracy of the heat-transfer coefficients computation.

Local Radius Smoothing algorithm

The Local Radius smoothing algorithm, has been specifically studied to be applied for the aerothermodynamics block, with the perspective of providing a better approximation of the heat transfer distribution over an object re-entering the earth atmosphere. Even if it is presented with the very application on the surface radius distribution, the smoothing algorithm can be applied to a general surface property distribution, e.g.: for smoothing the heat-transfer coefficients or the pressure over a simulated object. Therefore, it has been thought with a general and wide-applicable structure (Figure 2.21), providing a high degree of flexibility. The computation of the local radius depends on many variables, such as the mesh refinement degree (number of panels), panels size distribution, the geometry complexity, and the features to be resolved. To perform an accurate computation it is generally required to perform an initial tuning phase in order to properly determine the optimal combination of initial parameters to better represent the property and phenomena which is to be smoothed (i.e.: heat transfer coefficient).

The smoothing algorithm uses the following inputs:

- STL geometry triangulation matrix: Vertexes and Faces
- Minimum reference radius
- Maximum reference radius
- A set of smoothing parameters

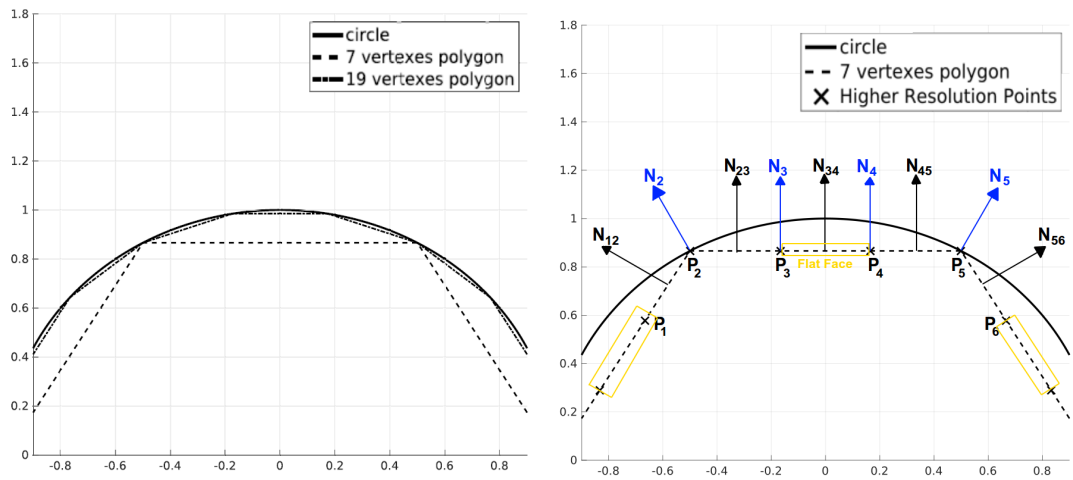


Figure 2.20: **Left:** simplified 2D meshing procedure for a circle with two different resolutions **right:** representation of flat surfaces recognition when meshing an STL with snappyHexMesh using a resolution higher than the original STL.

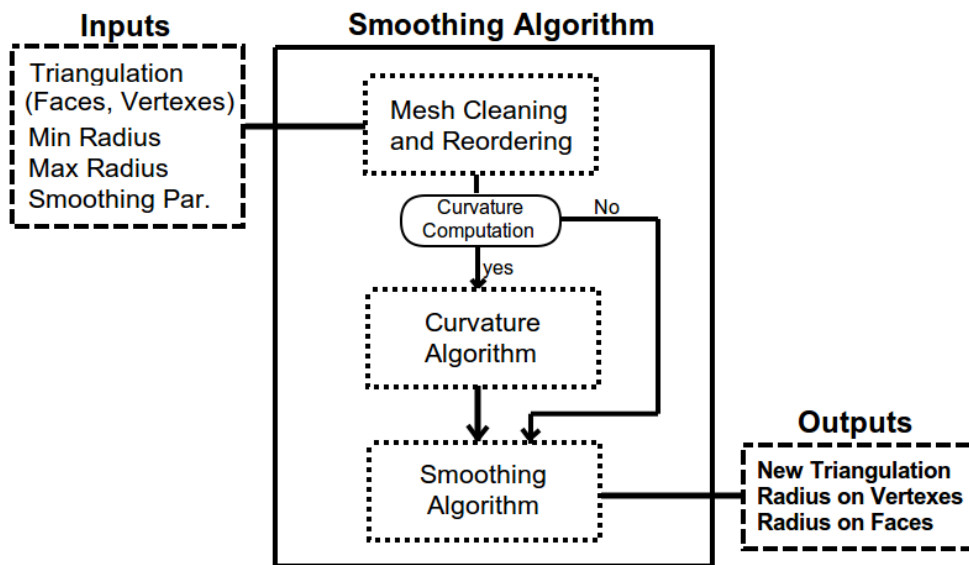


Figure 2.21: Smoothing algorithm block diagram

The STL geometry could be any unstructured triangulated geometry, and can be processed as a binary or ASCII file format, obtaining a list of vertexes and the associated triangular facets definition list, indicating the vertexes connected to form the panels. The minimum and maximum reference radius are the values that are assigned to the vertexes whose radius are respectively below or above those values; they can be defined by reference values depending on the object characteristic dimensions (e.g.: r_{ref}). A set of smoothing parameters has been thought to be used for the initial tuning of the smoothing results:

SmoothingPar = {N. smooth, average type, flat face edge, flat face weighting}

The smoothing parameters will be explained thoroughly with a series of examples. Briefly, N_{smooth} is the number of elements considered during the smoothing process, the average type can be selected between a standard average or an exponential weighted average of the closest N. smoothing points. The *flat face edge* is a limit value used to detect the flat faces. The flat face weighting is used to filter the *Flat Face Glitch* that has been previously explained. The algorithm, as it has already been briefly explained, has three main blocks:

- Mesh reordering and cleaning
- Curvature computation algorithm
- Smoothing algorithm block

The method may be used for smoothing any kind of surface-mapped property, the mesh re-ordering and cleaning will keep the consistency of the mapped property throughout the elaboration. Therefore, when the curvature computation block is bypassed, the algorithm will just smooth the input property.

The smoothing algorithm is thought to be very flexible, and allow to tune the parameters with the aim of achieving a good qualitative and quantitative representation of the surface-distributed local radius. The Number of smoothing points, is the number of closest vertexes values used for the averaging process. The higher the number of smoothing points, the smoother the surface property mapping will be. An example is shown in Figure 2.22. It is possible to observe as when the number of smoothing points increases, the effect of the *flat face glitch* decreases. In addition, the edge radius become less sharp (i.e.: the radius increases).

The “*Flat Edge*” parameter is the limit value that is used to determine whether a face (or a vertex) property must be considered as “*flat*” or not. Precisely, the algorithm identify among the closest N. smoothing points the number of faces having a “*flat*”

reference value” and the ones that have a finite value. Then, by computing the ratio between the number of flat and non-flat faces, the algorithm compares this number with the *Flat Edge* parameter. Afterwards, if the flat-non flat faces ratio is higher than the *Flat Edge* input, the face is considered as flat and assigns the flat property reference value to the considered face. Otherwise, the average among the closest point is computed. The algorithm block diagram is shown in Figure 2.23.

This is the simplest form of the smoothing computation, and the *average_Type* represents the selected averaging method, which can be the average or the exponential weighted average of the N . smoothing+1 points.

The “*Flat Edge*” parameter may be selected in the interval from 0 to 1. The interval boundaries represent respectively the “All flat faces” and “All faces averaged”. This parameter has been introduced to guarantee the proper detection of a flat face, indeed, it is necessary to properly switch from a curved surface to a flat one, considering a possible transition zone. In addition, this parameter allows to select whether to have a smooth transition between a flat face and its corners/edges, which is desirable for sharp-edged objects e.g.: a cube or a flat cylinder. An example of how the *Flat Edge* influence the results is shown in Figure 2.24. The reader may observe that the *Flat Edge* value highly affects the value computed on the edges.

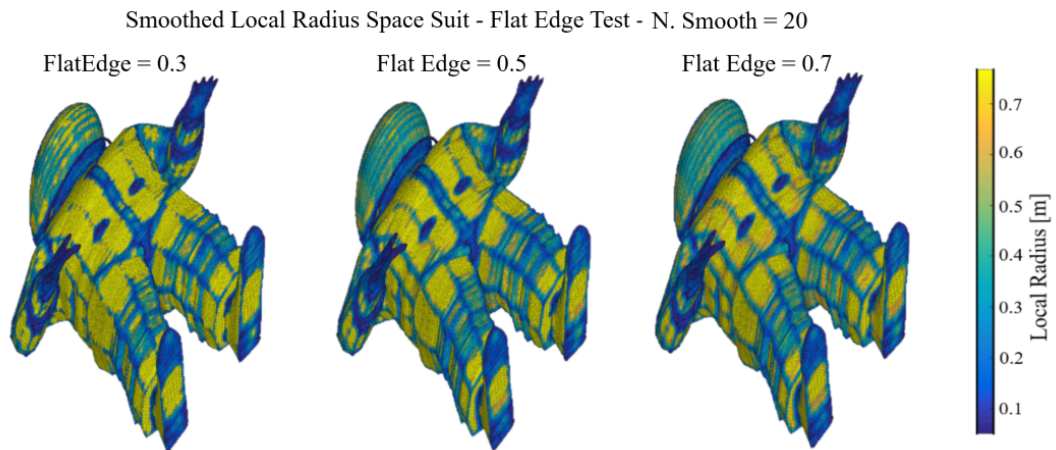


Figure 2.24: Flat Edge parameter effect on a complex geometry.

In addition to the flat-face detection, the algorithm has been developed with a weighted average for the flat face reference values. In this way, the flat face, will not just be assigned a reference value, but that value is going to be weighted according to the ratio of flat-non-flat faces (or vertexes). This has been proven to be beneficial for having a smoother transition from a flat face to its corners. Two different weighting function have been implemented:

- Linear weighting
- Sigmoid weighting

This approach has been thought to allow the evaluation of different weightings, and observe their qualitative and quantitative effects on the computed local radius distribution. The “flat weighting” could also be completely neglected, and in this way the reference radius chosen for the flat panels will have the highest impact. The two weighting functions are shown in figure 2.26, they are directly applied on the difference between the baseline value among the selected closest points and the reference flat value. The baseline value is defined as the average among the non-flat faces. Then, if the face has a flat-non-flat ratio lower than the *Flat Edge*, the flat faces radii is set accordingly to the specific weight before continuing with the averaging. Otherwise, if the flat-non-flat ratio is higher than the *Flat Edge*, the reference value is assigned to the considered face. For all the panels having a flat-non-flat ratio below the *Flat Edge*, the weighted radius may be computed with the following operations.

1) Defining the baseline reference radius as:

$$\bar{R}_{N,BL,i} = \frac{1}{N_{\text{non-flat}}} \left[\sum_{j=1}^{N_{\text{non-flat}}} R_{N,j} \right] \quad (2.108)$$

where $\bar{R}_{N,BL,i}$ is the baseline radius value for the i -th panel, $N_{\text{non-flat}}$ is the number of non-flat panels among the closest N_{smooth} panels, and $R_{N,j}$ is the j -th local radius of the closest non-flat elements that have to be averaged.

2) Computing the reference i -th flat reference radius as:

$$R_{N,i,\text{ref}} = \bar{R}_{N,BL,i} + (R_{\text{flat,ref}} - \bar{R}_{N,BL,i}) \cdot \mathbb{W} \left(\frac{N_{\text{flat}}}{N_{\text{non-flat}}} \right) \quad (2.109)$$

where $R_{N,i,\text{ref}}$ is the weighted reference flat panel radius, $R_{\text{flat,ref}}$ is the initial reference flat panel radius (to be provided as an input in dependence of the object’s characteristic length), N_{flat} is the number of flat panels among the closest N_{smooth} elements, and \mathbb{W} is the chosen weighting function.

3) The reference radius assigned to the N_{flat} flat-face elements is temporarily corrected to $R_{N,i,\text{ref}}$. In this way, the algorithm can still detect the flat-faces, but decreases their weight if the face is not completely flat (which happens when the flat-non-flat ratio is above *Flat Edge*).

4) It is now possible to perform the smoothing, with a simple or a weighted exponential

average:

$$\bar{R}_{N,i} = \frac{\sum_{k=1}^{N_{\text{smooth}}} R_{N,k} w_k}{\sum_{k=1}^{N_{\text{smooth}}} w_k} \quad (2.110)$$

where $R_{N,i}$ is the i -th smoothed local radius, k is the index used for averaging the closest N_{smooth} local radius ($R_{N,k}$) values, and w_k is the k -th element weight, dependent on the averaging type that is applied.

The weighting function applied to the flat-face reference radius at the 2nd step may be defined as a linear function (shown in Figure 2.26), or a sigmoid function, which is defined as:

$$\mathbb{W}_{(N_{\text{flat}}, N_{\text{non-flat}})} = \left[1 + \operatorname{erf} \left(4 \frac{N_{\text{flat}}}{N_{\text{non-flat}}} - 2 \right) \right] / 2 \quad (2.111)$$

The smoothing algorithm block diagram has been reported in Figure 2.25. The structure is very similar to the non-weighted method, but in this case the weighting functions are introduced before computing the average of the closest elements.

The general idea behind the weighting function is to obtain a smooth transition between a flat faces and its corners. The linear weighting function has a constant variation with respect to the flat-non-flat ratio, which means that the transition from a corner to the center of a face will be linear as well. The sigmoid weighting function has been defined in order to have lower values at the corners, and higher values toward the center of a flat face. Indeed, a lower weight for the smaller flat-non-flat ratios will decrease the radius values when the number of flat faces is less than the non-flat faces, which happens as the point approaches the edges. The opposite is also true: when the number of flat faces is higher than the non-flat faces the influence of the flat faces will be higher, and this happens as the points moves toward a flat zone. In conclusion, in comparison with a non-weighted smoothing, the two weighted smoothing will provide slower variation from the edges/corners to the flat face centers, which results in a wider “*flat-non-flat*” transition zone. The following series of examples (figures from 2.27 to 2.32) show the qualitative difference among the various options.

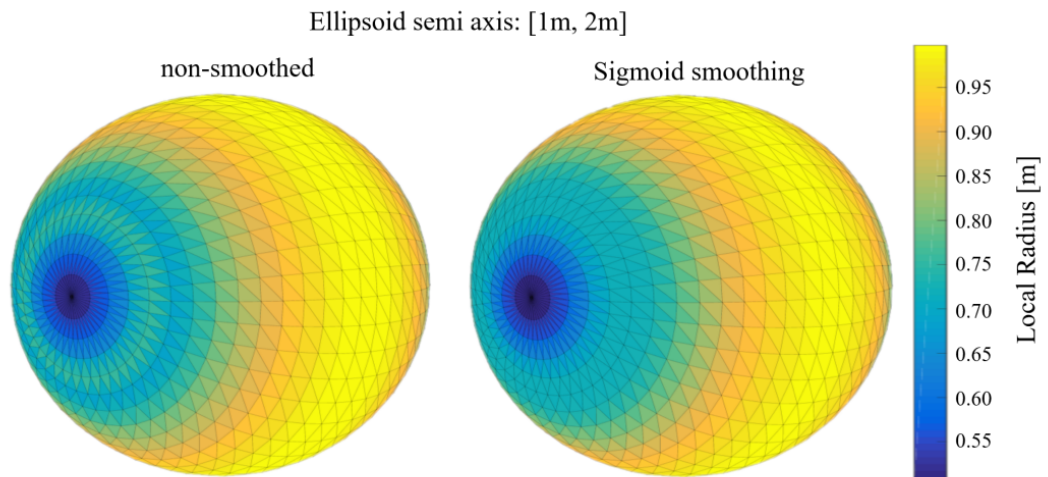


Figure 2.32: Ellipsoid local radius estimation. The non-smoothed and sigmoid-smoothed local radius shown respectively on the left and right. It is worth notice that the smoothed local radius give a better representation of the “true” surface curvature distribution.

2.4 Panels Visibility Detection method

The aerodynamic analysis with the local panel inclination method for simple geometries would require just the identification of panels with a inclination angle $\theta_i < 90\text{deg}$ (w.r.t. the flow direction) and then compute their aerodynamic contribution according to either the Modified Newtonian Theory or the Schaaf and Chambre theory. The panels with $\theta_i \geq 90\text{deg}$ can be assumed to have a negligible contribution by both theories. If the geometry is a complex shape it is required to detect the self shadowing (i.e.: the surface which is shielded from the direct flow by the spacecraft). Different 3D graphical rendering techniques may be used to perform these operations: ray-tracing algorithms, depth-sorting algorithms, and back-face culling and occlusion culling [Zhang, 1998]. In the tool developed for this Ph.D. project, an algorithm which can use both, the back-face culling and the occlusion culling technique has been integrated. The back-face culling allows to detect the panels which are leeward facing, (i.e.: $\theta_i \geq 90\text{deg}$). The occlusion culling has been integrated using the *Pixelator* approach, described by Mehta [Mehta et al., 2016a].

The combination of two techniques has been chosen with the purpose of obtaining an accurate identification of the visible panels. The occlusion culling is theoretically able to accurately identify the visible panels, but due to some practical and computational limitations (i.e.: rasterization errors which are described hereafter), it is applied after

the back-face culling filtering technique. Indeed, unless the object is an open shell (e.g.: a partially ablated fuel tank), the panels with $\theta_i \geq 90\text{deg}$ should be considered as shaded.

The application of the back-face culling is shown in an example (Fig. 2.33). The wind direction is characterized by an angle of attack of 35deg and a side-slip angle of 45deg .

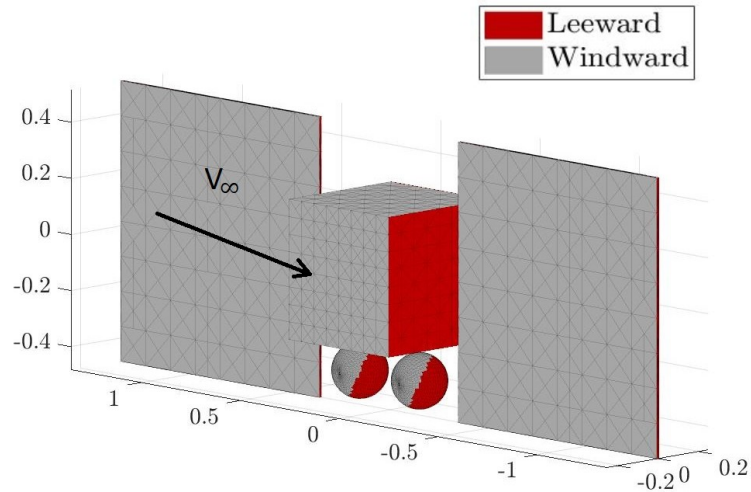


Figure 2.33: Back-face culling application example.

The occlusion culling technique, which is applied after the initial back-face culling filtering, is characterized by different steps:

1. a random color ID (256x256x256) is assigned to each panel
2. The background, black, and duplicated colors are replaced till all facets have a unique color
3. A digital image pixel representation of the windward-rotated object, with a parallel projection, and an equal aspect ratio is generated and stored in the RAM (Figure 2.34).
4. The visible color IDs are confronted with the previously generated panel color IDs
5. The visible and occluded panels are stored for the later analyses (Figure 2.35)

There few important notes for using this procedure: A) the pixel resolution which is used to generate the object representation influences the accuracy and computational time (figures 2.37-2.36), thus a compromise must be sought. Otherwise an automated

convergence process can be used, but it is generally more computationally expensive. The resolution required to detect all the visible panels depends on the spacecraft attitude, although the most difficult panels to identify are usually the least significant one, which are either very small or with a high inclination angle. B) the technical limitation for the digital rendering of the image for the rasterization: automatically applied by the graphic card, when changing from one color to another, some pixels have an "interpolated" color for producing a smooth transition, which can cause some shadowed panels to be wrongly identified as "visible". In this case, the wrongly identified visible panel color is indeed present in the digital image, but only due to the graphical smoothing rasterization. A lower number of randomly generated colors, statistically decreases the impact of this error, thus leading to the advantage of applying the occlusion culling after the back-face culling. Sometimes the wrongly identified visible panels may be leeward facing, the back-face culling completely avoid the rasterization error for these panels (Figure 2.38). C) the parts with a very high mesh resolution (represented by the two sphere in the bottom part of the spacecraft) may be improperly detected as occluded, due to the limited digital image resolution. The same kind of problem is recognized when the wind direction changes (e.g.: a lateral surface with an almost-head-on attitude will be very difficult to detect as visible), and this error is dependent on the pixel resolution used to create the digital image (Figure 2.39).

In light of the previous consideration, the use of the back-face culling and occlusion culling techniques have been considered a good compromise between computational cost and visibility panel identification accuracy. The visibility detection phase has to be performed for each simulated attitude, therefore, seen the computational cost exponential growth (in figures 2.37-2.36), a pixel resolution between 1500x1500 and 3000x3000 should be employed. It must be noted that some graphic adapters, or operating systems, will not allow the use of a resolution higher than the maximum display resolution, thus limiting the maximum accuracy.

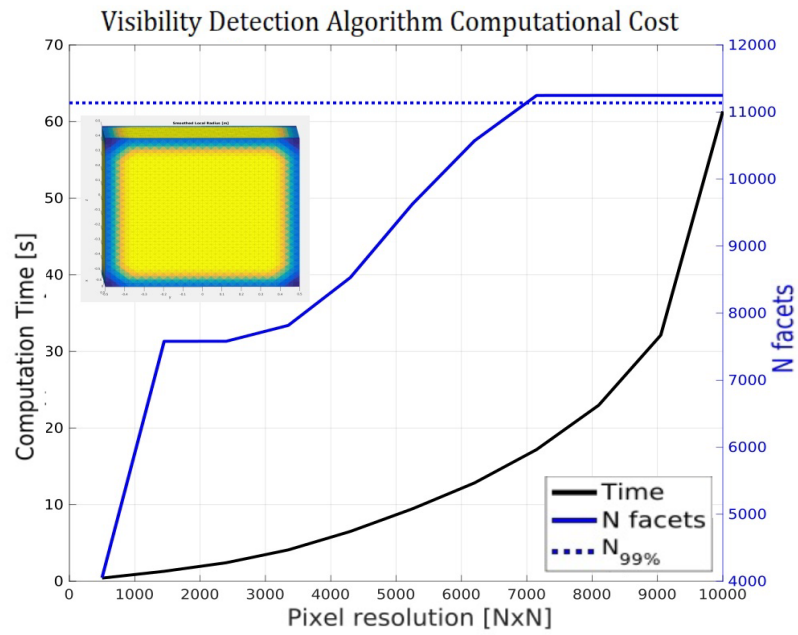


Figure 2.36: Visibility panels detection algorithm computational cost and accuracy for a cube with a fixed attitude (small angle of attack and side-slip).

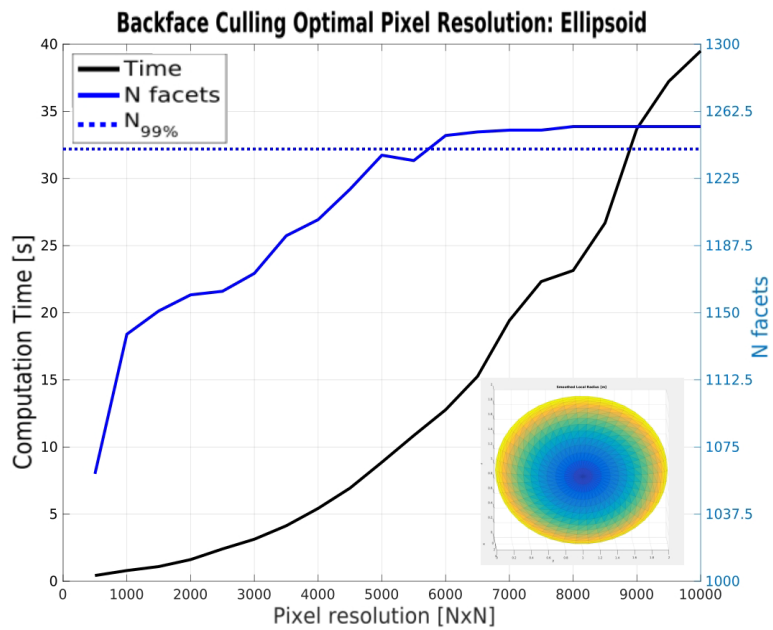


Figure 2.37: Visibility panels detection algorithm computational cost and accuracy for a cylinder with a fixed attitude.

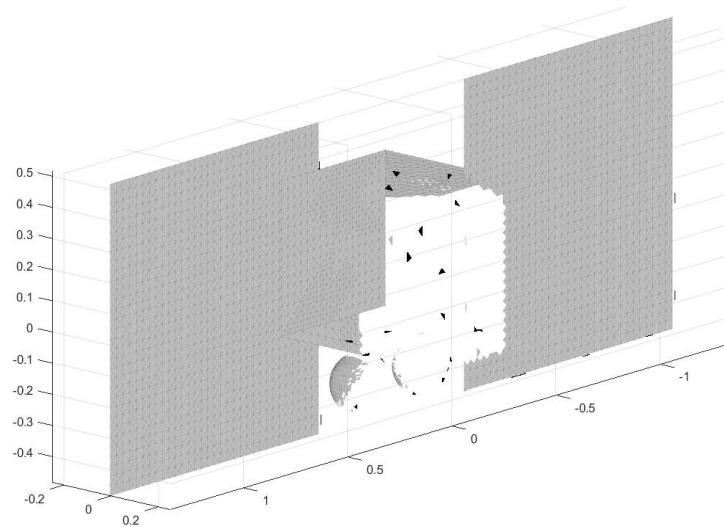


Figure 2.38: Rasterization error on the occlusion culling, the black panels should be shadowed but have been misidentified, the back-face filtering avoid this kind of error.

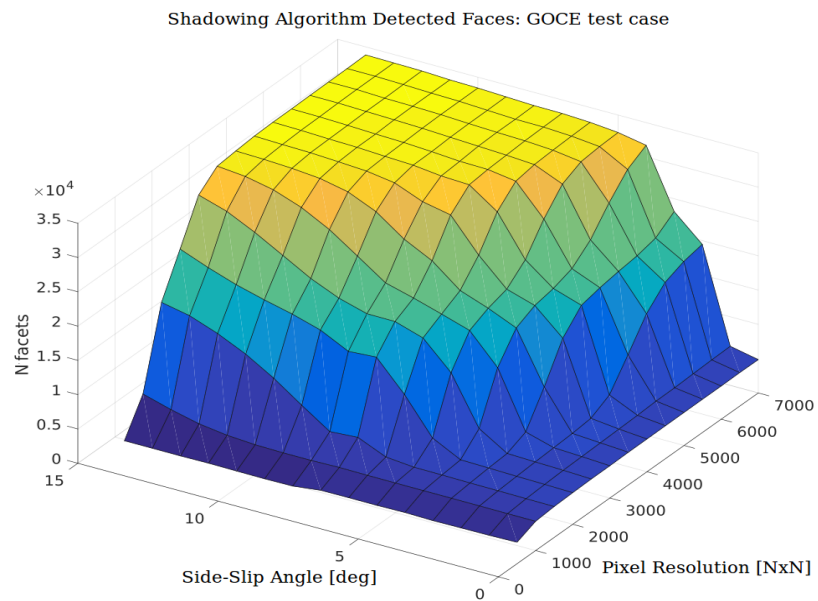


Figure 2.39: Occlusion culling dependence on the attitude and pixel resolution for the GOCE study case.

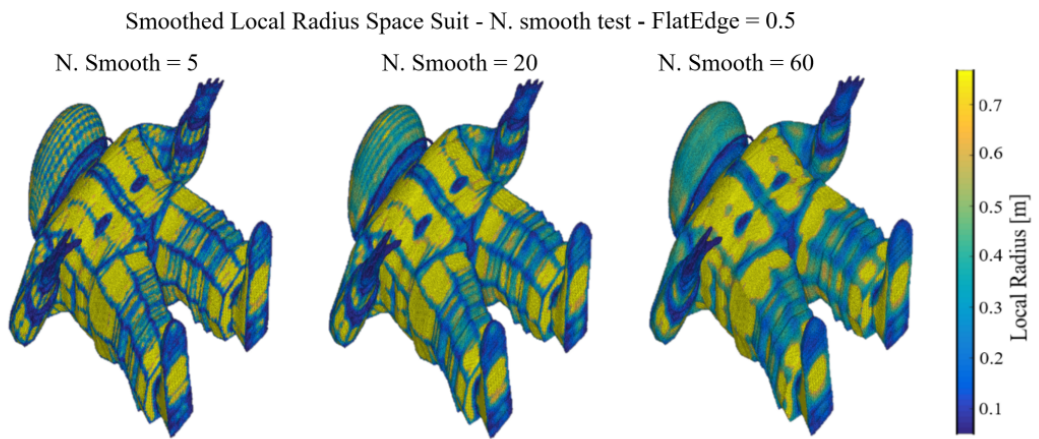


Figure 2.22: $N. smooth$ parameter (number of closest values taken for the average) comparison on a complex geometry.

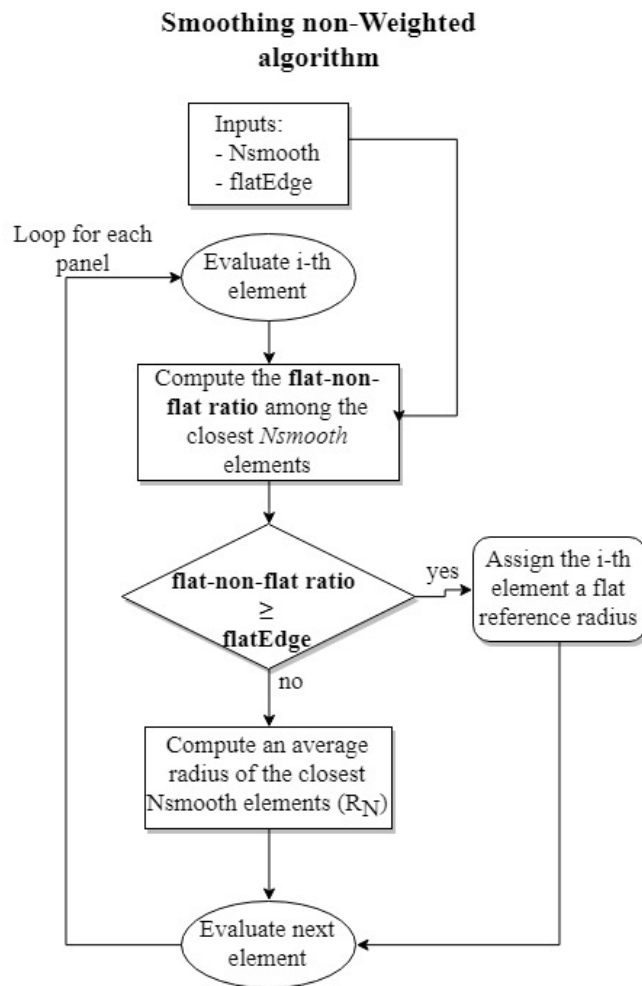


Figure 2.23: Non-weighted smoothing local radius algorithm block diagram.

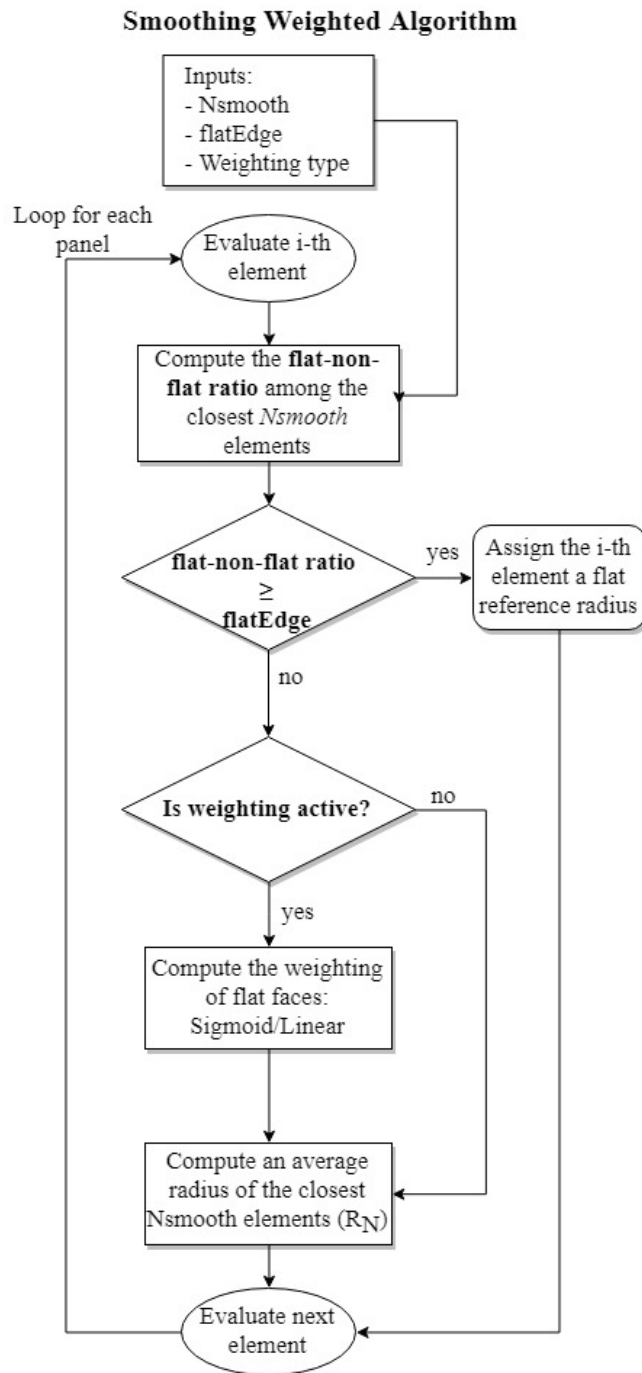


Figure 2.25: Weighted smoothing local radius algorithm block diagram.

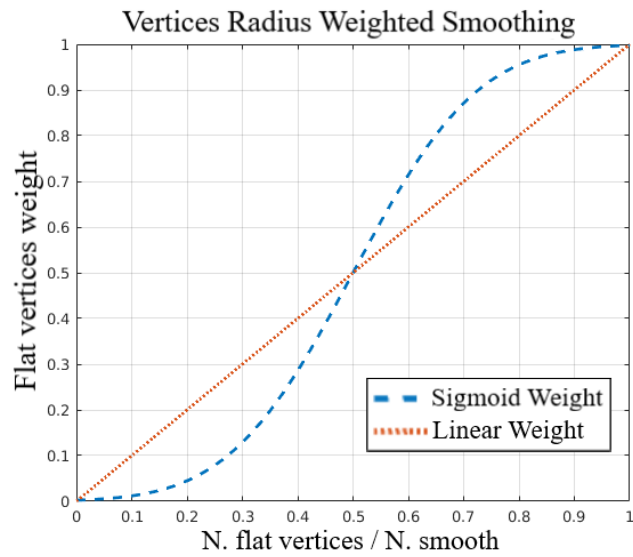


Figure 2.26: *Linear* and *Sigmoid* Flat faces weighting functions

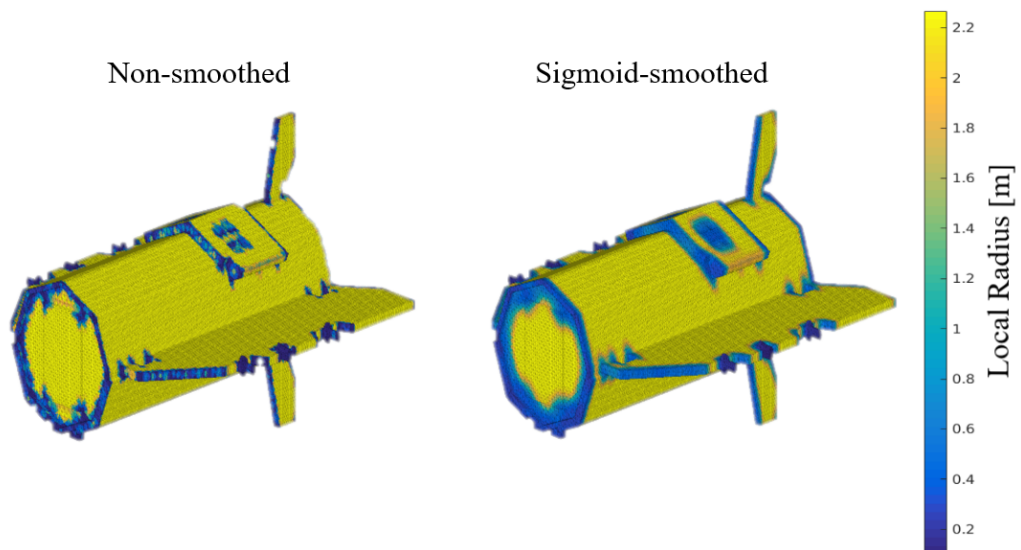


Figure 2.27: Local radius estimation of GOCE high resolution mesh. **left:** non-smoothed local radius. **right:** sigmoid-smoothed local radius.

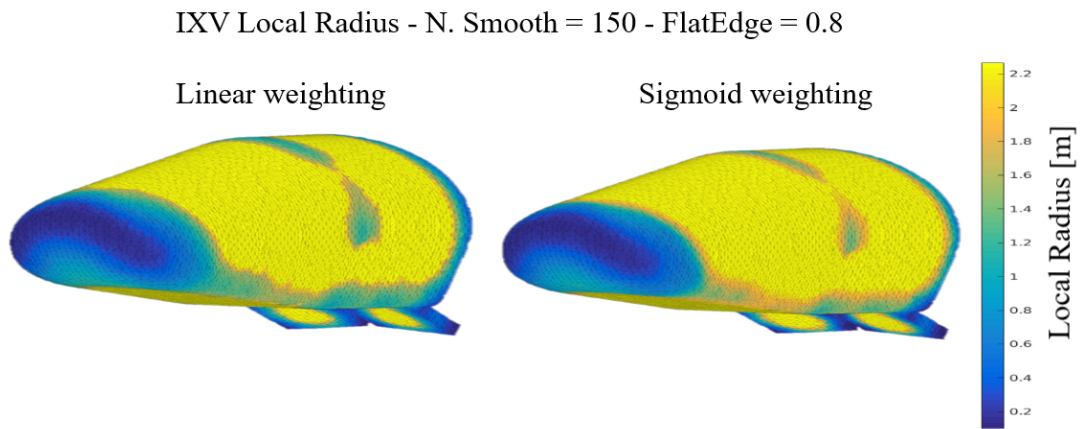


Figure 2.28: Local radius estimation of IXV high resolution mesh. Comparison of the different flat-faces weighted smoothing options: linear weighted (left), sigmoid weighted (right).

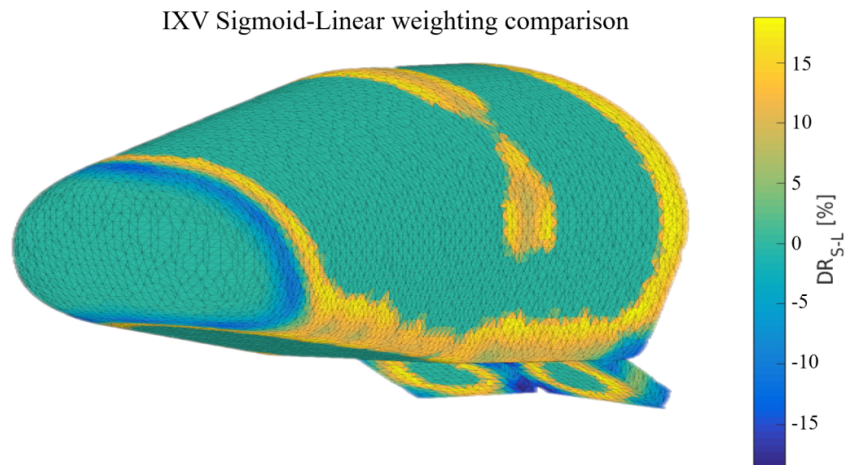


Figure 2.29: Difference of local radius estimation sigmoid-linear smoothing mapped on the surface, directly taken from Figure 2.28. The relative differences are computed as $\frac{(R_{i, \text{sigmoid}} - R_{i, \text{linear}})}{R_{i, \text{sigmoid}}} \%$, the sigmoid smoothing shows lower radii at the corners and higher values close to the flat faces.

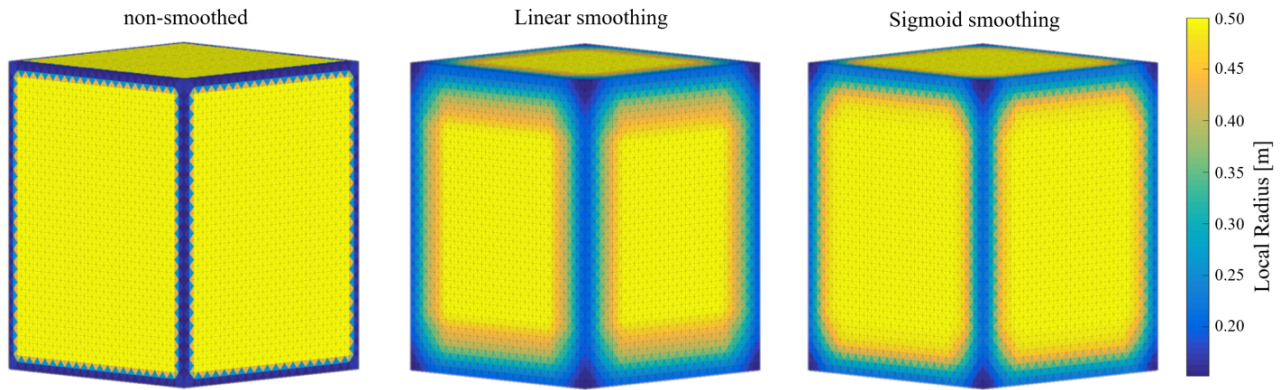


Figure 2.30: Cube local radius estimation, respectively from the left to the right: the non-smoothed, linear-smoothed, and sigmoid-smoothed. Noteworthy comparison with the thermal mapping shown in Figure 2.14. It can be observed that the sigmoid smoothing better approximate the relative magnitude distribution in the corners. In addition, since a high number of points is being averaged, the flat-non-flat faces ratio at the corners is always >0.5 , therefore, the sigmoid smoothing computes a higher radius at the corners.

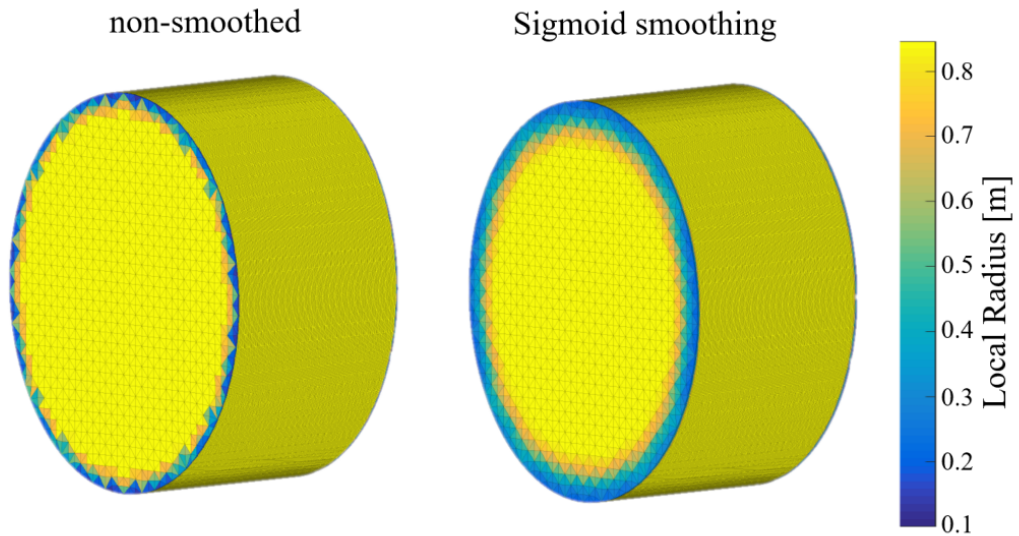


Figure 2.31: Flat Cylinder ($R = 0.8\text{m}$) local radius estimation. The non-smoothed and sigmoid-smoothed local radius shown respectively on the left and right. It may be observed that the sigmoid smoothing can give a better representation than the non-smoothed of a possible surface thermal heating distribution for a head-on flow condition within the transitional and continuum regime.

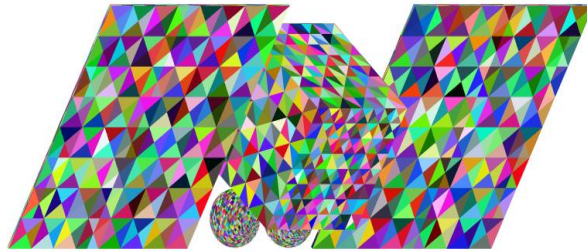


Figure 2.34: Occlusion culling, random color IDs assignment and windward direction rotated object.

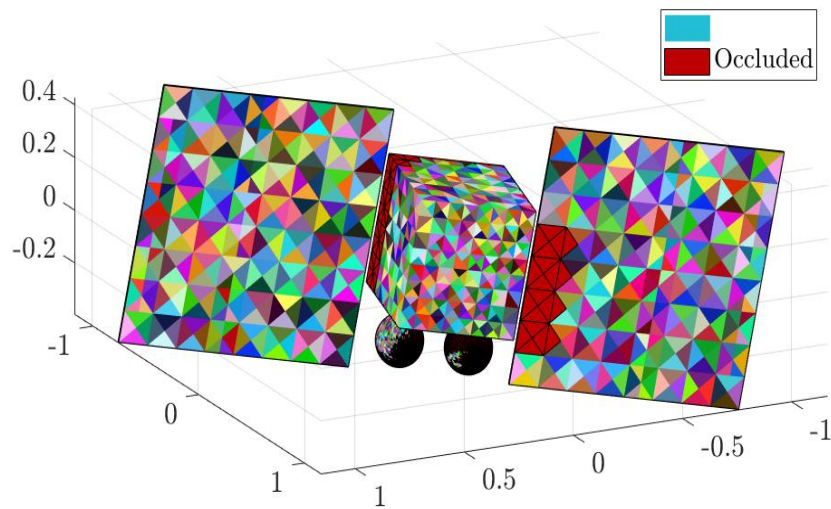


Figure 2.35: Occlusion culling, occluded panels red colored with black border.

Aerodynamics Computation

Methodology

The aerodynamic computation is performed after the atmospheric parameters, the mesh operations, and the panels visibility detection has been successfully concluded, as shown in Figure 2.1. The aerodynamic properties which are computed by default are the aerodynamic coefficients (C_D , C_L , C_S , $C_{M,x}$, $C_{M,y}$, $C_{M,z}$). In order to compute the properties of the entire object, the pressure coefficient contribution of each panel on the main axis (x,y,z) have to be evaluated.

In order to compute the aerodynamic coefficients, the reference cross section (S_{ref}) and the reference cord length (l_{ref}) are required. It is possible to estimate them automatically from the geometrical model, or provide them as inputs. The cord length can be estimated as the length in the axial direction of the object as:

$$l_{ref} = \max(\mathbb{V}_x) - \min(\mathbb{V}_x) \quad (3.112)$$

where \mathbb{V} represents the geometrical vertexes matrix. For the estimation of the reference cross section, it can be used the Visibility detection algorithm with a virtual wind direction in the direction of the longitudinal axis of the object (i.e.: AofA = 0deg and Side-slip = 0deg). In this way only the visible panels are identified, and projecting their area on the cross-sectional plane, the reference area can be computed as the sum of each visible panel projected area. An example for GOCE satellite is shown in Figure 3.1. The reference area computed with the visibility detection algorithm is $S_{ref} = 1.129\text{m}^2$, against the commonly used 1.131m^2 for the GOCE satellite. The S_{ref} computed with this method can change with the resolution and number of panels used for discretization of the geometrical model.

A detailed work-flow of the aerodynamic computation methodology applied is reported in Figure 3.2. The aerodynamic models used for the computation in the continuum and free molecular regime are thoroughly described in the introductory chapter; in the continuum regime the modified Newtonian theory is applied eq. 1.46, while in

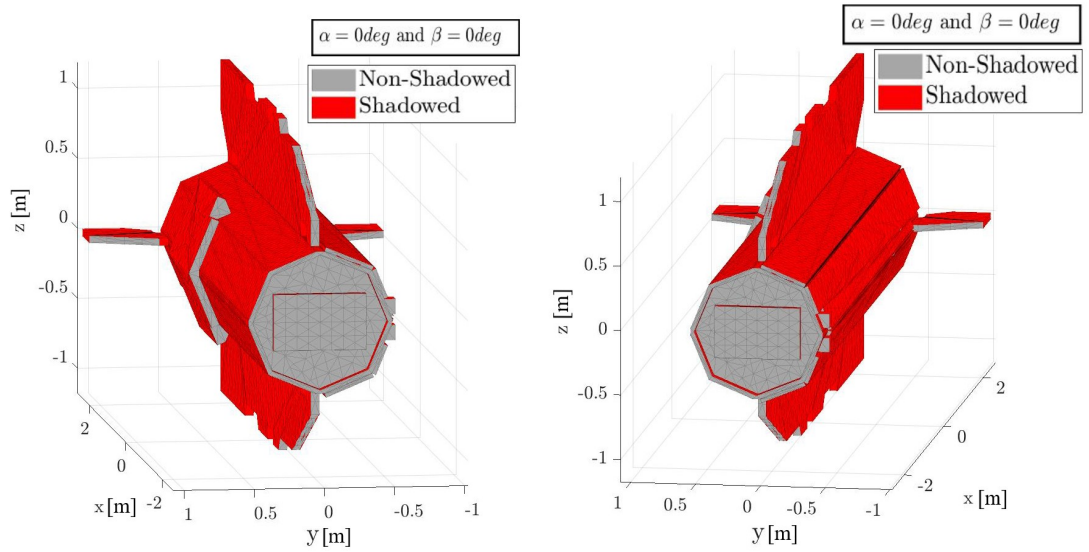


Figure 3.1: GOCE model automatic cross sectional reference computation.

the free molecular regime the flat-plate Schaaf and Chambre theory is employed (eq. 1.71 and 1.72). As highlighted in the work-flow, in case the simulated altitude is in the rarefied transitional regime, it is necessary to compute the two reference values of the continuum and rarefied regime, which are then used to build the bridging model. The details of the aerodynamic bridging models are reported in the following chapter.

3.1 Aerodynamic Bridging Function

Before evaluating the aerodynamics with the Modified Newtonian Method or the Schaaf and Chambre flat plate theory, it is necessary to compute the external flow properties, for example: mass density, pressure, specific gas constant, constant pressure specific heat, viscosity, viscosity exponent coefficient, Mach, Knudsen, and Prandtl numbers. Depending on the flow regime (continuum or free molecular), the different models are applied, in accordance to what has been described in the 1st chapter. In the transitional regime, a bridging function obtained with a normalized and corrected form of a typical error function is used. The error function defined as (Figure 3.3):

$$\text{erf}(x) = \frac{2}{\sqrt{\pi}} \int_0^x e^{-t^2} dt \quad (3.113)$$

The error function is applied to a normalized Knudsen number range (representative of the transitional regime). The normalization of Kn in the transitional regime is per-

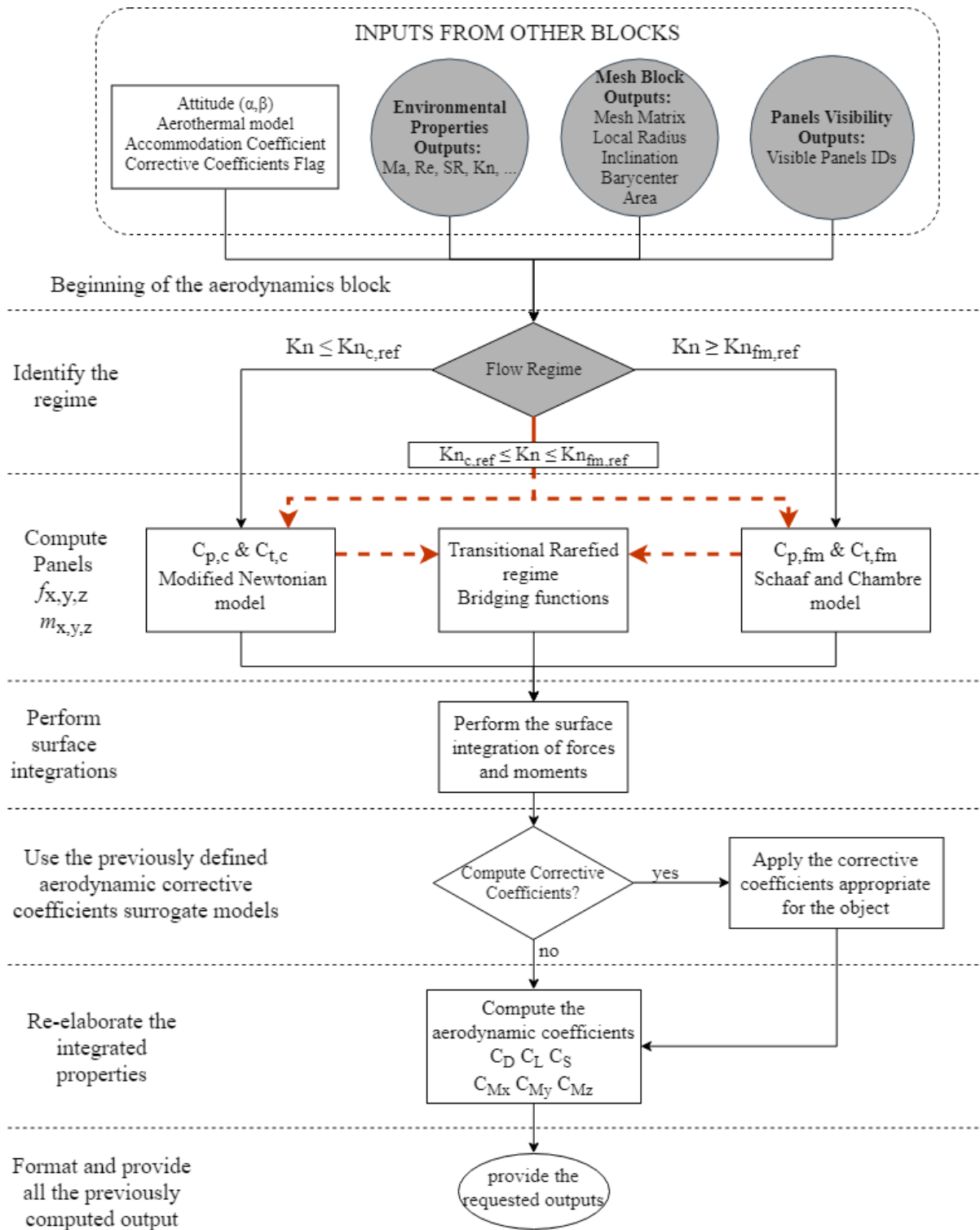


Figure 3.2: Aerodynamic computation methodology detailed work-flow.

formed with a logarithmic scale:

$$\text{Kn}_{\text{norm}} = \frac{\log(\text{Kn}_{\text{trans}}) - \log(\text{Kn}_{\text{c,ref}})}{\log(\text{Kn}_{\text{fm,ref}}) - \log(\text{Kn}_{\text{c,ref}})} \quad (3.114)$$

where Kn_{trans} are the values laying in the transitional regime, while the subscripts fm and c represents the free molecular and continuum regime reference values respectively, which can be calibrated to obtain a better accuracy.

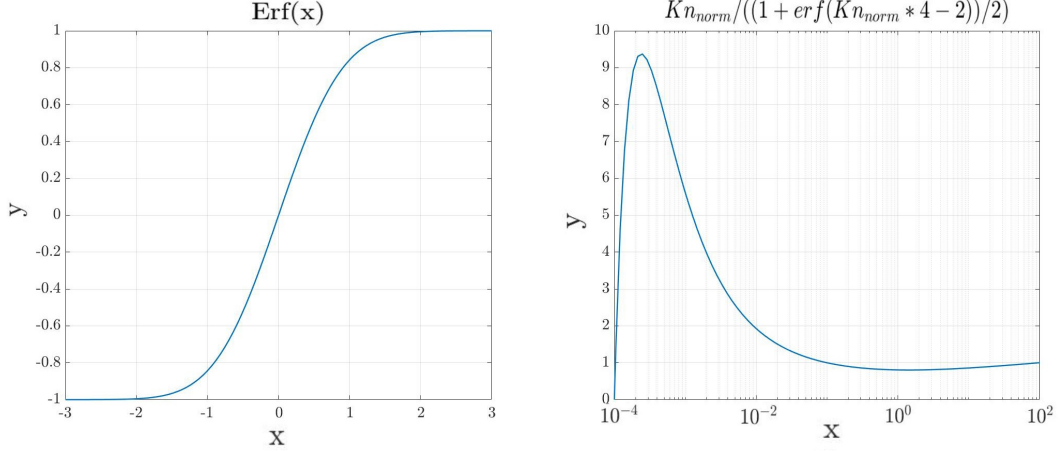


Figure 3.3: left: Standard Error function ($Erf(x)$), right: auxiliary function corrective function.

Using Kn_{norm} a corrective function which takes into account the differences between the $Erf(x)$ shape and transitional regime aerodynamics was obtained. The corrective function, defined as:

$$\text{Kn}_{\text{cf}} = \frac{\text{Kn}_{\text{norm}}}{((1 + \text{erf}(4\text{Kn}_{\text{norm}} - 2))/2)} \quad (3.115)$$

where Kn_{cf} is the weighting function. changing the weight of the function it is possible to obtain an optimal fitting on the various transitional regime aerodynamics analysis found in the literature [Rault, 1994, Moss et al., 1997, Moss et al., 2006a, Moss et al., 2006b, Dogra et al., 1992]. The corrective function has been scaled taking into account a pivotal point (Kn_p) in the transitional regime range, which depends on the reference free molecular and continuum reference values. In this way, the two regions defined as $[\text{Kn}_{\text{c,ref}} < \text{Kn}_{\text{trans}} < \text{Kn}_p]$ and $[\text{Kn}_p < \text{Kn}_{\text{trans}} < \text{Kn}_{\text{fm,ref}}]$ can be scaled independently.

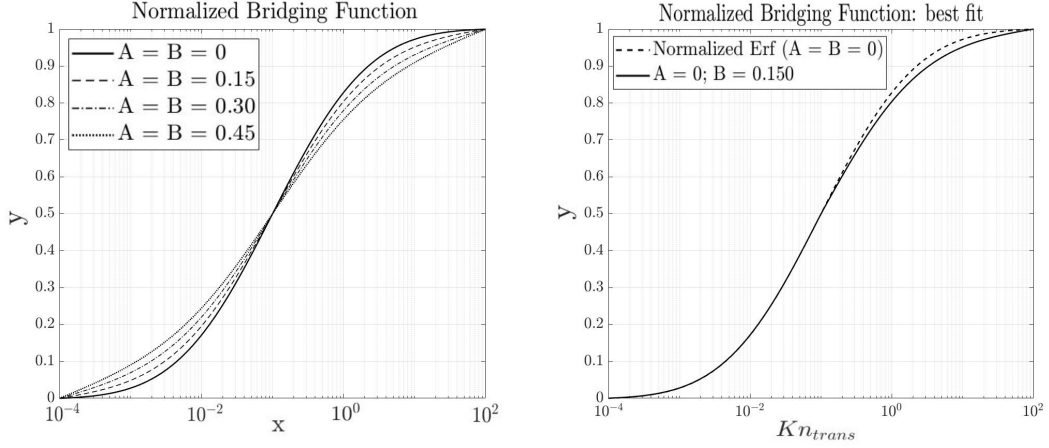


Figure 3.4: Left: general shape of the aerodynamic bridging function. Right: bridging function fitted on the aerodynamic references ($A = 1e-6$, $B = 0.150$, $Kn_{c,ref} = 1.0e-4$ and $Kn_{fm,ref} = 1e2$)

The scaling is performed as it follows:

$$\begin{aligned} Kn_{cf} &= (Kn_{cf} - 1) A && [Kn_{c,ref} < Kn_{trans} < Kn_p] \\ Kn_{cf} &= (Kn_{cf} - 1) B && [Kn_p < Kn_{trans} < Kn_{fm,ref}] \end{aligned}$$

The Bridging function is then defined as:

$$Kn_{bridge} = Kn_{cf}(1 + \operatorname{erf}(4Kn_{norm} - 2))/2 \quad (3.116)$$

where Kn_{bridge} is a bridging function dependent on the reference edges of the transitional regime $Kn_{c,ref}$ and $Kn_{fm,ref}$, and the two weighting parameters A and B . This particular bridging function is normalized (shown in Figure), and must be used in accordance to the asymptotic free molecular and continuum regime aerodynamic values.

This specific form of bridging function was chosen to simplify the mathematical computation of the aerodynamics in the transitional regime, as only one bridging function is necessary for all the aerodynamic coefficients. In addition, the generalized fitting for different geometries, condition, and shapes will be provide a bridging which can be applied to many different geometries without any further calibration. A different approach which has been previously tested [Benedetti et al., 2018], and it was based on a calibrated auto-regression approach, which required to simulate several altitudes per step; additionally, some computationally instability were discovered dependent on the simulated condition. The current approach has been proven to be more stable and comparably accurate.

3.2 Aerodynamic Module Validations

In this paragraph, a set of validations throughout the different regimes on different well known test cases is described. Initially, the aerodynamic convergence wrt to the number of panels used to build the geometry is investigated for various test cases. Some comparisons to assess the aerodynamic coefficients accuracy are performed on the Space Shuttle Orbiter [Rault, 1994], the Orion CEV [Moss et al., 2006a], a sphere of 1.6m diameter [Dogra et al., 1992]. More aerodynamic analysis in the free molecular regime have been carried out and are presented in the following paragraph used to define attitude and shape-dependent corrective factors within the free molecular regime. In the past, more analyses have been performed by [Benedetti et al., 2018] and [Mehta et al., 2015b].

3.2.1 Mesh Convergence Validation

Depending on the geometry complexity and attitude, a variable number of panels is required to discretize the mesh and properly detect the self-shadowed surface of a complex object. In addition, due to the specific panels visibility detection approach (described in section 2.4) the imaging resolution used to capture the visible panels affects the accuracy of the detection and computation aerodynamics or aerothermodynamics properties. Therefore, the number of facets used to discretize the geometry has to be normalized on the used resolution. As reported in section 2.4, depending on the actual implementation of the visibility detection algorithm and the operative system, the maximum image pixel resolution may be limited by the maximum screen resolution (at hardware level). This means that some machines have a limitation up to 1920x1080 pixels resolution. The direct consequence of such limitation is that for a high number of facets used to discretize a geometry (i.e.: $N_p > 10'000$) some of the facets will not be properly identified due to the rasterization error moving from a facet color to the adjacent one. The same kind of error is inherently applicable for low angle of attacks or side-slip angles; at these conditions, the projected area of lateral panels is small, thus a high pixel resolution is required to capture those panels. Such problem prevents a percentage of the lateral surface from being properly identified (examples reported in Figures 2.36, 2.37 and 2.39). Such type of error causes an underestimation of the active aerodynamic surface, and a lower aerodynamic drag will be computed.

Another kind of error has been observed for complex objects due to the self-occlusion. In fact, a small number of big panels used to discretize a complex object will prevent the algorithm from correctly capturing a shadow cast on the surface of the object [Falchi et al., 2017b]. The shadowed surface should not contribute to the aerodynamic

drag, therefore not identifying a shadowed surface causes the overestimation of the aerodynamic coefficients. Summarizing the two possible source of errors the following two cases may be observed:

- type I error: drag overestimation on complex geometries - low number of panels, self-occlusion not properly detected, and geometrical features not properly represented
- type II error: drag underestimation - high number of panels, low angle of attack or side-slip, visibility detection algorithm used with low imaging resolution, or high-aspect ratio geometries.

Considering the contrasting errors when operating on a complex geometry, it is clear that a compromise on the number of panels for discretizing the geometry is required. Different test cases were performed for identifying a normalized parameter to determine a qualitative and approximated mesh refinement convergence degree aiming at preventing the type II error. The parameter that seemed most promising for this purpose was found to be a normalized average number of panels per imaging pixels resolution (N_{pl}), defined as:

$$N_{pl} = \frac{N_p}{\sqrt{N_{pix,x}N_{pix,y}}} \quad (3.117)$$

where N_p is the number of panels, $N_{pix,x}$ and $N_{pix,y}$ are the pixel resolution used for generating the visibility detection image respectively on the x and y axis. This normalization choice was driven by the imaging processing requirement of framing the entire object during the visible panel detection phase.

In this section the aerodynamic analyses of three different geometries (i.e.: GOCE, Space Shuttle Orbiter, and Mars Microprobe) have been performed. A reference visibility detection resolution was used (i.e.: 1920x1080) due to the necessity of reducing the computational time required by the panels visibility detection phase (which exponentially increases with the increasing imaging resolution, see Figures 2.36 2.37), along with the possible hardware limitation on the resolution.

The convergence simulations have been performed in a free molecular flow condition, according to data used as a reference. Specifically, the STS-orbiter has been simulated at the condition reported in [Rault, 1994] at the altitude of 170km (see also section 3.2.3). The Mars Microprobe test case has been simulated according to the condition reported in [Moss et al., 1997] (see also section 3.2.5), for $Kn \approx 400$. To perform an analysis with a complex geometry, the test case of GOCE has been considered. The reference DSMC aerodynamic simulations data reported in [Benedetti et al., 2018] have been used.

For the different geometries, a refinement of the mesh with a number of panels

ranging from 1000 to 100'000 was tested. The mesh refinement was achieved with the previously described algorithm (see section 2.3.2), using a area-based refinement method and 300 refinement iteration steps. In this way, it has been possible to ensure a uniformly distributed panels sizing. The convergence error was computed as:

$$\delta_{CD} = \text{abs} \left(\frac{C_{D,i} - C_{D,\text{ref}}}{C_{D,\text{ref}}} \% \right) \quad (3.118)$$

where δ_{CD} is the C_D convergence error, $C_{D,i}$ is the single step drag coefficient (with a fixed mesh refinement degree, N_{pl}), while $C_{D,\text{ref}}$ is the reference drag coefficient from the literature of the specific case, which has been also reported in the correspondent plots.

The simplest test case is the Mars Microprobe, which has been tested at a head-on attitude, and does not have any complex self-occlusion shadowing effect. The results is reported in Figure 3.5 where the reader may observe only the type II error due to the increasing number of visible facets wrongly identified as shadowed. However, for a simple geometry it is possible to observe a very low aerodynamic error even for a very high number of facets.

The STS-orbiter convergence test results have been reported in Figure 3.6. Also in this case, the type II error due to the limited imaging resolution slowly and gradually increases as the number of panels increases. In fact, the C_D is progressively more underestimated as the number of facets increases. Although, the error remains below 5% for more than 100'000 facets.

The GOCE test case has been performed for various side-slip angles, the reference data have been taken from [Benedetti et al., 2018] where the authors have performed simulations of GOCE aerodynamics in the free molecular regime using dsmcFOAM at various attitudes. The simulations have been evaluated with the currently developed tool (STRATH-A) and have been reported in Figure 3.7. For low side-slip angles, the local panel inclination methods fails to compute an accurate drag coefficient due to the high lateral to front surface ratio of GOCE (the use of a shape- and attitude-dependent corrective coefficient was investigated in [Falchi et al., 2017b]). As the side-slip angle increases above $\pm 3\text{deg}$, the method provides a very accurate drag coefficient estimation (below 5%). Using as a reference the dsmcFoam values reported, three different attitudes (-4deg, -7deg and -10deg) have been simulated with a progressively refined mesh. The simulated conditions for GOCE study case have been reported in table 3.1. The results of the three different simulated attitudes wrt to the increasing number of panels have been reported in Figure 3.8. The convergence test shows that for a low number of facets the type I error occurs (i.e.: visible panels wrongly identified). The type I error falls below 5% for all three cases when the number of facets become

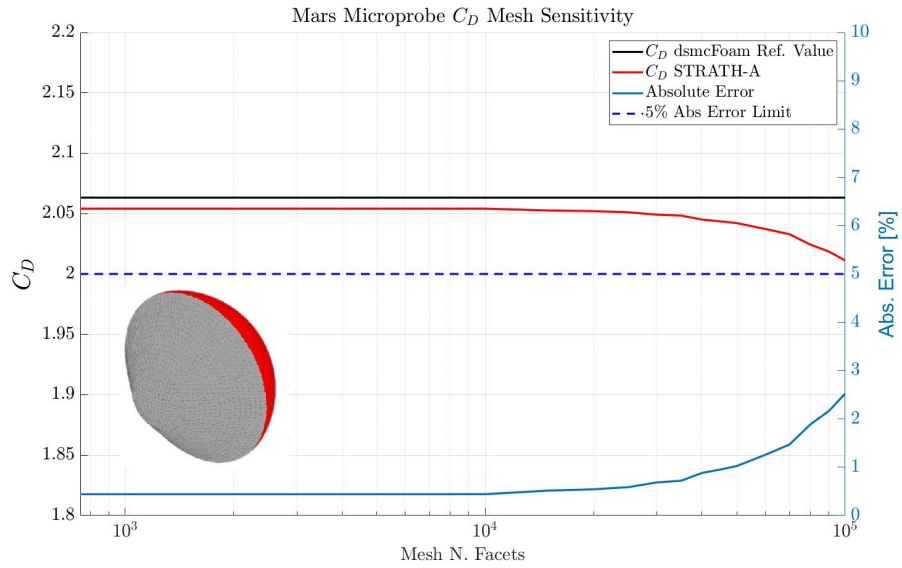


Figure 3.5: Mars Microprobe C_D (left y-axis) convergence wrt to the number of mesh panels (x-axis log scale). On the right y-axis the absolute error wrt the reference value from [Moss et al., 1997] is reported.

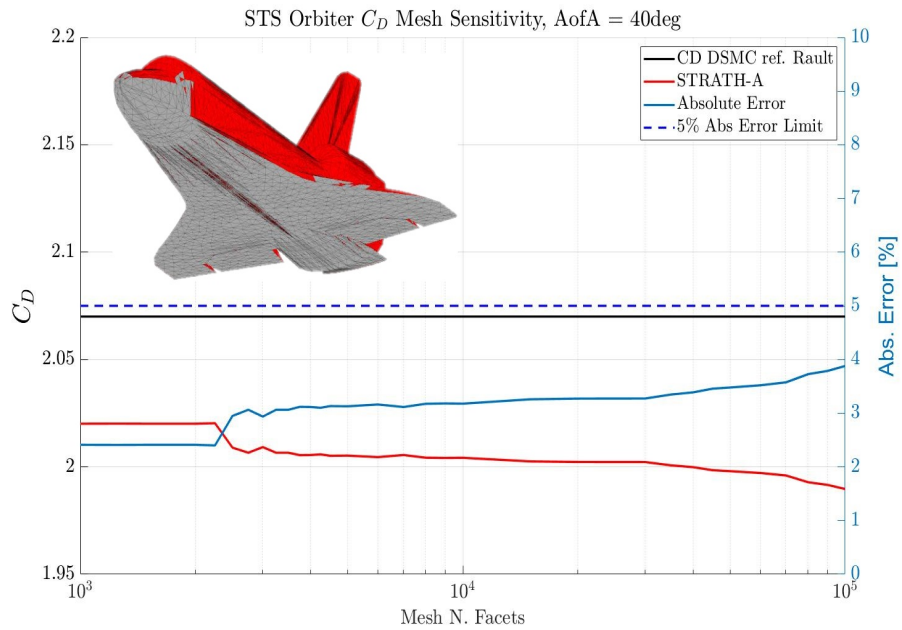


Figure 3.6: STS-orbiter C_D (left y-axis) convergence wrt to the number of mesh panels (x-axis log scale). On the right y-axis the absolute error wrt the reference value from [Rault, 1994] is reported.

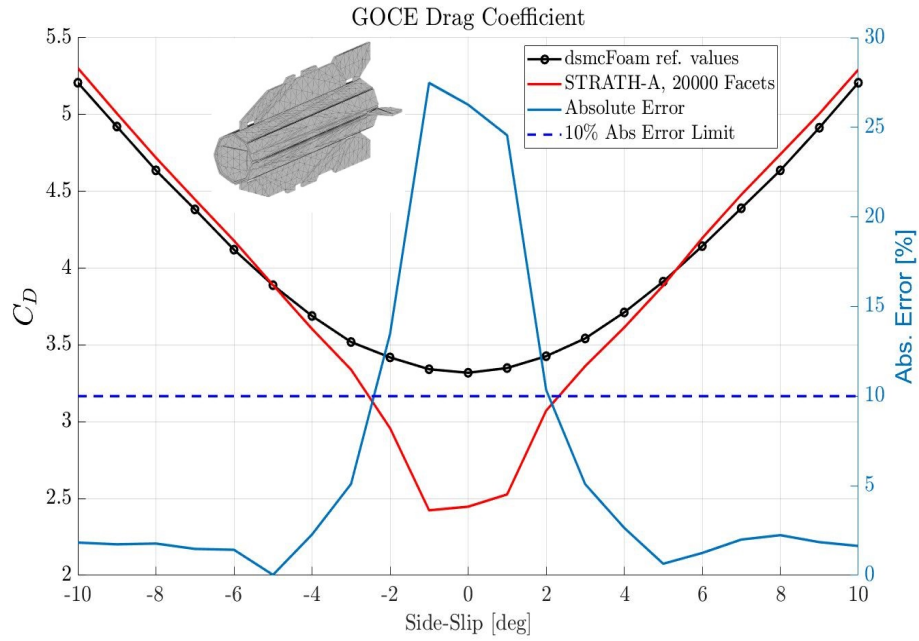


Figure 3.7: GOCE C_D (left y-axis) reported against the side-slip angle for a fixed number of panels (20'000). On the right y-axis is reported the relative error wrt the correspondent reference values computed with dsmcFoam from [Benedetti et al., 2018].

higher than 5'000. Although, as the number of panels increases above 20'000, the type II error becomes progressively significant, especially for the case with the lowest angle of attack. Therefore, it is possible to observe an optimal number of panels which minimizes the two type of errors, which is between 5'000 and 20'000. It can also be observed that for higher side-slip angles, the error stays below 5% for a wider range of panels. In addition, the GOCE study shows the performance of the visibility detection algorithm of a high aspect ratio geometry. In fact, GOCE is a slender body, meaning that low side-slip or angles of attack represent a challenging condition to be simulated, which results in a fast increment of the type II error as the number of panels increases. Comparing GOCE results against the STS-orbiter and Mars Microprobe, a faster increment of the type II error may be observed.

The three cases simulated for verifying the aerodynamic convergence process demonstrate that simple geometries can be simulated without producing any significant error on the aerodynamic coefficients with any number of panels. A complex geometry, characterized by features which may cause self-occlusion conditions or by overlapping panels, should be progressively refined until a stable aerodynamic coefficient plateau is found. A better overview of the mesh convergence process can be observed considering the nor-

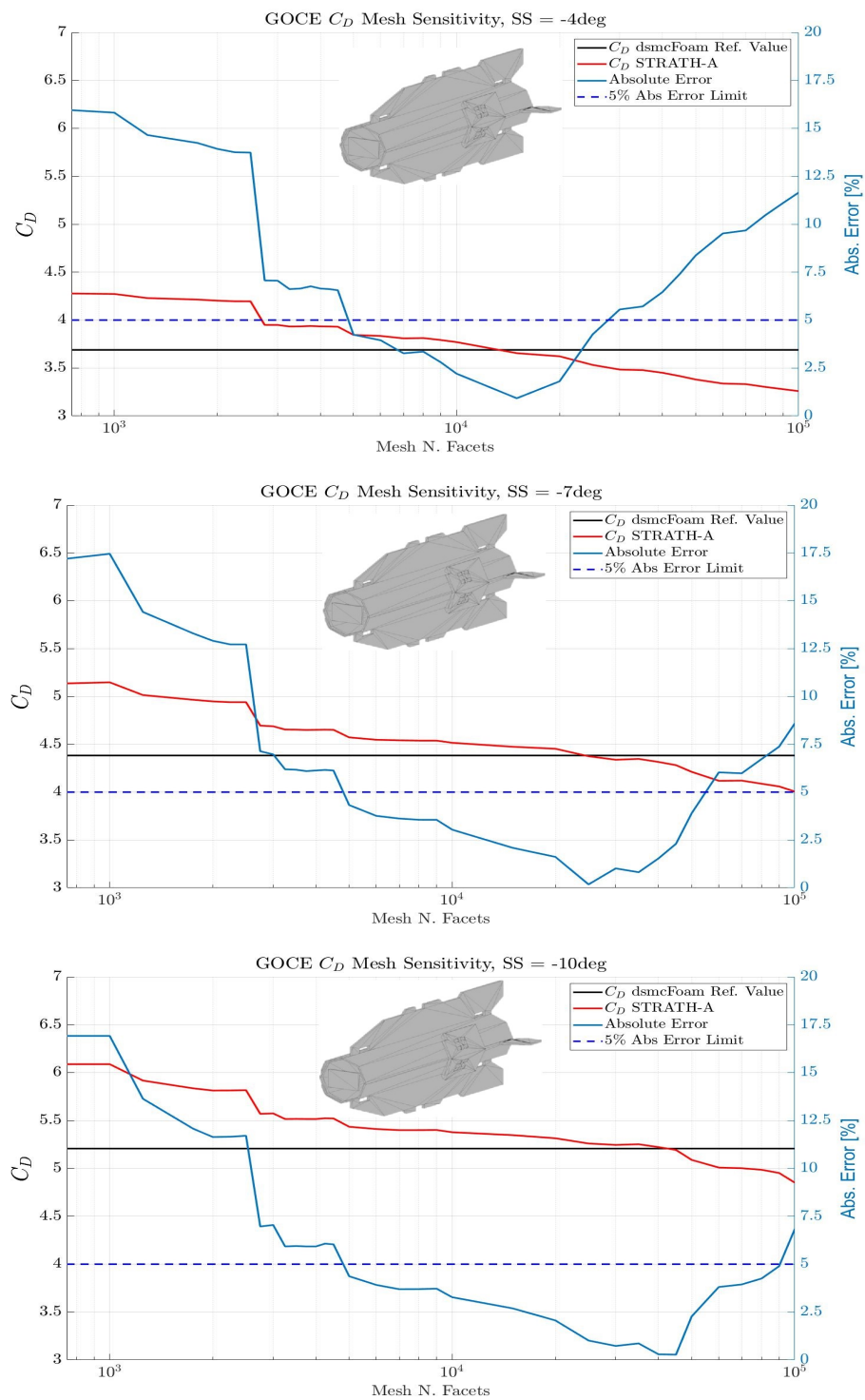


Figure 3.8: GOCE C_D convergence test (left y-axis) reported against the number of panels for three different side-slip angles: -4deg (top), -7deg (middle), and -10deg (bottom). On the right y-axis is reported the relative error wrt the reference correspondent values computed with dsmcFoam from [Benedetti et al., 2018].

Table 3.1: GOCE test case inputs for the comparison wrt to [Benedetti et al., 2018]

Input Parameter	Value
Accommodation Coefficient	0.93
Velocity	7760m/s
Altitude	260km
Aref	1.13m ²
Lref	5.26m
AofA	0deg
Side-Slip	from -10 to +10deg
T wall	350K
N panels	20'000

malized number of panels per average pixel resolution (eq. 3.117), reported in Figure 3.9. The overall analysis show that a sufficiently high number of panels per pixel resolution will provide accurate aerodynamic results for both complex and simple geometries at all angle of attacks.

Considering the analysis presented in this chapter, it can be concluded that an N_{pl} between 5 and 15 should provide accurate aerodynamic coefficients results. All the previous analysis have been performed using a pixel resolution of 1920x1080. Therefore, these limits correspond to 5x1440 and 15x1440 panels. Reducing the pixel resolution will decreases the computational time, and as long as the pixel ratio (i.e.: ratio pixel resolution on x/y axis) is kept constant the type II error will not significantly change. The reader should observe that the lower number of panels is always determined by specific geometrical features of the considered object and is not strictly related to the used imaging resolution.

In the following sections, the aerodynamic validations for various test cases and the different aerodynamic coefficients is presented. The simulations have been performed using a sufficiently refined mesh in order to optimize the aerodynamic accuracy.

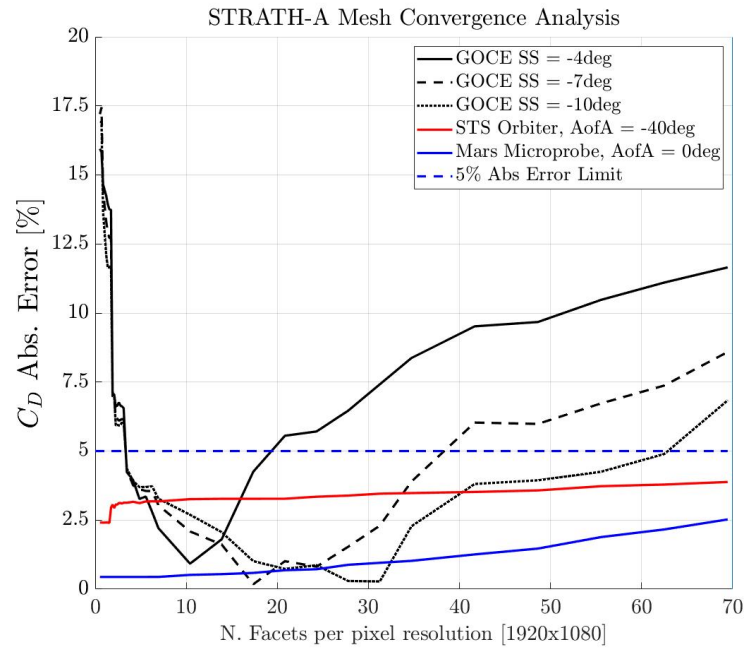


Figure 3.9: Overview of the mesh convergence analyses wrt to the number of panels normalized on the averaged pixel resolution (eq. 3.117). The pictures shows the drag coefficient convergence for complex and simple geometries at different condition.

3.2.2 Sphere

This paragraph presents the drag coefficient of a sphere (1.6m diameter) validation within the transitional and free molecular hypersonic regime based on the analysis performed by Dogra [Dogra et al., 1992]. The analysis have been performed with a reference atmospheric database in the altitudes from 90 to 200km, at the lowest altitude the flow is in a quasi-continuum regime, while at 200km the flow is in the free molecular regime. The free flow velocity is 7.5km/s with a wall reference temperature of 350K and a fully diffusive accommodation coefficient. The comparison is shown in figure 3.10; the maximum error wrt to the reference data is below 5%, which provides a good quantitative comparison.

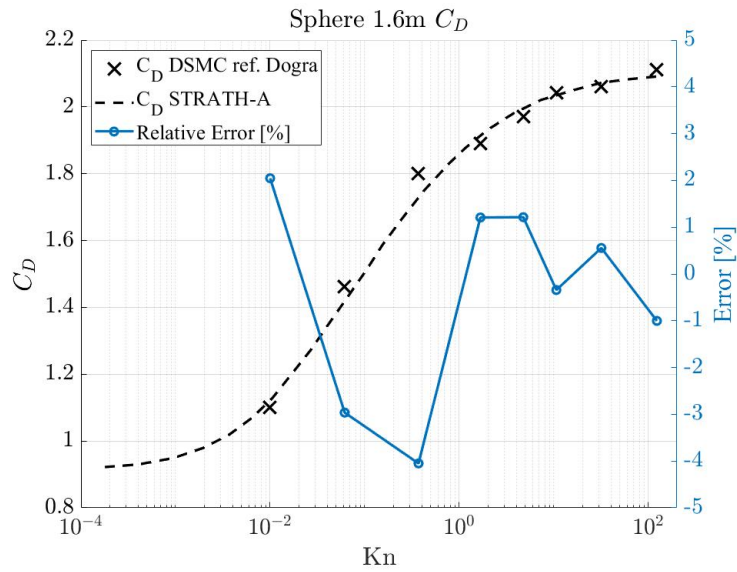


Figure 3.10: Sphere C_D free molecular, transitional and continuum regime validation [Dogra et al., 1992].

3.2.3 Space Shuttle Orbiter

The Space Shuttle Orbiter analysis are based on the research by [Rault, 1994]. The analysis have been performed on a generic Shuttle geometry 3.11. The reference data have been obtained through DSMC simulations and flight data measurements. The drag coefficient analysis have been performed on a set of altitudes: 100, 110, 120, 145, 170km. The reference surface used for computing the C_D is $S_{ref} = 249.909m^2$, a reference length $L_{ref} = 12.09m$, while the velocity was 7.5km/s, $\sigma_{diff} = 0.93$. The analysis on the drag to lift ratio have been compared with a set of reference data, provided by [Rault, 1994]. The results show a good agreement with both, flight and DSMC data (Figure 3.12), the minor difference could be due to the not exactly matching geometries and or slightly different atmospheric conditions. The lift to drag ratio show an average error between 5% and 10% when compared to DMSC data, although, the errors rapidly increases in the free molecular regime. Anyhow, the absolute discrepancy is not as significant. In fact, even the flight data show a wide range of measurements, meaning that the uncertainties in the upper atmospheric flight are more significant.

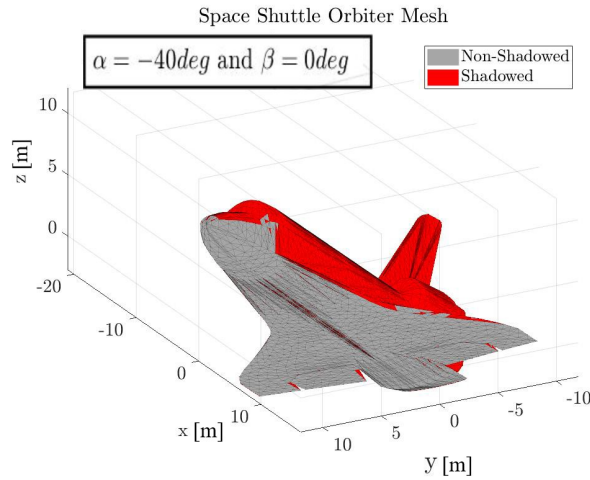


Figure 3.11: Space Shuttle Orbiter Mesh.

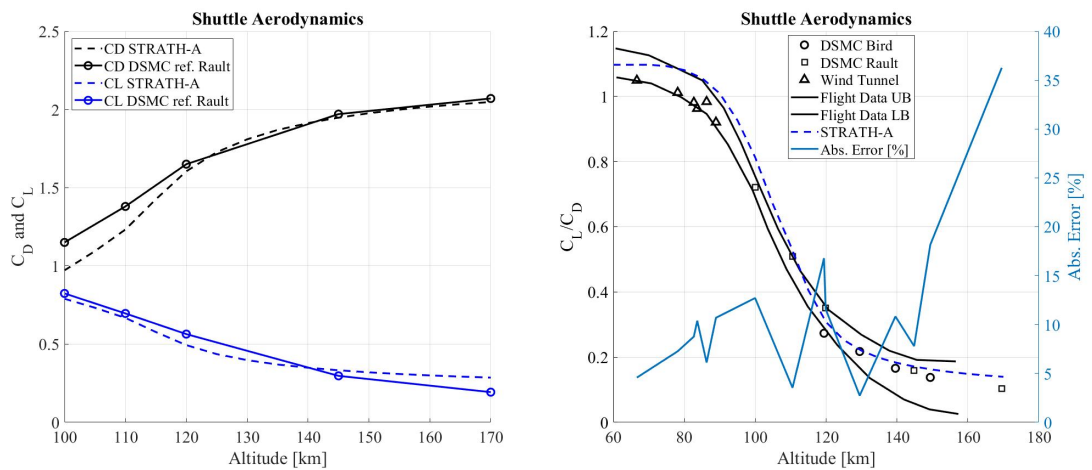


Figure 3.12: Left: C_D and C_L comparison. Right: L/D ratio for a wider set of literature data [Rault, 1994], UB and LB represents the flight data upper and lower boundaries respectively. On the right y-axis the relative error wrt to DSMC data is reported for the L/D ratio.

3.2.4 Orion Crew Exploration Vehicle

An extensive dataset is available for both the Orion Crew Exploration Vehicle [Moss et al., 2006a] and the Apollo Command Module [Moss et al., 2006b], in this paragraph only the Orion CEV was simulated. The results reported in the literature comprise different simulation tools: DAC, DACFREE, DS3V, and LAURA. The comparisons with

STRATH-A show a good agreement, with an average overestimation of $\sim 4\%$ (Figure 3.13). The relative error has been computed referencing to the most appropriate data for the considered Kn number. I.e.: in the continuum regime STRATH-A results have been compared to LAURA, while in the rarefied transitional and free molecular regime the results have been compared to the DSMC code (DS3V). The geometry used for the simulations with STRATH-A is a complex geometry, and it is not simplified as in the reference. Although, the geometric differences are visible only for angle of attacks greater than the simulated one (AofA = 26deg). A good agreement is found also on the L/D ratio (Figure 3.14), the results in these cases show some discrepancies due to the different geometries used; the afterbody geometry causes the discrepancies framed in the right Figure 3.14 for angles above $\pm 75\text{deg}$). The pitching moment coefficient ($C_{m_{z,0}}$, Figure 3.15) has been studied with respect to the angle of attack and was computed with a center of rotation fixed on the nose.

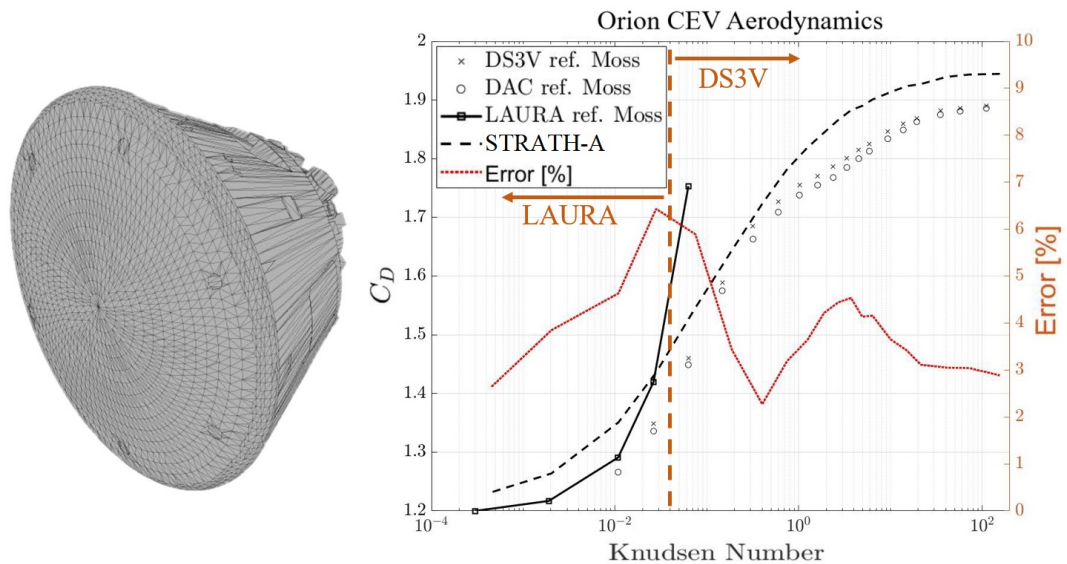


Figure 3.13: Orion CEV C_D comparison, $V_\infty = 7600\text{m/s}$, $\text{AofA} = -26\text{deg}$, $S_{\text{ref}} = 19.865\text{m}^2$ [Moss et al., 2006a]. The relative error has been computed in accordance to the flight regime validity of the reported references (i.e.: continuum or transitional rarefied regime).

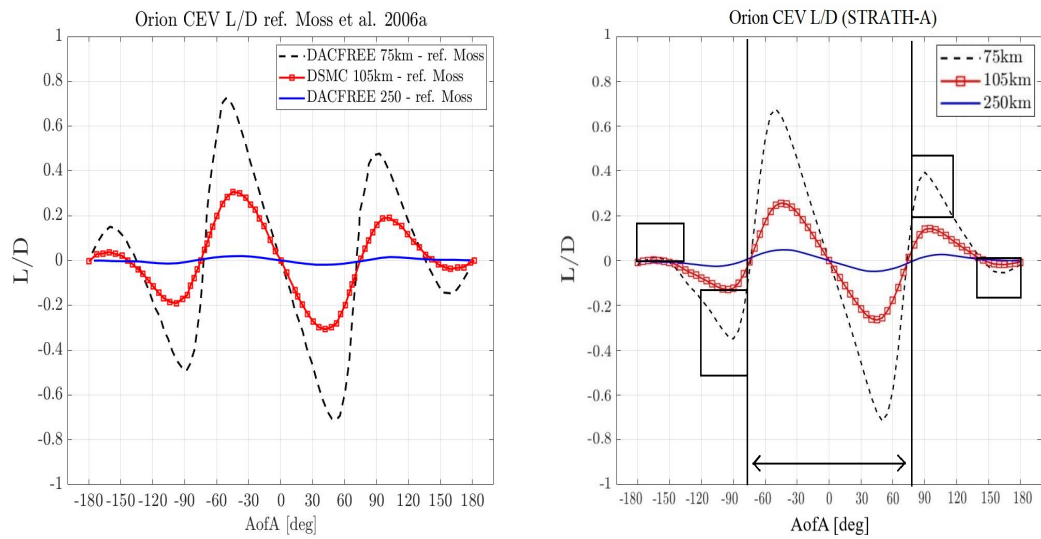


Figure 3.14: Lift to Drag ratio comparison for Orion CEV. Left: [Moss et al., 2006a], right: simulations performed with STRATH-A.. The discrepancies for angles higher than ± 75 deg are due to the afterbody geometric differences

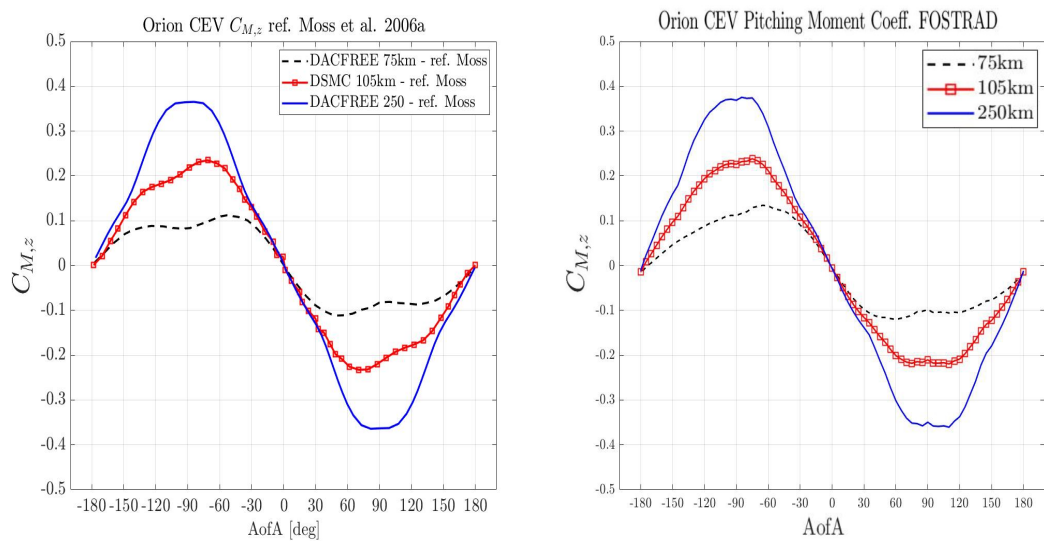


Figure 3.15: Pitching moment coefficient, center of rotation on the nose, ref. length = 5.0292m. left: [Moss et al., 2006a], right: simulations performed with STRATH-A..

3.2.5 Mars Microprobe

Another interesting case that has been simulated is the Mars Microprobe [Moss et al., 1997]. Although, this case is a Martian re-entry, and not an Earth atmospheric re-entry like the previous cases, the results show a good agreement (Figure 3.16), even though the

bridging function have been built for the typical earth atmospheric properties profile. The average relative error is around 8%, although it gradually decreases further in the free molecular regime.

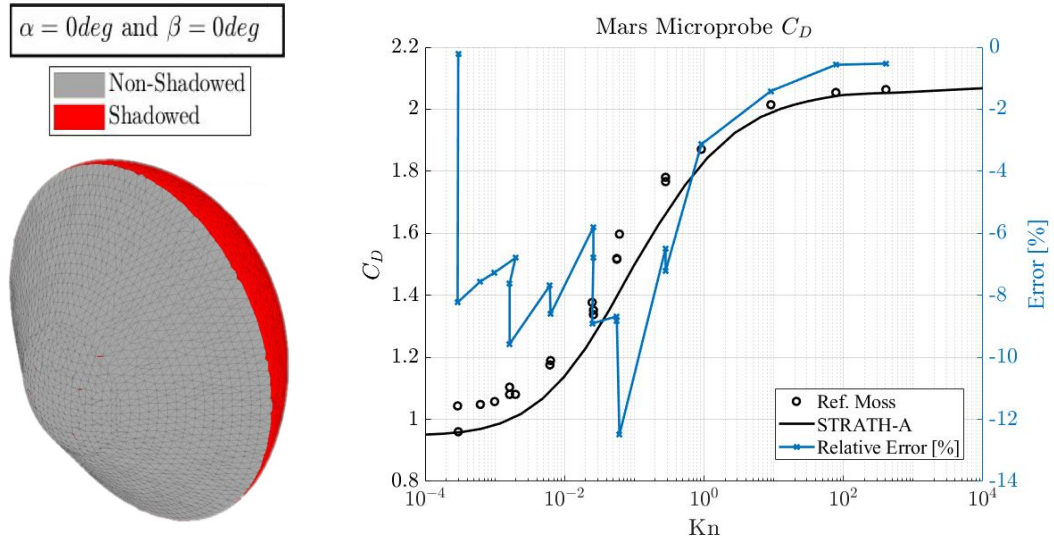


Figure 3.16: Left: Mars Microprobe geometry. Right: Microprobe Martian atmospheric C_D , $S_{ref} = 0.0962$ V_∞ from 6900 to 6100m/s, $AofA = 0deg$ [Moss et al., 2006a]. On the right y-axis the relative error wrt reference data is reported.

3.3 Free Molecular Regime Correction Factors

The local panel inclination method can provide fairly accurate results when applied to blunt bodies, as shown by the previous validation cases. Although, FOSTRAD has been tested on sharp-edged bodies like flat cylinders and parallelepiped, and a decreased accuracy has been observed. A recent investigation [Benedetti et al., 2018] on GOCE (the Gravity field and steady-state Ocean Circulation Explorer), which is characterized by a high lateral to frontal surface ratio and sharp-edged corners, has shown an underestimation between -30% and 5%. The comparison was performed against a DSMC software (dsmcFoam [Scanlon et al., 2015]), and the underestimation highly depends on the attitude of the object (both: angle of attack and side-slip), with the maximum discrepancy when the flow is parallel to the longitudinal axis of the object. The attitude-dependent error causes a higher uncertainty when the software is used for performing re-entry trajectory propagations or uncertainty quantifications. Although, if a random tumbling motion is assumed during the re-entry, a lower impact will be identified by this error. Additionally, even though this error was identified only in the free molecular regime, also the transitional regime will be highly affected, thus increasing the uncertainty all over the trajectory propagation, and having a great impact on the final ground footprint estimation. If the software is used for performing shape optimization, this error would make any result less reliable. These few examples clarify the necessity of reducing the impact of the attitude-dependent error. In this paragraph, a surrogate model (SM) of an attitude-dependent correction factor ($Aero_{CF}$, Eq. 3.119) for parameterized primitive shapes has been defined.

The $Aero_{CF}$ has been defined in the free molecular regime, thus it influences the aerodynamics computed with the bridging functions in transitional regime. The correction factors described in this paragraph, have been presented in the investigation [Falchi et al., 2017b]. The C_F has been computed by coupling FOSTRAD, a high-fidelity Direct Simulation Monte Carlo (DSMC - dsmcFoam [Scanlon et al., 2015]) and an Adaptive Derivative High Dimensional Model Representation-based algorithm [Kubicek et al., 2015] (AD-HDMR).

$$Aero_{CF} = \frac{C_{D,DSMC}}{C_{D,FOSTRAD}} \quad (3.119)$$

where $C_{D,DSMC}$ and $C_{D,FOSTRAD}$ are representative of the chosen aerodynamic coefficient (drag) computed with the DSMC and FOSTRAD respectively. A different SM will be generated for each parameterized shape: parallelepipeds, and cylinders. A particular geometrical parametrization has been chosen: the frontal area to total area ratio. This specific parametrization allows the SMs to be used independently from the absolute di-

mension, which could grant their general implementation within FOSTRAD depending on the analyzed shape similarity wrt the simulated geometries. The particular parallelepiped parametrization is suitable also for CubeSats. The defined cylindrical C_F model has been tested also on GOCE aerodynamics, where its application has shown a sensible error reduction on the estimated drag.

Direct Simulation Monte Carlo

The DSMC software that has been used in the current work is the dsmcFoam solver developed by Scanlon et al. [Scanlon et al., 2015, Scanlon et al., 2010]. The DSMC method allows to resolve steady and unsteady flow fields within the FM flow and rarefied transitional regime by simulating the statistical collisions among particles and object surfaces. Provided enough computational power, it would also be usable to model the continuum regime.

This work has been focused on the FM regime, where the inter-particles collisions are unlikely to occur. In the FM flow an inter particles collision-less model is able to properly represent the flow field, as indeed only the collisions with the object walls are evaluated. The method allows the computation of the macroscopic properties by averaging the simulated particles properties. In this case, only the aerodynamic properties are deemed of interest, specifically the aerodynamic forces and moments with respect to a fixed center of rotation.

For all the simulations in the current work, the collisions between particles and object's walls have been simulated with a mixed specular-diffusive reflective model with a diffusive energy accommodation assumed to be $\alpha_{\text{diff}} = 0.93$. The accommodation coefficient is a source of uncertainty which should be taken into account when performing aerodynamic simulations; as it has been thoroughly explained by Moe et al. [Moe et al., 1998, Moe and Moe, 2005], α_{diff} is highly variable, mainly depending on the orbital parameters, object's materials, solar activity and temperature. The last two, along with the molecular composition and the free flow velocity have an influence on the molecular speed ratio (S_R , eq. 3.120):

$$S_R = \frac{V_\infty}{\sqrt{2RT_\infty}} \quad (3.120)$$

where V_∞ is the assumed satellite velocity, R is the specific gas constant, and T_∞ is the free flow temperature. As it was reported by Cook [Cook, 1965], the S_R has a great impact over the drag, therefore it must be blocked during the C_F modeling phase.

When performing DSMC simulations, a mesh is initialized with a number of simulated particles, in this case representative of the atmospheric composition and properties

at a predefined altitude of 500km. Usually, the mesh refinement level is based on the free flow mean free path [Sun et al., 2011] (λ), but in the FM regime, the minimum mesh cell size is chosen in order to properly estimating the averaged macroscopic flow field properties and to accurately modeling the object's surface. For all the performed DSMC simulations, the flow field was initialized with 40 particles per cells, which is representative of a high accuracy. The atmospheric properties were directly obtained from a reference MSISE00 database. The atmospheric properties of interest were the 5 species molecular densities (O, O₂, N, N₂, Ar) and the average atmospheric temperature ($T_\infty = 960\text{K}$). As it has been shown by Bailey [Bailey and Hiatt, 1972], another parameter that influences the computed C_D is the wall to free flow temperature ratio: T_w/T_∞ . In this work, a reference $T_w = 300\text{K}$ has been used for all the simulations. The flow velocity has been fixed to 7600m/s, which in accordance with all the others properties leads to a molecular speed ratio equal $S_R = 7.66$.

For this work aims, few hundreds of simulations were expected to be performed for the different parameterized geometries; therefore, it had been required to build a general DSMC automated simulation interface which performs the following tasks: 1) Atmospheric Database and general inputs preprocessing; 2) the modification of the object's geometry according to the input parametrization; 3) mesh preprocessing definition and initialization; 4) initialization of the simulated particles properties; 5) initialization of the boundary conditions, and simulation control (e.g.: time step, averaging time frame, etc...); 6) particles, forces and moments convergence control; 7) post-processing and data management. Since the simulations were all performed on the ARCHIE-WeST high performance computer, an additional job management interface had to be coded in order to control the entire process.

Adaptive Derivative High Dimensional Model Representation

The AD-HDMR approach developed by Kubicek et al [Kubicek et al., 2015], which has already been employed for performing uncertainty quantification and sensitivity analyses of GOCE [Falchi et al., 2017a], has been used in this work for preliminarily evaluating the aerodynamic C_F surrogate models.

The AD-HDMR algorithm begins the initialization decomposing the N-Dimensional statistical domain, predefined in accordance to a set of input statistical distributions (e.g.: uniform distributions for α , β , and A_{ratio}). The algorithm selects the most influencing defined sub-domains, according to a procedure based on the HDMR-cut methodology. From those domains, the AD-HDMR performs a sampling for the next set of inputs to be tested. The function of interest is then evaluated with the selected inputs, it must be noted that in this specific case, the inputs are sent to the DSMC automated

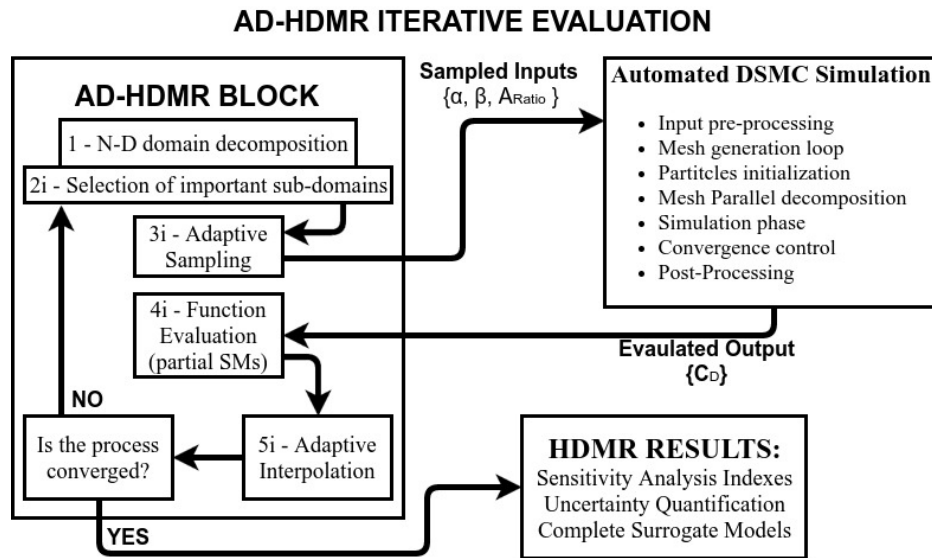


Figure 3.17: Iterative AD-HDMR process flow chart and DSMC coupling scheme: (1) The AD-HDMR starts decomposing the input domains. (2i) Selects the important sub-domains according to the latest results. (3i) Performs the adaptive sampling and requests a new DSMC simulation. (4i) Evaluates the function with respect to the sampled inputs. (5i) Adaptively selects an interpolation method. Performs the steps from 2i to 5i till the process has reached a statistical convergence.

simulation interface. The DSMC block automatically performs a preprocessing of the given inputs, generates the mesh, and initializes the DSMC simulation. After the DSMC simulation has reached a user-defined level of convergence, the C_D is returned to the AD-HDMR algorithm as if it were the results of a function evaluation. After an adaptive number of tested samples, the algorithm begins the creation of preliminary SMs used to evaluate the problem's statistical properties, defining which models best interpolate the sampled points via an adaptive interpolation, where the models are chosen from a given set of interpolants. When the process is properly converged from a statistical point of view, the algorithm provides the final sensitivity analysis results, the investigated property statistical distribution (e.g.: a probability histogram), and the SMs of "important" inputs and their interactions.

3.3.1 Methodology

In spite of the efforts for improving and correcting FOSTRAD's aerodynamic module, for non-hemispherical objects characterized by sharp edges and flat surfaces, FOSTRAD still shows a sensible error on the computed drag. The FM regime aerodynamic errors depend mainly on objects' lateral area and attitude. Therefore, for further improving

the aerodynamic module, two different C_F SMs have been defined and tested. Although the C_F have been computed only for the FM regime, the corrections will also improve the results within the transitional regime, which are based on the bridging function between the FM and the continuum regime.

The C_F SM have been defined for two different kind of geometries: parallelepiped and cylinders. The geometries have been parameterized based on the front area to total area ratio:

$$A_{\text{ratio}} = \frac{A_{\text{ref}}}{A_{\text{tot}}} \quad (3.121)$$

where A_{ref} for the parallelepiped has been fixed to $A_{\text{ref,p}} = 0.01\text{m}^2$ (equivalent to a parallelepiped with a square frontal face of side 0.1m) and for the cylinder $A_{\text{ref,c}} = \pi(0.1/2)^2 [\text{m}^2]$. It is interesting to highlight that when $A_{\text{ratio}} = 0.1\bar{6}$ the geometries are cubic, and that the parallelepiped parameterization covers the different CubeSats configurations (Figure 3.19 on the left). As long as the aerodynamics are computed within the FM regime, the scale of the object is not relevant, therefore, the C_F are applicable to different scaled objects. In addition, they would be usable also for similar shaped geometries, e.g.: GOCE geometry resembled a cylinder with two big fins, therefore, the cylindric C_F would be usable for that geometry.

The ranges of analyzed parameters are reported in Table 3.2. For the symmetric nature of the analyzed geometries, it will be possible to extend the use of the C_F to wider attitudes. The area ratio has been chosen to stay within the boundary limits of a finite length geometry and "not-flat-plate" cases. The infinite length cylinder or parallelepiped and the flat-plate case would be equivalent to a $A_{\text{ratio}} \rightarrow 0$ and $A_{\text{ratio}} \rightarrow 0.5$ respectively. This two cases have not been presented here because they would need a specific implementation on the DSMC side with a subdivision of the attitude ranges and their application would be limited to extreme cases.

The preliminary C_F models were built using the the integrated approach of the AD-HDMR controlling the DSMC automated interface and FOSTRAD. Both the software used the atmospheric inputs listed in Section 3.3, in this way the atmospheric variables were blocked, thus the C_F takes into account only the variation due to the attitude and the shape. The AD-HDMR built the dataset to be used by the surrogate model generation phase directly computing the C_F .

The preliminary SM evaluation performed via the AD-HDMR identified that all the considered variables and their interaction were significant. Therefore, the parallelepiped correction factor surrogate model ($C_{F,p}$) was built as the combination of three 1st-order models, three 2nd-order interactions, and one 3rd-order interaction. Meanwhile, the ($C_{F,c}$) was defined by 3 models: two 1st order models and one 2nd order interaction. The

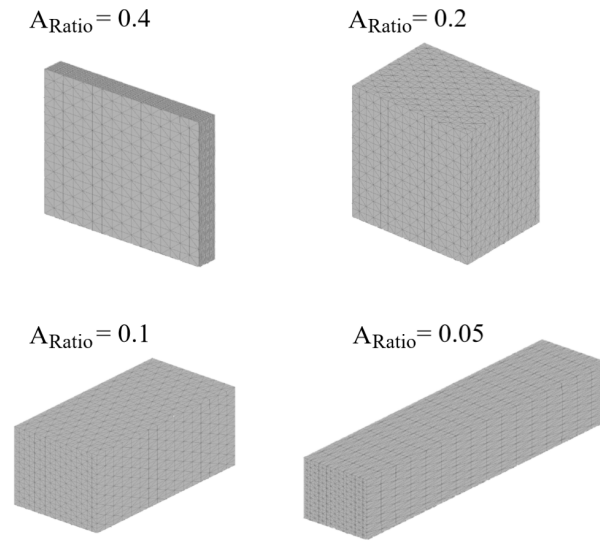


Figure 3.18: parallelepiped parameterization based on the A_{ratio} .

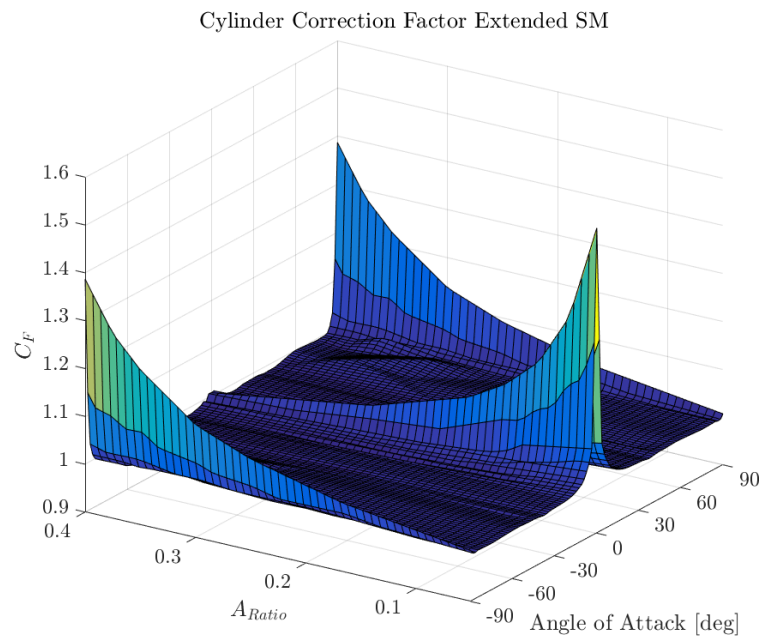


Figure 3.19: cylindrical geometry C_F surrogate model.

Table 3.2: Configurations evaluated for the C_F .

Case	A_{ratio}	α	β
Parallelepiped	[0.05; 0.4]	[0; 90]	[0; 90]
Cylinder	[0.05; 0.4]	[0; 90]	-

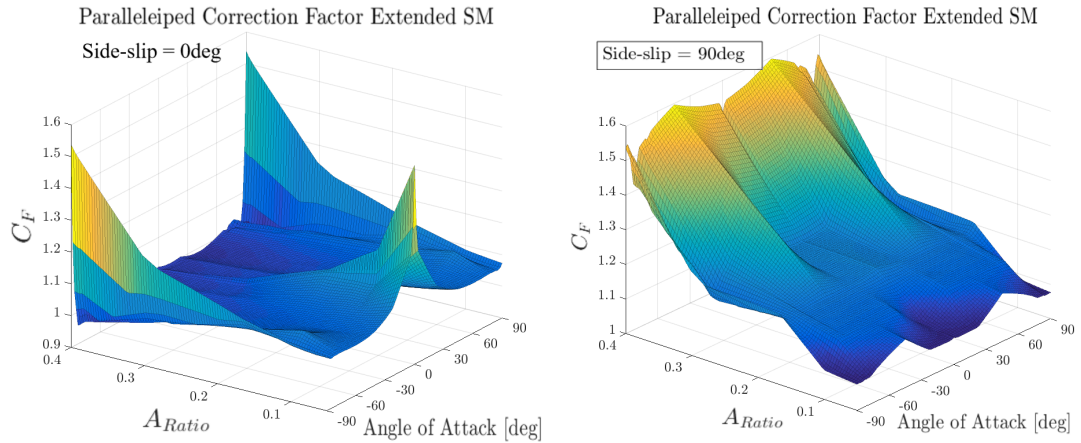


Figure 3.20: Parallelepiped C_F surrogate models for two different constant side-slip angles 0deg (on the left) and 90deg (on the right). It is possible to notice the strong interaction between all different variables taken into consideration.

preliminary S.M. interpolation datasets defined by the AD-HDMR have been thoroughly analyzed and locally refined to increase the SM accuracy. The parameterized cylindrical $C_{F,c}$ is shown in Figure 3.19 on the right. An example of the N-Dimensional $C_{F,p}$ is shown in Figure 3.20 for two different side-slip iso-surfaces respectively at 0deg and 90deg. The surrogate models have been defined using a different interpolation methods: 1-D Piecewise Hermitian Cubic Interpolation, polynomial and linear N-D interpolation.

The created drag coefficient C_F has been used to perform a Monte Carlo analysis for both geometries. The results are shown in Figure 3.21; the analyses are representative of the statistical discrepancy between FOSTRAD and the DSMC for the parameterized geometries. Assuming a random tumbling attitude, the average DSMC-to-FOSTRAD error would be very low. It must be highlighted that the SM are subject to minor errors due to the used interpolation techniques and accuracy, thus the errors could be higher (or lower), but the results are representative of the random tumbling aerodynamic drag error magnitude.

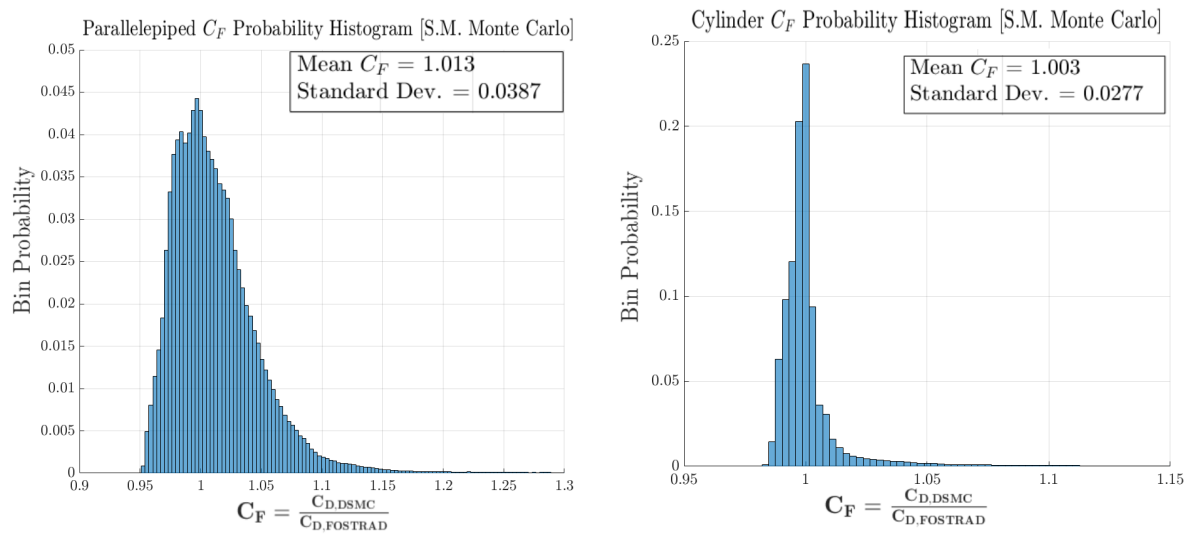


Figure 3.21: Monte Carlo analysis results on the drag C_F , representative of the average random tumbling discrepancy between FOSTRAD and the DSMC code. The parallelepiped and cylinder are shown on the left and the right respectively.

3.3.2 Cylinder and Parallelepiped Correction Factor Tests

In order to test the validity of the created C_F SMs, a set of tests have been carried out on both geometries. As the SMs have been defined according to a finite number of sampling points, the models are expected to present a higher error when they are used far from the sampled points. For this reason, arbitrarily chosen intervals have been analyzed, comparing the FOSTRAD corrected C_F with DSMC results. Numerous tests have been performed for different α , β , and A_{ratio} . For the sake of brevity, only some of the most significant results have been chosen to be presented.

In Figure 3.22 the corrected FOSTRAD C_D for a parallelepiped (on the left) and a cylinder (on the right) are shown. For the parallelepiped, the raw FOSTRAD results are underestimating the actual C_D , while the corrected model presents some discrepancy for low angles of attack. This is due to the interpolation techniques used for building the SMs and the limited number of used points. Using a better refined sampling database would provide more accurate SMs. For the cylinder, FOSTRAD simulations show an underestimation at both low and high angles of attack, while the corrected version greatly reduces this error. For intermediate attitudes, FOSTRAD does not present a sensible discrepancy, as it would have been expected considering that the lateral cylindrical surface has a hemispheric shape.

The analyses have been performed also for the lift and pitching moment coefficients (C_L and $C_{M,z}$ respectively). The $C_{M,z}$ has been analyzed with a reference center of

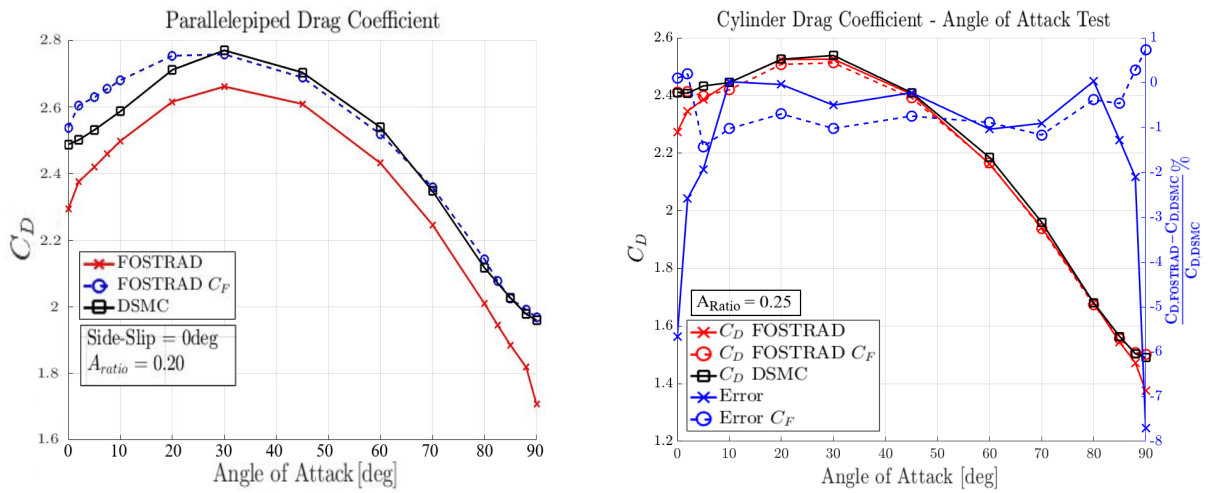


Figure 3.22: FOSTRAD-DSMC C_D comparisons for parallelepipeds (on the left) and cylinders (on the right).

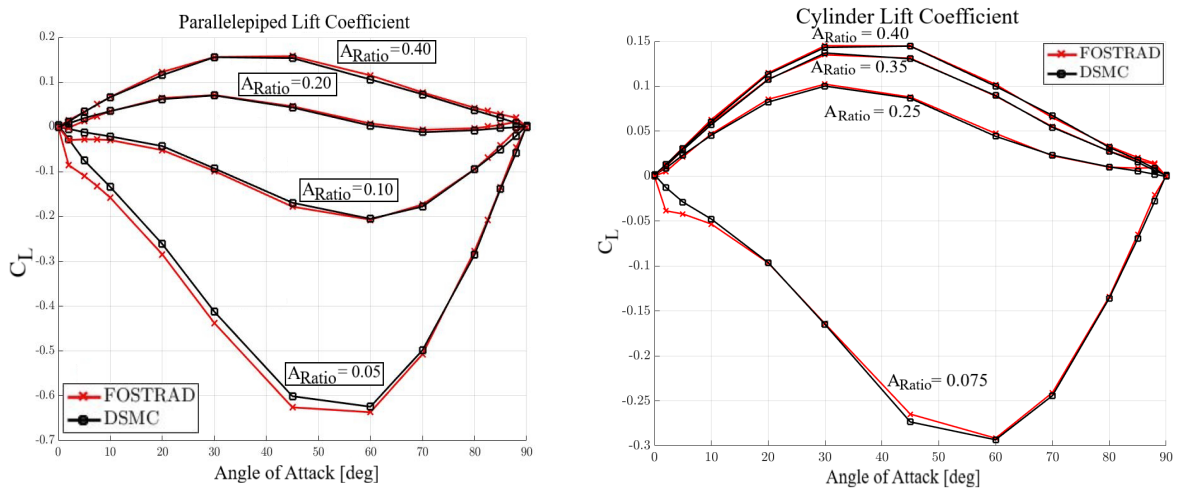


Figure 3.23: FOSTRAD-DSMC C_L comparisons for parallelepipeds (on the left) and cylinders (on the right). No correction has been applied to the C_L .

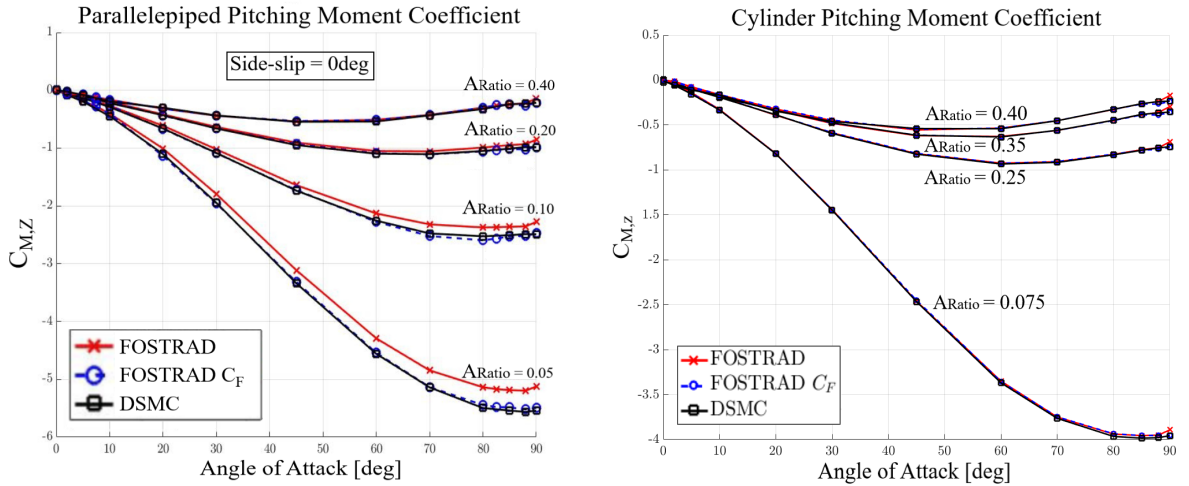


Figure 3.24: FOSTRAD-DSMC $C_{M,z}$ comparisons for parallelepipeds (on the left) and cylinders (on the right). The same drag C_F has been applied to the moments, the corrected models show a very accurate agreement.

rotation (CofR) chosen to be at the center of the backward face for each parametrized case; $CofR = [X_{b,f} \ 0 \ 0]$, where $X_{b,f}$ is the x position for the backward face. The C_L analyses have shown that FOSTRAD slightly overestimates the lift when the geometries are at a low angle of attack (Figure 3.23). By observing the results, and considering the mathematical challenges for defining a C_L when the coefficients are very low ($C_L \rightarrow 0$), it was decided not to apply any correction to the lift. A different approach could be proposed by observing the trend for the two geometries: running two FOSTRAD simulations at $\alpha = 0deg$ and $\alpha = 10deg$ and linearly interpolating between the obtained C_L values. This would make the computation of the lift slightly more accurate, but also twice as expensive, therefore this approach would be usable only when an accurate C_L is required; in addition, this approach would definitely be case dependent.

Taking into consideration the moments shown in Figure 3.24, it is possible to observe that FOSTRAD estimates the cylinder $C_{M,z}$ very accurately. Although, analyzing the moments for parallelepipeds it is evident that they show the same underestimation highlighted for the drag. Applying the drag C_F the underestimation and the average error is greatly reduced.

3.3.3 GOCE Drag Coefficient test case

The study on GOCE has been deemed as a good benchmark for testing the cylindrical C_F . In fact, the complex and elongated shape of GOCE (Figure 3.25), makes it an interesting case for testing FOSTRAD's panel method application. Previously per-

formed analyses had shown a considerable discrepancy between the C_D computed via FOSTRAD and DSMC [Benedetti et al., 2018], therefore, testing C_F application would provide useful information to understand whether or not is it possible to apply the corrective factors to similar shapes and geometries. Indeed, GOCE's main body could be easily simplified with a cylindrical body with two big fins.

In order to test the accuracy of the cylindrical C_F , a previously defined C_D DSMC SM [Falchi et al., 2018] has been compared to a Monte Carlo sampling performed via FOSTRAD with and without the correction. The C_D DSMC SM was defined for a broad range sensitivity analyses of GOCE aerodynamics in the FM regime considering 5 different parameters within the respective ranges: $S_R = [8; 12]$, $T_{ratio} = [0.01; 1.5]K$, $\sigma_{diff} = [0.5; 1.0]$, $\alpha = [-5; 5]deg$ and N_2 atomic density (which as long as the flow is in a FM regime resulted negligible). Using uniform distributions and the same 4500 samples for both DSMC and FOSTRAD, the results of the Monte Carlo sampling is shown in Figure 3.25 on the right. Observing the figure it is possible to notice that the cylindric C_F application greatly improves FOSTRAD accuracy. It must be reminded that the side-slip angle interval used for the sampling is very challenging for local panel inclination methods. Even though the corrected C_D distributions still present a lower tail, the average C_D has been greatly improved. In fact, FOSTRAD without correction underestimates the C_D of a $\sim 18\%$, whereas the corrected values show just a minor discrepancy.

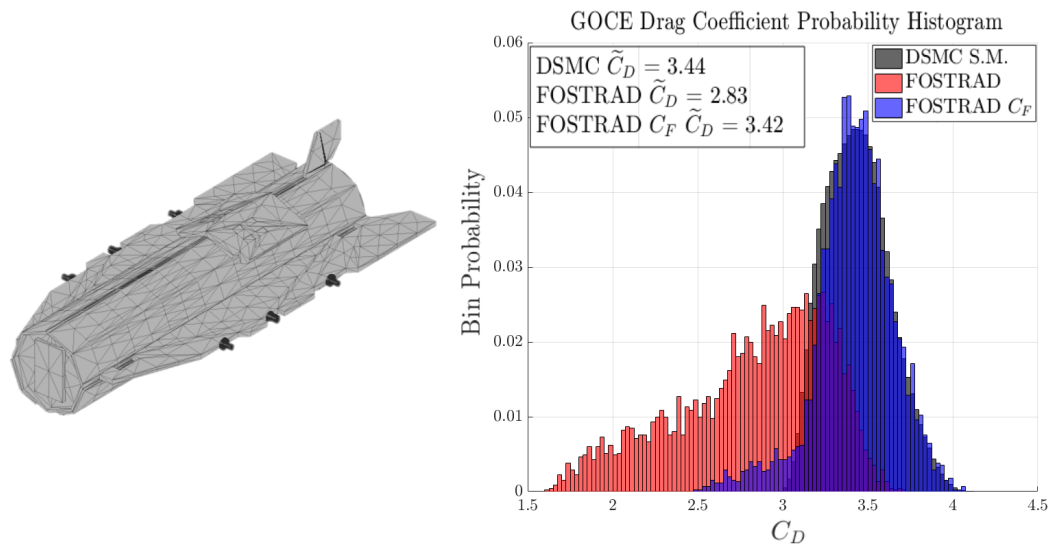


Figure 3.25: On the left: GOCE triangulated mesh used for FOSTRAD simulations. On the right: Monte Carlo probability distribution (4500samples) of a DSMC predefined SM and FOSTRAD with and without C_F

Aerothermodynamics Computation Methodology

4.1 General description

The aerothermodynamic block allows the computation of the heat transfer during the entire re-entry phase, from the free molecular regime using the Schaaf and Chambre flat plate theory [Schaaf, 1953], to the continuum regime, where different correlation and simplified models can be applied (as explained in the introduction chapter: Fay-Riddell, Kemp-Rose-Detra, Van Driest or Detra-Hidalgo models). In the transitional regime the heat transfer is commonly computed with knudsen number-dependent bridging functions, which provide a smooth transition between the two asymptotic values at the continuum and free molecular regime. Commonly, low-fidelity tools for atmospheric re-entries estimate the heat-flux at the stagnation point using a reference nose radius, which is then used to compute the heat transfer distribution with a local panel inclination correlation. In this work, instead of using a constant nose radius (CNR) for every panel, a local radius-based method has been evaluated and tested. Each panel has a radius based on the geometrical local curvature, as the initially proposed by Kemp [Kemp, 1956, Kemp et al., 1959], and similarly to what was previously proposed by [Annaloro et al., 2014]. A major difference from the past research was the introduction of a flexible smoothing method of the geometric local radius in order to allow for a smooth transition from flat surfaces to curved ones.

This approach allows a detailed resolution of the heat flux distribution, keeping the stagnation point heat transfer the same. Although, a more complex elaboration of the geometry and the mesh is required. The aerothermodynamics block work-flow description has been reported in Figure 4.1. The work-flow is very similar to the aerodynamic block, although in this case, when the simulated altitude is within the rarefied transitional regime, the bridging functions are computed using pre-defined surrogate models (SM) which depend on: R_N , Kn of the simulated scenario. The final value of the heat transfer in the transitional regime also depends on the asymptotic values of $C_{H, fm}$ and

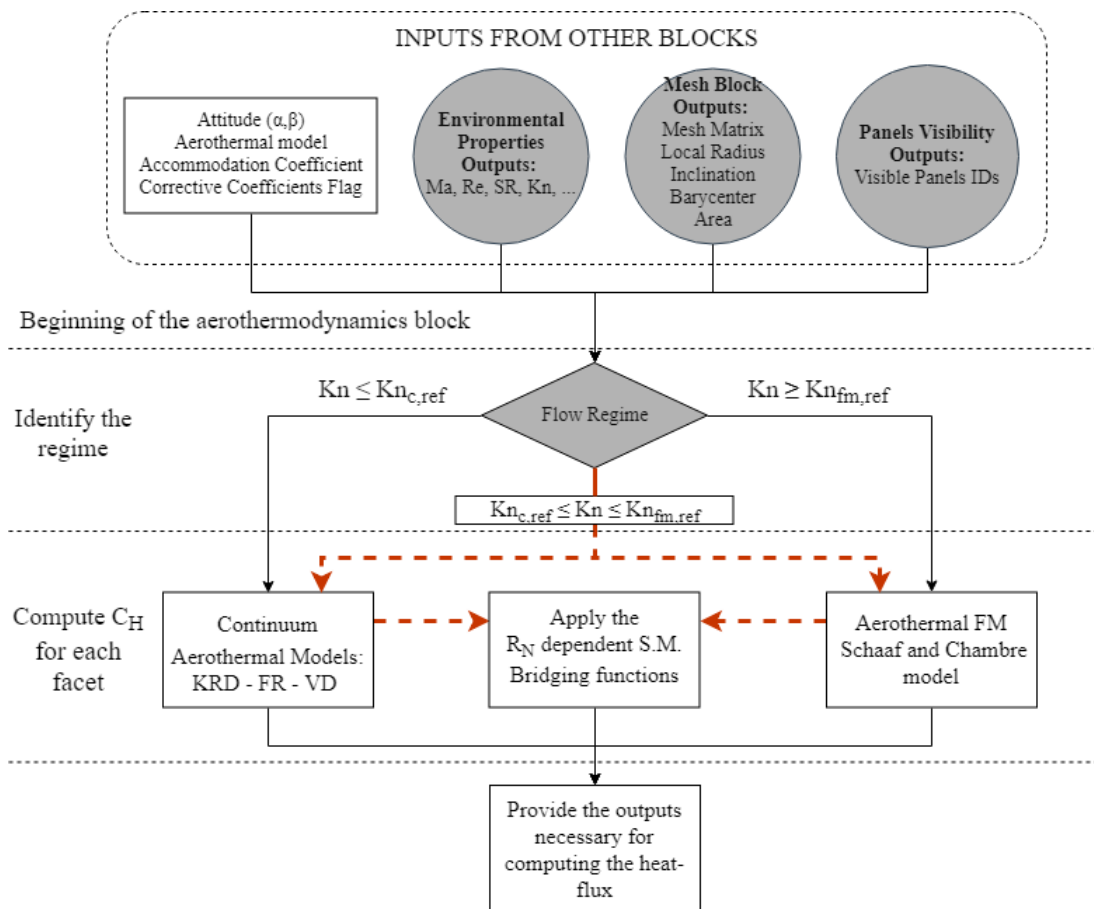


Figure 4.1: Aerothermodynamics block work-flow description

$C_{H,c}$. Since R_N , $C_{H,fm}$ and $C_{H,c}$ change for each facet, the SMs must be applied to each facet individually. A thorough explanation of the proposed bridging function SMs is provided in the following chapter.

As already highlighted in the local radius algorithm paragraph, the mesh quality will have a great impact on the computation of the local radius and on the heat-flux distribution. In fact, a sufficiently high number of panels is required to allow a good quality local nose radius (LNR) computation and its smoothing process. An example is shown in Figure 4.2, where the meshes of two different resolutions have been compared.

The mesh resolution will greatly affect the heat flux distribution in the continuum regime, and influence the lower transitional regime. The different parameters of the local radius computation algorithm can be calibrated to obtain a characteristic representation of the heat-flux distribution. In order to provide a qualitative comparison of a constant nose radius and a local nose radius approach, an atmospheric re-entry of the 0.5m

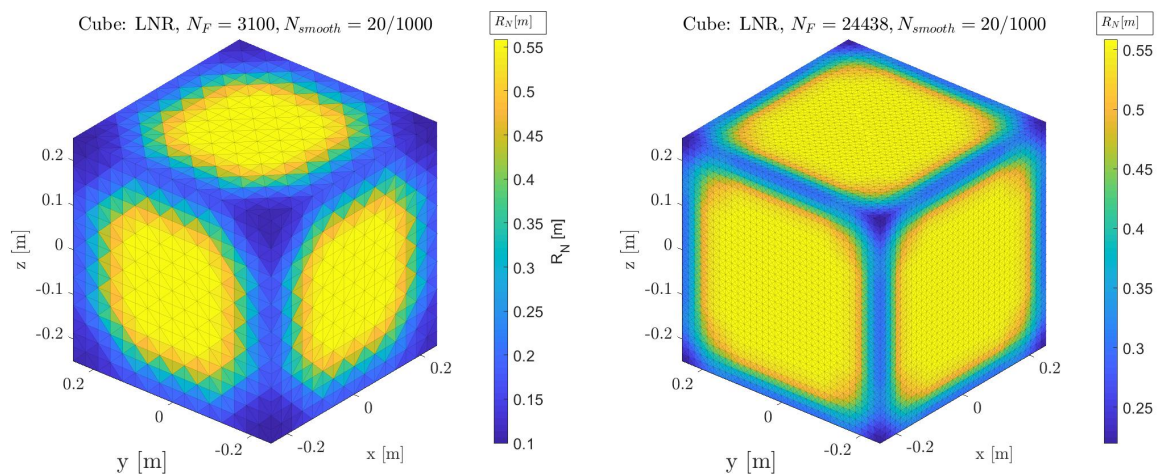


Figure 4.2: Local nose radius quality depending on the mesh resolution, left: 3100 faces, right: 24000 faces

cube was simulated with STRATH-A. The results are reported in Fig. 4.3, the results obtained with the LNR provide a better qualitative heat flux distribution, as it is observable by visual comparison with Figure 2.14 on page 102.

An extensive testing campaign of cubes, cylinders and spheres was performed by Mehta et al. [Mehta et al., 2015c], with the aim of developing an analytical model to determine the heat transfer distribution over flat surfaces. The same approach was then used in [Ostrom and Abercromby, 2017]. An analytical approach would provide better results when the testing condition are exactly the same, but changing the conditions (i.e.: angle of attack, side-slip, altitude, and rarefaction regime) would require a different calibration. The LNR approach would instead allow a general applicability to any simple or complex geometry. In fact, in transitional regime, the heat flux distribution is automatically adjusted by the bridging functions, moving from a radius-inclination-based distribution in the continuum regime, to a inclination-based only distribution in the free molecular regime. An example of the heat flux variation on the diagonal of the frontal flat face of the cube at different altitude is provided in Figure 4.4. Using different parameters for the local radius smoothing algorithm, may increase or decrease the heat-flux at the corners. The use of such approach requires an extensive testing and validation to allow a confident use of the method. During this research work, different simple and complex geometries have been tested, although, due to the high number of involved variables, it is difficult to find experimental or high fidelity comparative test cases.

Although the use of the LNR is automatically extended in the transitional regime by the work flow of the software, its application was thought for the continuum regime, as

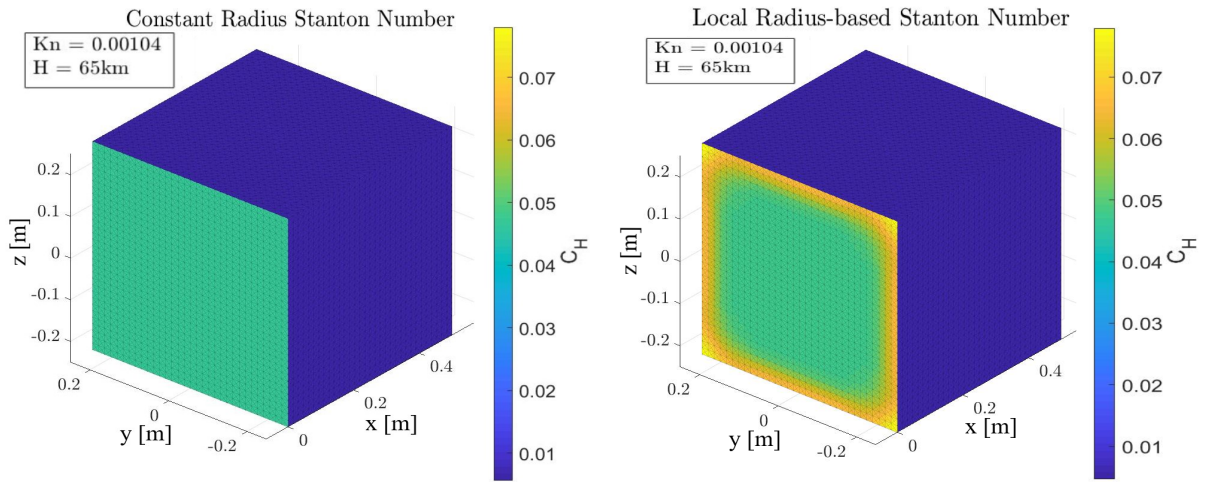


Figure 4.3: Qualitative comparison of the atmospheric re-entry of a cube with the classical approach and the local nose radius approach.

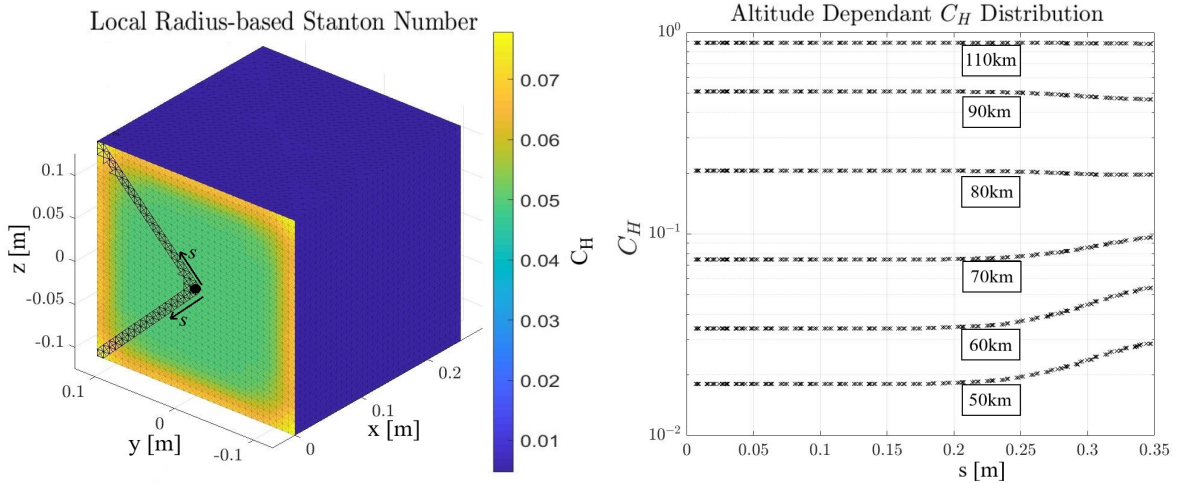


Figure 4.4: Left: C_H mapping of a cube for a head-on flow at 60km showing the diagonal sampling points. Right: Heat transfer distribution on the diagonal for different altitudes. The centre of the front face is taken as the origin, and the panels with a black edge are the ones reported on the right.

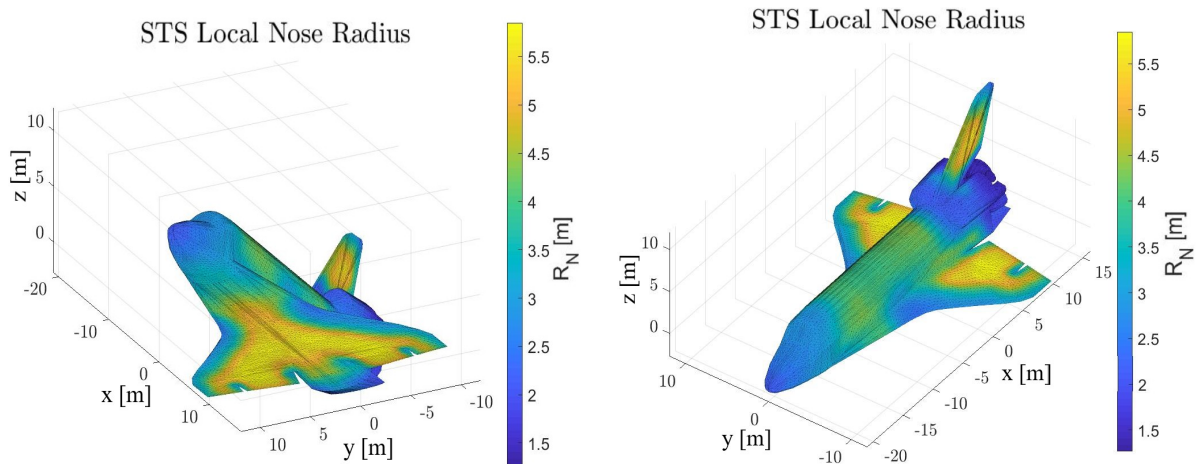


Figure 4.5: Shuttle local radius distribution. The flat faces are assigned a reference hydraulic radius for the equivalent cross-section.

it has been described in the Local nose radius paragraph (Figure 2.15). The use of the LNR approach would allow the accurate heat-flux representation of complex geometries with wide variation of the geometric features. Taking for example the Space Shuttle Orbiter geometry, the curvature distribution and the magnitude greatly change across the surface, as shown in Fig. 4.5. An example simulation to show the difference between the typical use of a reference nose radius on a Fay-Riddell model and a local nose radius has been performed for the STS Orbiter, using a 40deg angle of attack and the typical reference velocity [Rault, 1994]. The resulting heat-flux distribution at 80km is shown in Figure 4.6. For this case, the reference nose radius was $R_{N,ref} = 5.9\text{m}$, and it was used for both: the CNR case and the flat-faces reference radius. By Observing Fig. 4.6, some differences may be highlighted:

- The LNR approach automatically detects the geometric features which will be exposed to a higher heat-flux
- The heat transfer computed with the LNR on the "flat-faces" will have the same heat transfer of a CNR approach
- The reference nose radius chosen for the CNR approach has a high influence on the most critical areas (i.e.: the nose), whereas with the LNR approach it can be chosen as a scale reference length (which is used just for the identified flat-faces)
- The LNR allows to compute a more "realistic" heat flux distribution, which is not only based on the inclination angle.

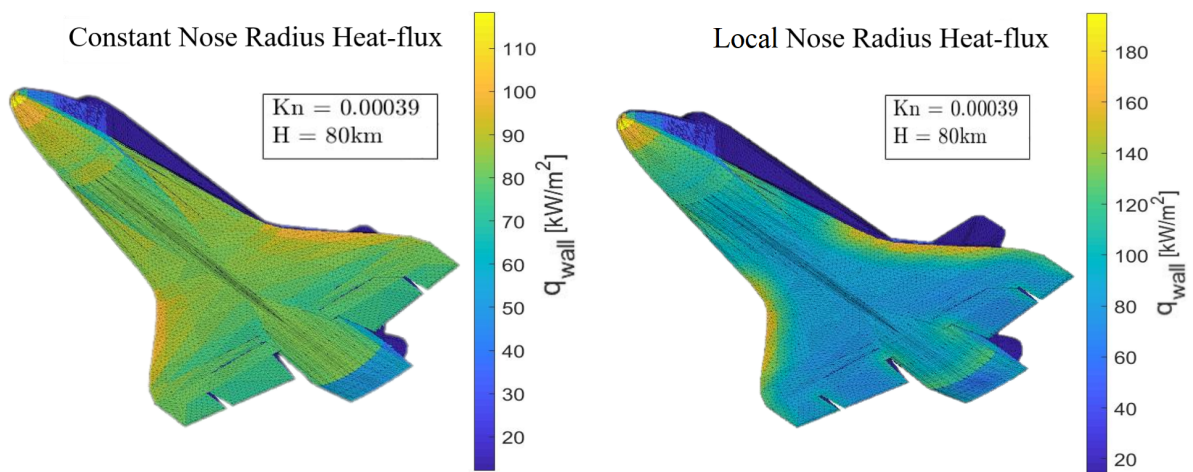


Figure 4.6: Comparison of the heat flux distribution for a reference nose radius (on the left), and the local nose radius Fay-Riddell heat-flux estimation for the STS Orbiter. The two different colorbar scales highlight the differences due to the local radius approach.

Although the previous analysis have shown just a brief overview of the local nose radius application, the local radius computation algorithm has the flexibility of being adapted on different types of geometries using the smoothing parameters. Indeed, as it was previously described in the local radius algorithm paragraph, the choice of a higher or lower number of smoothing facets, or a different "flat-face" detection limit, could modify the local radius distribution on the geometry thus modifying also the heat-flux distribution. The use of a local radius approach should be considered not only as a more precise use for the local panel inclination methods, but also as a possible application to estimate the heat-flux on sharp-edged corners and their proximity. In the following paragraphs, the Knudsen and local-radius bridging functions, along with a set of atmospheric re-entry validations will be presented.

4.2 Aerothermodynamics Bridging functions

The introduction of the local radius formulation for the aerothermodynamics module leads to the need to the introduction of the rarefied transitional regime local radius-based heat-flux computation. Indeed, the local radius formulation implies that in the continuum regime, beside the atmospheric properties, the heat-flux is going to be computed as a function of the i -th facet radius and inclination. In the free molecular regime the heat-flux is radius-independent, implying that the transitional bridging model had to shift from a radius/inclination-based model in the near-continuum regime to a inclination-based model in the near-free-molecular regime.

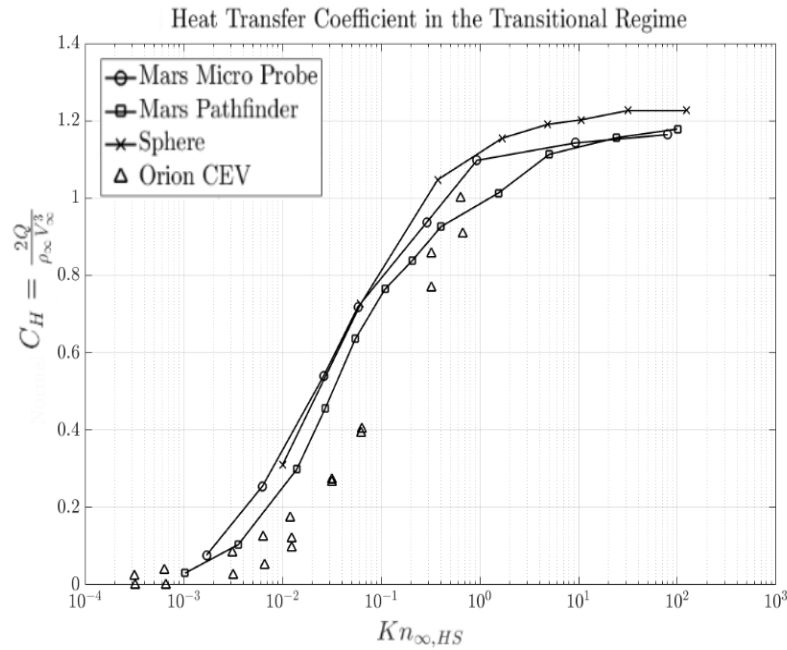


Figure 4.7: Heat transfer coefficients for different re-entry scenarios and objects characterized by a different nose radius; Mars Pathfinder [Milos et al., 1999], Mars Microprobe [Mitcheltree et al., 1999], 1.6m diameter sphere [Dogra et al., 1992], and Orion CEV [Mehta et al., 2015b].

By comparing the data of different re-entry heating analyses for geometries with a different effective nose radius, it is evident that using the same bridging function for different nose radius would not bring to accurate results, as it is highlighted for the Mars Pathfinder [Milos et al., 1999], Mars Microprobe [Mitcheltree et al., 1999], a 1.6m diameter sphere simulated by Dogra [Dogra et al., 1992] (which were extended with a set of in-house performed DSMC analyses), and the Orion Crew Exploration Vehicle [Mehta et al., 2015b] shown in fig. 4.7. In addition, considering the continuum and free molecular transitional regime boundaries to be respectively $Kn_c = 0.001$ and $Kn_{fm} = 100$, the heat transfer coefficient derivative over Kn is different for different effective nose radii; therefore, using an averaged bridging function would cause discontinuities at the two transitional regimes boundaries. Considering only the reference data falling within the transitional regime, and creating the bridging models the differences are more evident (fig. 4.8).

Due to the previous consideration, a more accurate bridging model as a function of Kn and the effective nose radius has been proposed. The model has been created using a recursive 1-D Piecewise Cubic Hermite Interpolation on referenced data, and it

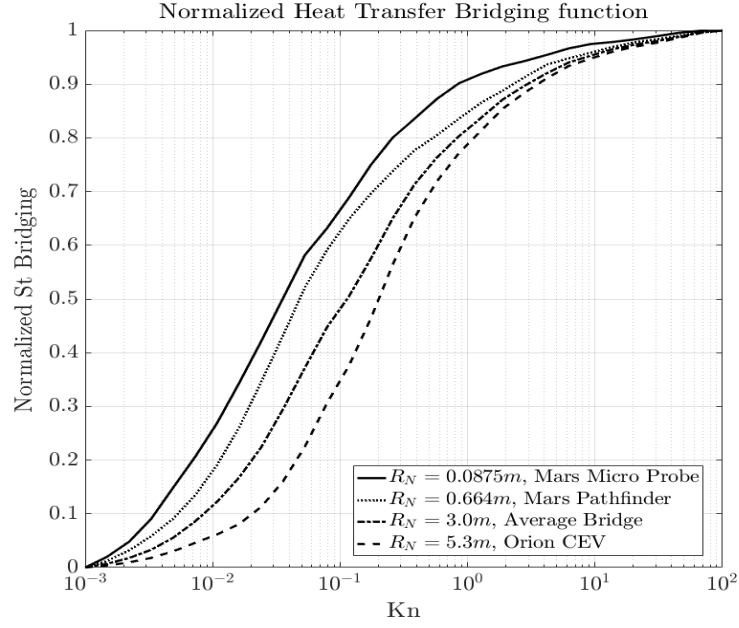


Figure 4.8: Normalized bridging functions for different space objects and scenarios, characterizing the geometries with different nose radius. Based on the normalization of data reported in Figure 4.7

is shown in Fig 4.9. The bridging model is applied as it follows:

$$St_{i,t} = St_{i,c} + \mathbb{B}(R_{N,i}, Kn) \cdot (St_{i,fm} - St_{i,c}) \quad (4.122)$$

Where St is the Stanton number, i refers to the i -th considered facet, the subscripts c , t , fm refer to the continuum, transitional, and free molecular regime respectively, \mathbb{B} is the developed bridging model, and R_N is the local nose radius.

The newly introduced bridging model formulation, allows STRATH-A to operate using the multi-threaded computation on all the facets and given trajectory parameters. Once the mesh has been initialized (depending on the required resolution the initialization usually requires from 2 and 10 seconds), and for a constant space object attitude, it usually takes less than 1 second to compute the the aerodynamics and aerothermodynamics, including the heat-flux surface distribution for each and every trajectory point given as input, on a machine operating with an Intel[®] Core[™] i7-4790 CPU 3.60GHz x8.

An example of the application of this bridging model has been shown in Figure 4.4, on the right, the values of the transitional regime are influenced by the Knudsen-radius-based bridging function. Indeed, the object has a characteristic altitude for

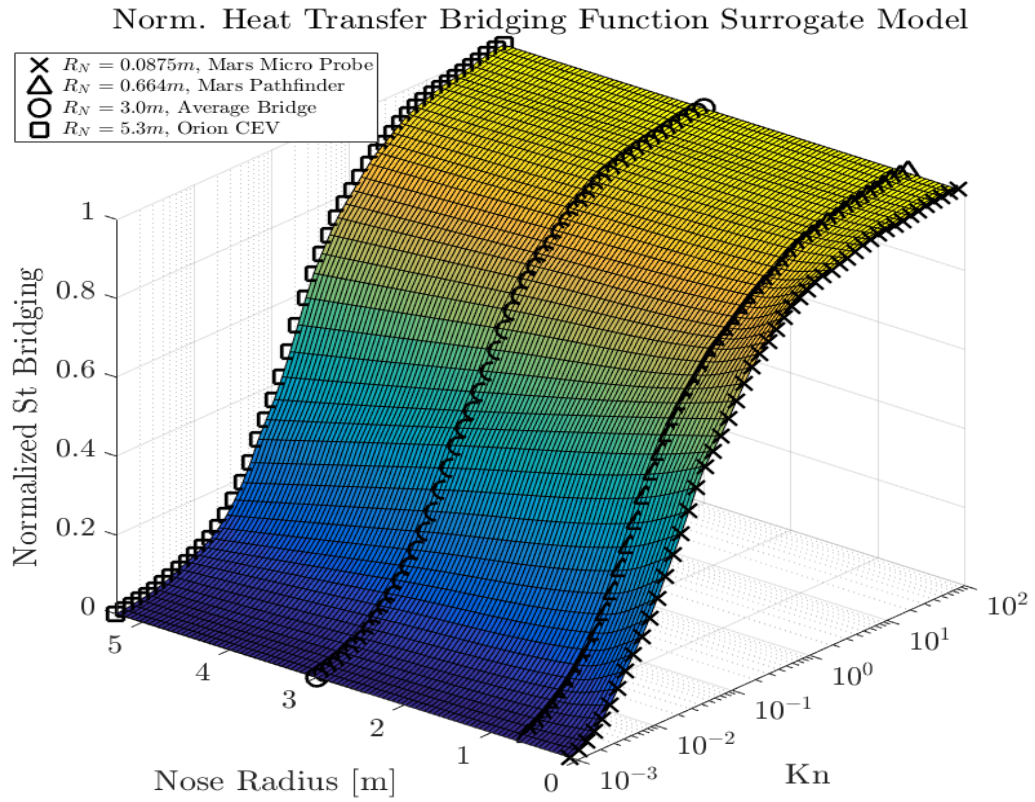


Figure 4.9: Transitional regime normalized bridging model as a function of the local radius and Knudsen number.

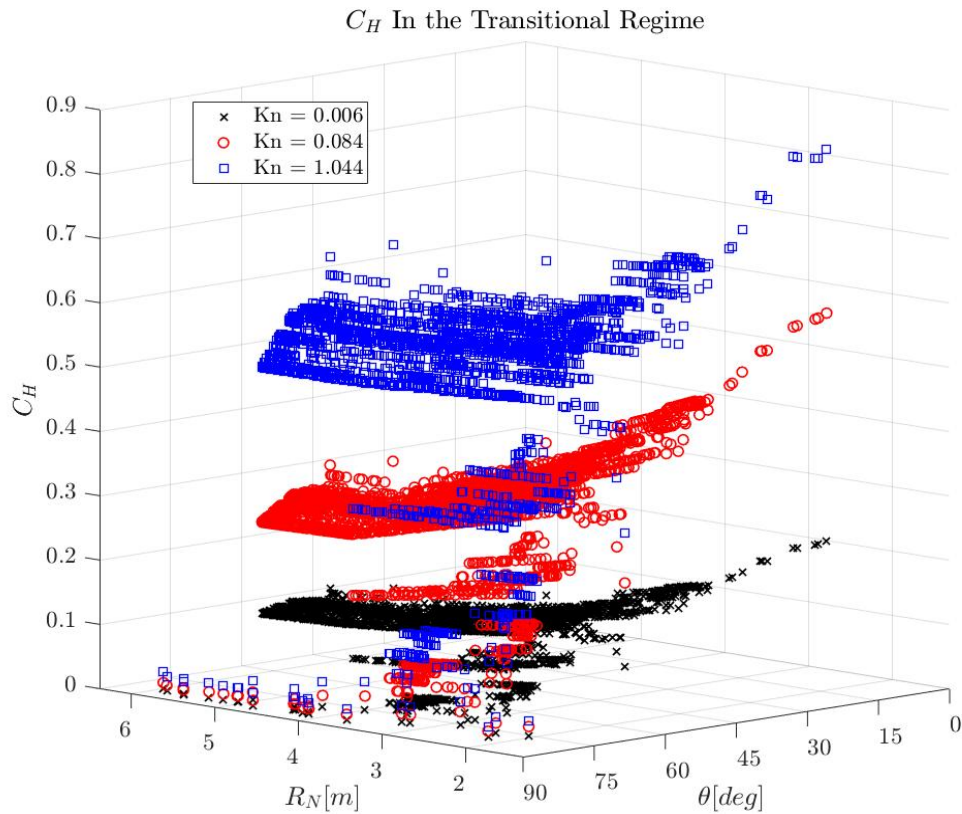


Figure 4.10: Transitional regime normalized variation of the C_H w.r.t. to the local panel radius and inclination angle. Data extracted from the STS-orbiter validation case, reported in page 174.

each reference Knudsen number, therefore, the only parameter influencing the Stanton number of a facet within the transitional regime is its reference value of the continuum regime and the relative bridging function value. Another example of the qualitative variation of the C_H due to the local radius on the simulation of the STS Orbiter for with respect to the panel inclination angle is shown in Figure 4.10. The analysis shows the increment of the C_H due to the decreasing radius for at a constant Kn and θ . With a classical constant reference radius approach, such a variation would not be possible.

4.3 Aero-thermodynamics Module Validations

The application of the local nose Radius approach requires a validation which ranges from the continuum to the free molecular flow. Due to the nature of the software, which has been designed and programmed for performing atmospheric re-entry analyses, the validation requires very specific test cases, and often the commonly used laboratory experimental test case cannot be easily reproduced without altering the work flow of the software. Therefore in this paragraph, it has been possible to analyze only few re-entry comparative test cases, such as the Space Shuttle Orbiter [Moss and Bird, 2003], the hypersonic re-entry of the Stardust sample return capsule (SRC) [Trumble et al., 2010, Olynick et al., 1999], and the blunted 5deg cone [Moss and Simmonds, 1987], some additional analyses were performed on the Intermediate Experimental Vehicle comparing the data with the analysis by [Roncioni et al., 2011]. An initial set of validations and analyses was performed in order to understand which parameters range could be used to apply the local radius smoothing, indeed recalling the local radius smoothing algorithm parameters:

- Number of closest panels to average (N_{smooth})
- Flat faces ratio limit (*Flat-Edge*)
- Weighted smoothing type (linear or sigmoid)

Summarizing briefly what has been thoroughly described in the local radius algorithm paragraph: N_{smooth} is the number of closest panels that are taken for the smoothing process. The *Flat-Edge* is the limit ratio among the closest N_{smooth} panels. If the ratio between flat-to-non-flat panels is above that limit, the flat panels are assigned a weighted reference "flat-radius", dependent on the average cross section of the geometry (representative of the geometric scale). The weight assigned to the flat faces is dependent on the flat-no-non-flat panels and the weighting type and may range from 0 to 1. A thorough description of the following preliminary validation cases may be found in [Falchi et al., 2017c].

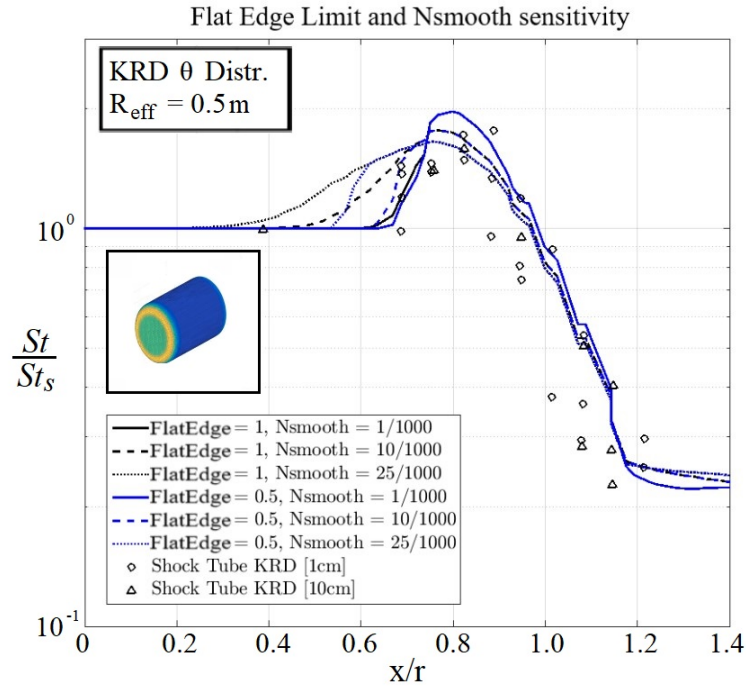


Figure 4.11: STRATH-A relative heat-flux distribution computed with the smoothed-local radius formulation, compared to the experimental data reported in [Kemp et al., 1959].

4.3.1 Preliminary Smoothing Algorithm Validation Cases

In Figure 4.11, the comparison between the experimental data used by Kemp et al [Kemp et al., 1959] and the analysis performed with STRATH-A employing the smoothed-local-radius formulation is shown. The comparison previously shown in Figure 2.15 makes evident that the local radius formulation provides an accuracy far better than the constant nose radius approach, especially at the rounded corner. In Figure 4.11, it is also reported the influence of the various setup parameters, i.e.: N_{smooth} , and the Flat Edge (identified as FF). The result shows that, for a geometry without sharp edges, a possible setup configuration would be using $N_{\text{smooth}} = 10/1000$ and a Flat Edge = 0.8 (identified as FF in the figure). The use of a low flat edge will make the variation between different radius areas sharper and will result in a higher local heat transfer.

In order to provide a quantitative comparison between the CNR and LNR, the experimental test cases reported in [Kemp et al., 1959] have been considered. The rounded cylinder has been simulated with both methods, and the relative error wrt to the experimental data has been reported in Figure 4.12 (on the left). The LNR approach was computed using a Flat Edge ratio = 0.5, and $N_{\text{smooth}} = 10/1000$. In order

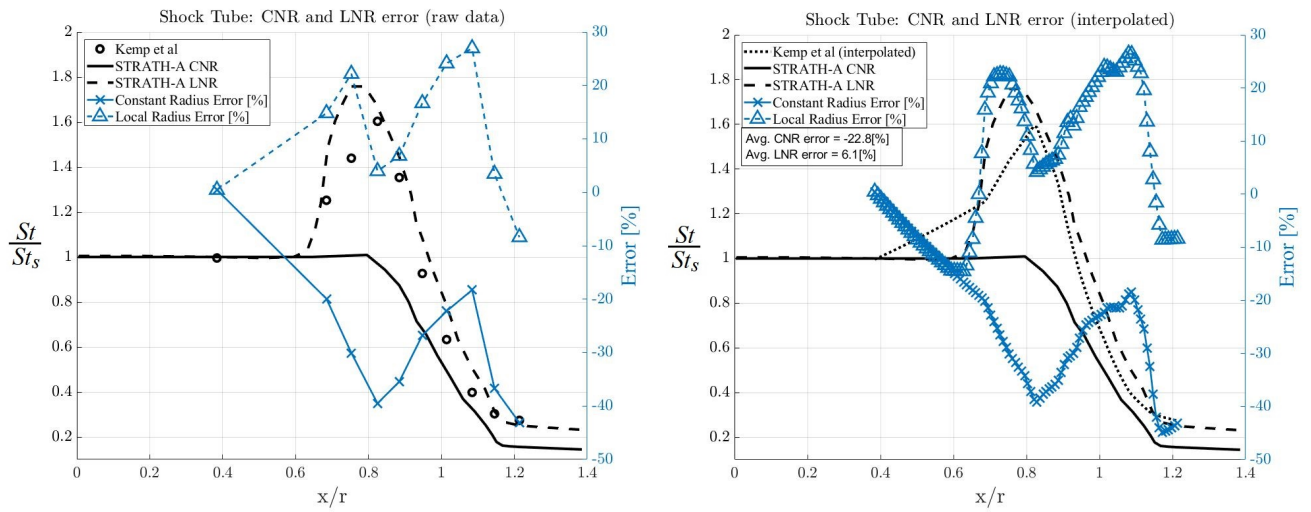


Figure 4.12: STRATH-A relative heat-flux distribution comparison of CNR and LNR approach. On the left: the comparison of the relative error on the raw experimental data [Kemp et al., 1959]. On the right: comparative analysis of interpolated data aiming at evaluating an averaged relative error for the CNR and LNR.

to quantify an average relative error, the experimental points have been interpolated and averaged over the surface starting from $x/r = 0.4$ up to $x/r = 1.2$. The results are reported in Figure 4.12 (on the right): the CNR shows an average error of -22.8%, while the LNR reduces the average error to 6.1%. It is interesting to notice that the CNR approach shows a general underestimation wrt to the LNR. In fact, this is due to the reference nose radius which is generally conservative for neglecting the local heating in the edges of an object.

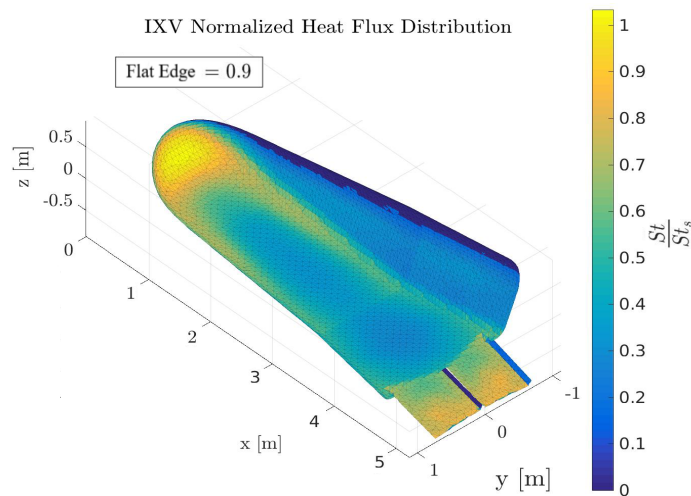


Figure 4.13: STRATH-A relative heat-flux distribution: hypersonic continuum regime with local radius formulation.

IXV Heat-Flux distribution

Another interesting case which allows to make some observation is the comparative analysis based on IXV geometry. In Figures 4.13 and 4.15, a preliminary calibration of STRATH-A local radius formulation setup on the IXV geometry is reported. The relative heat-flux distribution of CFD data provided by Roncioni [Roncioni et al., 2011] et al. is compared to different N_{smooth} values. It is shown that for a complex geometry with sharp corners, a higher number of smoothing point should be used (the best fit is shown using 30 smoothing points per 1000 facets), the analysis has shown that the optimal flat-edge was between 0.75 and 0.9. The comparison shows also the underestimation of the relative heat-flux on the flaps. This could be due to very high heat-flux on the flaps due to the shock impingement and a different flap inclination angle on the simulated geometry. During this work, it has not been possible to estimate the influence of different flap inclination angles on the heat flux distribution estimated with STRATH-A or the DSMC, therefore the heat-flux estimation on the flaps should not be considered. Additionally, in the quest of finding alternative methods for calibrating the local radius smoothing algorithm, a very low-fidelity DSMC simulation was run at the same CFD conditions simulated by Roncioni, using a mesh with the same number of cells (i.e.: 2 millions cells). Surprisingly, the relative heat-flux distribution computed by the dsmcFoam code is very close to the CFD one, except on the flaps, as the DSMC could not be able to properly resolve the shocks impingement and interactions. The advantage of using a low-fidelity DSMC simulation to calibrate the smoothing algo-

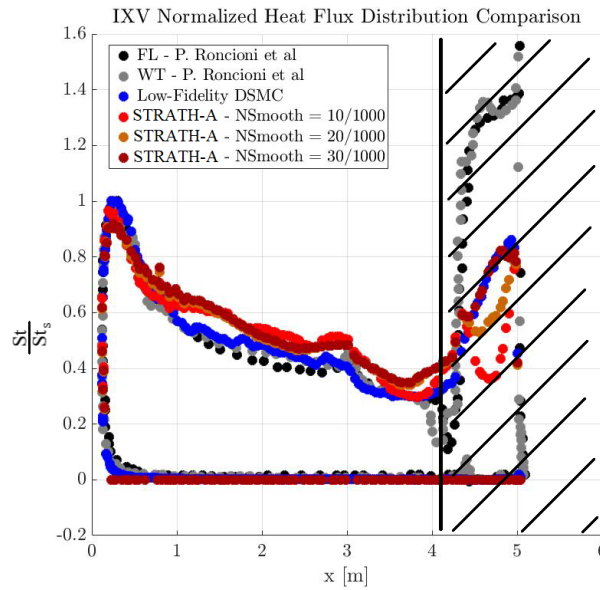


Figure 4.14: Relative heat transfer coefficient distribution comparison of CFD, DSMC and STRATH-A data on the IXV model. Sensitivity analysis on the number of local radius smoothing points.

rithm would be that a DSMC simulation requires a systematic setup, and additionally, STRATH-A had already been coupled with the `dsmcFoam` code via an automated simulation interface [Falchi et al., 2017a], which could lead to an automated calibration process for any geometry. Even by using a coarse mesh for the DSMC simulation it would still require the use of a High Performance Computer. Even though the comparison shows some differences, the local radius approach allows a good quality estimation of the heat transfer distribution. Indeed, if we were to simulate the same case with a constant radius approach, the results would be far worse, as it is shown in Figure 4.15. With a constant radius approach the heat transfer overestimation on the entire fore-body would be significant, ranging from 25% to 40% more.

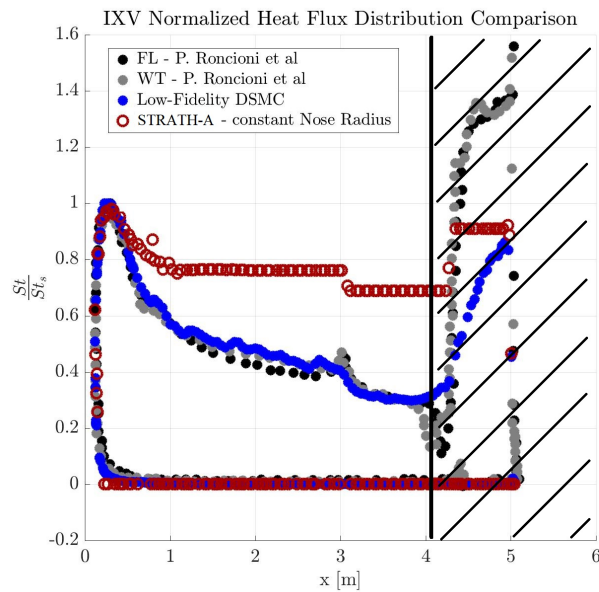


Figure 4.15: Relative heat transfer coefficient distribution simulated with a classical constant radius approach.

4.3.2 Space Shuttle Orbiter

In this paragraph the aerothermodynamics simulations of the Space Shuttle Orbiter are presented and compared with the DSMC simulation performed by Moss [Moss and Bird, 2003]. The comparisons contains also some flight data measurements. The simulation conditions used are: a reference fixed velocity of 7500m/s, a fully accommodated diffusive coefficient, a wall temperature ranging from 300K to 1043K (at the lowest altitude), and an angle of attack of 40deg. The simulation with STRATH-A were performed using the Local Nose Radius approach. In Figure 4.16 the heat transfer of the shuttle at a close distance to the nose is reported for two different models: Kemp-Rose-Detra (super catalytic wall) and Van Driest model (non catalytic wall). A good match between the flight data of STS-2 and STS-3 is observed, showing that the best model would be a partial catalytic one. It must be reminded that the flight data, take into account also the heat loss due to the radiation, but in STRATH-A this is not considered. This causes the heat flux measured by the shuttle to decrease as the altitude decreases (the temperature will increase thus increasing the heat-loss), and the same trend cannot be followed by STRATH-A, without implementing the radiation cooling. The heat flux distribution over the shuttle surface at the lowest simulated altitude (80km), is reported in Figure 4.17.

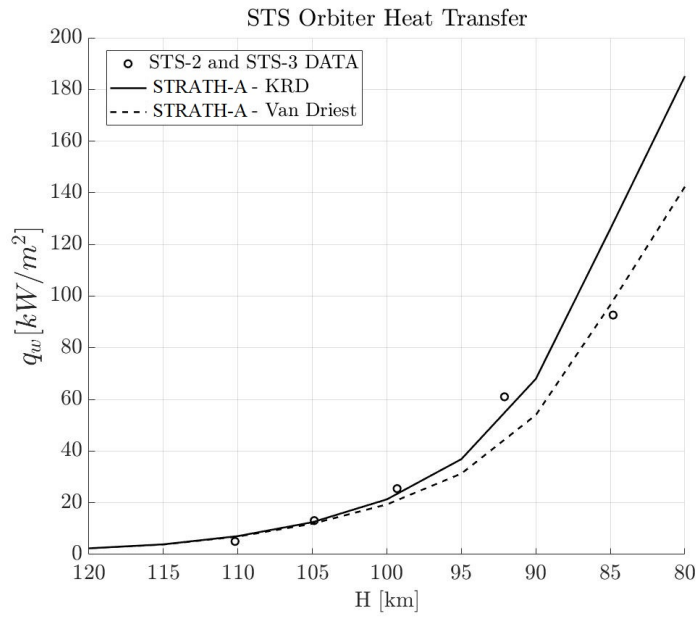


Figure 4.16: Shuttle Heat Transfer comparison of flight data with STRATH-A using different models.

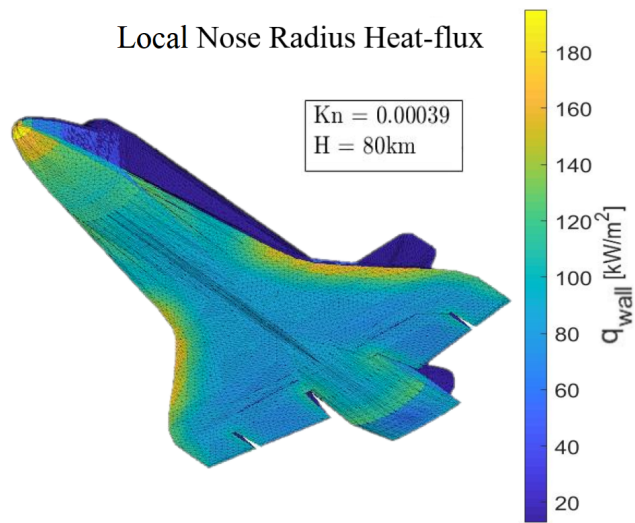


Figure 4.17: Shuttle heat transfer distribution over the surface at 80km computed with STRATH-A using the KRD model and the LNR approach.

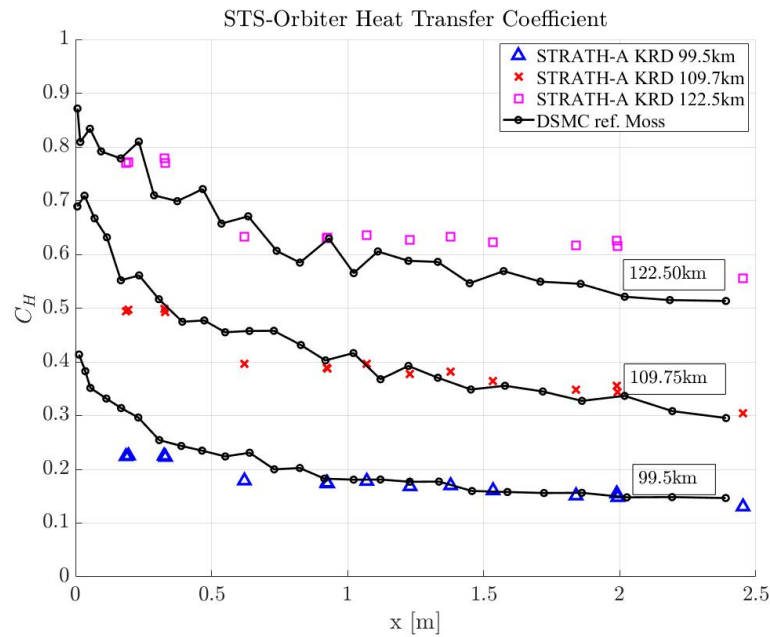


Figure 4.18: Shuttle heat transfer distribution at different altitude on the centerline. The simulations have been performed using STRATH-A with a KRD aerothermal model and Local Radius approach.

Another comparison was made with the DSMC simulation results reported by Moss on the centerline. The results for different altitudes are shown in Figure 4.18, in this case the simulations were performed with a KRD model. The simulations were performed using the following parameters: $N_{\text{panels}} = 10 \times 1440$, $N_{\text{smooth}} = 10$, Flat-Edge = 1.0, AofA = -40deg, $L_{\text{ref}} = 5.9\text{m}$, maximum flat face ref. radius $R_{\text{max,ref}} = 5.9\text{m}$ (equal to the reference nose radius), and the other previously cited parameters. The agreement between STRATH-A and the literature data is very good, although at the highest altitude the simulated results show a slight overestimation.

Observing the nose heat transfer w.r.t. Knudsen number both, DSMC and STRATH-A show an overestimation of the heat transfer (Figure 4.19), this could be due to the use of a fully diffusive model (a mixed specular-diffusive reflective model could be used for the gas-surface-interaction) as reported by Moss.

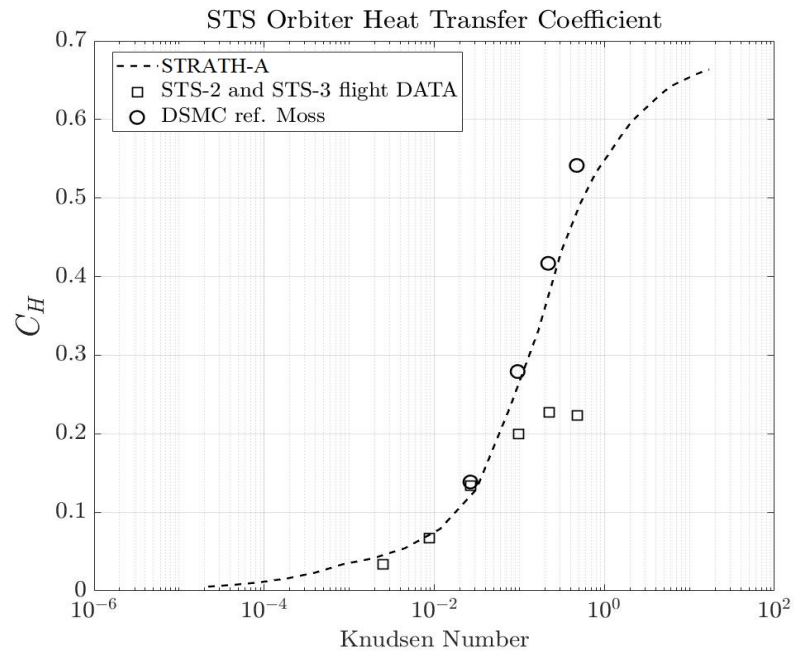


Figure 4.19: Shuttle heat transfer coefficient at the nose for different altitudes.

4.3.3 Stardust Sample Return Capsule

The Stardust Sample Return Capsule (SRC) was a capsule designed to collect dust samples from the coma of a comet, due to its specific space mission design, the capsule nominal atmospheric re-entry trajectory was characterized by a very high velocity (12.8km/s), and a nominal AofA = 0deg (even though the actual re-entry showed a slightly tilted attitude). In this case the validations have been performed to compare the different models implemented in STRATH-A: Van Driest, Kemp-Rose-Detra, Fay-Riddell, and the simplification used within SCARAB:

- Van Driest model can be conservatively used for design for demise re-entry analyses as it represents the lower heat-flux boundary
- SCARAB model shows the highest heat-flux estimation, representative of a super-catalytic wall condition. It can be conservatively used for TPS burn-up estimation
- Kemp Rose Detra and Fay Riddell models fall between the highest and lowest boundaries, and in STRATH-A they are implemented with a fully catalytic wall condition.

The analyses shown in Figure 4.20, do not include the radiative thermal heat-flux. Another interesting result is the comparison between the heat-flux distribution computed with STRATH-A and by Trumble [Trumble et al., 2010]. The results highlight that STRATH-A compares well on the fore-body, even though it shows a significant heat-flux overestimation on the shoulder radius. In addition, the picture shows an x-axis off-set between the two shoulder heating peaks, this is due to a slightly different geometry (Figure 4.22). The offset of the geometric position of the shoulder is roughly the same as the one shown by the peak heat-flux. Therefore, it can be concluded that with the same geometry the heating peaks would have been computed at roughly the same x-axis length.

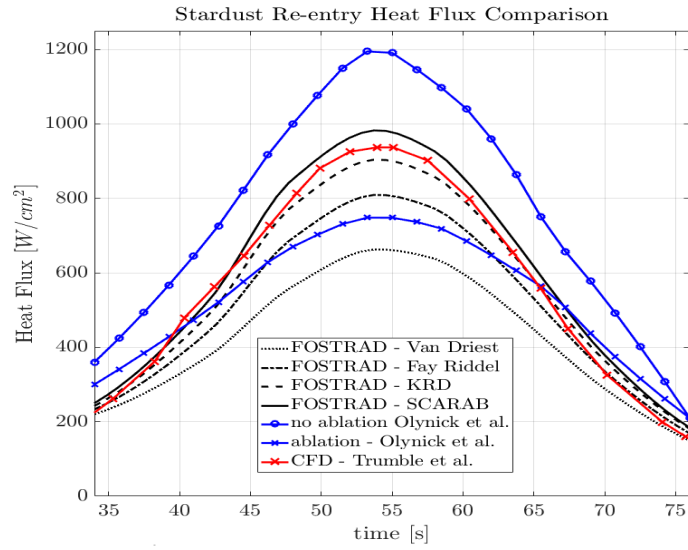


Figure 4.20: Validation of the different aerothermal models tested in FOSTRAD and also implemented STRATH-A.

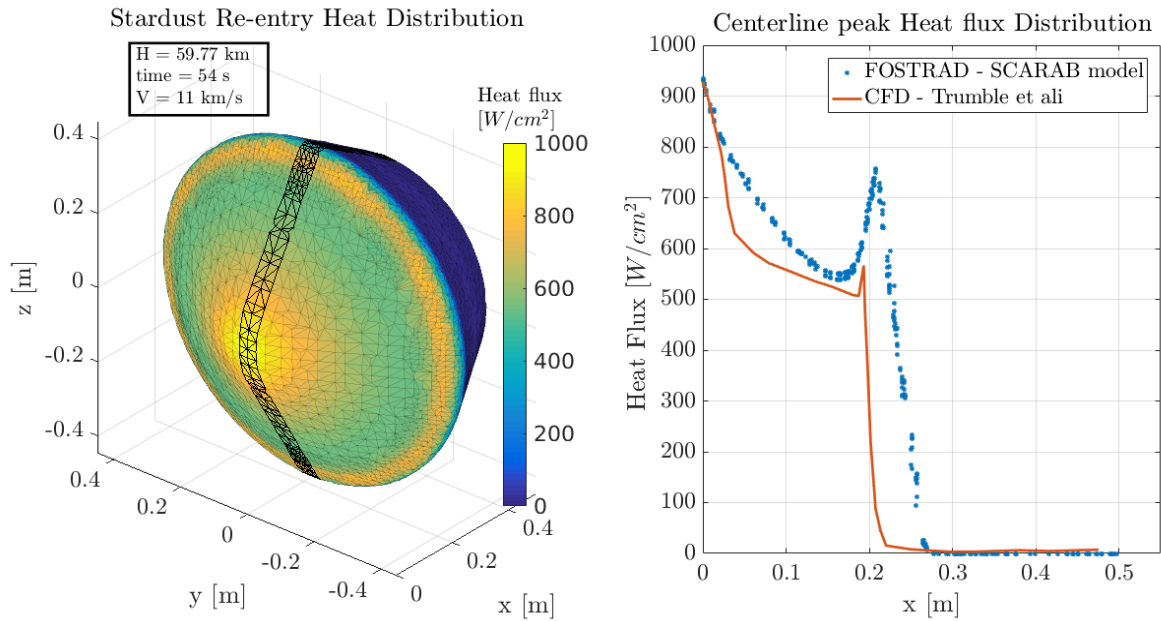


Figure 4.21: Preliminary validation of FOSTRAD heat-flux surface distribution on Stardust SRC geometry [Falchi et al., 2017c].

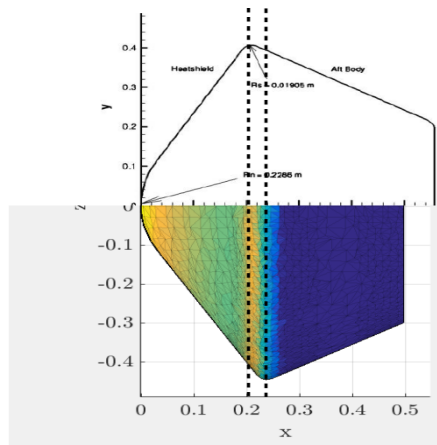


Figure 4.22: Geometrical differences between the Stardust SRC simulated in the present study (bottom) and the one simulated by Trumble [Trumble et al., 2010] on the top.

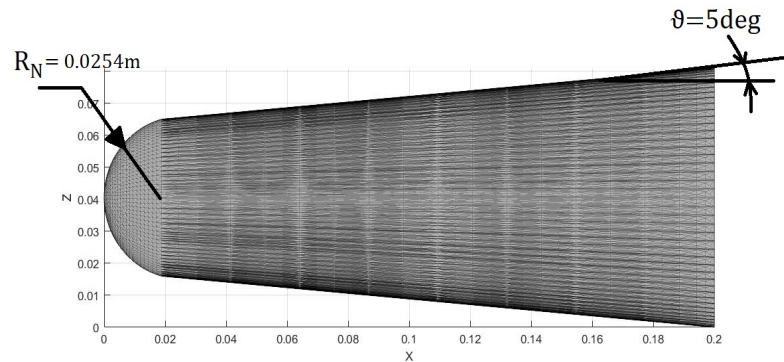


Figure 4.23: Mesh and Geometry used for the blunted cone test case.

4.3.4 Blunted Cone

The blunted cone has been used for many reference tests by Moss [Moss and Simmonds, 1987]. In this test case the 5deg angle blunted cone is taken as a reference. The results have been compared against the DSMC analysis performed by Moss et al. The blunted spherical nose radius is $R_N = 0.0254\text{m}$, the longitudinal length is 0.2m and an the aperture angle is 5deg (Figure 4.23), with an angle of attack $\text{AofA} = 0\text{deg}$. Just as a reference, also the local radius distribution has been reported in Fig 4.24. The testing condition are thoroughly reported in the reference, although the required inputs for the simulation with STRATH-A are the following: $V_\infty = 7.5\text{km/s}$, fully diffusive accommodation coefficient, $T_w = 1000\text{K}$. For this specific case, the nose reference radius is lower than the minimum one used for the calibration of the bridging function, an ad-hoc normalization has been used. The analysis performed with a reference atmospheric database for the heat transfer coefficient w.r.t. Kn have been reported in Figure 4.25. The agreement between DSMC and STRATH-A results is good throughout all regimes. the use of the standard implemented radius-based bridging function would compute a slightly overestimated heat transfer in the lower transitional regime. Although, the absolute error wrt to the literature data is always below 6% throughout all regimes.

The results were compared also regarding the surface C_H distribution along the spherical cap (Figure 4.26). The coordinates are expressed as the curvilinear abscissa (normalized on the nose radius). The results show a good agreement, beside the slight overestimation of STRATH-A for the 70km case, and the sudden drop around $x = 1.3$, which has been caused by a not perfectly tangential mesh at the intersection between the spherical cap and the cone.

The same comparison on the rest of the surface at the altitudes of 80km and 100km

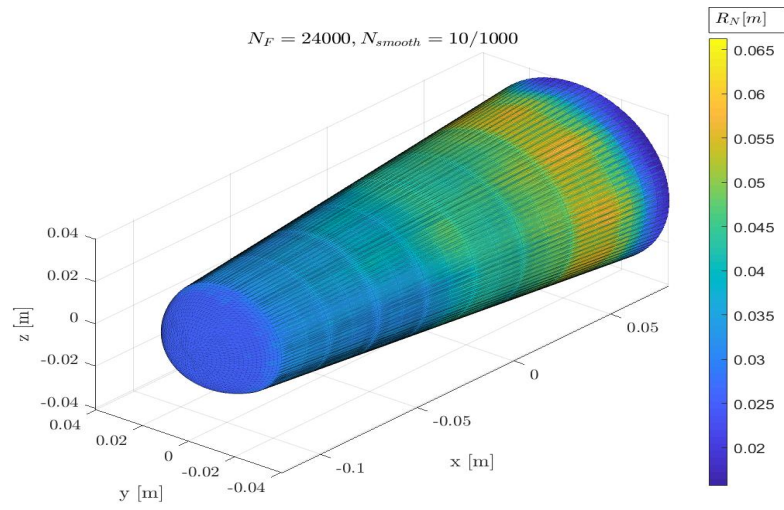


Figure 4.24: Blunted code heat transfer coefficient over Knudsen Number.

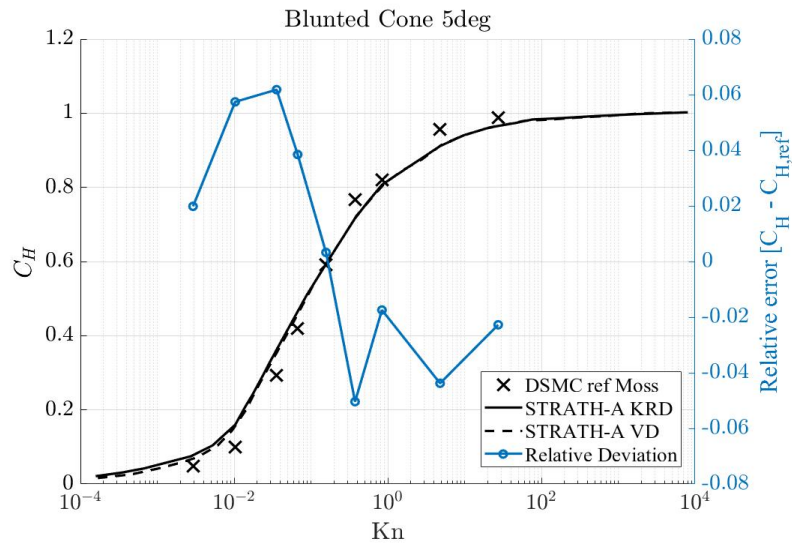


Figure 4.25: Blunted code heat transfer coefficient over Knudsen Number. On the right y-axis the relative error is reported wrt to literature data.

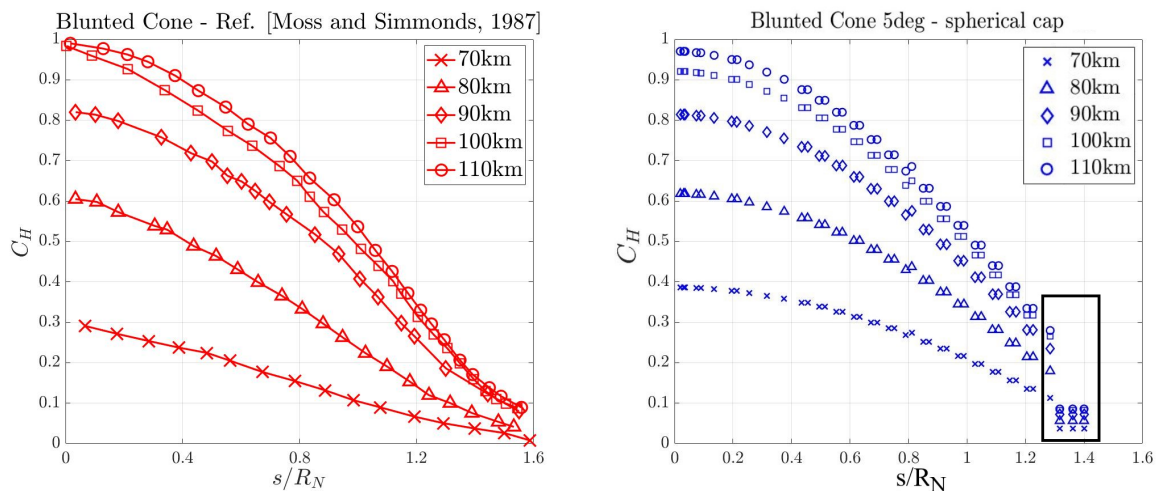


Figure 4.26: Comparison between the C_H distribution on the blunted cone spherical cap. Left: reference data from Moss [Moss and Simmonds, 1987]. Right: simulation results obtained with STRATH-A.

has been reported in Figure 4.27. On right side of the same figure, a comparative analyses between the Local Radius and the constant reference radius has been reported, showing how the increasing radius on the longitudinal axis causes a decreased heat-flux. The analysis shows also the possible benefit of implementing a running-length correction, which is used in the Simplified Aerothermal Model (SAM, [Merrifield et al., 2015b]), which would allow to capture the heat-transfer reduction with the increasing longitudinal distance from the stagnation point.

4.3.5 Launcher Vehicle Payload Fairing

In a recent research [Falchi et al., 2019], the aerothermal heat transfer methodology has been tested and compared against high-fidelity DSMC simulations within the transitional and rarefied regime. The study aimed at investigating the accuracy of the methodology to launcher vehicle (LV) ascent scenarios. A simplified geometry of VEGA multistage LV has been studied, focusing on the payload fairing and 3rd stage geometries [frntr, 1999], shown in Figure 4.28. The atmospheric data, along with the typical LV trajectory ascent profiles (velocity and altitude) have been taken from VEGA user manual [Arianespace, 2014]. The open source software dsmcFoam+ [White et al., 2018] has been used to perform the dsmc simulations, a non-reacting chemistry model was employed [Palharini et al., 2015] and an upper boundary for the heat-transfer has been computed.

One of the most significant sources of uncertainty in the computation of the LPI

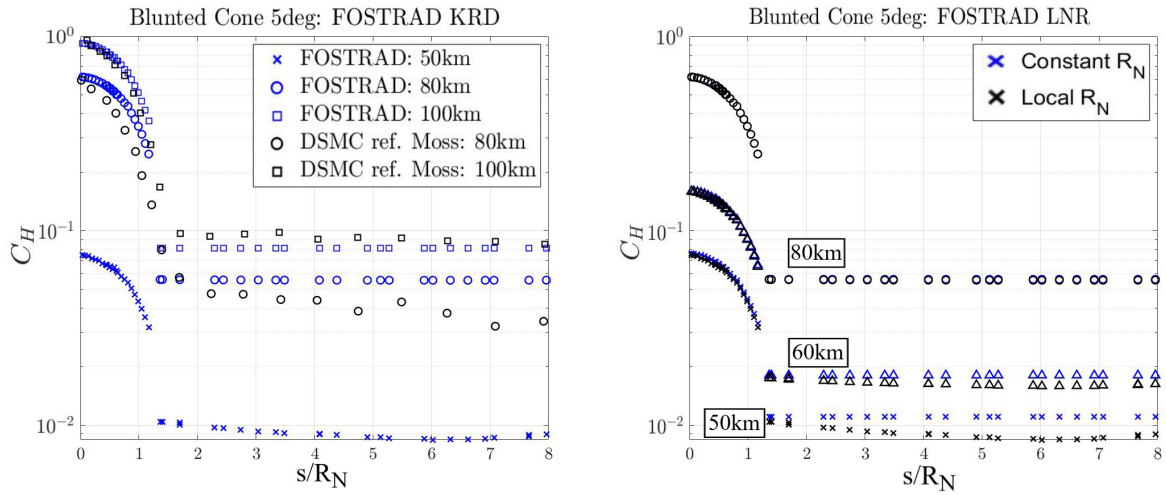


Figure 4.27: Left: Comparison between the C_H distribution on the entire geometry between the DSMC data and STRATH-A results. Right: comparison between the use of a Local Radius approach and the constant reference nose radius approach.

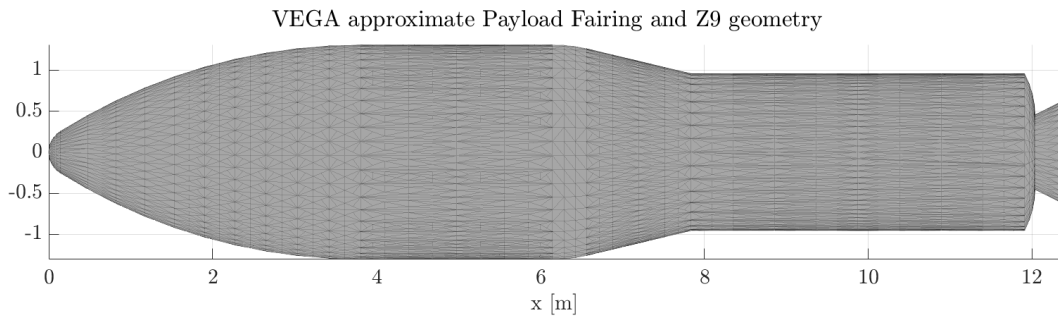


Figure 4.28: Payload Fairing and 3rd stage solid rocket motor geometry.

aerothermal heat transfer in the transitional regime is due to the reference length used for computing the Knudsen number. In fact, the transitional bridging function are characterized by a high uncertainty due to the limited number of data used to generate them, and therefore a small variation on the reference length is propagated to the estimated heat transfer. Three simulations were performed at the altitude of 107km using different reference lengths ($L_{ref} = [0.5m, 2.6m, 5.0m]$, Figure 4.29). The DSMC simulations have been performed with an average flow velocity of 3950m/s, and a fixed wall temperature of 350K with a fully diffusive wall boundary conditions. The assumed atmospheric properties have been reported in Table 4.1 as a function of altitude. The same conditions have been simulated with STRATH-A, and the wall heat transfer distributions at the altitudes 105km, 107km, 115km, and 130km have been reported in Figures 4.31 and 4.32. The simulations with STRATH-A have been performed using the nose diameter as a reference length ($L_{ref} = 0.56m$). The reported results distributions show an error which ranges from 15% to 5% decreasing moving from the nose to the ogive/cylindrical part. The highest error is found at the lowest altitude where the transitional regime bridging function affect the accuracy of the results. In the free molecular flow regime, the average error is below 5%.

A typical Lagrangian flow-field post-processing representation is reported in Figure 4.30, showing the particles velocity distribution along with the surface heat transfer distribution.

Table 4.1: DSMC atmospheric properties: altitude, temperature, mass density, and molecular density

H [km]	T_{∞} [K]	ρ_{∞} [kg/m ³] $\times 10^{-9}$	N_{He} [1/m ³] $\times 10^{12}$	N_O $\times 10^{15}$	N_{N_2} $\times 10^{15}$	N_{O_2} $\times 10^{15}$	N_{Ar} $\times 10^{15}$	N_H $\times 10^{12}$	N_N $\times 10^9$
105.0	210.8	340.28	154.8	537.7	5640.9	1132.9	51.3	21.8	393.6
107.2	231.6	232.44	142.9	450.2	3849.0	739.2	32.4	18.6	456.3
110.4	270.4	134.51	129.6	334.8	2222.1	398.0	16.6	14.5	567.5
115.4	340.5	53.14	97.3	178.0	872.9	140.1	5.4	8.2	687.9
120.0	409.9	24.74	74.4	101.6	403.8	58.7	2.1	4.8	828.3
125.2	483.1	13.11	61.2	64.1	212.0	27.7	1.0	3.0	1140.0
129.7	539.3	8.57	54.6	47.4	137.4	16.4	584.7	2.2	1583.0

The PLF nose C_H computed with STRATH-A and dsmcFoam+ has been compared has been reported in Figure 4.33. The comparison between STRATH-A and dsmcFoam+ show an excellent agreement on both the absolute heat transfer and the relative distribution. The stagnation point C_H are reported in Table 4.2, STRATH-A underestimates the C_H with a maximum relative error below 10% which decreases with an increasing altitude.

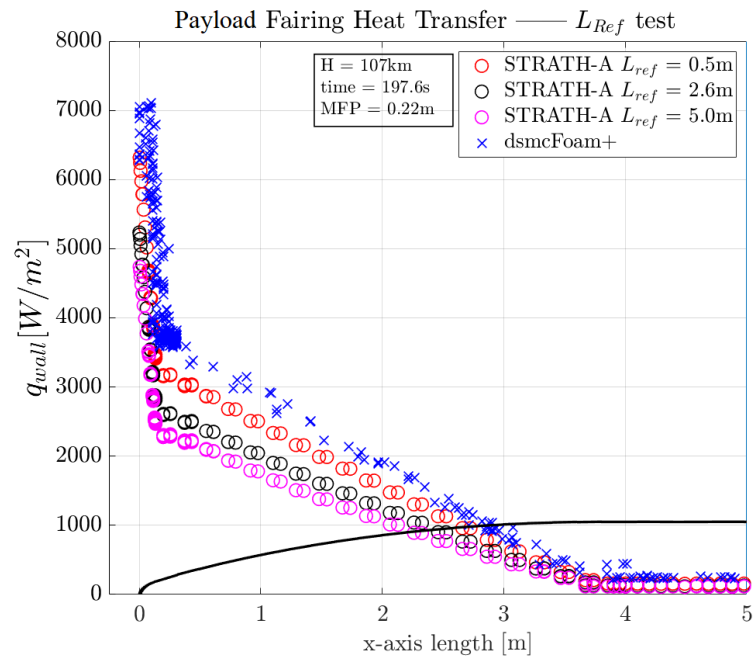


Figure 4.29: Sensitivity of the local heat transfer distribution to the reference length in the transition rarefied regime.

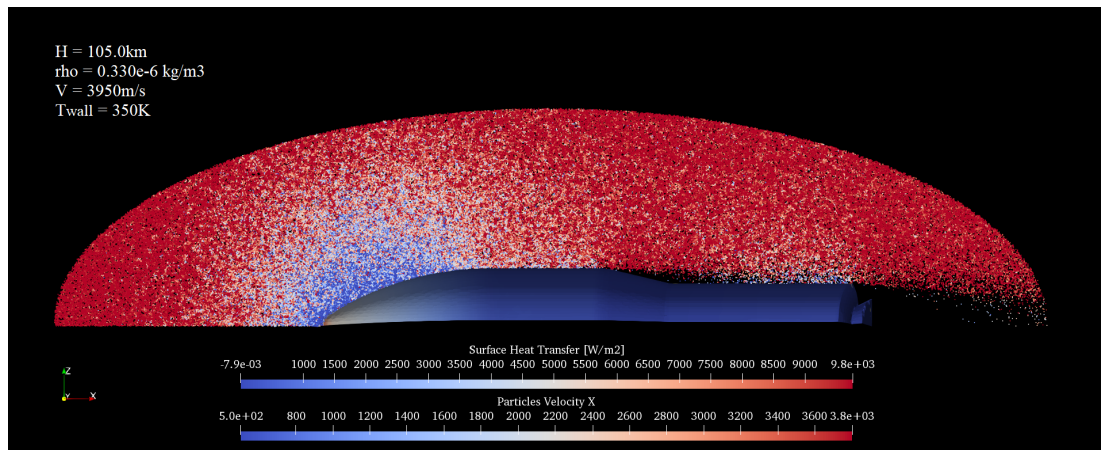


Figure 4.30: Payload Faring and Z9 SRM simplified geometric model simulated at 105km, the particles velocity distribution and the surface heat transfer are reported in the two displayed color scales

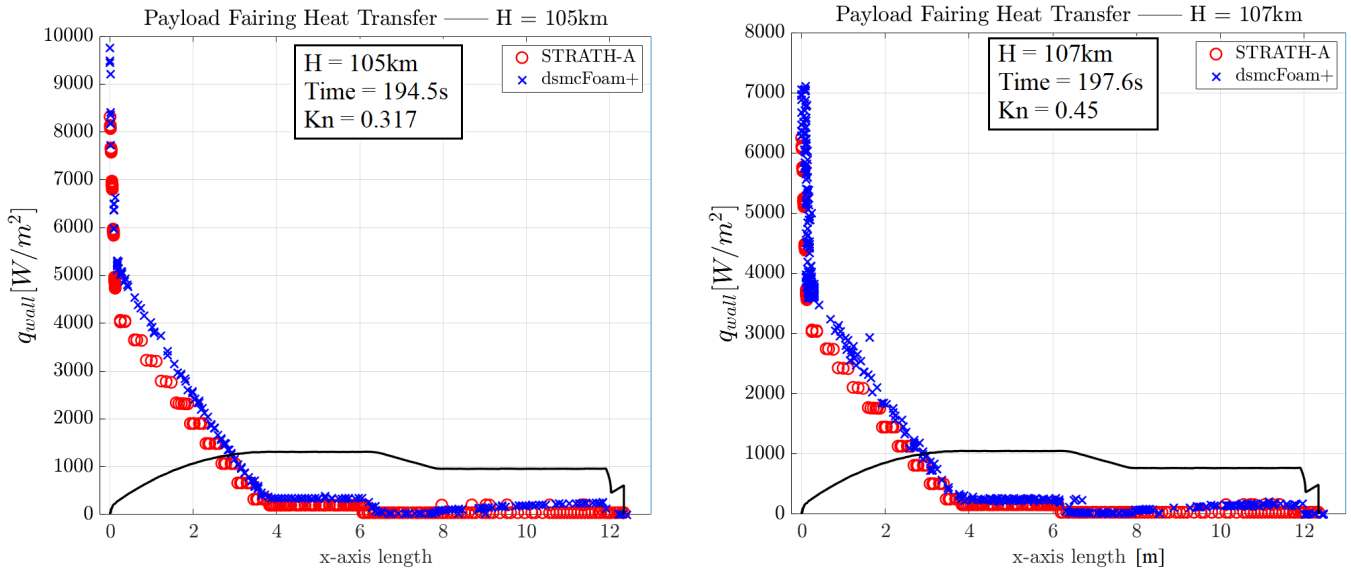


Figure 4.31: Payload fairing Heat transfer distribution comparison between STRATH-A and dsmcFoam+ at 105km (on the left), and 107km (on the right)

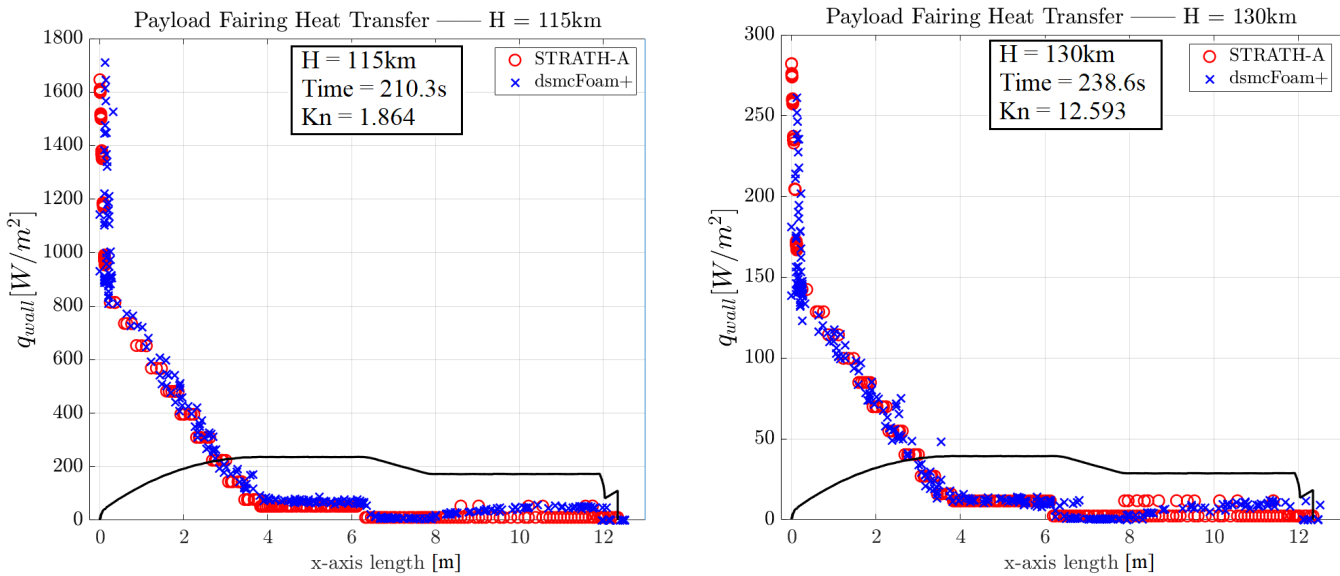


Figure 4.32: Payload fairing Heat transfer distribution comparison between STRATH-A and dsmcFoam+ at 115km (on the left), and 130km (on the right)

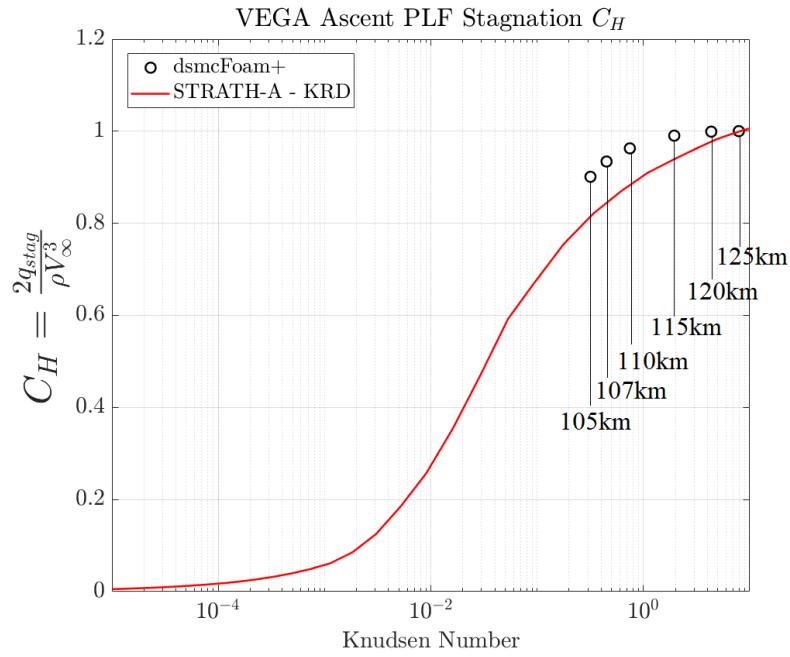


Figure 4.33: Comparison of the PLF nose heat transfer coefficient for a nominal VEGA trajectory.

Table 4.2: PLF stagnation point heat transfer coefficient comparison between dsmcFoam+ and STRATH-A

H [km]	$C_{H,stag,dsmc}$	$C_{H,stag,STRATH-A}$	Error [%]
105.0	0.902	0.816	-9.60
107.2	0.935	0.847	-9.44
110.4	0.963	0.886	-7.97
115.4	0.992	0.940	-5.27
120.0	1.000	0.979	-2.12
125.2	1.000	0.998	-0.16

Coupled Aero-thermodynamics Applications

In this chapter different application of STRATH-A are presented. The first one is the use of STRATH-A for the Intermediate Experimental Vehicle re-entry aiming at estimating the surface temperature. The second application is the atmospheric re-entry of Stardust Sample Return Capsule, this study focused on the Thermal Protection System ablation and recession over the entire trajectory. The third application is the uncontrolled re-entry of space debris and the statistical evaluation of the debris impact footprint and the associated Casualty Risk, as expected by the NASA Standard 8719-14 for limiting the space debris.

5.1 IXV Atmospheric Re-entry

In this section, the application of STRATH-A to study the re-entry phase of the Intermediate Experimental Vehicle (IXV) is described. The study case focuses on the use of STRATH-A to simulate the atmospheric re-entry of IXV, estimating the wall temperature distribution using a previously obtained optimal control law which minimizes the averaged absorbed aerothermal heating [Falchi et al., 2017c].

The IXV project was intended to be a re-entry technology demonstrator with a particular focus on aerothermodynamics and thermal protection systems (during the re-entry, IXV was expected to reach wall temperature up to 1700°C). The purpose of this study case was to highlight both STRATH-A aerodynamic and aerothermodynamic accuracy, while testing also its computational efficiency and the overall software stability. The mesh used for performing the simulation is reported in Figure 5.1; in the same figure the reference points used for reporting the wall temperature are reported.

STRATH-A itself does not allow to estimate the temperature propagation within a solid material, therefore, it must be coupled with a thermal code which allows the study of the temperature within the outer layers of the spacecraft. For this purpose, STRATH-A was coupled with the Ablative Response Code (ARC) [Renato, 2018].

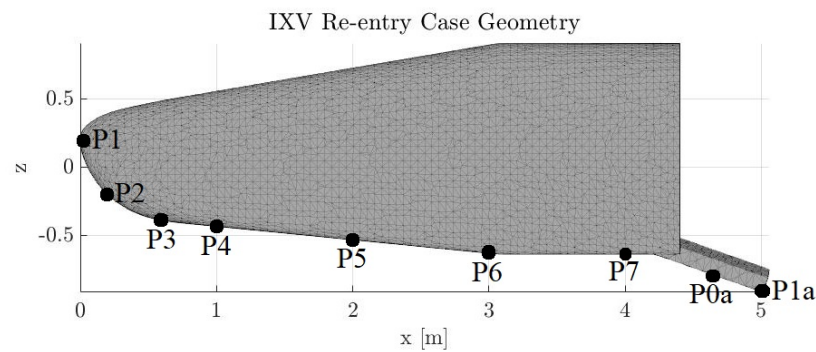


Figure 5.1: IXV mesh used for simulating the atmospheric re-entry via STRATH-A. In the mesh are also shown the points later used for reporting the wall temperature distribution over the surface.

5.1.1 Ablative Response Code

The code used to produce the ablation simulation is a one dimensional code based on the implicit finite difference method. This code has the capability to estimate the pyrolysis phenomenon progression and the consequent changes of density and temperature in the thermal protection material. The program governing equations are briefly illustrated in the following section. The capability of the code to produce reliable re-entry results has been proven for both Earth re-entry [Renato et al., 2017b] and Martian entry [Renato et al., 2017a].

The program is based on three main equations. The first one is the Arrhenius equation which describes the ablator degradation rate and calculates its density and change of state at every time step. The second equation is the in-depth energy equation, which represents the different energy rates existing inside the ablative material, e.g.: the storage of sensible energy, the thermal conduction and the pyrolysis energy consumption. The last main equation is the energy balance at the external surface which calculates how much of the heat flux estimated by the aerodynamic model reaches the material external surfaces and influences the ablative process [Moyer and Wool, 1970]. A precise material model containing the thermochemical properties of the material, e.g.: the specific heat flux, the thermal conductivity, the density and the pyrolysis characteristics, is essential to produce accurate simulations of the thermal protection system behaviour. These properties are empirically estimated during extensive and expensive characterization campaigns by the material producer; that is the reason why it is not always possible to find exhaustive data in literature.

In the case of the IXV simulation a non ablative material has been selected to better represent the real thermal protection system materials used in this vehicle. Un-

fortunately, to the authors' knowledge, the thermochemical characteristics of the real materials used are not available in literature; therefore an approximated material model has been generated to produce the IXV re-entry. Stardust fore-body was made of an ablative material called PICA, Phenolic-Impregnated Carbon Ablator. A number of adequate thermochemical models are present in literature for this specific material, the most complete of those was selected for the Stardust re-entry analysis. In both test cases a singular material was utilized to characterize the entire geometry of the spacecraft; it was decided to do so for simplicity of the model and lack of information regarding the real materials properties. In reality both spacecraft used different materials in different part of the geometry; in case the full set of data for the materials becomes available the code is already capable to simulate a multi-material geometry.

5.1.2 Problem Description and Results

The initial trajectory parameters have been taken as a reference from [Roncioni et al., 2011]: initial entry altitude was 120km, flight path angle of -1.6deg, and an initial velocity of 7400m/s. The target trajectory parameters were set to a velocity of $\approx 450\text{m/s}$ (equivalent to a Mach ≈ 1.5), an altitude of 25km, and an angle of attack of 45deg, which was a boundary condition required for allowing the deployment of parachutes.

The heat-flux was computed using the implemented local radius formulation and the KRD super-catalytic wall formulation, with the smoothing calibration parameters identified in the previous section (i.e.: $N_{\text{smooth}} = 30$, and Flat Edge = 0.8). A diffusive accommodation coefficient $\sigma_{\text{diff}} = 0.93$ was used for the aerothermal heating computation.

The optimal control law is reported in in Figure 5.2. The use of this control law along with the other inputs allows the study of the 3DOF atmospheric re-entry of IXV. The aerodynamics (i.e.: lift and drag are computed at step of the trajectory propagation in order to allow the coupled propagation of the problem variables. The trajectory obtained by the use of STRATH-A is illustrated in fig. 5.3 (only the vectorial acceleration and not its components have been shown). The trajectory results shows the typical heat flux over time representation of a lifting body re-entry. An example of the maximum temperature distribution reached during the trajectory is shown in fig. 5.4, which is slightly lower ($\approx 6\%$) than the nominal temperature peak of 1700°C . In the same picture, the stagnation heat transfer over time is reported.

The temperature distribution over the surface for various points is reported hereinafter. Taking as a reference the points reported in Figure 5.1, the points from P1 to P7 are referred to IXV body centerline, while P0a and P1a referers to the flaps centerlines. The wall temperature distributions are reported respectively in Figures 5.5 (on

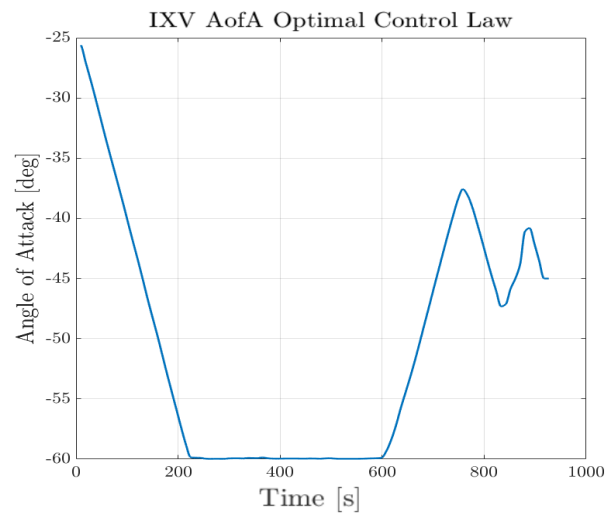


Figure 5.2: IXV Trajectory optimization: angle of attack optimal control law.

the body) and 5.6 (on the flaps).

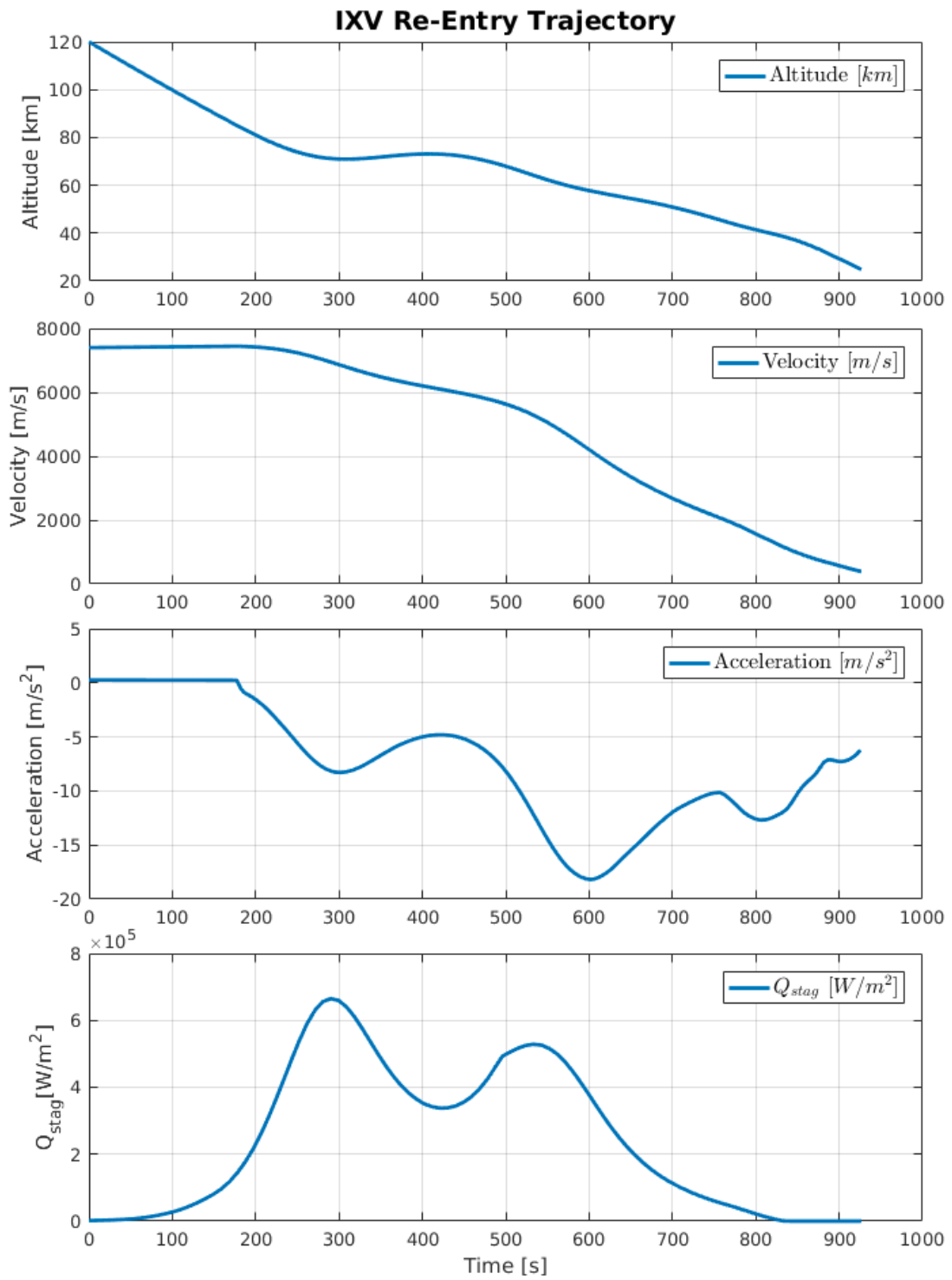


Figure 5.3: IXV atmospheric re-entry: heat-flux optimized trajectory.

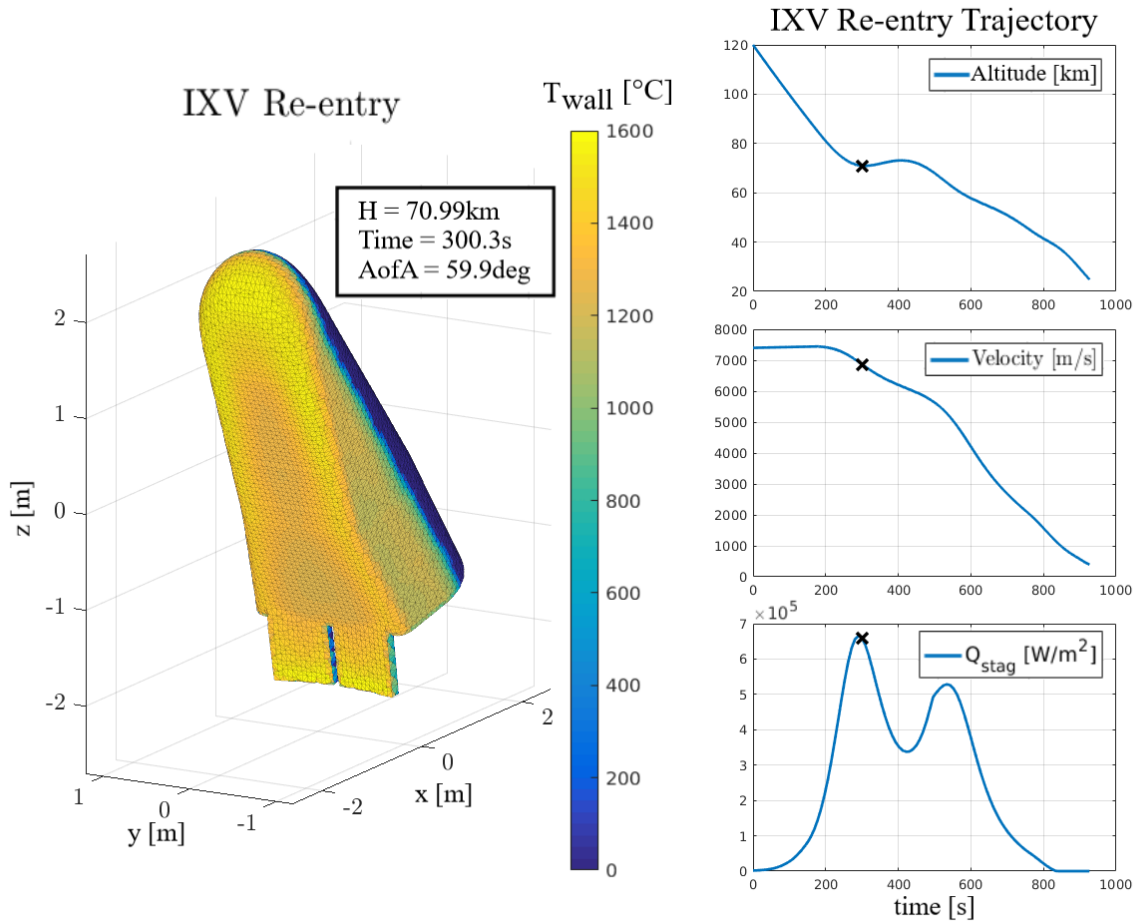


Figure 5.4: IXV atmospheric re-entry: surface temperature distribution computed by STRATH-A and the coupled thermal code.

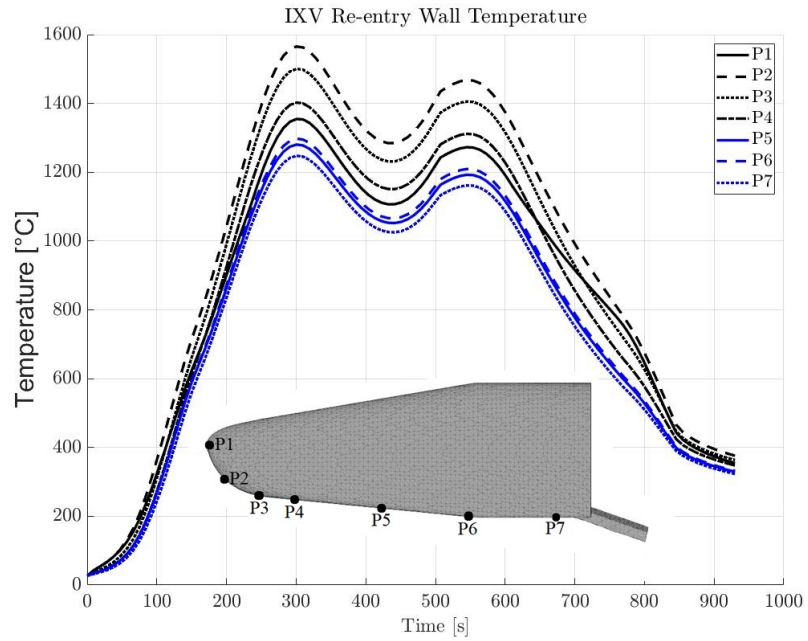


Figure 5.5: IXV wall temperature distribution for the re-entry simulated with STRATH-A on the main body centerline.

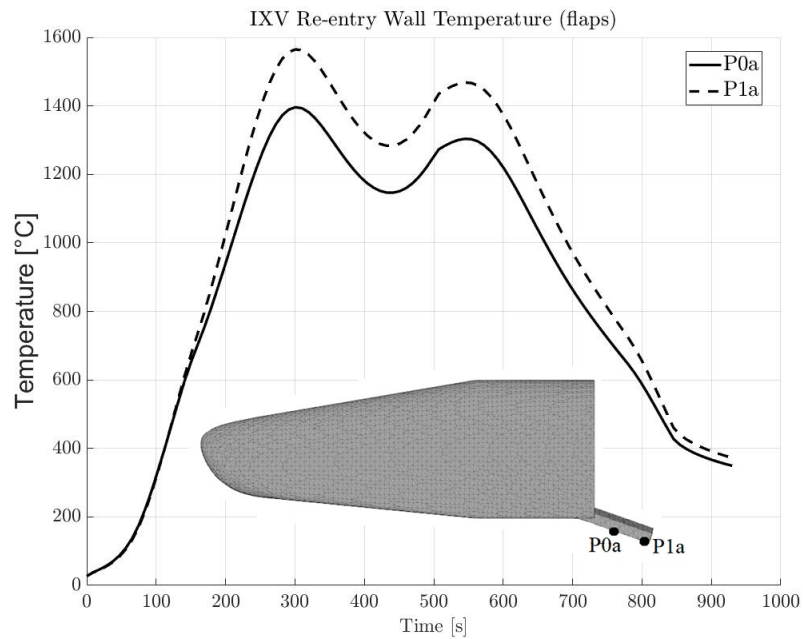


Figure 5.6: IXV wall temperature distribution for the re-entry simulated with STRATH-A over the flaps.

5.2 Stardust TPS Ablation Modelling

In this study case STRATH-A and the Ablative Response Code (ARC) [Renato, 2018] were couple to perform the simulation of Stardust Sample Return Capsule TPS ablation. The re-entry of Stardust SRC was identified as a suitable test case for the coupling, due to the extensive dataset available. Stardust is a small robotic probe (weighting just 46kg) that was designed for a flyby to the comet Wild 2 in order to collect dust samples and return them on the earth. The capsule was expected to re-enter the atmosphere with a very high velocity 12.8km/s, a flight path angle of -8.2deg [Desai and Qualls, 2010], the entry interface was assumed at 125km, and the attitude was fixed at 0deg. The trajectory was stopped around the expected hypersonic drogue opening altitude and speed, which were 32km and Mach 1.37 respectively.

Initially, the re-entry trajectory analyses were performed using the previously integrated 3DOF tool and STRATH-A. Since the thermal analyses performed with the ablative response code are computationally expensive, and no major alterations of the aerodynamic properties were expected due to the ablation, the trajectory was obtained with computing the ablation. The trajectory results are shown in fig. 5.7. The results show a very good agreement with the analyses reported by Desai [Desai and Qualls, 2010] et al. Different parameters for the Stardust trajectory had been considered by Olynick [Olynick et al., 1999] et al, even though they still compare well with STRATH-A results. The acceleration curve reported in fig 5.7 is in agreement with the maximum acceleration peak of 38.1g reported by Willcockson [Willcockson, 1999].

To simulate the actual burn-up, STRATH-A has been run with SCARAB aerothermal model [Koppenwallner et al., 2005], using the trajectory parameters (i.e.: altitude, velocity) previously computed, and a constant angle of attack of 0deg. The real-time coupling between STRATH-A and the thermal ablation code granted that every geometrical feature change was correctly captured (i.e.: surface inclination and local-radius variation). Indeed only a step-by-step geometrical evolution is able to expose new facets to the flow, e.g.: as the rounded corners tend to recede, they leave new facets exposed to the aerothermal flux. In Figures 5.8 and 5.9 are shown two different time steps of the actual atmospheric re-entry simulation, the heating peak and the final time step respectively.

It is interesting to observe how the recession progressively exposes facets that were shadowed by the corner, and the code is able to accurately adapt the mesh evolution. By analyzing the actual stagnation point heating, it is possible to observe some small fluctuations at the peak. This is most likely due to the input data used for the simulations, which showed small fluctuations on the velocity, then amplified on the heat-flux. The final geometrical shape is representative of the actual model that was tested for

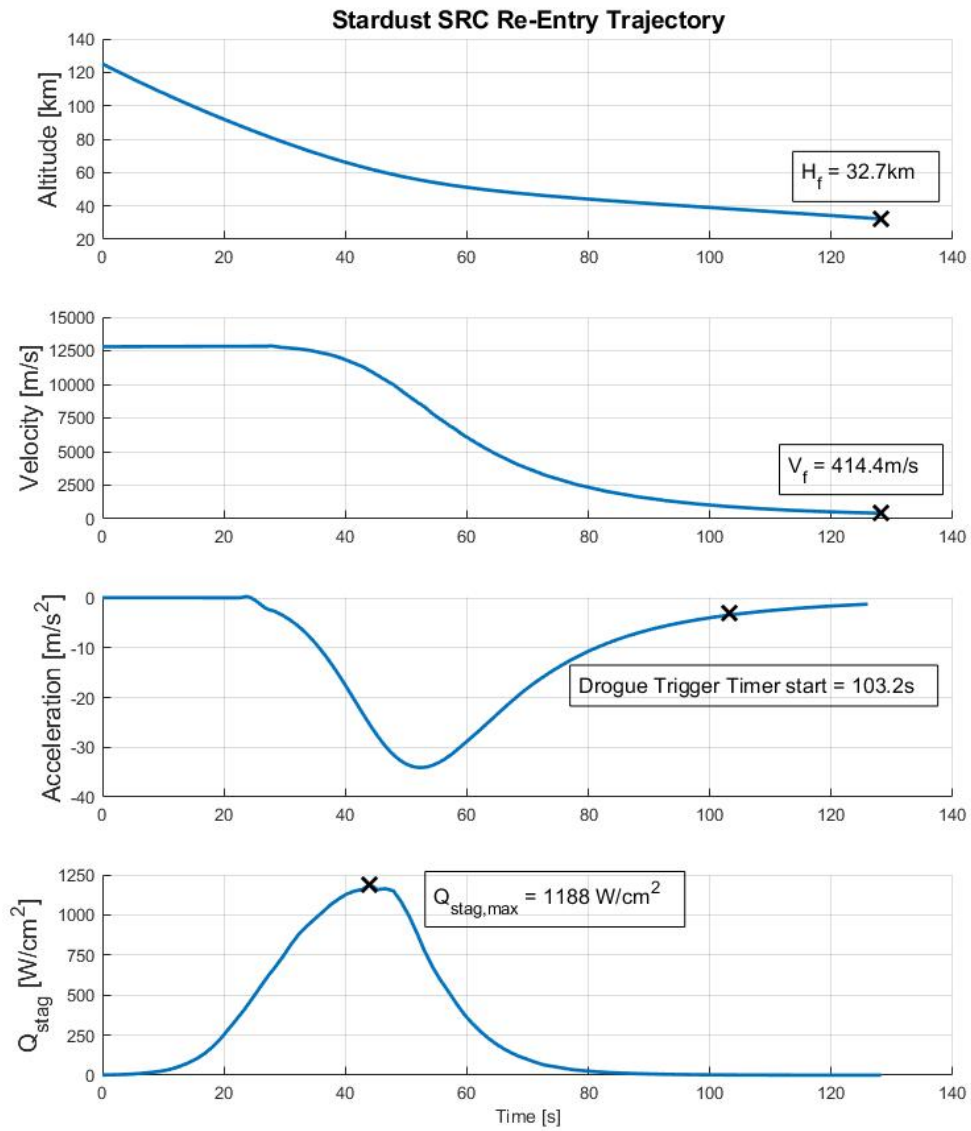


Figure 5.7: Stardust atmospheric re-entry simulated with STRATH-A using 3DOF, highlighting different representative points: final altitude and velocity, drogue trigger timer activation, and maximum heat flux.

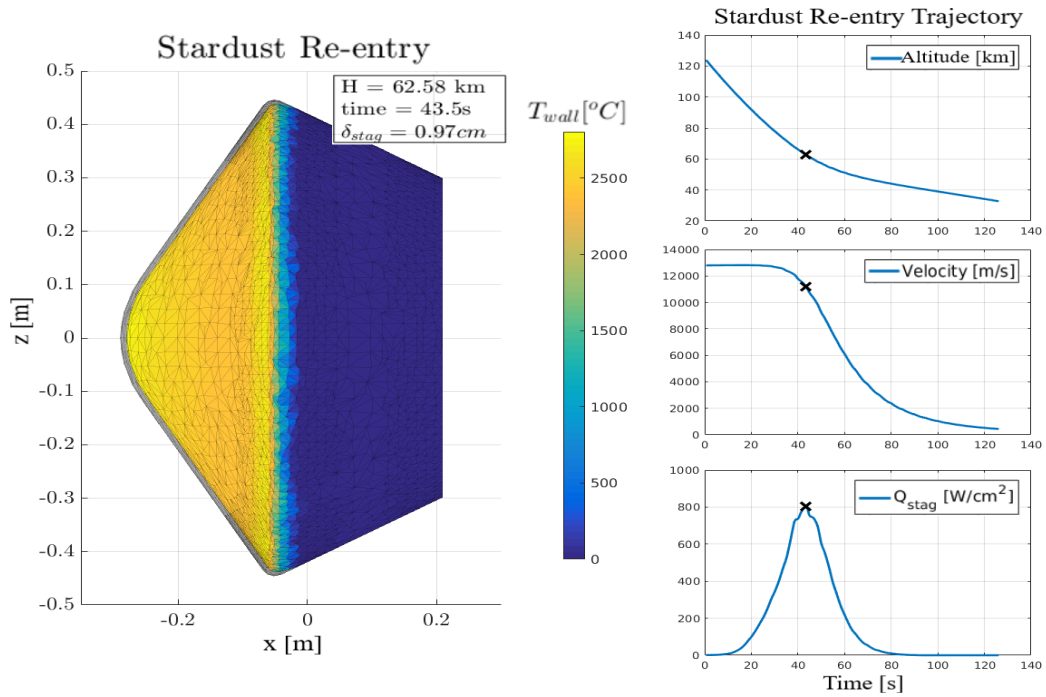


Figure 5.8: Stardust SRC atmospheric re-entry simulation: recession and temperature distribution at the heat-flux peak. The gray mesh is the initial geometry.

the aerodynamic stability during the pre-drogue triggering phase by Willcockson [Willcockson, 1999] et al.

The analyses on the Stardust re-entry maximum and average wall temperature shows a good agreement with the telescope observation reported by Winter [Winter and Trumble, 2010] et al (Figure 5.10). STRATH-A averaged temperature have been computed on the fore-body only. Although, it is possible to observe an off-set on the altitudes at which the maximum temperature occurs, which has been considered in the picture on the right (a 6km offset has been added). In this way it was possible to directly compare the predicted temperature, which compares very well with negligible errors on both the average and maximum observed temperatures. The trajectory offset may be due to several factors:

- Uncertainty on the re-entry attitude
- Uncertainty on Stardust SRC mass
- the neglected recession (causing a mass decrement)
- aerodynamics propagated errors on lift and drag
- actual atmospheric properties differences from the used dataset (mainly density)

Neglecting the offset on the altitudes, STRATH-A and ARC overestimate the maximum

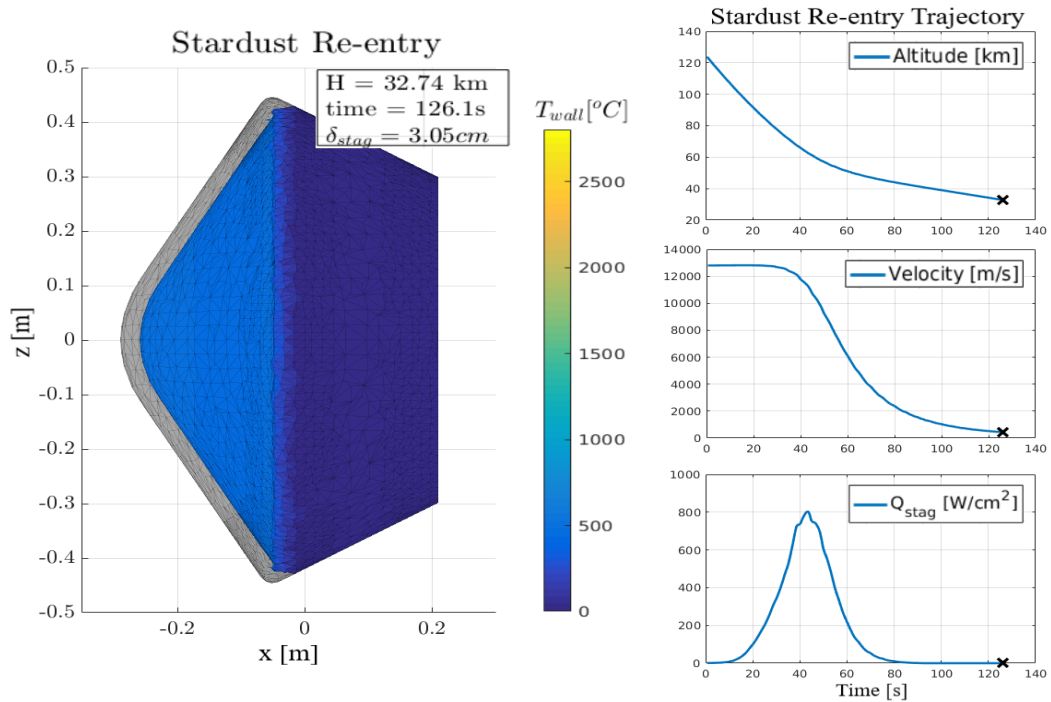


Figure 5.9: Stardust SRC atmospheric re-entry simulation: final time(before the hyper-sonic drogue opening triggers).

wall temperature by 4.8%, while the average wall temperature appears to be slightly underestimated at higher altitudes (with error below 2.5%). Such differences are deemed to be acceptable under the consideration that the tools are yet low-fidelity and the complete simulation required less than ~ 15 minutes.

The same results have been compared also to the CFD simulations performed by [Olynick et al., 1999] in Figure 5.11. The results show that the simulated wall temperature compares well with the estimation reported by Olynick et al., considering that Stardust re-entry is simulated with the ablation. A slight underestimation of the wall temperature is visible in the early re-entry (i.e.: below 40s), the same result was highlighted with the SLIT telescope comparison. Such underestimation is likely to be explained by the differences between the atmospheric model used for the simulations and the actual re-entry atmospheric condition.

Another interesting observation can be made on the computed recession distribution, shown in Figure 5.12. The maximum recession is shown at the stardust nose, and close to the fore-body shoulder. The heat-flux absorbed at close to the shoulder causes an early recession, that progressively increases the exposure of the lee-ward side of the shoulder itself, as it is better shown by the progressive recession in the figures 5.8 and 5.9. This particular effect changes also the local surface inclination and radius, increasing and

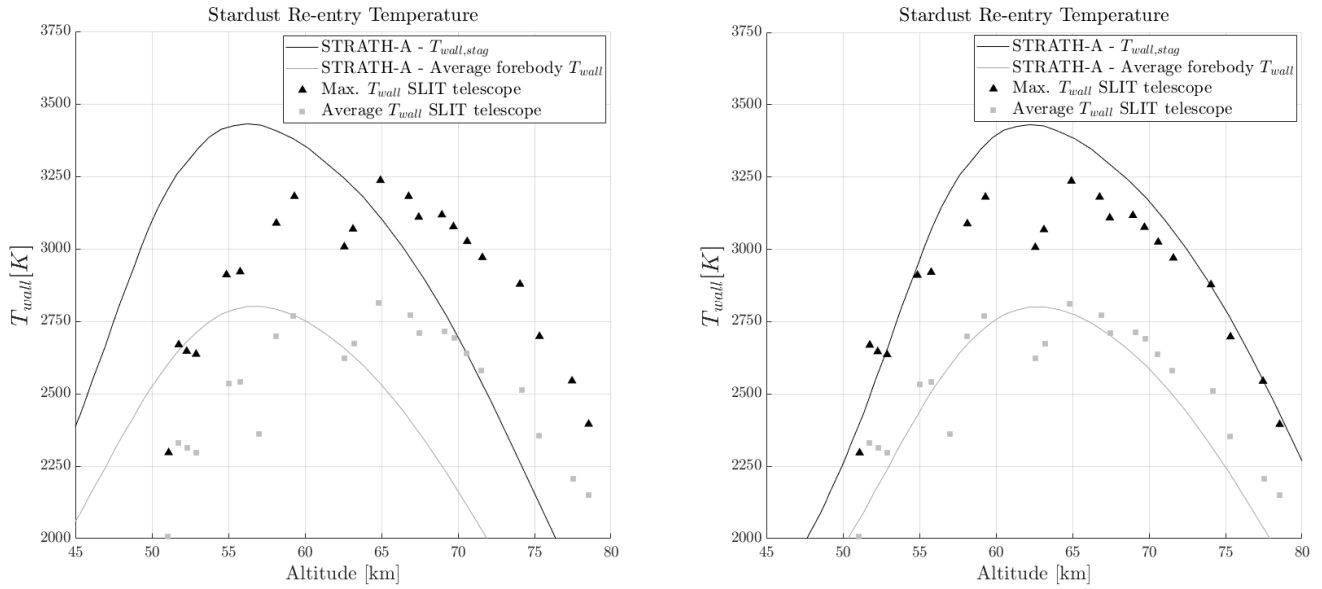


Figure 5.10: Comparison of Stardust re-entry maximum and averaged wall temperature over altitude, computed with STRATH-A and observed with the SLIT telescope [Winter and Trumble, 2010]. On the left: nominal re-entry trajectory. On the right: re-entry trajectory considering an offset of +6km on the results.

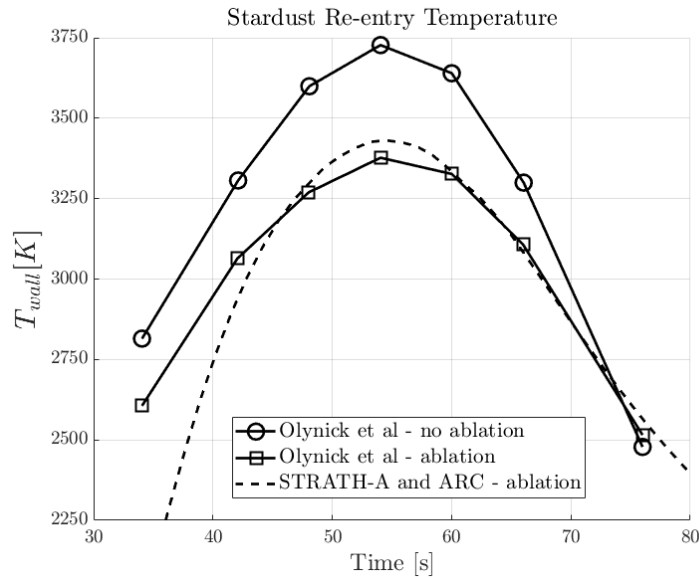


Figure 5.11: Stardust SRC wall temperature estimation comparison between the re-entry simulated with STRATH-A and ARC against the CFD simulations reported in [Olynick et al., 1999].

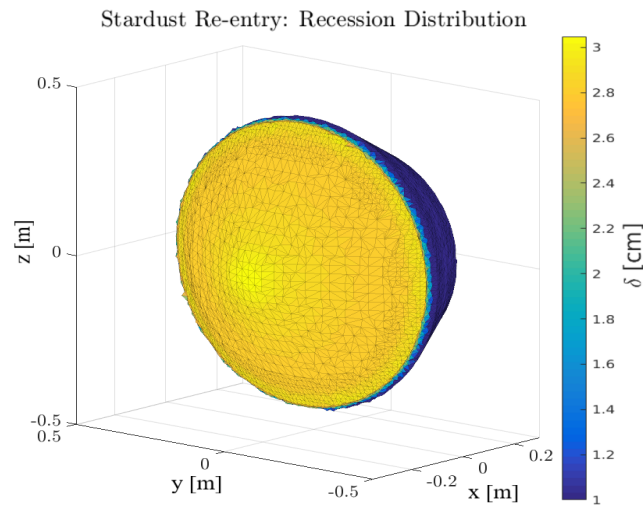


Figure 5.12: Stardust SRC predicted recession distribution at the hypersonic drogue opening time.

decreasing the local heat-flux. Indeed, the recession on the shoulder causes the angle between the flow and the facets' normals to decrease, inducing an increased heat-flux, in accordance with KRD model [Kemp, 1956]. At the same time, the surface geometric variation induces a shoulder-rounding, thus increasing the local radius and decreasing the local heat-flux. The conjunction of these phenomena can only be captured by a constant evolution of the mesh. During the presented study, it has been observed that the accuracy of the geometry evolution changed with the simulation time-step. Indeed, the recession is applied on the mesh vertexes normals direction, which are recomputed by STRATH-A mesh handler at each iteration; thus, highlighting the importance of the real-time coupling between STRATH-A and the aerothermal ablation code.

The recession has been compared with the results reported in [Olynick et al., 1999] at 80s from the re-entry, and have been shown in Figure 5.13. The results show the recession distribution on the forebody surface of Stardust SRC; STRATH-A and ARC overestimates the recession when compared against the CFD simulation performed by Olynick et al. Such differences have to be sought in the longer simulation time (i.e.: Olynick starts the simulations at 34s), and the differences between the actual ablative material models and properties employed for the simulation [Renato, 2018]. Although, the significant differences in the recession absolute value, the qualitative trend is similar and shows that STRATH-A was able to properly capture the differences in the geometrical radius which directly influences the differences in the recession rates.

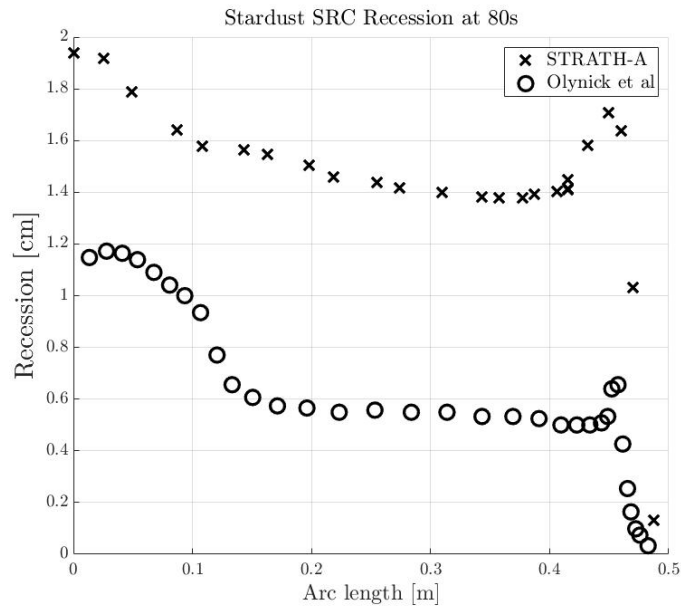


Figure 5.13: Stardust SRC wall recession estimation on the forebody starting from the stagnation point (i.e.: arc length = 0); comparison between the re-entry simulated with STRATH-A and ARC against the CFD simulations reported in [Olynick et al., 1999] for a re-entry time of 80s.

5.3 VEGA PLF and payload temperature estimation

This application case is focused on identifying a theoretical PLF separation time (or altitude) for a nominal VEGA ascent trajectory. Two different phases have been defined for performing the simulations: in the first one the PLF ascent was simulated, and its thermal model temperature was estimated, in the second phase, the internal heat radiated by the back-wall of the PLF was used as a boundary condition to estimated the dummy payload temperature. Even though this is not a re-entry scenario, the analysis were performed to understand and observe the applicability of the same low-fidelity methodology in a different field.

In order to simulate the ascent scenario with STRATH-A, a coupled analysis between the aerothermal heat fluxes and a thermal model of the PLF had to be programmed. In Figure 5.14, the PLF thermal model schematic has been reported; the external thermal protection system (TPS) has been generated using 3 nodes through the thickness and 1 node to simulate the back-wall sandwich panel. The conductive links have been generated using a typical lumped thermal network approach. The specific model has been generated using approximately 10'000 nodes. Temperature-dependent properties (i.e.: thermal capacity and conductivity) have been used for both TPS and aluminum

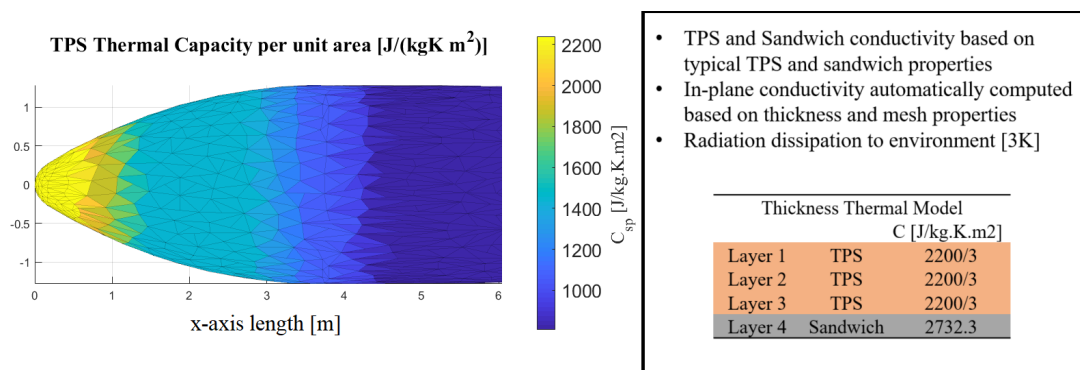


Figure 5.14: Payload fairing thermal model used to simulate the ascent trajectory, TPS and sandwich thermal capacities are based on typical values found in the literature

(sandwich). The internal radiation was neglected for simulating the ascent (the dummy payload was evaluated in a different uncoupled simulation), while the external surface has been assumed to be exposed to sun and albedo heat fluxes and an equivalent infrared Earth radiation. The external TPS infrared emissivity (ϵ) has been assumed equal to 0.9, while the solar absorptivity was assumed equal to 0.3.

The VEGA nominal ascent trajectory profile has been taken as an input from the user manual [Arianespace, 2014]. The trajectory was discretized in a sufficiently high number of steps; the PLF thermal model was coupled with the STRATH-A code to evaluate the aero-thermal heat fluxes to be used as boundary condition for each step. The internal convergence of the thermal model temperature was ensured using a variable time-step ODE solver (very high temperature gradients through the thickness and surface were expected).

The external TPS was simulated as a non-ablative material (such approach provides the highest back-wall temperature estimation). In order to apply an enveloping aerothermal heating, the simulations were performed assuming a reference angle of attack (AofA) of 10deg. Afterwards, the PLF length was discretized in 100 longitudinal stations, and the maximum aerothermal heating was computed and applied uniformly around the entire PLF circumference. In such a way, for the lower PLF longitudinal stations, a higher boundary aerothermal heating was applied. The 0deg and the enveloping 10deg angle of attack aerothermal heating distribution for a typical ascent trajectory over the PLF longitudinal axis are reported in Figure 5.15. The application of the enveloping Q_{wall} has been used as a boundary condition to simulate the PLF ascent. It may be observed that the reference heat fluxes have been computed assuming a cold wall (i.e.: $T_{wall} = 300K$), which is a conservative assumption for estimating the maximum aerothermal fluxes.

The results of the PLF ascent simulation for the wall temperature of the first TPS

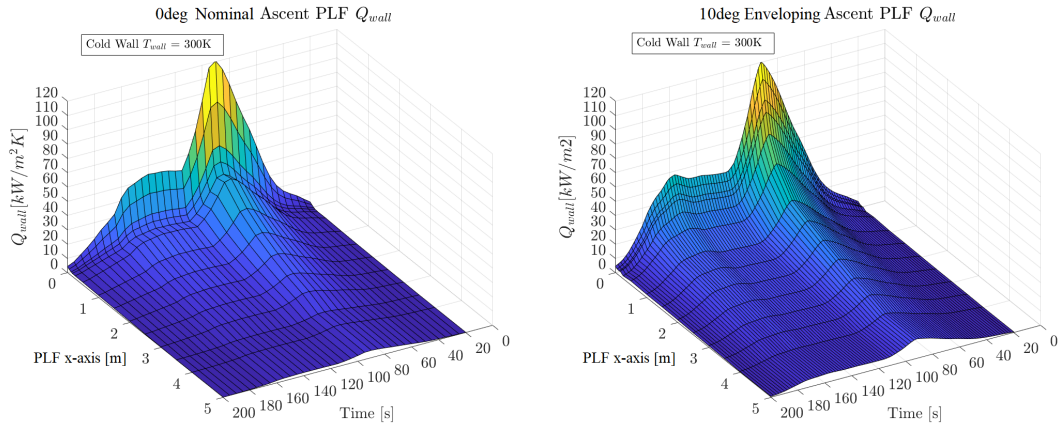


Figure 5.15: **On the left** - PLF heat transfer for the nominal ascent trajectory simulated with STRATH-A for AofA = 0deg. **On the right** - enveloping surface heat transfer for AofA = 10deg

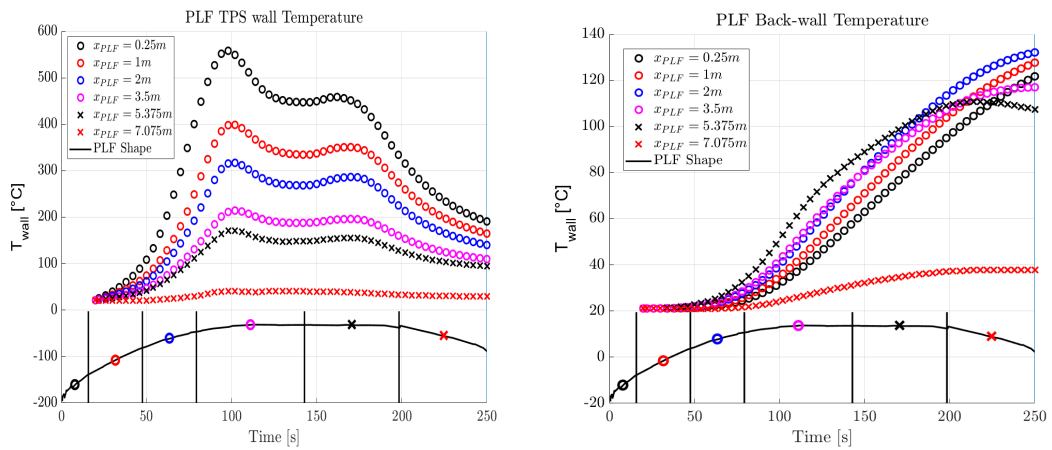


Figure 5.16: **On the left** - PLF averaged external TPS layer estimated wall temperature. **On the right** - PLF back-wall estimated temperature

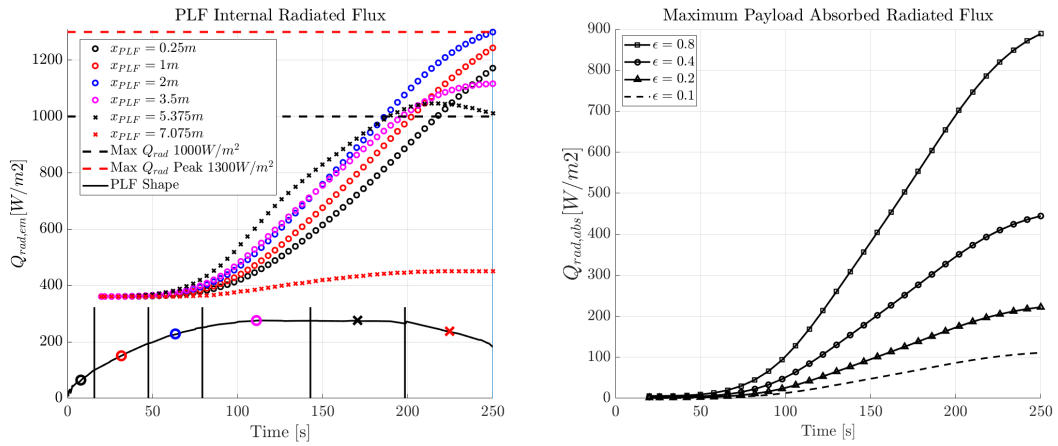


Figure 5.17: **On the left** - PLF internally emitted infrared radiation assuming $\epsilon = 0.85$ for the different averaged longitudinal stations. **On the right** - maximum radiative heat flux absorbed by the payload assuming an unitary view factor and four different infrared emissivity values

layer and the sandwich panel back-wall are reported in Figure 5.16. It is interesting to observe that the maximum back-wall temperature is not reached at the nose, but at the intersection between the ogive and the cylinder instead. Such result is due to the assumed progressively reducing TPS thermal capacity (and thickness) moving from the nose to the cylinder (Figure 5.14). Analyzing the results, and assuming a back-wall infrared emissivity equal to 0.85, the PLF internally emitted infrared radiation per unit area may be estimated with the Stefan-Boltzmann law. According to VEGA user manual [Arianespace, 2014], the payload thermal environment requirement states that time-averaged or space-averaged internal PLF emitted radiation per unit area has to be lower than $1000W/m^2$ and the maximum transient value should be below $1300W/m^2$. In Figure 5.17, both the emitted and the maximum absorbed radiative flux have been reported, the absorbed flux has been computed assuming a unitary view factor and the maximum back-wall temperature.

5.3.1 Dummy payload temperature estimation

The estimation of the dummy payload (PL) temperature has been performed assuming different boundary conditions depending on the PLF separation, and three different PLF separation times have been simulated: 200s, 215s and 231s (nominal separation time). The dummy payload has been simulated with a thermal model with 2 nodes through the thickness, using typical properties of sandwich panels and aluminum temperature-dependent properties (with an equivalent thermal capacity $C = 2950J/kg.m^2.K$ per thickness node). In-plane and transverse conductivity have been assumed from equiva-

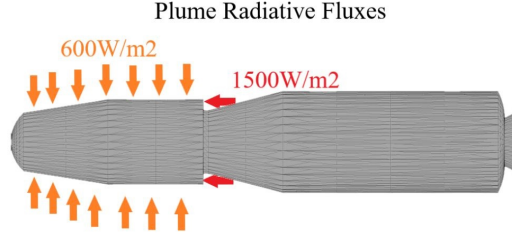


Figure 5.18: Z9 plume radiative heat fluxes as defined in VEGA user manual [Arianespace, 2014]

lent sandwich panel properties. The PL infrared emissivity has been assumed equal to one, to estimate the maximum temperature increment for a given thermal capacity.

Before the PLF separation, only the back-wall radiative emitted heat flux is considered. At the front of the dummy payload (i.e.: rounded nose) the radiative links have been assumed with the PLF internal wall temperature estimated at $X_{\text{PLF}} = 2.0\text{m}$, while on the lateral surfaces the radiative link has been assumed with the PLF back-wall temperature at $X_{\text{PLF}} = 3.5\text{m}$ (see Figure 5.16 on the right). The radiative heat flux is computed as:

$$q_{\text{rad,PL},i} = \sigma A_i V_{i,j} \epsilon_j \epsilon_i \left(T_{\text{PLF,wall}}^4 - T_{\text{PL},i}^4 \right) \quad (5.123)$$

where $q_{\text{rad,PL},i}$ is the net radiative flux absorbed by the external PL i -th node, A_i is the node surface, $V_{i,j}$ is the view factor which has been assumed equal to 1, ϵ is the correspondent infrared emissivity, $T_{\text{PLF,wall}}$ is the reference back-wall PLF temperature, and $T_{\text{PL},i}$ is the PL i -th external panel temperature.

After the PLF separation, the aerothermal convective heat-flux is computed with STRATH-A, assuming the fluxes computed with a cold wall temperature assumption and a 10deg AofA envelope. When the nominal Z9 ignition time is reached (i.e.: $t = 226\text{s}$) the plume heat-fluxes defined by the VEGA user manual are applied [Arianespace, 2014] (Figure 5.18), and typical sun and albedo environmental heat fluxes are applied.

The results of the three different simulations for evaluating the PLF separation time influence on the PL external temperature have been reported in Figures 5.19-5.20, where the PLF separation and Z9 ignition time are also reported as dashed vertical lines. The results show different features: at the lowest simulated separation time, the aerothermal have a high impact on the front wall temperature, while at the other stations it is possible to observe that environmental and plume heat-fluxes have a higher contribution. Comparing $T_{\text{PLF,sep}} = 215\text{s}$ and $T_{\text{PLF,sep}} = 231\text{s}$, the temperature difference on the PL at 250s is almost negligible. In addition, it is possible to observe that between 215s and 231s, the PLF emitted infrared radiation becomes significant on the lateral surface, causing a temperature increment higher than the one that the external

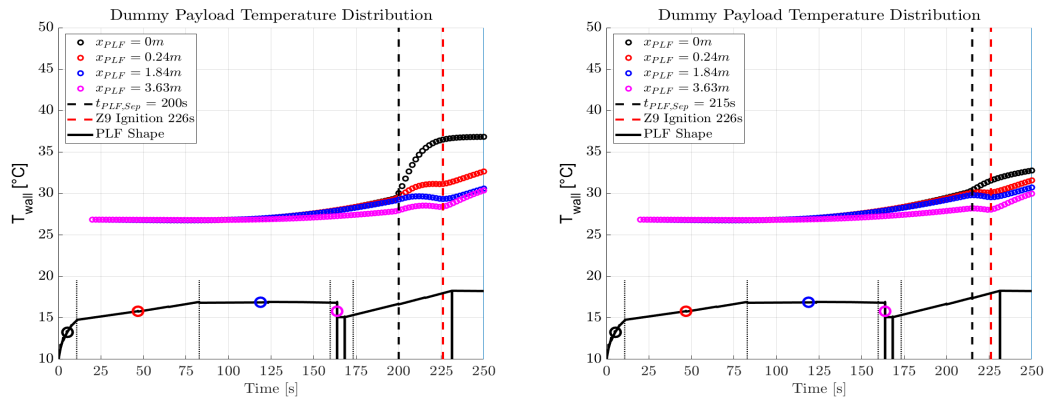


Figure 5.19: Dummy payload external wall averaged temperature predictions for different PLF separation times at different reference stations; on the left $T_{PLF,sep} = 200s$ and $T_{PLF,sep} = 215s$ on the right

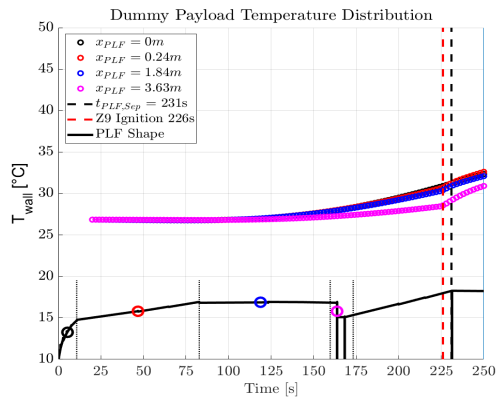


Figure 5.20: Dummy payload external wall averaged temperature predictions for different PLF separation times at different reference stations at the nominal $T_{PLF,sep} = 231s$

aerothermal fluxes would have caused. To further investigate the relative heat fluxes, the aerothermal and the PLF emitted fluxes have been compared, and they have been reported in Figure 5.21. Comparing the external convective heat fluxes with the PLF emitted radiation, it is possible to deduce that the optimal PLF separation time would be at 214s. In addition, for the lateral payload stations, an earlier separation would be even more beneficial in order to minimize the incident heat-flux; such observation anchors the lateral stations higher wall temperature prediction reported by releasing the PLF at 231s (in Figure 5.20).

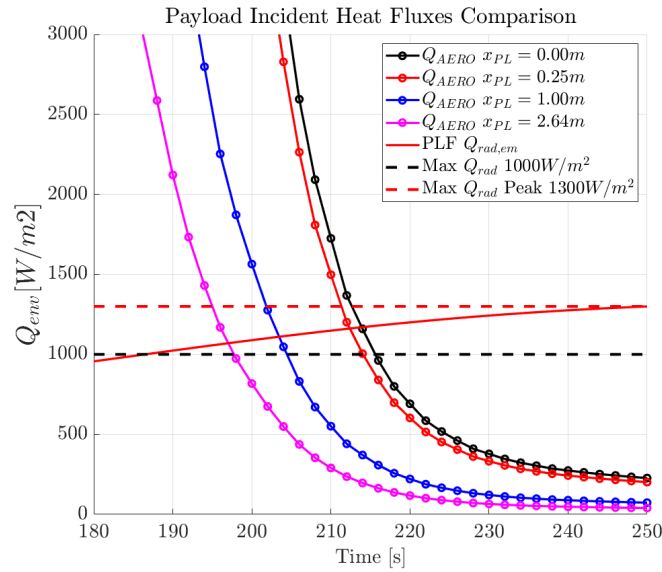


Figure 5.21: Dummy payload potential external aerothermal convective fluxes and maximum PLF emitted radiative heat fluxes comparison at various reference stations

5.4 Re-entry Casualty Risk Statistical Modelling

An important role in the development of space missions is taken by the End-of-Life disposal strategies, which could be performed in many ways. One of those which applies to LEO missions, is the controlled or uncontrolled atmospheric re-entry. The controlled re-entry assumes that the spacecraft will have enough fuel to perform a maneuver in order to crash away from land masses. The uncontrolled re-entry assumes that the satellite will re-enter in a passivation state, unable to be controlled, and it will break up and re-enter the earth atmosphere. Small satellites will often demise completely during the atmospheric re-entry, even though heat resistant materials (e.g.: titanium) may survive the harsh environment and pose a threat to the human population. In the past, guidelines for the limitation of space debris associated casualties have been published by both NASA and ESA, and a general consensus appeared to be accepted by the inter-Agency Space Debris Coordination Committee. In the NASA-STD 8719-14 it is described the best practice for analyzing the Casualty Risk associated with controlled or uncontrolled re-entry of space debris released by the NASA. A thorough description of the analysis to be performed concerning atmospheric re-entry casualty risk may be found in the Space Debris Mitigation Compliance Verification Guidelines released by the European Space Agency. A general consensus has been found by defining a threshold for the acceptable human Casualty Risk, which must be below 1:10'000. The human

casualty expectation is defined as:

$$E = D_A * P_D \quad (5.124)$$

where D_A is the debris casualty area and P_D is the average population density for the particular orbit inclination. The Debris casualty area is defined as:

$$D_A = \sum_{i=1}^N \left(\sqrt{A_p} + \sqrt{A_i} \right)^2 \quad (5.125)$$

where $A_p = 0.36\text{m}^2$ is the average cross section of a standing individual, and A_i is the cross section of the surviving debris with a kinetic energy above 15J. The European Space Agency allows the compliance study to be performed with either object-oriented re-entry tools (e.g.: DRAMA, DEBRISK, ORSAT, DAS) or spacecraft-oriented ones such as SCARAB. The analysis should be performed taking into account the uncertainty on different inputs: atmospheric density, drag coefficient, spacecraft mass, initial state vector, break-up altitude. Additional uncertainty parameters should be considered for controlled re-entries with off-nominal conditions.

In this chapter, the interfacing of STRATH-A with different modules which allow the statistical evaluation of the Human Casualty Risk, surviving fragments and mass, and their ground impact location in terms of latitude and longitude is presented. In the first sub-paragraph, the initially tested concepts are presented, highlighting pros and cons of different modelling approaches. In the second sub-paragraph, a general description of all the required updates to the block structure of the code along with all the different assumption for the break-up will be described. In the last sections different test cases are presented, along with different ways for modelling the re-entry casualty risk with a statistical approach.

5.4.1 Initial Testing of 1D ablation modelling

In the previous study cases, STRATH-A had been interfaced with a 3DOF trajectory propagator and a 1D thermal ablation analysis code; the results were matching with both numerical and experimental results. Therefore the same 1D approach was tested for the complete demise simulation of spacecrafts components. Although, many difficulties and problems were found when modelling the complete demise of a general arbitrary shape. In fact, STRATH-A does not create a complete 3D mesh, but it uses a surface mesh to estimate the boundary conditions, which makes FOSTAD a boundary element simulation tool. The use of a 1D approach, would allow to propagate the heat transfer and temperature from the outer surface to the innermost shells of the object. Although,

if the object is expected to undergo a complete demise, the 1D mesh handling becomes complicated. Indeed, each discretized shell will greatly change its properties, and the temperature and energy balance should be considered depth-dependent. In addition, due to the general application to different metallic and non-metallic materials, different approach and discretization should have been applied. In addition, the recession of the outer surface makes the mesh handling very complicated; different approaches could have been used to treat the dynamic mesh evolution, but a thorough study should have been performed and its implementation within STRATH-A would have required a great change in the code structure. Some initial test using a simplified mesh modelling approach and a 1D thermal and ablation modelling, similar to the one used for Stardust and IXV study cases, were tested. Although, the results for full objects were not found to be accurate. The only cases where a 1D modelling approach could be used satisfactorily was when applied to thin shells. An example of using the 1D thermal-ablation modelling was presented at the 4th International Workshop on Space Debris Re-entry (Fig. 5.22). Some of the benefits of using a 1D shell modelling are:

- Better employment of the local radius approach
- Local heating and ablation attitude-dependent
- Geometric evolution dependent on the local ablation
- Ability to capture localized break-ups and detachments
- Localized heating on exposed internal components

Although, the 1D modelling of shell objects creates some difficulties in the computational procedures:

- Necessity to propagate not only the state vector, but also the temperature and recession on each mesh panel
- Detection and monitoring of the completely ablated panels
- Center of mass and inertia changing non-uniformly
- Computational cost scaling with the number of mesh panels (due to the integrated thermal problem required to be solved at each propagation step)
- Ability to treat differently shell and full objects

The increased computational time, along with the increased complexity of the problem to be handled, is one of the main reason for not using this approach in the following casualty risk analysis. Instead, a common 0-D (also known as a lumped mass approach) was used. A 1D approach against a 0D approach, on an average re-entry trajectory propagation, required 10 to 20 times the computational cost (dependent on the setup accuracy), limiting the statistical analysis that could be performed.

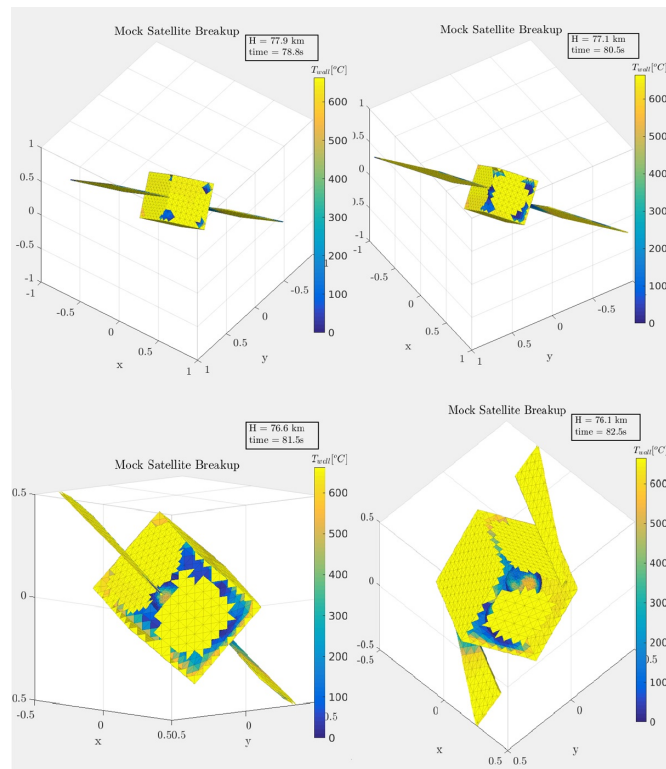


Figure 5.22: Local ablation of a cubic shell made possible by using a 1D thermal-ablation approach.

5.4.2 Lumped Mass Approach (0D), required modules, and assumptions

The lumped mass approach is used by most object oriented re-entry tools, and is the simplest modelling solution that can be applied to simulate the thermal-ablation of a re-entering body. The main assumptions are the following:

- The temperature is uniformly distributed
- The ablation is initiated once the body reaches the melting temperature
- The molten mass is supposed to be blown away from the outer flow
- The radiation cooling is dependent on the body temperature and the total radiating surface

This approach would be equivalent as simulating a 3D material with an infinite conductivity (i.e.: the body temperature will always be uniformly distributed and equal to the average body temperature). The limitation using this approach is that no local phenomena could be highlighted, and the radiation cooling will be generally underestimated; indeed, generally, the wall temperature will be higher than the averaged temperature of a re-entering body. Although, the ablation will begin only when the average body temperature will be equal to the melting temperature, which is very conservative. Indeed, in a real re-entry, the outer surface of an object will begin to melt before the average body temperature will be equal to the melting temperature. This means that a lumped mass approach generally overestimates the surviving mass and the surviving fragments cross section.

Geometric Scaling

The commonly used object oriented software, do not take into account the structural stress for performing the break-up, as a spacecraft oriented tool such as SCARAB would do, thus the single bodies are simulated as a whole till they demise completely. Even though, it is unclear how all the different available software (i.e.: DEBRISK, DAS, DRAMA) treat the geometry and shape evolution with the ablation, but as it was also highlighted in [Ling, 2015], the surface and mass reduction has a non negligible effect in both the trajectory propagation and the amount of absorbed heat. In fact, not considering the volumetric reduction with the progressive ablation will result in a significant overestimation of the absorbed heat flux, which leads to an underestimation of the casualty risk. In this work two types of bodies will be treated differently:

- Thin shells: no geometric variation is considered
- Full bodies: uniform scaling with the progressive ablation

The use of a 0-D thermal ablation model prevents the use of a local ablation approach, thus the only viable geometric evolution is the uniform scaling. The thin shells will have a negligible volumetric variation, which depends on the ratio between the shell thickness and shell size; The lower this ratio the more negligible the geometric variation becomes.

All the reference values along with the cross section, reference lengths, and mesh dimension change with the ablation progression. Thus the local radius computed for each object decreases with the progressive ablation, this is of particular importance as the decreasing of the radius causes an increasing heat-flux as the object become smaller. All the current software currently use a reference equivalent nose radius, which is thought to be fixed and defined for the complete object. This difference is thought to have a high impact on the derived final surviving mass; some tests have been conducted to evaluate this differences.

Mass and Inertia Estimation

Another important aspect is the estimation of the mass properties. STRATH-A, by itself does not allow to estimate the mass and inertia matrix of a body. Therefore a module which could allow this capability had to be programmed. For this purpose, a voxelization algorithm present in MATLAB file exchange has been adapted and integrated for creating the discretized voxelization of the object. The algorithm is based on the ray tracing implementation described in [Patil and Ravi, 2005]. The discretized voxelization of the object, associated with a material type, allows the estimation of the following:

- Mass distribution
- Center of gravity
- Inertia matrix estimation
- All the above mentioned properties evolution with the progressive ablation

Even though using an uniform geometric scaling does not take a significant advantage of this module, this method would have allowed STRATH-A to recompute the inertia matrix with the progressive non-uniform geometric scaling. The voxelization require a certain amount of time, which depends on the requested voxels resolution, volume to be ray-traced and number of facets and directions used for the ray-tracing, using a Intel® Core™ i7-4790 CPU 3.60GHz x8 and a resolution of 150 per maximum side length of the object the algorithm could require up to 5 6seconds for a cube.

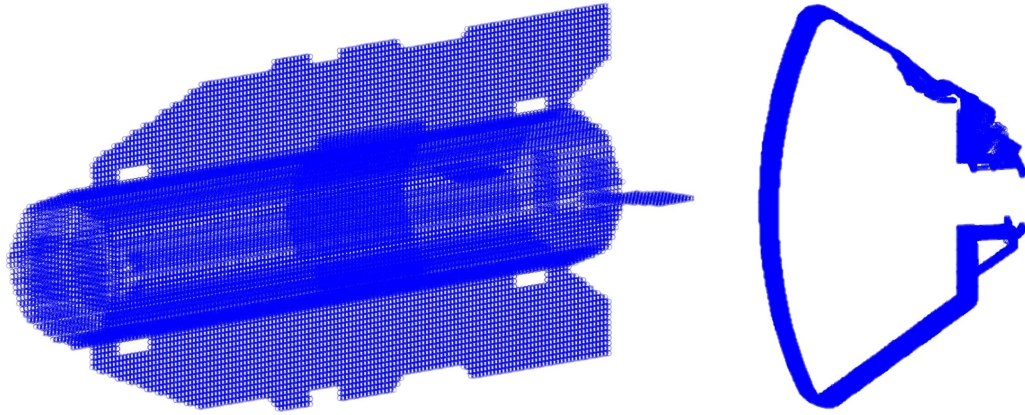


Figure 5.23: Voxelization example of complex objects. On the left: full body voxelization of GOCE, on the right: shell voxelization of a complex model of Orion CEV (only a slice has been shown).

The implemented voxelization algorithm allows the correct estimation of both mass and volumetric properties, with an accuracy comparable to a 3D mesh. Although, the computational time is significant (considering that a simulation with STRATH-A requires approximately 1 second), therefore, the re-voxelization to estimate the mass properties variation during the ablation phase needs to be performed with a discrete mass variation of the object. Indeed, it cannot be performed at each step, otherwise the computational cost will be too heavy, and the benefit will be negligible. An example of a complex geometry voxelization is shown in Figure 5.23, on the left a full voxelization of GOCE, and on the right a shell of the Orion CEV. The voxelization of shell objects requires that the thickness of the shell is higher than the voxelized grid resolution, otherwise it could not be properly captured.

3DOF and 6DOF uncontrolled Trajectory propagation

The trajectory propagation, along with all the properties that needs to be controlled during the re-entry, are managed directly with a Ordinary Differential Equation solver, which in this case is based on a simple 4th order Runge-Kutta. The trajectory propagation can be performed with either 3DOF, with a random tumbling motion, using a fixed rotational speed around the selected axis, or with 6DOF where the rotation angles velocities depend on the aerodynamic moments, the 6DOF implementation has been coherently programmed as in [Chao et al., 2015].

In order to implement an uncontrolled 6DOF re-entry, the body, which is composed by different parts needs to have an aggregated inertia matrix. Therefore, STRATH-

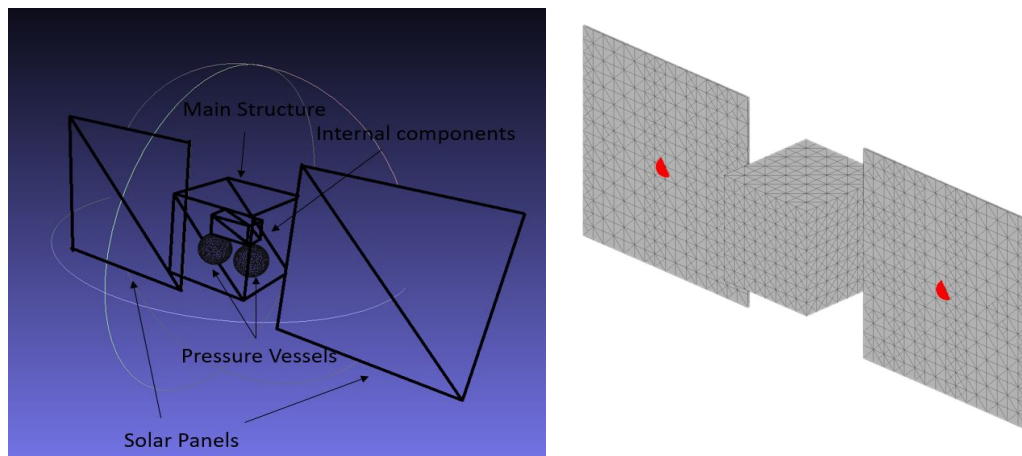


Figure 5.24: Toy satellite initial 3D .stl model assembly (left) and mesh (right) with center of gravities of each singular part (red dots).

A mesh module had to be updated in order to handle bodies composed by multiple parts. The voxelator allows to compute each component inertia matrix by based on the discretized mass distribution. The voxelized cloud allows to compute the inertia matrix of the assembly of multiple body parts, along with the center of gravity of the complete body. The geometries must be oriented and relatively spaced from a common reference system (example in Figure 5.24).

The 6DOF trajectory propagation requires that the computed aerodynamic moments are referred to the complete body center of mass, which is computable thanks to the voxelator. The center of mass may change during the re-entry, as the different bodies may start melting before the breakup, influencing the attitude of the re-entering body. During the first part of the trajectory (i.e.: before the breakup) the body may keep a stable attitude with small fluctuation on the angle of attack or side-slip, but after the breakup it is very likely that each singular part will begin to tumble. The 6DOF propagation requires a small time step (related to the rotational speed), which usually implies a higher computational time. The aerodynamic forces may cause the body to start tumbling before the break-up, the tumbling before the break-up may have an effect on the trajectory taken by the released components. The trajectory propagation is concluded when the particular component reach a very low mass, whose terminal velocity (for an equivalent spherical body) has a Kinetic energy lower than 15J, or when a reference altitude of 10km is reached.

Break-up Assumptions

Simulating the break-up of the satellite with a low-fidelity approach would at least require the computation of internal stresses on the joints and connection between the different components, which in this work could not be considered, as it would have required the implementation of the connection and definition of critical nodes, mechanical material properties, and the transfer of aerodynamic and mass forces on the critical nodes. The implementation of such approach was considered beyond the time-line and scope of this study case.

The approach that was considered in this application was very simple and similar to the one used in software such as DAS or DEBRISK: the break-up was considered to occur at a predefined altitude, where all the components are released at once from the main body. Such release could happen with different modes, taking into account the initial rotational speed of the complete spacecraft and considering the inertia and moment conservation, or simply neglecting the rotational speed during the break-up and allowing the released parts to just follow the main body trajectory. In the studies presented in this paragraph the assumption was the following:

- The break-up was considered to happen with a fragile rupture
- The contribution of the rotational momentum of each body part to the complete body is converted in linear momentum after the break-up
- The velocity direction of the released part depends on each part position with respect to the complete body center of mass.
- The rotational velocity of the released part is equal to the complete body rotational velocity (as per the conservation of kinetic energy)

It was decided to use this approach in order to be able to evaluate how different rotational speed could affect the ground footprint.

5.4.3 HDMR-based Sensitivity Analysis of Re-entry Survivability of an Aluminum Cube

The first test case was to quantify the influence of different parameters of the modelling approach and of the re-entry problem, a sensitivity analysis has been performed coupling the AD-HDMR software and the re-entry problem (a similar coupling was performed for the aerodynamics of GOCE, and has been thoroughly described in [Falchi et al., 2018]).

The goal of this analysis was to evaluate the influence of each singular variable and their interaction toward the computation of the surviving mass of an aluminum cube

with a side length 0.25m and a weight of 42.18kg. For the purpose different parameters were taken into account:

1. Initial Flight Path Angle (γ)
2. Rotational Velocity (ω)
3. Re-entry Velocity
4. Integration Time step
5. Number of Panels
6. Number of smoothing panels (local radius algorithm)

The choice of parameters was driven by the goal of comparing variables that are known to have a significant effect on the surviving mass of a re-entry (e.g.: flight path angle and velocity) with parameters which are commonly assumed as constants (the tumbling rotational velocity), and other setup parameters intrinsically used within STRATH-A. This sensitivity analysis would allow us to preliminarily evaluate the effect of the setup parameters and their interactions on a re-entry risk analysis. A particular parameterization for the rotational velocity was made, deciding to fix the rotational velocity of the tumbling object with:

$$\begin{bmatrix} \omega_1 \\ \omega_2 \\ \omega_3 \end{bmatrix} = \begin{bmatrix} 0 * R_{R,1} \\ 10 * R_{R,2} \\ 5 * R_{R,3} \end{bmatrix}$$

Defining the R_R [deg/s] as the rotational ratio for the three different components which are respectively the roll, angle of attack, and side-slip rotational velocities. Such parameterization would allow to quantify the different effects of different rotational speed combinations, which could allow the characterization in a random tumbling motion. For this specific study case it was chosen to use a simplification of $R_{R,1} = R_{R,2} = R_{R,3} = R_R$. As an example, using a $R_R = 5$ would lead to a rotational velocity of 50deg/s and 25deg/s on the pitch and yaw axis respectively. In this study case, the objective was not exactly to quantify the different combinations of tumbling motion rather than see if the rotational speed had a interaction with the setup parameters (e.g.: a resonance effect dependent on the initial attitude and the chosen time step).

In order to allow the statistical analysis with the HDMR methodology it is necessary to define the initial variables distributions. For this case only uniform distributions have been used, and the range are the following:

1. (γ): [-2.4; 2.6] deg
2. R_R : [-12 -6]; [-120 -60]deg/s (pitch) and [-60 -30]deg/s (yaw)
3. Velocity: [7400; 7800]m/s
4. Integration Time step [0.5; 1.5]s

5. Number of Panels [1600 3200] panels
6. N. smoothing panels: [4; 20]

Even though the code would be capable of performing 6DOF simulations, in this case, the simulations were performed with a 3DOF approach with an attitude determined by the constant rotational velocities only.

The AD-HDMR software performs an adaptive sampling of the N-dimensional domain according to the HDMR-cut approach [Kubicek et al., 2015], selecting the most important sub-domains for extracting the samples from the previously defined distributions. The algorithm stops when a predefined degree of statistical convergence has been reached, creating the N-D surrogate models of the significant variables and their interactions. Performing a Monte Carlo sampling on the selected variable within the defined intervals, and using the constructed surrogate models to evaluate the surviving mass, the probability histogram shown in Figure 5.25 was obtained.

In order to better evaluate the results, the sensitivity analysis of each variable and their interactions within the considered intervals must be considered, the results are reported in Table 5.1. To achieve these results 184 simulations were needed, at each simulation the entire re-entry simulation were performed with the parameters value selected by the AD-HDMR code, in order to construct the dataset to build the surrogate models and reach a statistical convergence of the sensitivity analysis variables. Different level of accuracy were progressively tested, using a lower accuracy would've required fewer simulations with a similar output; such an observation is useful to remind the reader that a significant randomness is intrinsic to such simulation approach.

The sensitivity analysis results show both the sensitivity on the mean and variance. The sensitivity on the mean represents how much the mean of the specific distribution is deviated from the central value, indicating the specific contribution to the variation of the mean of the statistical distribution. For example, a centered symmetric distribution would not have any influence on the sensitivity of the mean, even though it will have an impact on the sensitivity of the variance. The sensitivity of the variance is representative of the dispersion of the output around the central value, the higher the dispersion of the distribution the higher will the specific variable have an impact on the global outcome standard deviation.

The results reported in Table 5.1 highlight some interesting outcomes:

- The flight path angle (FPA) has a significant impact on both the mean and the variance. Also the FPA interactions are significant, with exception of the number of panels.
- The Rotational Ratio (representative of the tumbling rotational velocity) and its interactions with the other variables are significant

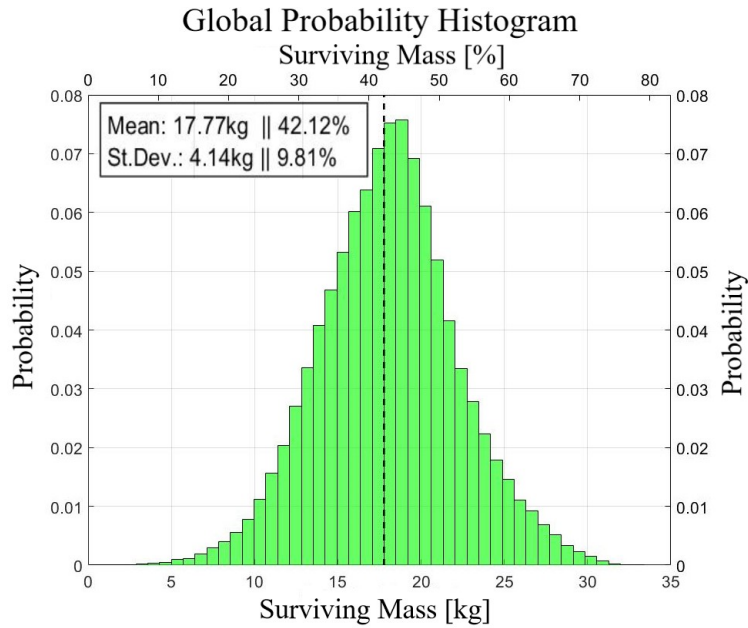


Figure 5.25: Surviving mass probability histogram obtained with the Monte Carlo sampling in the defined interval with the HDMR approach.

Table 5.1: Sensitivity analysis results of the surviving mass computed with the AD-HDMR.

ID - Variable	Partial Mean	Partial Variance	Mean Sensitivity	Variance Sensitivity
1 - γ (FPA)	0.5351	1.3598	12.1%	8.0%
2 - ω	-0.4973	0.2789	11.2%	1.7%
3 - Velocity	0.4448	7.5773	10.1%	44.8%
4 - Time Step	0.0689	0.8533	1.6%	5.0%
5 - N. panels	-0.1326	0.2259	3.0%	1.3%
6 - N. smooth	0.8279	0.7094	18.7%	4.2%
1.3	-0.6708	0.7103	15.2%	4.2%
2.4	0.2615	0.2002	5.9%	1.2%
2.6	0.2604	0.1605	5.9%	1.0%
2.3	-0.215	0.058	4.9%	0.3%
3.4	-0.1939	0.9591	4.4%	5.7%
1.4	-0.1766	0.857	4.0%	5.1%
1.2	-0.0781	0.167	1.8%	1.0%
4.6	-0.0385	0.9604	0.9%	5.7%
3.6	-0.0187	1.4249	0.4%	8.4%
1.6	-0.0046	0.4298	0.1%	2.5%

- The velocity, as it would've been expectable, has a high impact on both the mean and the variance. The variance sensitivity has a particularly high index value, which means that the variation of the velocity will significantly change the surviving mass.
- The time step does not have a high sensitivity index, even though it is still significant considering its interactions with other variables.
- The number of panels used for mesh does not seem to have a significant impact on the surviving mass
- The number of smoothing panels used for the local radius computation has a significant influence on the surviving mass.

The results must be analyzed considering both the variable distribution and its specific surrogate model. The surrogate model of a single variable is built blocking the other variables at their central value (defined as the mean of their maximum and minimum value). The variable distribution is built via a Monte Carlo sampling of the variable surrogate model, and it is expressed in terms of relative increment w.r.t. the output central value (i.e.: the surviving mass when all the variables are equal to their central values). Some examples are reported to clarify the results analysis. In Figure 5.26, the flight path angle relative increment distribution and surrogate model are reported. The FPA is an example of a variable with a significant deviation from the mean and a high variance. The rotational velocity, expressed in terms of the rotational ratio has been reported in Fig 5.27, the single variable surrogate model appears to have been computed within a stable interval, a wider interval should be better analyzed, even though it is already visible how the rotational velocity could affect the surviving mass, especially considering that all the interaction have been detected as significant by the AD-HDMR code. Another example is reported for the initial velocity, which appears to have a very high sensitivity variance index. In fact, as shown in Figure 5.28, the range covered by the relative increment distribution is by far the highest of the all the variables (highlighted by the tabular variance value of 7.58). Although, this value appears to be slightly altered by an accumulation of sampling points around the velocity value of 7450m/s. In fact, in the nearby points, a the stochastic variation determines a higher density of probability, which is highlighted by the increment function around the value of 6 on the left of Figure 5.28.

Another interesting variable to consider is the number of smoothing points, shown in Figure 5.29. In the previous chapters, it was highlighted how changing the number of smoothing points used for the local radius algorithm could affect the heat-flux distribution. It was noticed how using a low value of N_{smooth} could keep the increment of the heat-flux localized nearby the edges, while a high N_{smooth} could better represent the

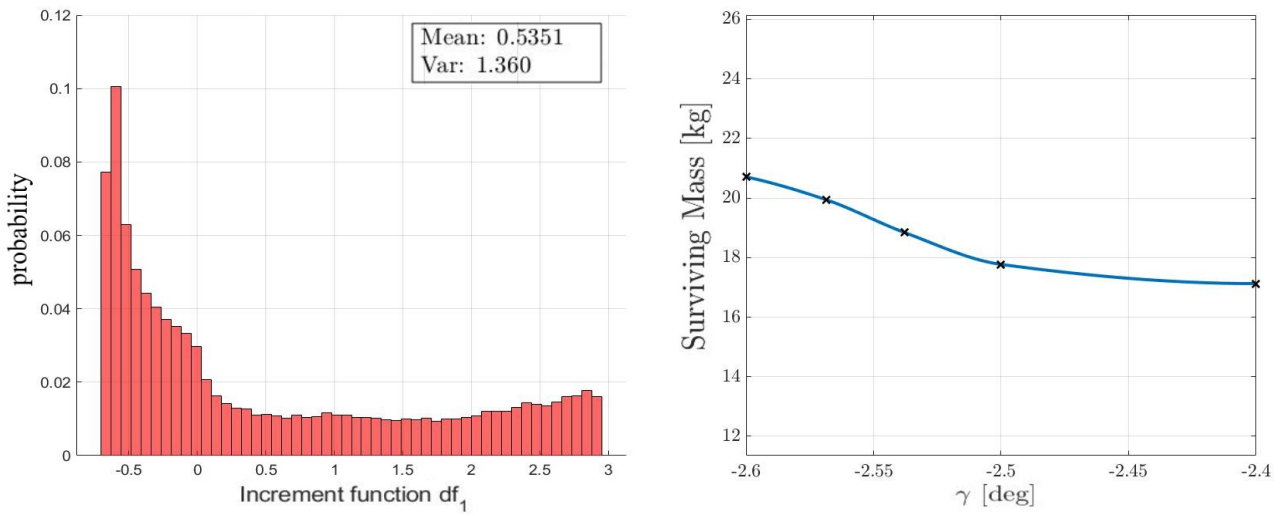


Figure 5.26: Left: Distribution of the flight path angle increment function (i.e.: surviving mass w.r.t. to the central value). Right: surrogate model used for building the increment function distribution.

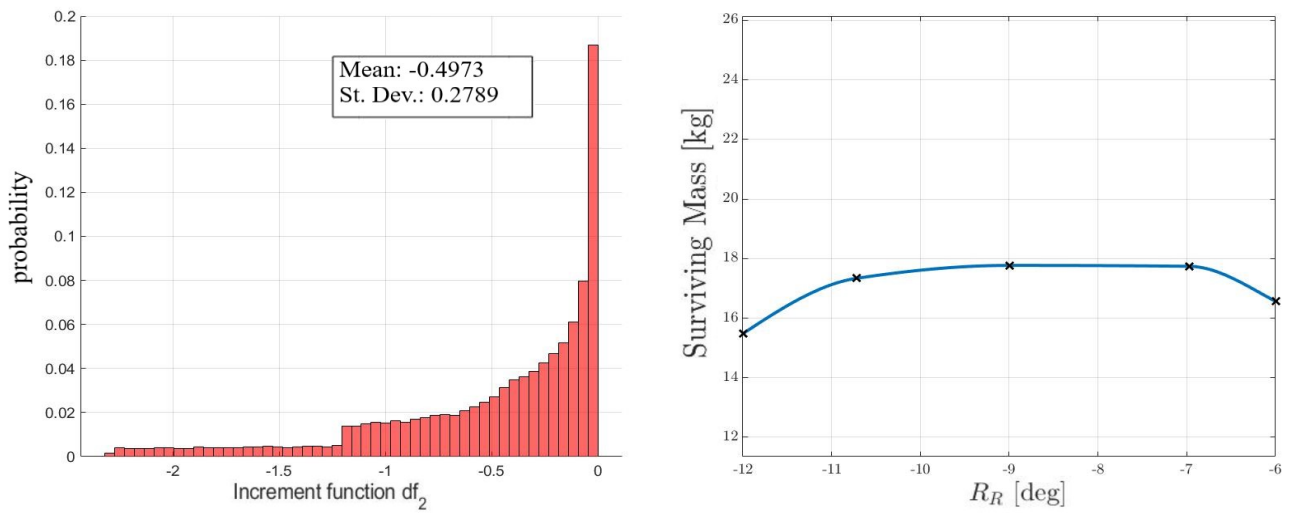


Figure 5.27: Left: Distribution of the rotational velocity increment function. Right: surrogate model used for building the increment function distribution.

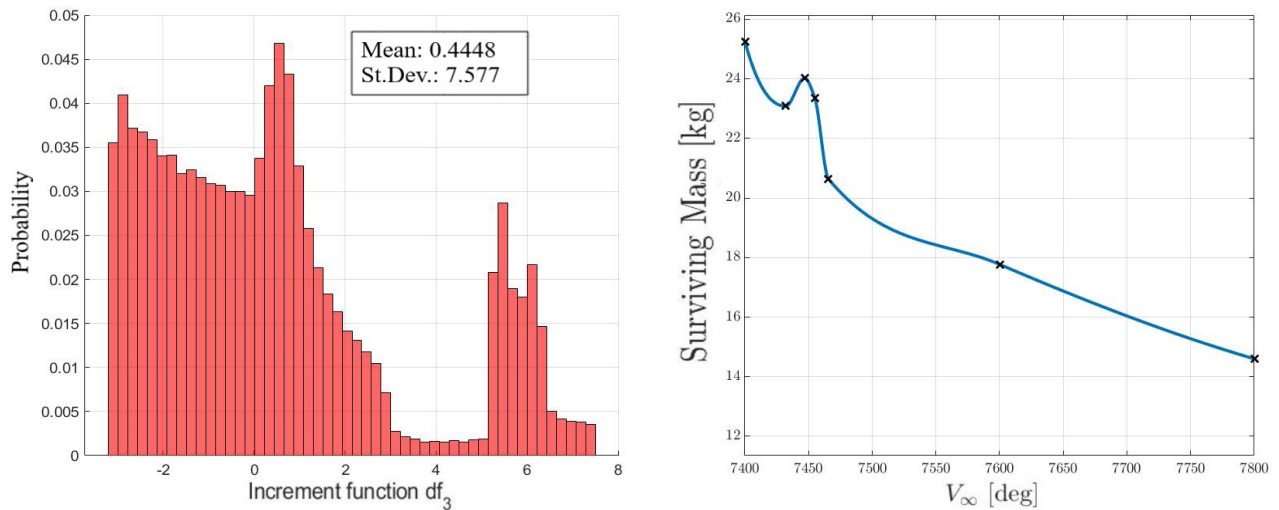


Figure 5.28: Left: Distribution of the initial re-entry velocity increment function. Right: surrogate model used for building the increment function distribution.

heat-flux distribution that was obtained with CFD tools. In this analysis, it is possible to observe that the mass variation due to the number of smoothing points, could reach a convergence for $N_{\text{smooth}} > 12$. It must be noted that the influence of the smoothing point appear to be extended to all the other interactions.

The same kind of analysis could be extended to the 2nd order surrogate models, even though in this case it would be required to analyze the response surfaces. In this analysis two different kind of parameters have been analyzed in the same instance, even though they belong to different categories. In fact, the velocity and flight path angle can be determined before the re-entry of the spacecraft takes place, thus a small uncertainty could be applied to their values. Although, a different degree of uncertainty should be considered for the rotational velocity and intrinsic modelling parameters. The rotational velocity and the combination of the random tumbling motion, as it was highlighted by this analysis, can have a great impact, and an exact value is very difficult to determine, even if using a 6DOF approach. Indeed, in order to be able to simulate a correct attitude during the trajectory propagation, a progressively decreasing integration time step is required as the rotational velocity increases. Additionally, the modelling approach has some clear limitation when it comes to simulate the rotational velocity. In fact, the local panel method, does not allow the estimation of the rotational velocity friction. Such limitation means that the complete spacecraft, or the single object, will not reach a steady rotational velocity if the attitude is unstable.

The results highlight also the necessity of performing more comparison between the local radius approach for estimating the heat-flux distribution and high-fidelity software

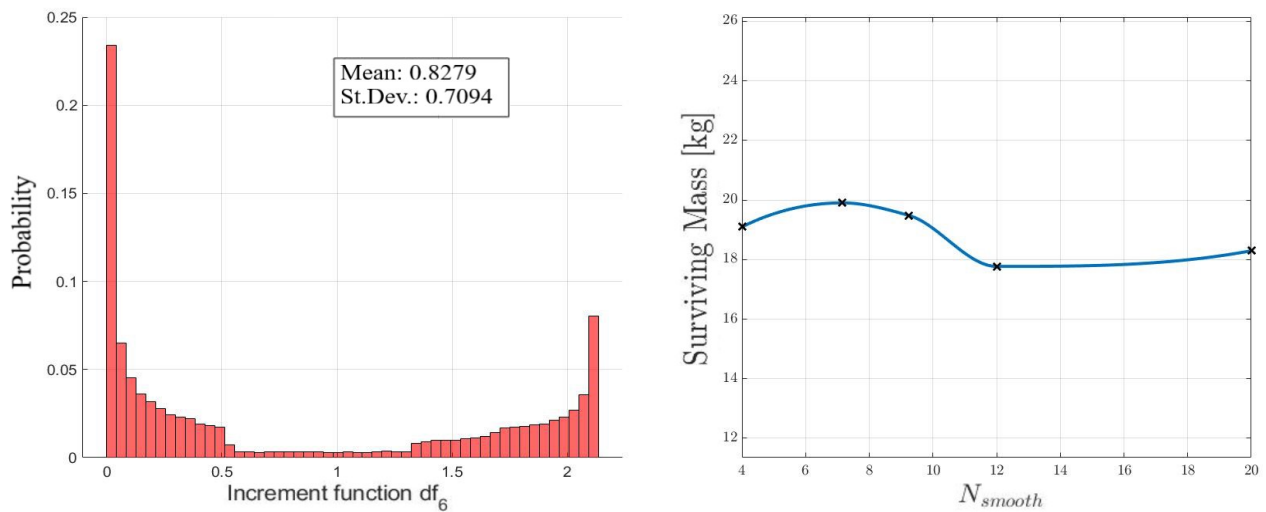


Figure 5.29: Left: Distribution of the initial re-entry velocity increment function. Right: surrogate model used for building the increment function distribution.

or experimental studies. In this way it would be possible to decrease the degree of uncertainty intrinsically present within the local radius heating estimation approach; this analysis can lead to a more general conclusion which can be applied to any local panel method-based re-entry tool. In fact, the local radius algorithm performs the same kind of analysis of any other re-entry tool, with a reference length and local radius which is automatically updated as the object shrinks due to the ablation, while other software keep the same reference length and nose radius.

Some additional simulations were performed to better investigate the influence of the Rotational Ratio, and extended the analysis to a wider interval with different FPA (which influences the re-entry time). The analysis have been reported in Figure 5.30. The results show some interesting facts:

- The rotational velocity (which increases with the rotation factor) is influenced by the FPA. In the previous HDMR analysis the interaction between the two variable was just slightly present, and it was mainly due to the small interval used for the flight path angle (which was between 2.4deg and 2.5deg).
- The FPA influences the total duration of the re-entry trajectory, a lower FPA leads to a longer re-entry. A longer re-entry implies a higher number of rotation around the axes, allowing the heat-flux to be better averaged. This is represented in the analysis by the higher amplitudes of the fluctuating surviving mass w.r.t. to the rotation factor.
- An increasing rotational velocity seems to increase the surviving mass of the ob-

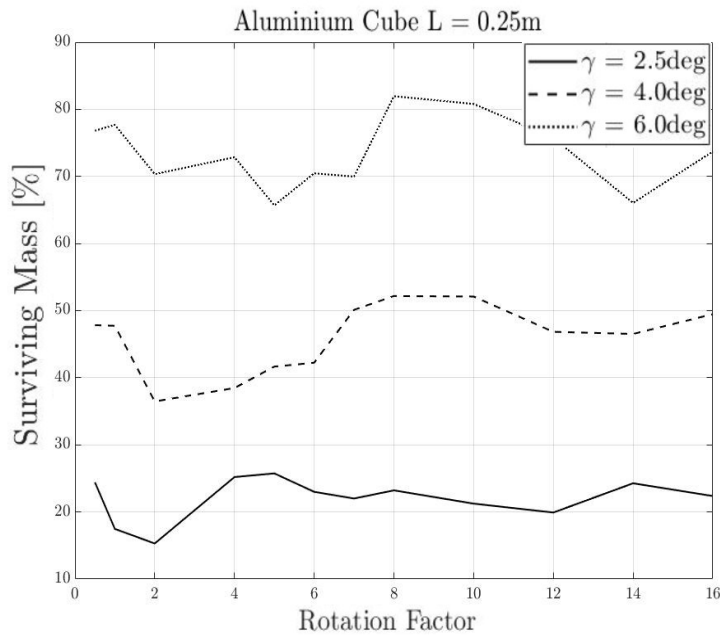


Figure 5.30: Aluminum cube angular rotational factor analysis for different initial flight path angles.

ject, slowly converging and decreasing the the fluctuations.

Even though this results highlight different aspects, it is still clear that the rotational tumbling velocity should be taken into account as an uncertainty variable. In fact, even though the fluctuations on the surviving mass w.r.t. to the rotational velocity can be reduced by using an increased tumbling velocity, the rotational velocity of a tumbling object during a re-entry cannot be exactly determined due to the many different simplified assumptions on the break-up triggering.

5.4.4 Demise altitude of a Sphere

The second preliminary test compares the demise altitude of a sphere of different materials with respect to the initial diameter computed with STRATH-A and the ones reported by Klinkrad [Klinkrad, 2005]. This analysis was performed to quantify and understanding the differences between the two approach and the assumptions used to propagate the entire re-entry.

The analysis have been performed using two different materials: copper and aluminum. For the aluminum temperature dependent properties have been used [Buyco and Davis, 1970] (Fig. 5.31) with a latent heat of fusion of 398.0kJ/kg and a melting temperature of of 933.4K , density of 2700kg/m^3 . For the copper the same properties

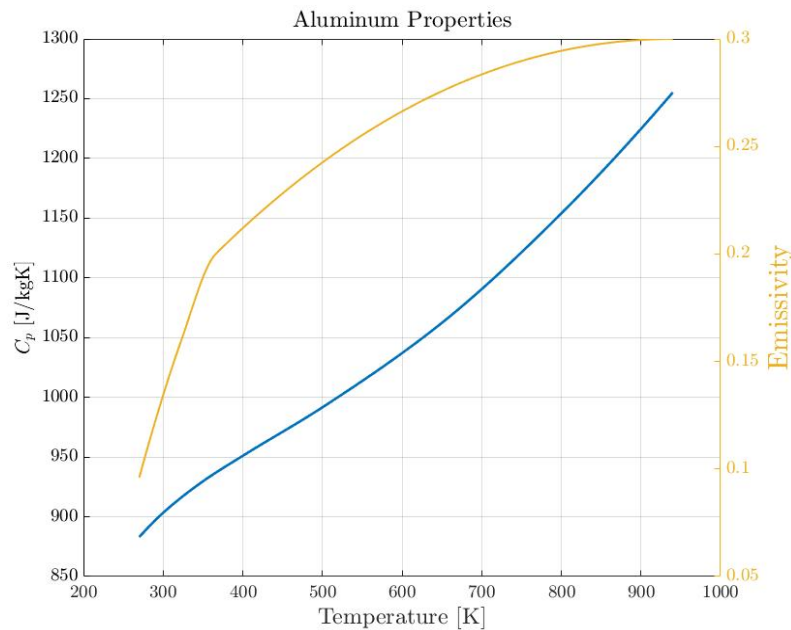


Figure 5.31: Aluminum temperature dependent specific heat and emissivity factor.

reported in [Klinkrad, 2005] were used: density of 8960kg/m^3 , specific heat 384.6J/kgK , melting temperature 1357.77K , latent heat of fusion 208.7kJ/kg , emissivity of 0.78 (for heated and oxidized copper).

A preliminary analysis on the sphere terminal velocity, useful to understand which diameters should be considered as a threat has been performed. The analysis is reported in Figure 5.32, and shows the terminal velocity of the different materials w.r.t. to the diameter (in black on the left axis) and the correspondent kinetic energy (in blue on the right axis), the edge of 15J marking the casualty risk has been reported as well. The results show that spherical objects with diameters smaller than 1cm will generally not pose a threat (by the definition reported in the space debris re-entry risk analysis guidelines).

The re-entry trajectory simulation started at 200km , with an initial flight path angle of 2.5deg , and an initial velocity of 7800m/s . A reference database for the NRLMSISE-00 atmospheric was used to compute the atmospheric properties. The comparative results are reported in Figure 5.33. The Figure shows that STRATH-A underestimates the demise altitude for small diameters and overestimates the demise altitude of higher diameters. Although the general trend is the same, the differences are not negligible. The reason for such differences are not easy to be found due to the many variables and the different modelling approach which are used in the two codes.

Some of the differences could be attributed to the different aerothermal modelling

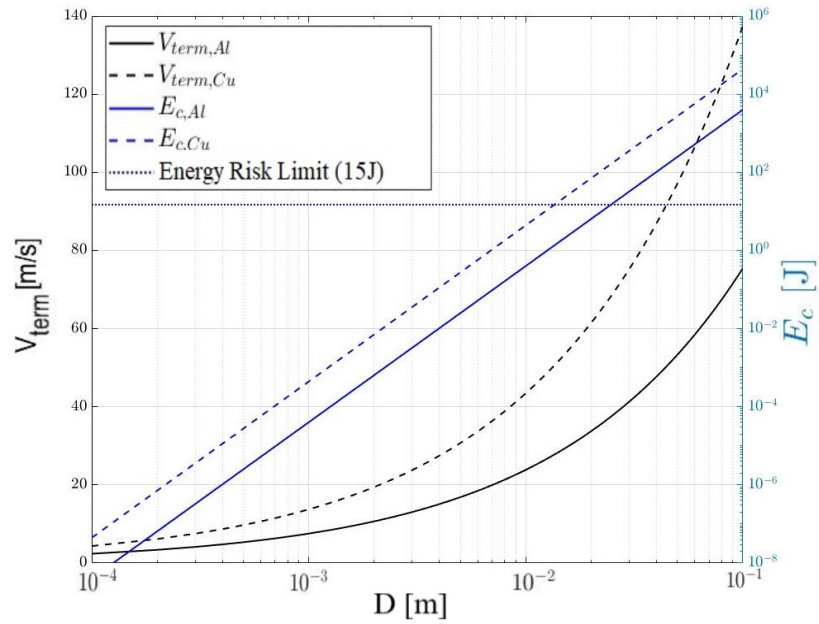


Figure 5.32: Aluminum and copper sphere terminal velocity and correspondent kinetic energy at sea level.

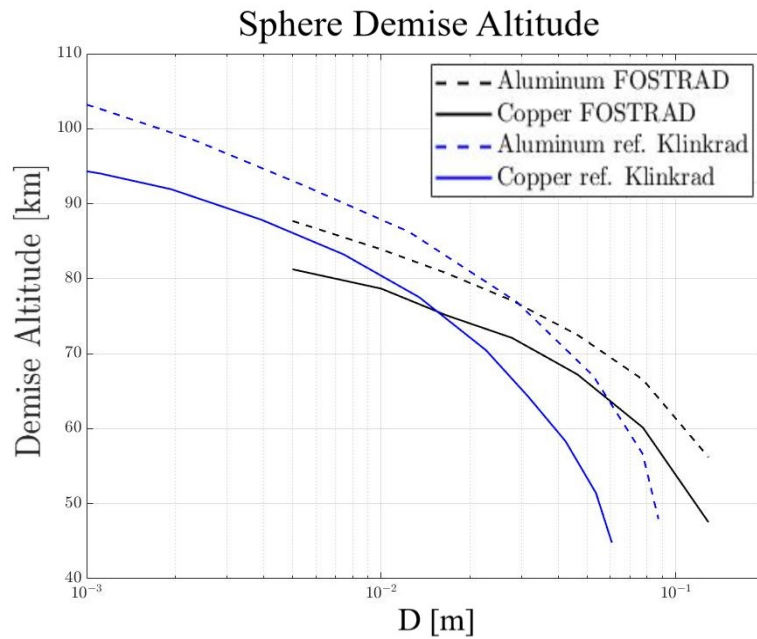


Figure 5.33: Sphere demise comparison between SCARAB [Koppenwallner et al., 2005] and STRATH-A.

formulation within the rarefied transitional regimes; in fact, in both the continuum and the free molecular regime the formulation used by STRATH-A and SCARAB should be the same (in this specific case it was used the SCARAB formulation within the continuum regime). Although, SCARAB uses a constant reference nose radius, whereas STRATH-A automatically updates the spherical radius with the progressive ablation, with an uniform scaling factor. This could lead to an increased absorbed heat-flux computed with STRATH-A in the lower altitudes. In fact, a lower radius in the continuum regime causes an increased heat-flux $\propto 1/\sqrt{R_N}$. Additionally, the progressive reduction of the spherical size with the progressive ablation, will directly change the reference length and reference cross section, which in turn will affect both, the aerodynamic and aerothermodynamic properties, as well as shifting the reference regime position (the Knudsen Number depends on the spherical diameter). The radiative cooling which depends on the total surface of the object is also affected by the progressive shrinking of the sphere, decreasing the amount of heat-flux re-emitted. It is unclear how SCARAB takes into account the shrinking of the sphere.

Another important difference could be due to the atmospheric model used. The model used for this analysis is the same that has been shown in the first chapter with a reference averaged latitude and longitude and a reference magnetic index, and it is unclear how the density, pressure and atmospheric composition over altitude compares with the atmospheric model used for SCARAB analysis.

In addition to the previous consideration, it must be reminded that the two trajectory propagators may perform very differently having a great impact on the final demise altitude. Another aspect is related to the underlying stochastic uncertainty present within the software. In fact, as it was shown in the previous chapter, minor variation in the initial flight path angle, velocity, time step, could have an impact on the surviving mass. Along with all the different modelling assumption, also this aspect will contribute to the different demise altitudes.

5.4.5 Toy Satellite Statistical Re-entry Casualty Risk Modelling

In this paragraph the previously described methodologies are employed to perform a statistical re-entry casualty risk analysis of a toy satellite (model shown in Figure 5.24). In the past, different uncertainty quantification analysis have been performed; an example shown in [Fritsche, 2015], although this analysis focus only on the break up altitude and surviving mass. Another interesting analysis, although not focused on the re-entry of spacecraft, was performed in [Mehta et al., 2015a], and in this case also the ground impact location was taken into account. The focus in this study case is on the methodological approach to perform directly the statistical analysis of the re-entry casualty

Table 5.2: Geometric dimensions and mass information for the toy satellite.

	Body_ID	Dimensions [m]	Mass [kg]	Shell Thickness [mm]
Solar Panels	1-2	0.01x1.0x1.0	13.5	/
Main Body	3	0.5x0.5x0.5	19.85	5.0
Fuel Tanks	4-5	$\phi = 0.2$	1.61	5.0
Electronic Box	6	0.125x0.250x0.125	5.27	/

risk as defined by the guidelines proposed by the IADC, NASA, and ESA. The goal of such simulation is to evaluate the application of a methodology such as AD-HDMR statistical modelling to simultaneously evaluate the impacting latitude and longitude, along with the surviving cross section of each surviving object, allowing in this way to evaluate the re-entry casualty risk with a probabilistic approach.

The mock satellite used for this study case is very simple, it is an assembly of 6 different components: 2 solar panels, 2 fuel/oxidizer tanks (shells), a main body structure (a cubic shell), and a parallelepiped (representative of an electronic box). All the components were made of aluminum, and the solar panels were assumed to have an equivalent density of 1350kg/m^3 . The geometric properties are reported in Table 5.2. All the shells have a thickness equal to 5mm.

The number of input variables and number of sampling points was limited, as the goal was not to obtain a high accuracy in the results, rather than to show the approach to model the probabilistic casualty risk and the statistical properties of the outcomes. The problem was studied according to the break-up altitude, the initial flight path angle, and the rotational velocity (once again expressed in terms of rotational ratio, see the previous paragraphs for the explanation). The use of only three input variables allows the creation of surrogate models with the linear decomposition as in the High Dimensional Model Representation approach, allowing to compute the influence of all the variables and their reciprocal interactions without neglecting any input. The output variables considered were the final propagation latitude, longitude, and surviving mass. Four sampling points per variable were used, for a total number of 4^3 simulations, the ranges used were the following:

- Break-up altitude, $H_{\text{break}} = [76\ 78\ 80\ 82]\text{km}$;
- Flight Path Angle, $\gamma = [3\ 4\ 5\ 6]\text{deg}$;
- Rotational Ratio, $R_R = [0.5\ 1\ 2\ 4]$;

the rotational ratio was used along the following rotational velocity vector:

$$\begin{bmatrix} \omega_1 \\ \omega_2 \\ \omega_3 \end{bmatrix} = \mathbf{R}_R * \begin{bmatrix} 0 \\ 12.5 \\ 7.5 \end{bmatrix} \text{ [deg/s]}$$

which leads to a minimum and maximum rotational velocity of [6.25; 50]deg/s on the pitch axis and [3.75; 30]deg/s on the yaw axis.

The assumptions are the same as the one expressed in the previous paragraph, briefly:

1. the break-up is considered to occur at a single altitude, and all the internal components will be released according to the linear and angular momentum conservation
2. The propagation is stopped at a reference altitude of 10km or when the particular child object is considered as demised (i.e.: kinetic energy at the terminal velocity of an equivalent sphere below 15J)
3. objects do not undergo a progressive breakup (i.e.: they stay as a single child)
4. shell objects do not scale down their geometric dimensions with the progressive ablation
5. full objects decrease their geometric dimension with an uniform scaling.

The uniform scaling assumption allows the computation of each object surviving casualty cross-section, dependent on the surviving mass:

$$S_{\text{ref},f} = S_{\text{ref},i} \left(\frac{m_f}{m_i} \right)^{2/3} \quad (5.126)$$

where S_{ref} is the reference cross section, m is the object mass, and the subscripts i and f refers to the initial and final state.

A detailed block diagram work-flow has been reported in Figure 5.34. The block diagram summarizes the steps and the general inputs, functions and their concatenation in order to be able to generate a complete dataset which allows the definition of a statistical re-entry casualty risk by means of surrogate models.

In order to compute the casualty risk a world population density model is required, for the purpose the Gridded Population of the World, Version 4 (GPW - v4): Population Density may be used [for International Earth Science Information Network (CIESIN) Columbia University, 2016]. The population dataset comes with a maximum resolution of 0.0417deg per latitude and longitude grid spacing. Some specific area of the world could not be mapped though, see the reference for more information. The population density mapping is shown in Figure 5.35. The original resolution is very high and

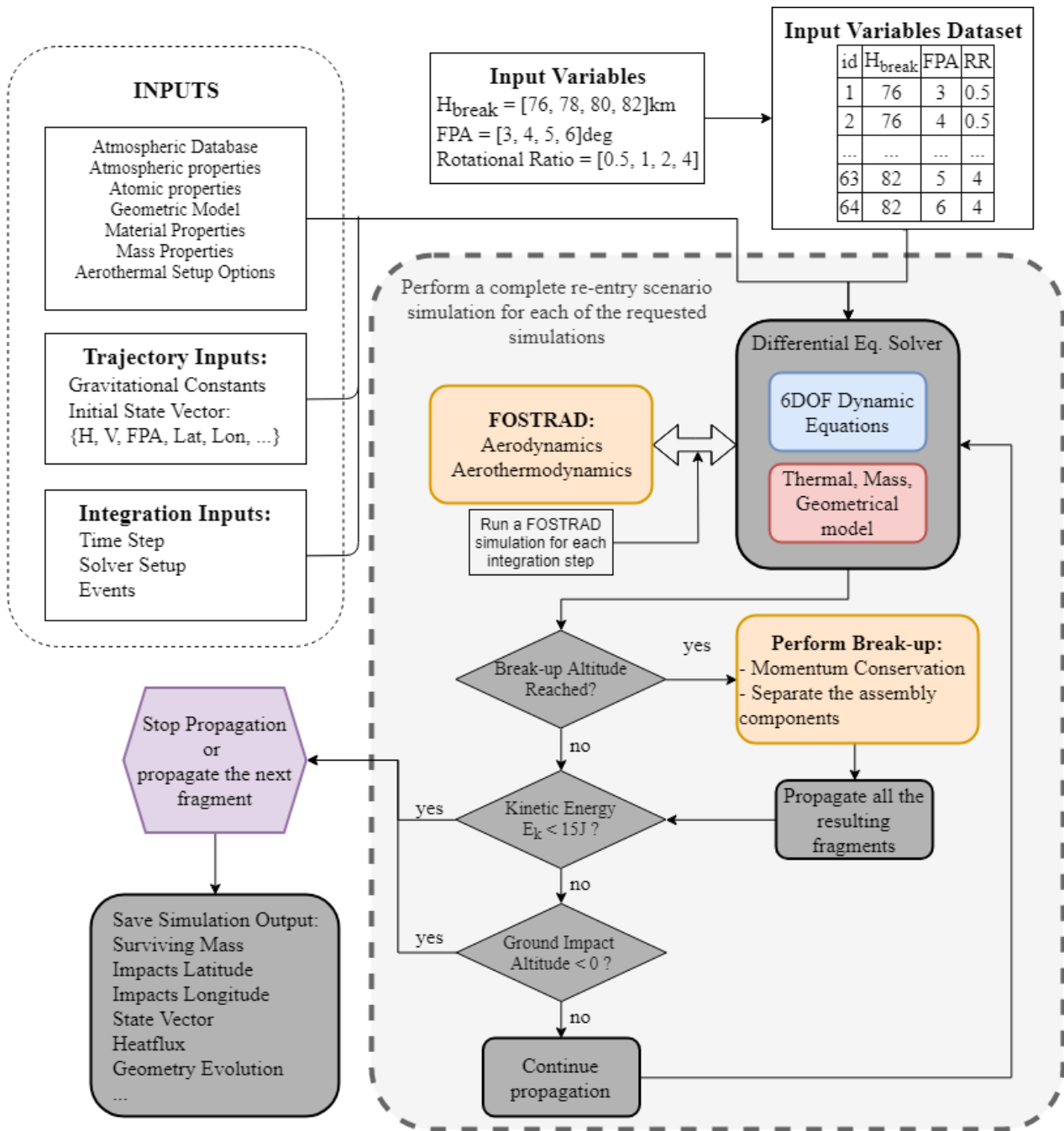


Figure 5.34: Re-entry scenario simulation block diagram and work-flow for a single break-up event and using a step-by-step aero-aerothermodynamic integration.

presents some gaps, in order to have a better statistical representation and to obtain smoother casualty risk models, it could be useful to use reduced resolution models. The reduced models can be obtained by manipulating and correctly averaging the original datasets. In Figure 5.36 it is shown a reduced resolution grid (0.5deg).

The complete re-entry dataset was composed by the 4^3 combinations of resulting latitude, longitude and surviving masses per each part of the spacecraft. Having the access to all the information of each singular re-entry case allowed the study of different methods to evaluate the probabilistic casualty risk which will be described in the following sub-paragraphs:

1. Scenario-averaged statistical casualty risk: creating a surrogate model for the global casualty risk of each case to be evaluated with a Monte Carlo sampling
2. Object-specific statistical Casualty Risk: combination of the statistical casualty risk for each singular object, and then combining them together to obtain a probabilistic distribution of the mapped risk

A visual summary of all the impact locations has been reported in Figure 5.37. The circles represent a debris falling in a uninhabited area, while the crosses are impacting a populated area with a non negligible risk. A detailed analysis of the resulting datasets has shown some general results:

1 - Ablated aluminum shells - The results of the performed re-entry scenario shown that the aluminum spherical tanks with a 5mm thickness reach a negligible mass for every simulation, thus they will not contribute to the casualty risk.

2 - skipping trajectories - For some specific test cases, the solar panels acquired a skipping trajectory, which is due to the combination of a slow rotational speed and the high area to mass ratio. In fact, for some attitudes the lift of the solar panel could cause the same skipping effect of a lifting body, causing the impact location to be very different from the other body parts. To avoid such phenomena a non-lifting re-entry could be used, even though the same effect could be achieved by using a faster rotational speed. In fact, such effect could be seen only if the solar panel had a specific lifting attitude when the altitude reached 50-60km, when the increasing atmospheric density in combination with the hypersonic velocity could cause the inversion of the flight path angle. A faster rotational speed would prevent this skipping effect due to the reduced time in which the object will have a lifting attitude. This behavior would not be detected if the solar panel were to be modelled with a progressive break-up which is likely to happen due to the combination of extreme temperatures and aerodynamic forces. The result of the skipping trajectory taken by the solar panels can be seen in the isolated impact points shown in Figure 5.37.

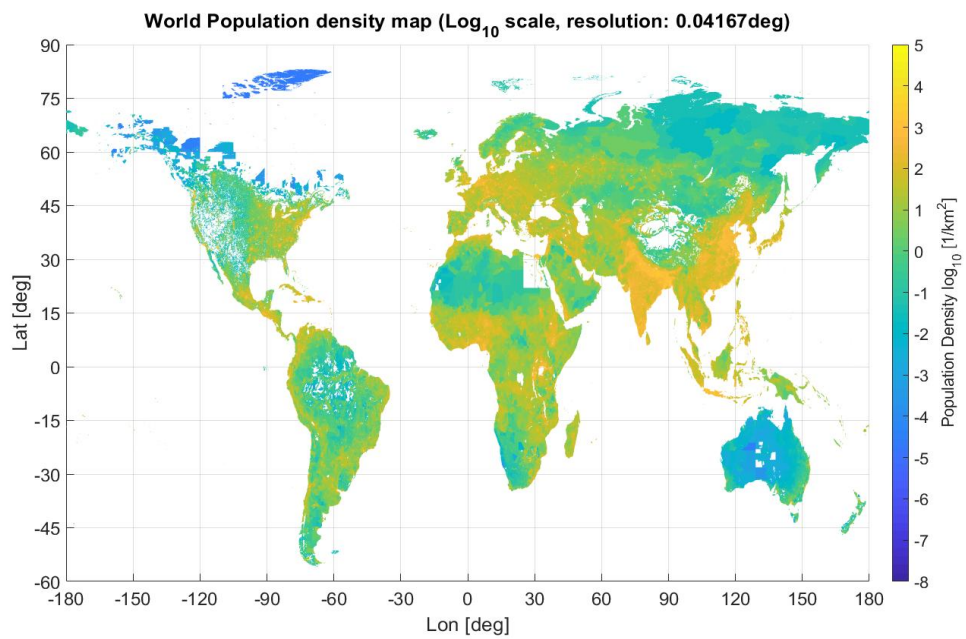


Figure 5.35: Gridded population density of the world, original resolution (0.0417deg) reported in a base-10 log scale.

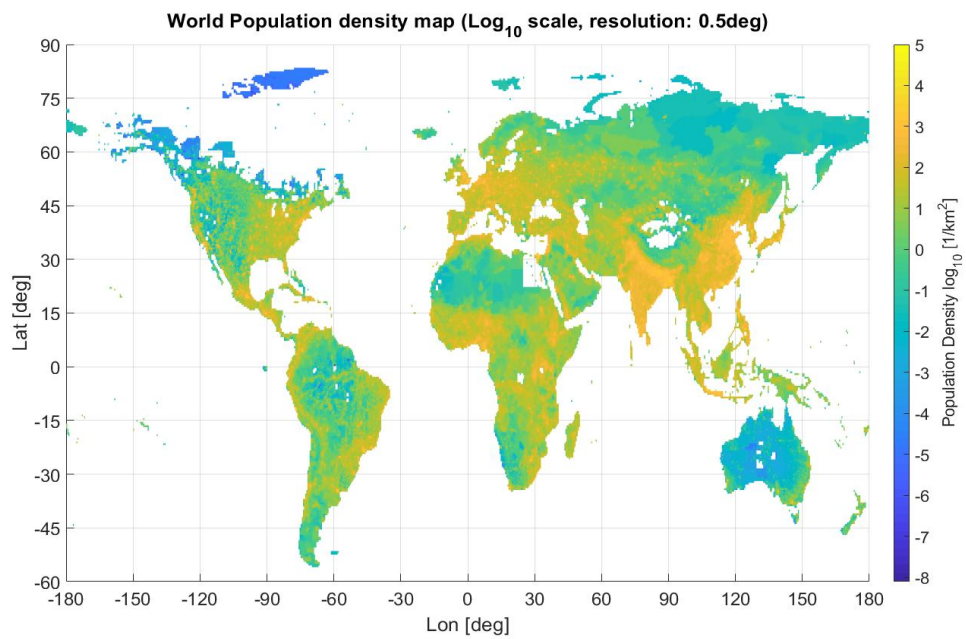


Figure 5.36: Gridded population density of the world, reduced resolution (0.5deg) reported in a base-10 log scale.

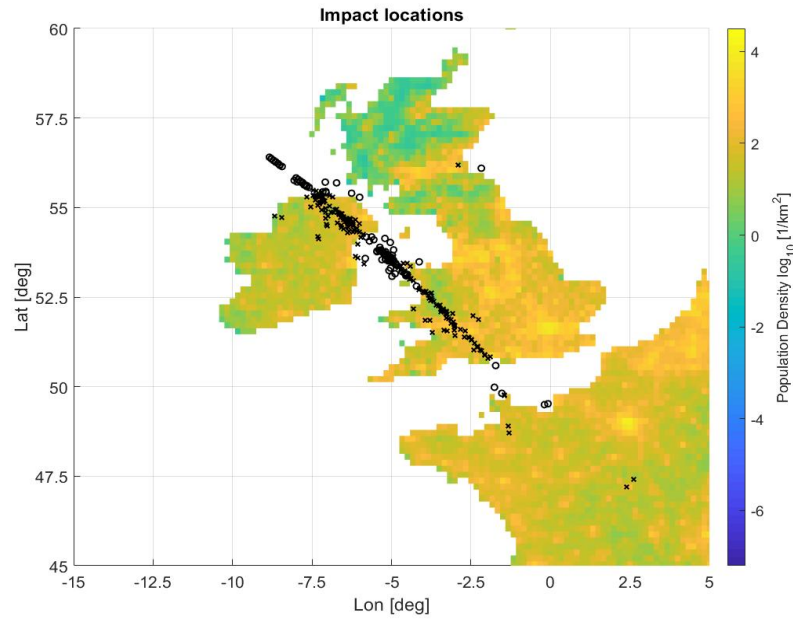


Figure 5.37: Cloud of ground impact points for all the 64 simulated re-entry scenarios.

Re-entry Scenario-Averaged Statistical Casualty Risk

The averaged probabilistic casualty risk associated with the considered variable intervals was computed considering the total casualty risk associated with each simulated re-entry scenario as:

$$E_k = \sum_{i=1}^6 P_D(\text{lat}_i, \text{lon}_i) * \left(0.6 + \sqrt{A_i}\right)^2 \quad (5.127)$$

where E_k is the casualty risk estimate for the specific scenario (k ranges from 1 to 64), P_D is the population density as a function of latitude and longitude of each surviving fragment (i.e.: with a non-negligible mass or kinetic energy) and A_i is the surviving cross section (which for the non-shell objects is scaled accordingly to the surviving mass). The expression is in the same form of the casualty risk estimate to be used from the guidelines (eq. 5.125).

The casualty risk computed in such way for each single re-entry scenario is then used to build a surrogate model with a similar approach as the HDMR, using a linear decomposition of all the variables and their interactions. The use of such approach was chosen to increase the accuracy of the surrogate model, and in order to reduce the fluctuations around the sampled points, the following surrogate models have been used:

- Single variables: Piecewise Cubic Hermite Interpolating Polynomial

- 1st order interactions: bilinear interpolation
- 2nd order interactions: trilinear interpolation

Thus the final surrogate model takes the form of:

$$\mathbb{E} = \mathbb{F}_1(H_b) + \mathbb{F}_2(\gamma) + \mathbb{F}_3(R_R) + \mathbb{F}_{12}(H_b, \gamma) + \mathbb{F}_{13}(H_b, R_R) + \mathbb{F}_{23}(\gamma, R_R) + \mathbb{F}_{123}(H_b, \gamma, R_R) + C_{val} \quad (5.128)$$

where \mathbb{F}_i is the surrogate model of the correspondent increment functions, and C_{val} is the central value used for the linear decomposition. This surrogate model was used to perform a statistical evaluation of the probability risk in the defined interval. The work-flow diagram for a the re-entry scenario averaged human casualty risk evaluation is reported in Figure 5.38.

Two different resolutions (0.0417deg and 0.5deg) have been used to compute the probability risk distribution (each one is characterized by a specific surrogate model). The results have been reported in Figure 5.39 and 5.40.

Observing the two figures it is evident that the resolution of the GPW density has a direct influence on the outcome. This is due to the presence of the zero-population location present in the high resolution grid, and the more accurate allocation of the impact points on the sea, which results in a 0 risk probability, which decreases by using a lower resolution GPW.

Another analysis has been performed creating a surrogate model using an average population density $\bar{P}_D = 38.1[1/km^2]$ (equivalent to the landmass averaged world population). Using an average values would provide results which are more in line with the definition reported in the guidelines (which require to use the orbit-specific average population). The probabilistic casualty risk obtained with the Monte Carlo sampling of this surrogate model is shown in Figure 5.41.

Observing and comparing the different casualty risk distribution, it is evident that for a latitude-longitude-specific population density the average casualty risk is higher than the simplified averaged population model. This result is strictly dependent on the expected ground footprint, while the population-averaged probabilistic distribution is more dependent on the surviving mass and the correspondent casualty area.

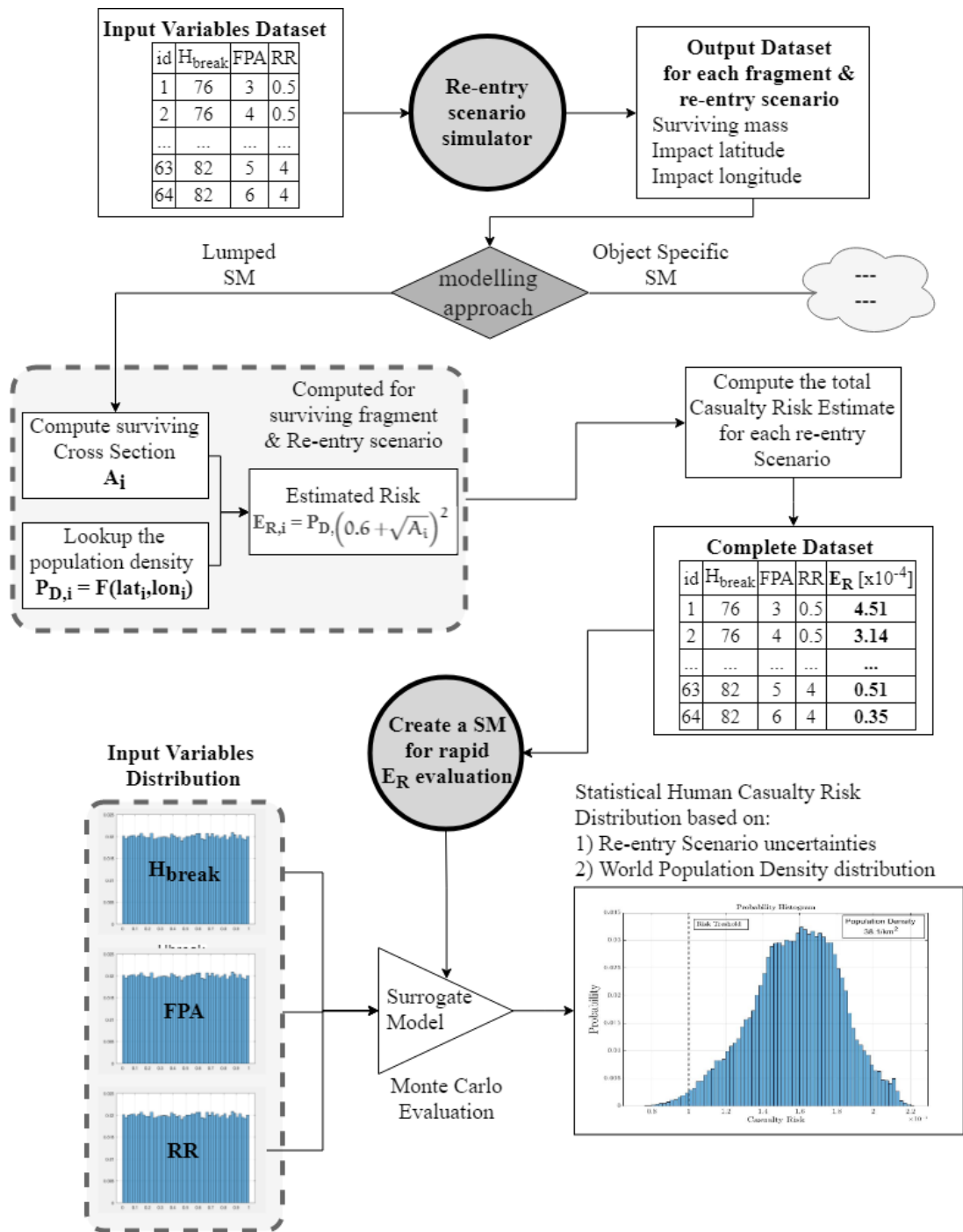


Figure 5.38: Work-flow diagram for the computation of scenario-averaged statistical casualty risk using surrogate models.

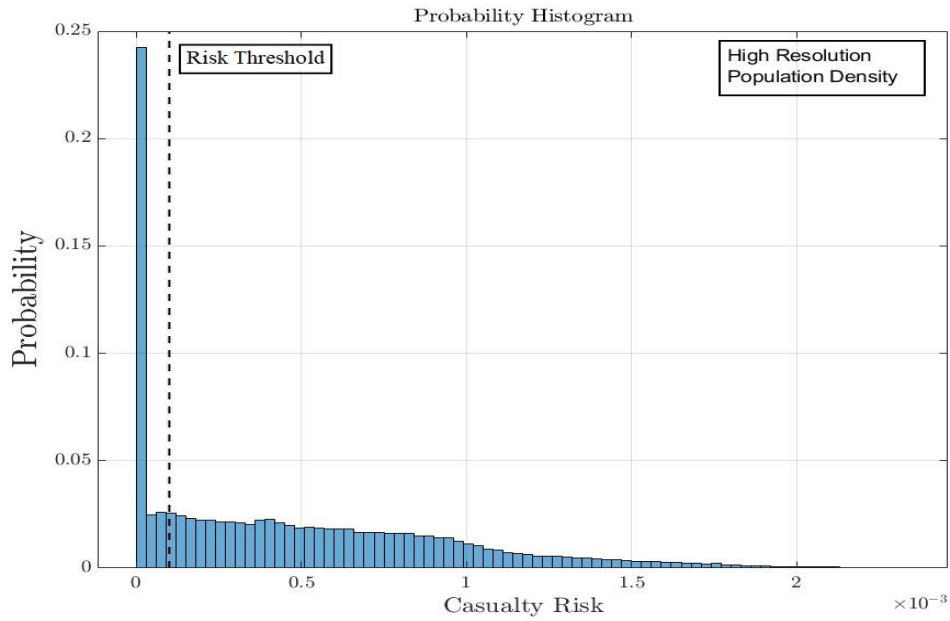


Figure 5.39: Monte Carlo sampling of the Casualty Risk surrogate model (high resolution grid: 0.0417deg).

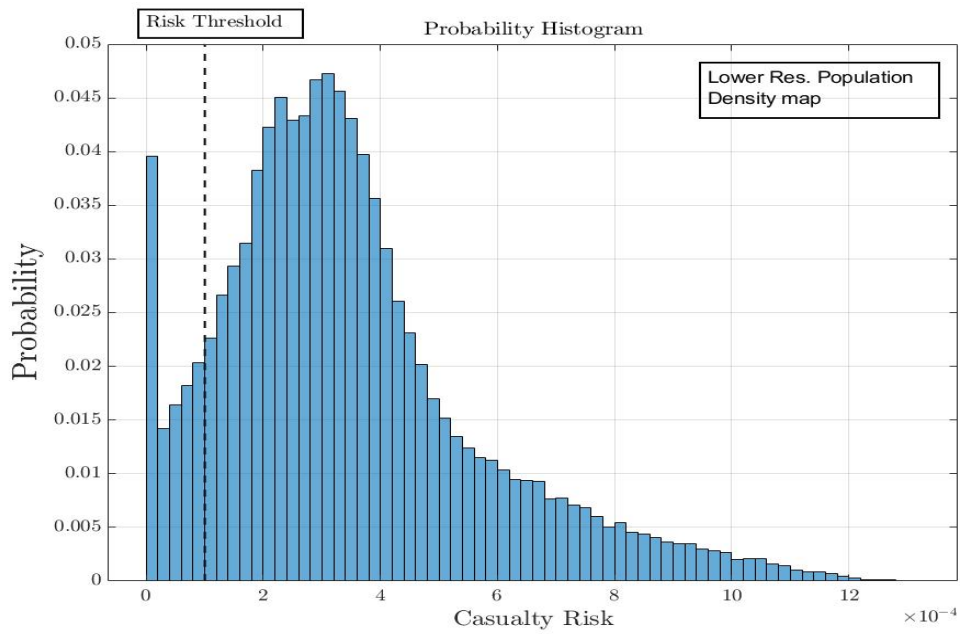


Figure 5.40: Monte Carlo sampling of the Casualty Risk surrogate model (low resolution grid: 0.5deg).

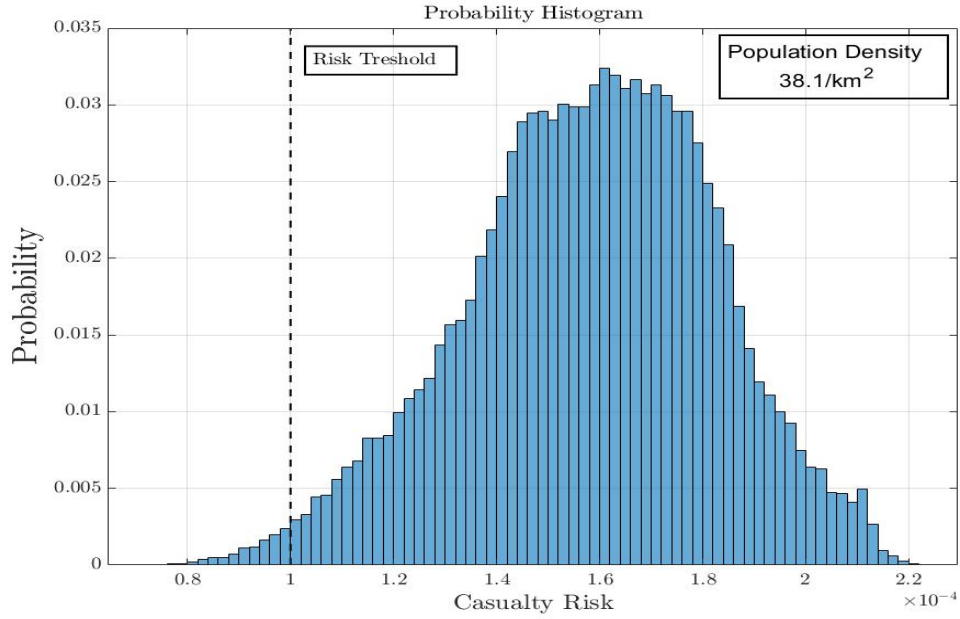


Figure 5.41: Monte Carlo sampling of the averaged population density casualty risk surrogate model

Object-specific Statistical Casualty Risk

In this analysis the surrogate models were singularly built for each object. This more detailed approach allows different advantages:

- Evaluate the contribution of each object to the total casualty risk
- Identify which objects could be redesigned with a design for demise approach
- Evaluate the ground footprint dispersion and uncertainty of each child object

The work-flow diagram for computing the object-specific statistical casualty risk is reported in Figure 5.42.

The approach for building the surrogate models is the same, even though instead of evaluating only the re-entry casualty risk of a re-entry scenario, the latitude, longitude, and surviving mass surrogate models are created:

$$\mathbb{M}_{A,i} = \mathbb{G}_1(H_b) + \mathbb{G}_2(\gamma) + \dots + \mathbb{G}_{123}(H_b, \gamma, R_R) + C_{val,1} \quad (5.129)$$

$$\mathbb{L}at_i = \Phi_1(H_b) + \Phi_2(\gamma) + \dots + \Phi_{123}(H_b, \gamma, R_R) + C_{val,2} \quad (5.130)$$

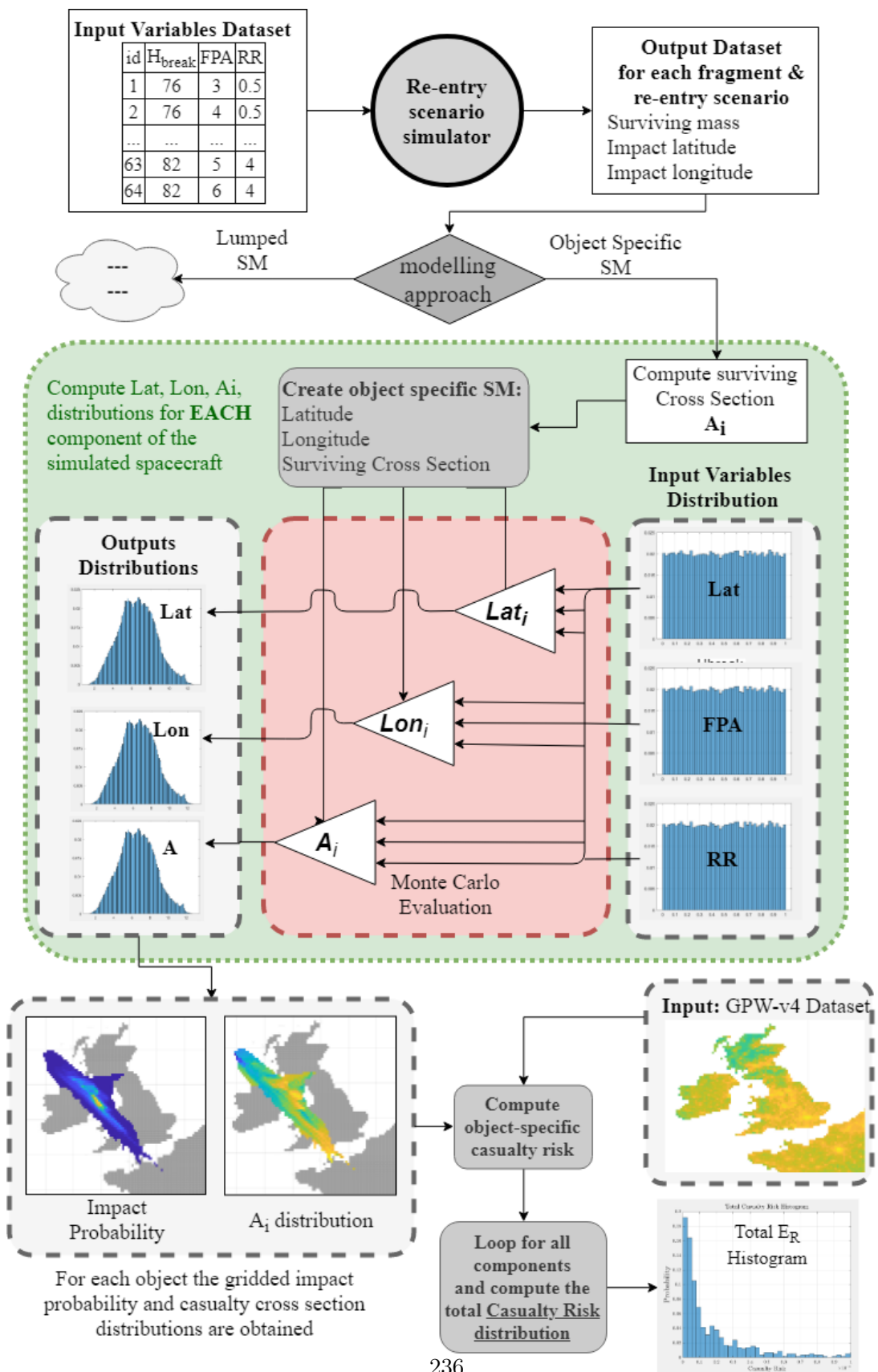


Figure 5.42: Work-flow diagram for the computation of object-specific statistical casualty risk using multiple surrogate models for latitude, longitude, and casualty cross section of each spacecraft component.

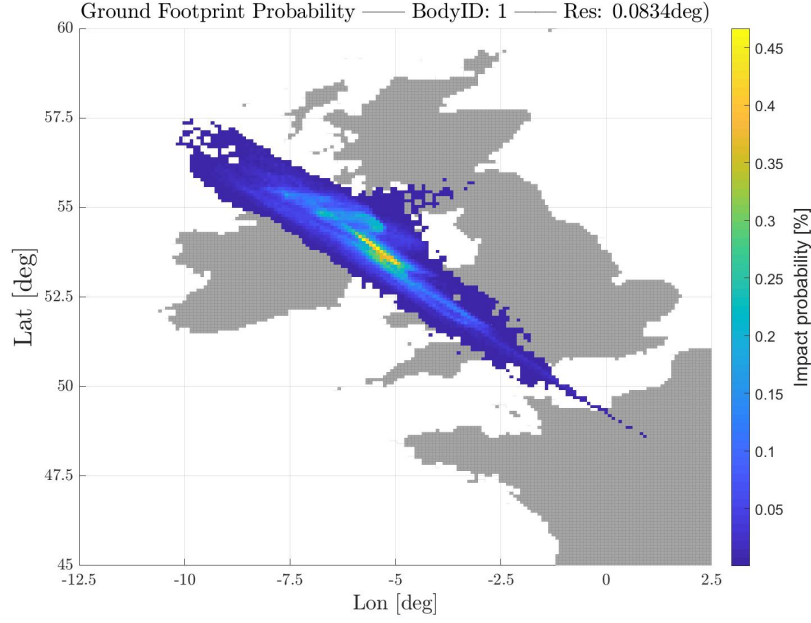


Figure 5.43: Discretized ground footprint probability for the first object (BodyID: 1 - one of the two solar panels).

$$\mathbb{L}on_i = \Psi_1(H_b) + \Psi_2(\gamma) + \dots + \Psi_{123}(H_b, \gamma, R_R) + C_{val,3} \quad (5.131)$$

where the subscript i represents the index of each object, and the math-type symbols represent the correspondent output surrogate model. The use of these surrogate models allows the evaluation of the impact location in terms of latitude and longitude ($\mathbb{L}at$ and $\mathbb{L}at$) and the debris casualty area (\mathbb{D}_A) for each combination of H_b , γ , and R_R for each singular object. In fact, in this specific case 6x3 surrogate models for each object and requested output were generated. It is reminded that even though only three input variables have been used, the creation of the surrogate models through the use of the HDMR method could be extended to any number of input variables.

Performing a Monte Carlo sampling of the surrogate model for each object (i.e.: $\mathbb{L}at$, $\mathbb{L}at$ and \mathbb{D}_A) allows to create a statistical distribution of the impact footprint. In fact, by using the same grid of latitude and longitude as the one defined in the GPW dataset (original or reduced resolution), a number of fragments landing in a specific gridded location can be computed. The process is the equivalent as of creating a 1D histogram, just with a 2D latitude and longitude grid an example for one of the two solar panels is shown in Figure 5.43.

Additionally, Each fragment will land with a specific casualty area, therefore, a statistical distribution of the casualty area for each gridded location will be automatically

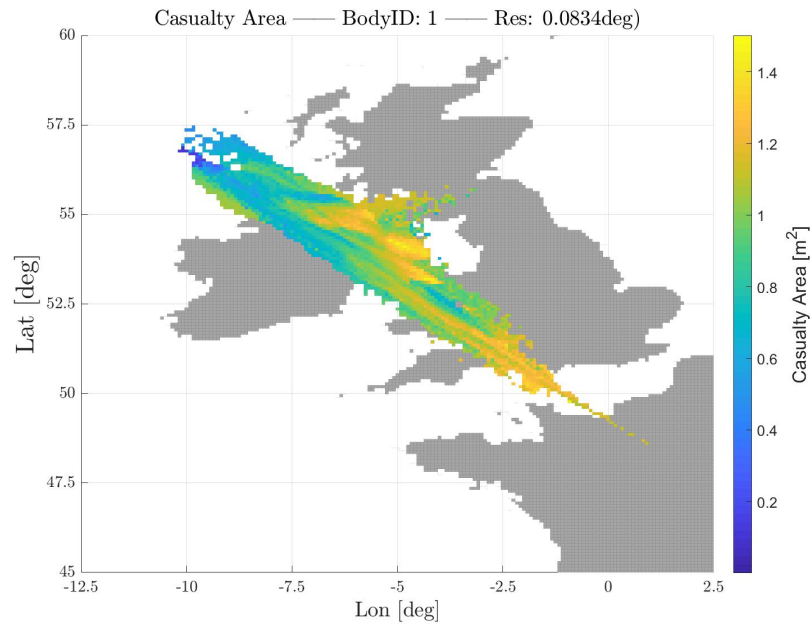


Figure 5.44: Casualty Area mapped distribution (averaged per bin) for the solar panel.

generated. Of such distribution it is possible to compute both an average value and a standard deviation, respectively reported in Figure 5.44 and 5.45 (enough number of samples are required, for the examples shown the MC analysis was performed with 200'000 samples). The possibility of computing the statistical distribution of the casualty area per gridded location allows to perform additional best case and worst case scenario analysis for the estimated casualty risk.

The probabilistic ground footprint is highly dependent on the aerodynamic properties and attitude of the simulated object, different shapes will have different probabilistic ground footprint distribution, as shown for the main body (cubic shell) and the electronic box (parallelepiped) in Figure 5.46.

The probabilistic casualty risk can be computed for the gridded value of the mean casualty area and the population density of each body part; the casualty risk distribution for one of the solar panels and the central body is shown in Figure 5.47.

Adding each body casualty risk distribution (coherently with the mapped grid) leads to the total average casualty risk distribution (Figure 5.48); such distribution is the result of the summation of each body part gridded casualty risk estimate. Which can be visualized as an histogram, by considering only the non-null casualty risk present in the ground footprint.

The reported analyses highlight how different approach could lead to different com-

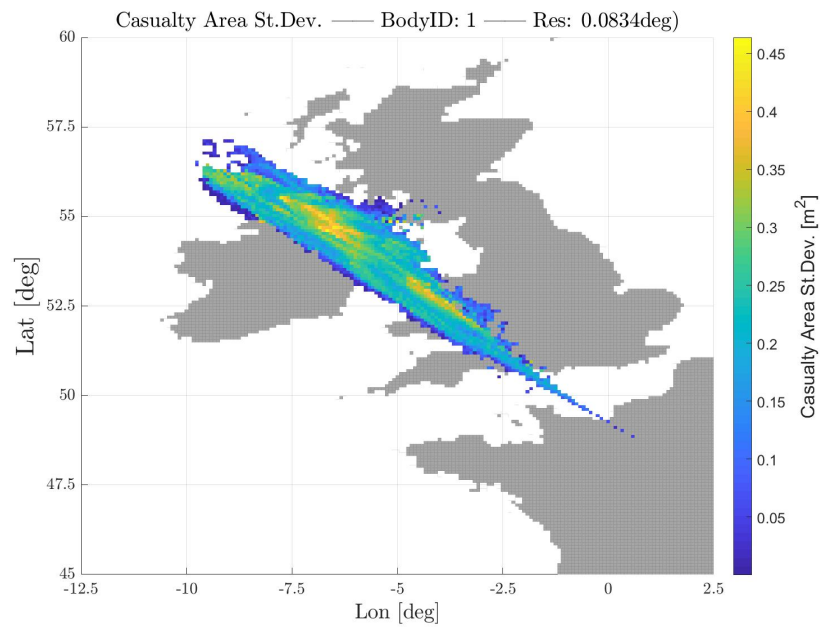


Figure 5.45: Casualty area standard deviation distribution for the solar panel.

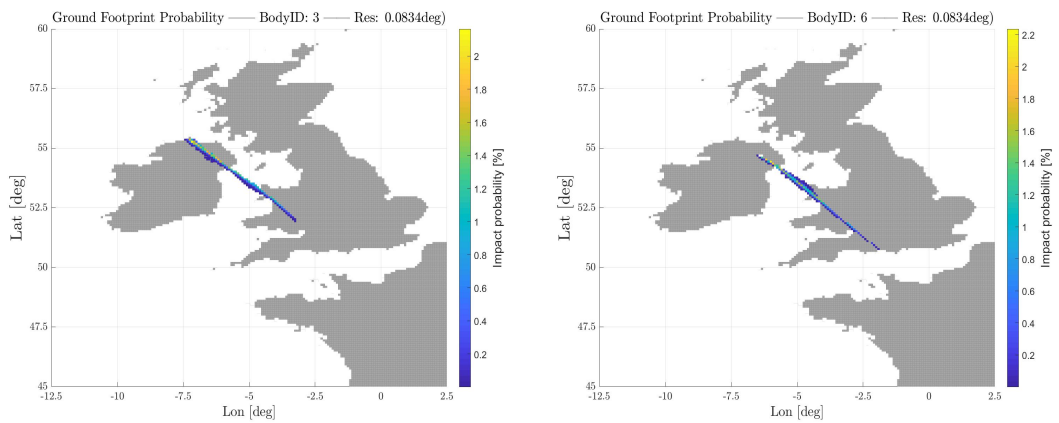


Figure 5.46: Probabilistic ground footprint for cubic shell (left), and for the electronic box (right).

Chapter 5. Coupled Aero-thermodynamics Applications

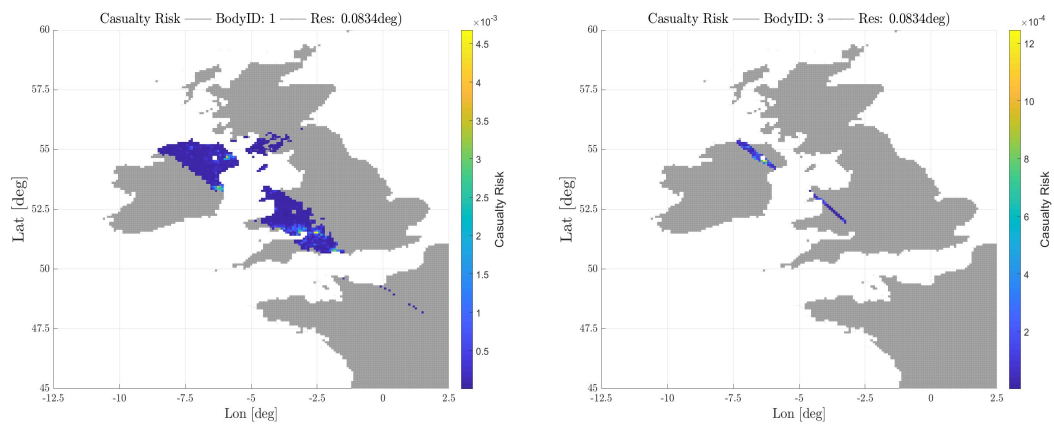


Figure 5.47: Probabilistic casualty risk distribution for one solar panel (left), and for the main body (right).

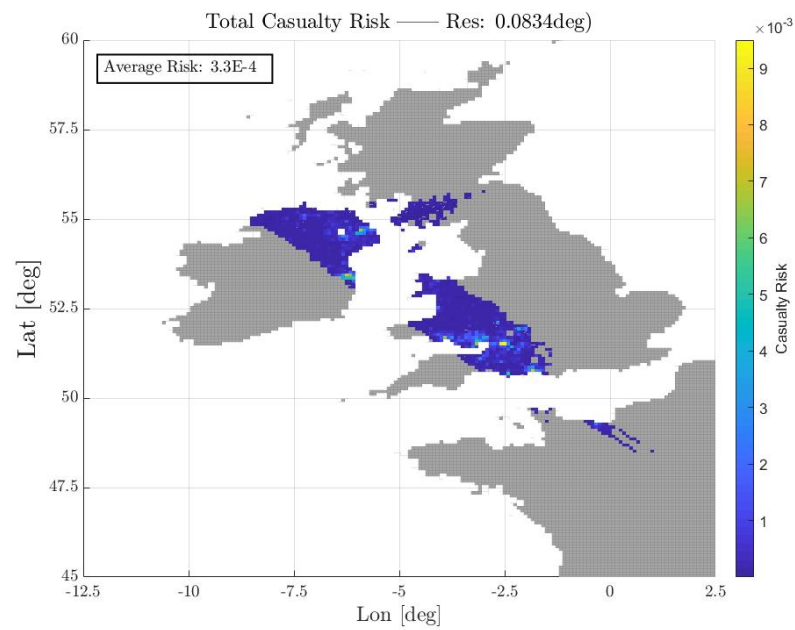


Figure 5.48: Total casualty risk distribution computed for the average casualty area.

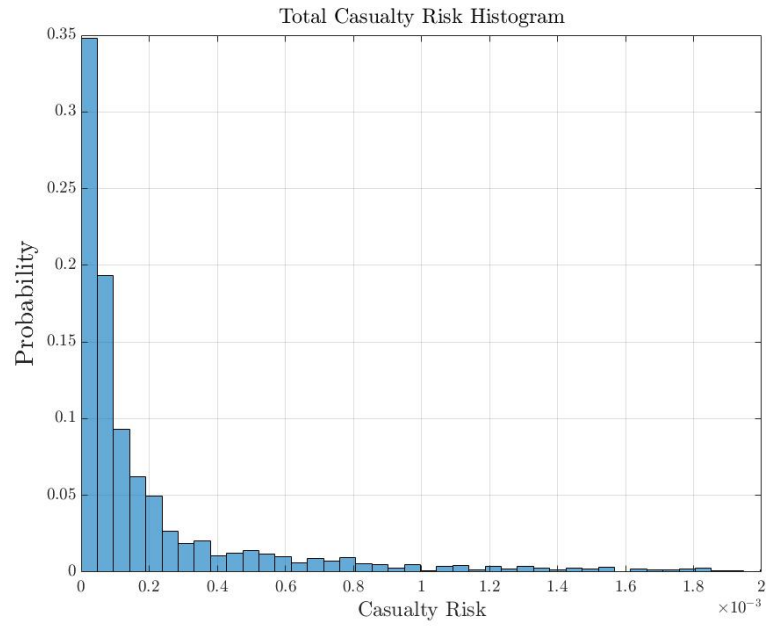


Figure 5.49: Total casualty risk histogram computed for the average casualty area, neglecting the non-null casualty risk of the footprint.

putation of the probabilistic casualty risk, resulting in different mean values and distributions. The application of such methodology could allow the estimation of the uncertainty in the computed casualty risk. Although, to perform such analysis it is necessary to evaluate the uncertainty ranges and distributions of the considered variables, e.g.: velocity, flight path angle, initial state vector, atmospheric density, aerothermal models, material and geometrical properties. Such approach could be employed in an efficient way making use of the High Dimensional Model Representation for the creation of efficient and accurate surrogate models with a limited number of evaluations.

Conclusions

With the aim of studying the re-entry aerodynamics and aerothermodynamics of space objects a software based on the simplified hypersonic local panel inclination (LPI) method has been developed. The developed tool has been employed to understand and investigate different ways of improving the accuracy of the classical approach.

Initially, in order to allow for the simulation of arbitrary complex objects a facets visibility detection method has been identified through the occlusion and back-face culling techniques. These two techniques allows the identification of the self-shadowed facets, and the lee-ward facing panels respectively. Different tests have been performed to understand the dependency on the pixel resolution and the objects shapes and attitude.

In order to characterize complex objects, a local radius smoothing algorithm has been integrated. Such approach allows the correct use of the LPI methods for estimating the heat-flux within the continuum regime. The implemented methodology has been characterized for different classes of objects, showing the influence of the the correct estimation of the local curvature.

The application of the developed methodology was conceived for studying atmospheric re-entries of space objects, therefore a set of aerodynamic and aerothermodynamics validation cases were simulated. In order to allow the simulation of a generic object, the implementation of aero-thermal bridging functions for estimating the aerodynamics and heat-fluxes between the continuum and rarefied flow regime.

The aerodynamic coefficients computed with the implemented methodology have been compared to a set of reference study cases: a sphere, the Space Shuttle Orbiter, Orion Crew Exploration Vehicle, and the Mars Microprobe. All the cases have shown an accurate computation of both forces and moments coefficients, which have shown differences w.r.t. to the reference values always below 10%.

Another interesting study case which has been investigated concerned the aerodynamic uncertainty quantification of a complex shape: the Gravity Field and Steady-State Ocean Circulation Explorer (GOCE). The shape which is highly elongated, with a high lateral to frontal surface ratio had shown a high underestimation of the drag coefficient for close to head-on attitudes within the free molecular flow regime. A study

involving the application of high-fidelity methodology (Direct Simulation Monte Carlo) in connection with the developed low-fidelity tool, has shown a possible correlation deriving from the underestimation of the lateral viscous forces highly dependent from the shape of the object (lateral to frontal area ratio) and the simulated flow direction. A set of surrogate models used to correct the attitude and shape dependent error has been identified for different classes of objects, i.e.: parallelepipeds, cylinders. It has been shown that the application of such corrective factors greatly reduced the aerodynamic coefficients errors for elongated shapes.

Concerning the study of the aero-thermodynamics, the application of the local radius smoothing methodology has proven to be very useful for studying complex objects which cannot be just simulated with a single reference radius. In order to allow the use of a local radius, a set of local radius and Knudsen Number-based bridging functions had to be defined within the transitional rarefied flow regime. For the definition of such bridging functions, a set of literature study cases was identified, comprising: Orion CEV, Mars Pathfinder, Mars Microprobe and a sphere. The different study cases have shown that the bridging function should have been dependent on the reference radius and the Knudsen number. A general bridging function depending on the two parameters was developed and integrated.

The aerothermodynamic module was tested on four well known study cases from the literature: the re-entry of the space shuttle orbiter, and stardust sample-return capsule, some experimental and high-fidelity CFD simulations of the Intermediate Experimental Vehicle (IXV) and a blunted cone, and other experimental observations present in the literature. The validations have shown a good match on both the stagnation heat-fluxes and heat transfer coefficients distributions, with the results showing absolute differences in the range of 10%. Another important result was shown in the IXV study case, where the local radius method was compared to the most common constant reference nose radius approach. The local radius was able to reproduce high-fidelity heat transfer coefficients distributions, while the constant radius approach provided a sensible overestimation (see Fig. 4.13-4.14-4.15).

After the successful preliminary validation test cases, the implemented methodology was extended for studying innovative applications employing the benefit of a low computational cost and a good aerodynamics and aerothermodynamics accuracy. Various re-entry and ascent scenarios have been reported: the absorbed heat-flux controlled re-entry trajectory optimization of IXV, the thermal protection system local ablation estimation for Stardust Sample Return Capsule atmospheric uncontrolled re-entry, the ascent simulation of VEGA launcher vehicle with a simplified payload fairing and dummy payload thermal models, and the statistical estimation of the ground foot-

print and Human Casualty Risk estimation of a toy spacecraft uncontrolled re-entry and fragmentation.

The IXV re-entry trajectory has been performed with the employment of a surrogate model-based optimization, and the results have shown an optimal trajectory similar to the nominal IXV actual re-entry. After the initial trajectory optimization, the complete re-entry was simulated using a 1D thermal structural coupling for non-ablative materials, and the estimated temperature was found to be adherent with the expected re-entry wall temperatures.

The simulation of Stardust SRC has been performed coupling the developed software with a 1D thermal ablation code for ablative materials (i.e.: PICA), the TPS recession distribution over the surface was found to be consistent with different references, and the estimated wall temperature during the re-entry was in a good match with the SLIT telescope observations.

The simplified hypersonic methodology for aerothermal heating estimation has been applied also to an ascent trajectory scenario based on VEGA launcher vehicle and its payload fairing. The enveloping aerothermal heat-fluxes estimated on the payload fairing have been simulated with a coupled multi-layer thermal model network. The thermal model involved more than 10'000 nodes for simulating 3 layers of the thermal protection system and the structural sandwich panels; the temperature evolution of the payload fairing was studied for evaluating the maximum radiative dissipated thermal flux toward a dummy payload. The theoretical optimal payload fairing separation altitude (and timing) was found taking into account the external aerothermal heat-fluxes and internally emitted radiative flux. The study case showed that the methodology can be easily adapted and applied for different scenarios other than the most focused atmospheric re-entries. In fact, the methodology may be applied also for various other purposes, such as preliminary sizing of thermal protection systems, evaluating enveloping heat-fluxes for studying temperature boundaries at a system level, and for identifying critical areas and condition where high-fidelity simulations could be used to provide more accurate results.

Last but not least, the simulation of the uncontrolled re-entry of the toy satellite has shown the potential of an innovative surrogate model-based methodology for tackling the estimation of the ground footprint and human casualty risk. Indeed, such re-entry scenarios involve many and different uncertain parameters, such as the actual breakup progression, the attitude and rotational velocity influence, along with all the more common atmospheric uncertainties and aerothermodynamics errors. The study case was limited to a set of three input variables for identifying different ways of creating statistical representative surrogate models, allowing to compute a ground footprint distribution along with its confidence levels and the associated re-entry human casualty

risk distribution.

The aerodynamics and aerothermodynamics low-fidelity methodologies have been implemented and tested in a wide range of scenarios, providing reliable results on all the different aspects involved in a atmospheric re-entry: aerodynamic coefficients estimation, heat transfer coefficients and their local surface distributions. The applicability of the holistic approach has been tested also in an launcher vehicle flight ascent scenario, and a good qualitative and quantitative match was obtained. The methodology has proven to be promising for rapid assessments of hypersonic re-entry and ascent aerodynamics and aerothermodynamics. Thanks to the rapid evaluation of aerothermal heat-fluxes, the methodology may be used in various engineering and contexts, such as: preliminary design evaluation, multidisciplinary design optimization, concurrent engineering design working groups, multi-objective trajectory optimization, and aerodynamics and aerothermodynamics database generation of complex objects. The advantage of the methodologies described in this Ph.D. work may be fully captured in application where the computational expense of performing high-fidelity simulation vastly exceeds the benefits provided in terms of better accuracy.

The integrated aerodynamic and aerothermodynamic computation capability allows the study of re-entry ablation and fragmentation process; the evaluation and simulation of an uncontrolled re-entry requires a coupling between the re-entry trajectory dynamics of the space object and the aero-thermodynamics. Although, it would be possible to study the aerodynamics and aerothermodynamics using high-fidelity methodologies for a step-by-step trajectory propagation, at the time of writing it is still computationally unfeasible. The integration of the methodologies described in this work would allow the evaluation of the aerothermodynamics with a deviation which has been shown not to exceed $\pm 10\%$ w.r.t. high fidelity methodologies and experimental observations.

In the context of a collaborative design working group, aero-thermal analysis play a central role to design thermal protection systems and estimate the correct mass-budgets during the interactions with the various sub-systems groups. The presented methodology would allow to provide fast and reliable results during the various iterations of a project preliminary design phase of a spacecraft. In such context, CFD and DSMC analysis may be limited to a minimum due to the computational time constrains; the presented approach may be used to characterized the worst cases and design points to be further analyzed via CFD, DSMC, and experimental tests. In such sense, the investigated approach will allow to reduce the costs and required time of each design loop, providing a useful tool for industrial and laboratory research applications.

The straightforward implementation of low-fidelity methodology can be of a great value even from the perspective of typical system engineering applications. In fact, in most system level analysis, the requirement is to provide fast and reasonably accurate

results with conservative approximations. The programmatic implementation of the approaches investigated within this Ph.D. thesis may be easily adapted for various programming languages (i.e.: C++ and FORTRAN), allowing the integration of the methodology within currently adopted industrial space system engineering tools.

6.1 Future Works

Although some progresses have been made for better understanding the re-entry phenomena in the recent years, many of the most severe aspects of an uncontrolled spacecraft re-entry remain highly unclear and uncertain. Such lack of knowledge requires the use of fast evaluation tools capable of performing statistical significant analysis, providing an estimation of the reliability of the analysis.

The work presented in this Ph.D. thesis had the aim to investigate and provide a tool that could be improved aiming at providing a statistical approach to the uncontrolled re-entry of spacecraft and space debris. Some possible improvements have been identified by the author for providing a better thermo-structural characterization:

- Integration of an efficient lumped thermal network approach
- Introduction of a steady-state thermal solver for initializing the temperature at the re-entry point due to solar and albedo heat-fluxes
- Evaluating the different effects of fragile and plastic fragmentation along with inertial rotational projections
- Implementation and study of a thermo-mechanical break-up due to aerodynamic and inertial forces

The above mentioned improvements would allow to quantify different scenarios along with the effects of material properties, providing useful information regarding the fragmentation processes and their influence on the impact footprint and the deriving human casualty risk. Such solutions could be efficiently introduced within a low-fidelity tool, without the need of moving to a Finite Element Method approach, allowing the fast computational characterization required for treating the problem with a statistical approach.

Bibliography

- [Anderson Jr, 2000] Anderson Jr, J. (2000). *Hypersonic and High Temperature Gas Dynamics*. AIAA Publications, AIAA, Reston, VA.
- [Annaloro et al., 2017a] Annaloro, J., Galera, S., Kärräng, P., Préveraud, Y., Vérant, J., Spel, M., Van Hauwaert, P., and Omaly, P. (2017a). Space debris atmospheric entry prediction with spacecraft-oriented tools. In *Proceedings 7th European Conference on Space Debris, Darmstadt, Germany*.
- [Annaloro et al., 2017b] Annaloro, J., Galera, S., Kärräng, P., Prigent, G., Lips, T., and Omaly, P. (2017b). Comparison between two spacecraft-oriented tools: Pampero & scarab. *Journal of Space Safety Engineering*, 4(1):15–21.
- [Annaloro et al., 2014] Annaloro, J., Omaly, P., Rivola, V., and Spel, M. (2014). Elaboration of a new spacecraft-oriented tool: Pampero. In *Proceedings of the 8th European Symposium on Aerothermodynamics for Space Vehicles*.
- [Arianespace, 2014] Arianespace (2014). Vega user’s manual, issue 4, revision 0. *April*.
- [Bailey and Hiatt, 1972] Bailey, A. and Hiatt, J. (1972). Sphere drag coefficients for a broad range of mach and reynolds numbers. *Aiaa Journal*, 10(11):1436–1440.
- [Beck and Merrifield, 2015] Beck, J. and Merrifield (2015). A heat balance integral method for destructive re-entry codes. In *8th European Symposium on Aerothermodynamics of Space Vehicles*.
- [Beck et al., 2015] Beck, J., Merrifield, J., Markelov, G., Holbrough, I., and Molina, R. (2015). Verification and application of the sam re-entry model. In *Space Safety is No Accident*, pages 437–443. Springer.
- [Benedetti et al., 2018] Benedetti, G., Viola, N., Minisci, E., Falchi, A., and Vasile, M. (2018). Low-fidelity modelling for aerodynamic characteristics of re-entry objects. In *Stardust Final Conference*, pages 247–264. Springer.

Bibliography

- [Bird, 1983] Bird, G. (1983). Definition of mean free path for real gases. *Physics of Fluids (1958-1988)*, 26(11):3222–3223.
- [Bird, 1976] Bird, G. A. (1976). Molecular gas dynamics. *NASA STI/Recon Technical Report A*, 76.
- [Bonnal et al., 2013] Bonnal, C., Ruault, J.-M., and Desjean, M.-C. (2013). Active debris removal: Recent progress and current trends. *Acta Astronautica*, 85:51–60.
- [BusEMANN, 1933] BusEMANN, A. (1933). F ussigkeits-and-gaswewegung, hand-worterbuch der naturwissenschaften.
- [Buyco and Davis, 1970] Buyco, E. H. and Davis, F. E. (1970). Specific heat of aluminum from zero to its melting temperature and beyond. equation for representation of the specific heat of solids. *Journal of Chemical and engineering data*, 15(4):518–523.
- [Chambre and Schaaf, 1961] Chambre, P. A. and Schaaf, S. A. (1961). *Flow of rarefied gases*. Princeton University Press.
- [Chao et al., 2015] Chao, W., Xinyu, L., and Feng, L. (2015). Six-dof modeling and simulation for generic hypersonic vehicle in reentry phase. *Procedia Engineering*, 99:600–606.
- [Chernyi, 1961] Chernyi, G. G. (1961). *Introduction to hypersonic flow*. Academic Press.
- [Cook, 1965] Cook, G. (1965). Satellite drag coefficients. *Planetary and Space Science*, 13(10):929–946.
- [Cowling and Chapman, 1970] Cowling, T. and Chapman, S. (1970). The mathematical theory of non-uniform gases. *Cambridge Mathematical Library*,.
- [Cox and Crabtree, 1965] Cox, R. N. and Crabtree, L. F. (1965). *Elements of hypersonic aerodynamics*. Academic Press.
- [Desai and Qualls, 2010] Desai, P. N. and Qualls, G. D. (2010). Stardust entry reconstruction. *Journal of Spacecraft and Rockets*, 47(5):736.
- [Detra, 1957] Detra, R. (1957). Addendum to heat transfer to satellite vehicle reentering the atmosphere. *Jet Propulsion*, pages 1256–1257.
- [Detra and Hidalgo, 1960] Detra, R. and Hidalgo, H. (1960). Generalized heat transfer formulas and graphs for nose cone re-entry into the atmosphere. *ARS Journal*, 31(3):318–321.

Bibliography

- [Dobarco-Otero et al., 2005] Dobarco-Otero, J., Smith, R., Bledsoe, K., Delaune, R., Rochelle, W., and Johnson, N. (2005). The object reentry survival analysis tool (orsat)-version 6.0 and its application to spacecraft entry. In *Proceedings of the 56th Congress of the International Astronautical Federation, the International Academy of Astronautics, and International Institute of Space Law, IAC-05-B6*, volume 3, pages 17–21.
- [Dogra et al., 1992] Dogra, V. K., Wilmoth, R. G., and Moss, J. N. (1992). Aerothermodynamics of a 1.6-meter-diameter sphere in hypersonic rarefied flow. *AIAA journal*, 30(7):1789–1794.
- [Dyke, 1958] Dyke, M. D. V. (1958). The supersonic blunt-body problem-review and extension. *Journal of the Aerospace Sciences*, 25(8):485–496.
- [Eggers et al., 1953] Eggers, A. J., Syvertson, C. A., and Kraus, S. (1953). A study of inviscid flow about airfoils at high supersonic speeds.
- [EGGERS et al., 1956] EGGERS, J., Resnikoff, M. M., Dennis, D. H., et al. (1956). Bodies of revolution having minimum drag at high supersonic airspeeds. Technical report, NATIONAL AERONAUTICS AND SPACE ADMINISTRATION WASHINGTON DC.
- [ESA, 2015] ESA (2015). Space debris mitigation compliance verification guidelines.
- [Estermann, 1955] Estermann, I. (1955). Gases at low densities. *Thermodynamics and Physics of Matter*, 1:742–744.
- [Falchi et al., 2019] Falchi, A., Gentile, L., Minisci, E., Tirelli, M., and Perugini, P. (2019). Launcher vehicle aerothermodynamics and fairing separation altitude effects on payload temperature. In *8th European Conference for Aeronautics and Space Sciences*, pages 1–16.
- [Falchi et al., 2018] Falchi, A., Minisci, E., Kubicek, M., Vasile, M., and Lemmens, S. (2018). Hdmr-based sensitivity analysis and uncertainty quantification of goce aerodynamics using dsmc. In *Stardust Final Conference*, pages 301–323. Springer.
- [Falchi et al., 2017a] Falchi, A., Minisci, E., Vasile, M., and Kubicek, M. (2017a). Aero-thermal re-entry sensitivity analysis using dsmc and a high dimensional model representation-based approach. In *7th European Conference on Space Debris*.
- [Falchi et al., 2017b] Falchi, A., Minisci, E., Vasile, M., Rastelli, D., and Bellini, N. (2017b). Dsmc-based correction factor for low-fidelity hypersonic aerodynamics of

Bibliography

- re-entering objects and space debris. In *7th European Conference for Aeronautics and Space Sciences*, pages 1–15.
- [Falchi et al., 2017c] Falchi, A., Renato, V., Minisci, E., and Vasile, M. (2017c). Fosttrad: An advanced open source tool for re-entry analysis. In *15th Reinventing Space Conference*.
- [Fay, 1957] Fay, J. A. (1957). Theory of stagnation point heat transfer in dissociated air. *Journal of the Aerospace Sciences*, 25(2):73–85.
- [for International Earth Science Information Network (CIESIN) Columbia University, 2016] for International Earth Science Information Network (CIESIN) Columbia University, C. (2016). Gridded population of the world, version 4 (gpwv4): Population density.
- [Fritsch and Carlson, 1980] Fritsch, F. N. and Carlson, R. E. (1980). Monotone piecewise cubic interpolation. *SIAM Journal on Numerical Analysis*, 17(2):238–246.
- [Fritsche, 2013] Fritsche, B. (2013). Modelling the thermal decomposition of carbon fibre materials during re-entry. In *6th European Conference on Space Debris*, volume 723.
- [Fritsche, 2015] Fritsche, B. (2015). Uncertainty quantification for re-entry survivability prediction. In *Space Safety is No Accident*, pages 469–478. Springer.
- [Fritsche et al., 2000] Fritsche, B., Klinkrad, H., Kashkovsky, A., and Grinberg, E. (2000). Spacecraft disintegration during uncontrolled atmospheric re-entry. *Acta Astronautica*, 47(2-9):513–522.
- [frntr, 1999] frntr (1999). Vega toy model rocket.
- [Goodman, 1980] Goodman, F. O. (1980). Thermal accommodation coefficients. *The Journal of Physical Chemistry*, 84(12):1431–1445.
- [Grassi et al.,] Grassi, L., Bianchi, S., Destefanis, R., Kanzler, R., Bassaler, P., and Heinrich, S. Design for demise techniques for medium/large leo satellites reentry.
- [Hamilton et al., 1991] Hamilton, H. H., Gupta, R. N., and Jones, J. J. (1991). Flight stagnation-point heating calculations on aeroassist flight experiment vehicle. *Journal of Spacecraft and Rockets*, 28(1):125–128.
- [Hayes, 1959] Hayes, W. (1959). *Hypersonic flow theory*. Elsevier.
- [Hedin, 1991] Hedin, A. E. (1991). Extension of the msis thermosphere model into the middle and lower atmosphere. *Journal of Geophysical Research: Space Physics*, 96(A2):1159–1172.

Bibliography

- [Hirschfelder et al., 1954] Hirschfelder, J. O., Curtiss, C. F., Bird, R. B., and Mayer, M. G. (1954). *Molecular theory of gases and liquids*, volume 26. Wiley New York.
- [Johnson and Stansbery, 2010] Johnson, N. L. and Stansbery, E. G. (2010). The new nasa orbital debris mitigation procedural requirements and standards. *Acta Astronautica*, 66(3-4):362–367.
- [Kelley, 2012] Kelley, R. (2012). Using the design for demise philosophy to reduce casualty risk due to reentering spacecraft.
- [Kemp, 1956] Kemp, FR Riddell, N. (1956). Heat transfer to satellite vehicles reentering the atmosphere. *Journal of Jet Propulsion*, 27(2):132–137.
- [Kemp et al., 1959] Kemp, N. H., Rose, P. H., and Detra, R. W. (1959). Laminar heat transfer around blunt bodies in dissociated air. *Journal of the aerospace sciences*, 26(7):421–430.
- [Kennard et al., 1938] Kennard, E. H. et al. (1938). Kinetic theory of gases, with an introduction to statistical mechanics.
- [Kessler and Cour-Palais, 1978] Kessler, D. J. and Cour-Palais, B. G. (1978). Collision frequency of artificial satellites: The creation of a debris belt. *Journal of Geophysical Research: Space Physics*, 83(A6):2637–2646.
- [Klett, 1964] Klett, R. D. (1964). Drag coefficients and heating ratios for right circular cylinders in free-molecular and continuum flow from mach 10 to 30. Technical report, Sandia Corp., Albuquerque, N. Mex.
- [Klinkrad, 2005] Klinkrad, H. (2005). Re-entry prediction and on-ground risk assessment. In *SIXTH US/RUSSIAN SPACE SURVEILLANCE WORKSHOP*.
- [Klinkrad et al., 2001] Klinkrad, H., Fritsche, B., and Kashkovsky, A. (2001). Prediction of spacecraft destruction during uncontrolled re-entries. In *Spacecraft Structures, Materials and Mechanical Testing*, volume 468, page 485.
- [Klinkrad and Johnson, 2009] Klinkrad, H. and Johnson, N. L. (2009). Space debris environment remediation concepts. In *Fifth European Conference on Space Debris*, volume 672.
- [Kopal, 1947] Kopal, Z. (1947). *Tables of supersonic flow around cones*. Massachusetts Institute of Technology.

Bibliography

- [Koppenwallner et al., 2005] Koppenwallner, G., Fritsche, B., Lips, T., and Klinkrad, H. (2005). Scarab-a multi-disciplinary code for destruction analysis of space-craft during re-entry. In *Fifth European Symposium on Aerothermodynamics for Space Vehicles*, volume 563, page 281.
- [Kubicek et al., 2015] Kubicek, M., Minisci, E., and Cisternino, M. (2015). High dimensional sensitivity analysis using surrogate modeling and high dimensional model representation. *International Journal for Uncertainty Quantification*, 5(5).
- [Lees, 1955] Lees, L. (1955). Hypersonic flow. In *Fifth International Aeronautical Conference (Los Angeles, Calif)*, pages 241–276.
- [Lees, 1956] Lees, L. (1956). Laminar heat transfer over blunt-nosed bodies at hypersonic flight speeds. *Journal of Jet Propulsion*, 26(4):259–269.
- [Ling, 2015] Ling, L. (2015). Simulation for prediction of entry article demise (spread): an analysis tool for spacecraft safety analysis and ascent/reentry risk assessment. In *Space Safety is No Accident*, pages 415–422. Springer.
- [Liou et al., 2010] Liou, J.-C., Johnson, N. L., and Hill, N. (2010). Controlling the growth of future leo debris populations with active debris removal. *Acta Astronautica*, 66(5-6):648–653.
- [Lips and Fritsche, 2005] Lips, T. and Fritsche, B. (2005). A comparison of commonly used re-entry analysis tools. *Acta Astronautica*, 57(2-8):312–323.
- [Lips et al., 2017] Lips, T., Fritsche, B., Kanzler, R., Schleutker, T., Gülhan, A., Bonvoisin, B., Soares, T., and Sinnema, G. (2017). About the demisability of propellant tanks during atmospheric re-entry from leo. *Journal of Space Safety Engineering*, 4(2):99–104.
- [Lips et al., 2004] Lips, T., Fritsche, B., Koppenwallner, G., and Klinkrad, H. (2004). Spacecraft destruction during re-entry—latest results and development of the scarab software system. *Advances in Space Research*, 34(5):1055–1060.
- [Masuda et al., 2015] Masuda, T., Masuoka, I., Kajiwara, K.-i., and Yamada, K. (2015). Demise characteristics evaluation for melting promotion-type tank. *Journal of Propulsion and Power*, 31(3):981–985.
- [Max, 1999] Max, N. (1999). Weights for computing vertex normals from facet normals. *Journal of Graphics Tools*, 4(2):1–6.

Bibliography

- [Mehta et al., 2015a] Mehta, P., Minisci, E., and Vasile, M. (2015a). Break-up modeling and trajectory simulation under uncertainty for asteroids. In *Proceeding of the 4th IAA Planetary Defense Conference, Frascati, Roma*, pages 13–17.
- [Mehta et al., 2015b] Mehta, P., Minisci, E., Vasile, M., Walker, A. C., and Brown, M. (2015b). An open source hypersonic aerodynamic and aerothermodynamic modelling tool. In *8th European Symposium on Aerothermodynamics for Space Vehicles*.
- [Mehta et al., 2016a] Mehta, P. M., Arnao, G. B., Bonetti, D., Minisci, E., and Vasile, M. (2016a). Computer graphics for space debris. In *Proceedings of the 6th International Conference on Astrodynamics Tools and Techniques, Darmstadt, Germany*, pages 14–17.
- [Mehta et al., 2016b] Mehta, P. M., Kubicek, M., Minisci, E., and Vasile, M. (2016b). Debris re-entry modeling using high dimensional derivative based uncertainty quantification.
- [Mehta et al., 2015c] Mehta, P. M., Walker, A., Brown, M., Minisci, E., and Vasile, M. L. (2015c). Sensitivity analysis towards probabilistic re-entry modeling of spacecraft and space debris. In *AIAA Modeling and Simulation Technologies Conference*, page 3098.
- [Merrifield et al., 2015a] Merrifield, J., Beck, J., Markelov, G., Leyland, P., and Molina, R. (2015a). Aerothermal heating methodology in the spacecraft aerothermal model (sam). In *Space Safety is No Accident*, pages 463–468. Springer.
- [Merrifield et al., 2015b] Merrifield, J., Beck, J., Markelov, G., and Molina, R. (2015b). Simplified aerothermal models for destructive entry analysis. In *8th European Symposium and Aerothermodynamics for Space Vehicles*.
- [Milos et al., 1999] Milos, F. S., Chen, Y.-K., Congdon, W. M., and Thornton, J. M. (1999). Mars pathfinder entry temperature data, aerothermal heating, and heatshield material response. *Journal of Spacecraft and Rockets*, 36(3):380–391.
- [Mitcheltree et al., 1999] Mitcheltree, R., DiFulvio, M., Horvath, T., and Braun, R. (1999). Aerothermal heating predictions for mars microprobe. *Journal of spacecraft and rockets*, 36(3):405–411.
- [Moe and Moe, 2005] Moe, K. and Moe, M. M. (2005). Gas–surface interactions and satellite drag coefficients. *Planetary and Space Science*, 53(8):793–801.

Bibliography

- [Moe et al., 1998] Moe, K., Moe, M. M., and Wallace, S. D. (1998). Improved satellite drag coefficient calculations from orbital measurements of energy accommodation. *Journal of spacecraft and rockets*, 35(3):266–272.
- [Moss et al., 2006a] Moss, J., Boyles, K., and Greene, F. (2006a). Orion aerodynamics for hypersonic free molecular to continuum conditions. In *14th AIAA/AHI Space Planes and Hypersonic Systems and Technologies Conference*, page 8081.
- [Moss et al., 2006b] Moss, J., Glass, C., and Greene, F. (2006b). Dsmc simulations of apollo capsule aerodynamics for hypersonic rarefied conditions. In *9th AIAA/ASME Joint Thermophysics and Heat Transfer Conference*, page 3577.
- [Moss and Simmonds, 1987] Moss, J. and Simmonds, A. (1987). Nonequilibrium effects for hypersonic transitional flows. In *25th AIAA Aerospace Sciences Meeting*, page 404.
- [Moss et al., 1997] Moss, J., Wilmoth, R., Price, J., Moss, J., Wilmoth, R., and Price, J. (1997). Dsmc simulations of blunt body flows for mars entries-mars pathfinder and mars microprobe capsules. In *32nd Thermophysics Conference*, page 2508.
- [Moss and Bird, 2003] Moss, J. N. and Bird, G. A. (2003). Direct simulation of transitional flow for hypersonic reentry conditions. *Journal of spacecraft and rockets*, 40(5):830–843.
- [Moyer and Wool, 1970] Moyer, C. B. and Wool, M. R. (1970). Aerotherm Charring Material Thermal Response and Ablation Program, Version 3. Volume 1. Program Description and Sample Problems. Technical report, AEROTHERM CORP MOUNTAIN VIEW CA.
- [Olynick et al., 1999] Olynick, D., Chen, Y.-K., and Tauber, M. E. (1999). Aerothermodynamics of the stardust sample return capsule. *Journal of Spacecraft and Rockets*, 36(3):442–462.
- [Omaly et al., 2015] Omaly, P., Annaloro, J., Wada, S., and Galera, S. (2015). A preliminary investigation of child object demise for uncontrolled re-entry.
- [Omaly and Dieudonne, 2010] Omaly, P. and Dieudonne, W. (2010). Debrisk. In *Making Safety Matter*, volume 680.
- [Omaly et al., 2013] Omaly, P., Magnin Vella, C., and Galera, S. (2013). Debrisk, cnes tool for re-entry survivability prediction: validation and sensitivity analysis. In *Safety is Not an Option, Proceedings of the 6th IAASS Conference*, volume 715.

Bibliography

- [Omalý and Spel, 2012] Omalý, P. and Spel, M. (2012). Debrisk, a tool for re-entry risk analysis. In *A Safer Space for Safer World*, volume 699.
- [Opiela et al., 2007] Opiela, J., Hillary, E., Whitlock, D., and Hennigan, M. (2007). Debris assessment software version 2.0 user’s guide. *Orbital Debris Program Office, NASA Johnson Space Center, Houston, TX*.
- [Ostrom and Abercromby, 2017] Ostrom, C. L. and Abercromby, K. (2017). Open source toolkit for reentry object modeling. In *AIAA Atmospheric Flight Mechanics Conference*, page 4208.
- [Palharini et al., 2015] Palharini, R. C., White, C., Scanlon, T. J., Brown, R. E., Borg, M. K., and Reese, J. M. (2015). Benchmark numerical simulations of rarefied non-reacting gas flows using an open-source dsmc code. *Computers & Fluids*, 120:140–157.
- [Patil and Ravi, 2005] Patil, S. and Ravi, B. (2005). Voxel-based representation, display and thickness analysis of intricate shapes. In *Computer Aided Design and Computer Graphics, 2005. Ninth International Conference on*, pages 6–pp. IEEE.
- [Picone et al., 2002] Picone, J. M., Heding, A. E., Drob, D. P., and Aikin, A. C. (2002). Nrlmsise00 empirical model of the atmosphere: Statistical comparisons and scientific issues. *Journal of Geophysical Research: space Physics*, 107(A12).
- [Probstein and Bray, 1954] Probstein, R. F. and Bray, K. N. (1954). Hypersonic similarity and the tangent-cone approximation for unyawed bodies of revolution. Technical report, PRINCETON UNIV NJ GAS DYNAMICS LAB.
- [Rault, 1994] Rault, D. F. (1994). Aerodynamics of the shuttle orbiter at high altitudes. *Journal of Spacecraft and Rockets*, 31(6):944–952.
- [Renato, 2018] Renato, V. (2018). *Multi-dimensional thermal response & permeability characterization for porous ablative materials*. PhD thesis, University of Strathclyde.
- [Renato et al., 2017a] Renato, V., Scanlon, T., and Brown, R. (2017a). Multi-dimensional ablation and thermal response program for martian entry analysis. *68th International Astronautical Congress*.
- [Renato et al., 2017b] Renato, V., Scanlon, T., and Brown, R. (2017b). Multi-dimensional ablation and thermal response program for re-entry analysis. *31st International Symposium on Space Technology and Science*.
- [Riley et al., 2016] Riley, D., Fuentes, I. P., Meyer, J.-C., Proffe, G., and Lips, T. (2016). Design for demise: Systems-level techniques to reduce re-entry casualty risk.

Bibliography

- [Rochelle et al., 1999] Rochelle, W., Kirk, B., and Ting, B. (1999). User’s guide for object reentry analysis tool (orsat) version 5.0, vol. 1, jsc-28742, nasa lyndon b. Johnson Space Center.
- [Roncioni et al., 2011] Roncioni, P., Ranuzzi, G., Marini, M., Paris, S., Cosson, E., and Walloschek, T. (2011). Experimental and numerical investigation of aerothermal characteristics of hypersonic intermediate experimental vehicle. *Journal of Spacecraft and Rockets*, 48(2):291.
- [Rose et al., 1958] Rose, P. H., Adams, M. C., and Probstein, R. F. (1958). Turbulent heat transfer on highly cooled blunt nosed bodies of revolution in dissociated air. In *Heat Transfer and Fluid Mechanics Institute*, pages 143–155.
- [Rusinkiewicz, 2004] Rusinkiewicz, S. (2004). Estimating curvatures and their derivatives on triangle meshes. In *3D Data Processing, Visualization and Transmission, 2004. 3DPVT 2004. Proceedings. 2nd International Symposium on*, pages 486–493. IEEE.
- [Scanlon et al., 2010] Scanlon, T. J., Roohi, E., White, C., Darbandi, M., and Reese, J. M. (2010). An open source, parallel dsmc code for rarefied gas flows in arbitrary geometries. *Computers And Fluids*, 39(10):2078–2089.
- [Scanlon et al., 2015] Scanlon, T. J., White, C., Borg, M. K., Palharini, R. C., Farbar, E., Boyd, I. D., Reese, J. M., and Brown, R. E. (2015). Open-source direct simulation monte carlo chemistry modeling for hypersonic flows. *AIAA Journal*, 53(6):1670–1680.
- [Schaaf, 1953] Schaaf, S. (1953). Theoretical considerations in rarefied-gas dynamics. In *University of Michigan, Engineering Research Institute, Heat Transfer Symposium*.
- [Sentman, 1961] Sentman, L. H. (1961). Free molecule flow theory and its application to the determination of aerodynamic forces. Technical report, LOCKHEED MISSILES AND SPACE CO INC SUNNYVALE CA.
- [Sims, 1964] Sims, J. L. (1964). Tables for supersonic flow around right circular cones at zero angle of attack. Technical report, NATIONAL AERONAUTICS AND SPACE ADMINISTRATION HUNTSVILLE AL GEORGE C MARSHALL SPACE FLIGHT CENTER.
- [Smits and Dussauge, 2006] Smits, A. J. and Dussauge, J.-P. (2006). *Turbulent shear layers in supersonic flow*. Springer Science & Business Media.

Bibliography

- [Sun et al., 2011] Sun, Z.-X., Tang, Z., He, Y.-L., and Tao, W.-Q. (2011). Proper cell dimension and number of particles per cell for dsmc. *Computers & Fluids*, 50(1):1–9.
- [Sutherland, 1893] Sutherland, W. (1893). Lii. the viscosity of gases and molecular force. *The London, Edinburgh, and Dublin Philosophical Magazine and Journal of Science*, 36(223):507–531.
- [Trumble et al., 2010] Trumble, K. A., Cozmuta, I., Sepka, S., Jenniskens, P., and Winter, M. (2010). Postflight aerothermal analysis of stardust sample return capsule. *Journal of Spacecraft and Rockets*, 47(5):765.
- [Van Driest, 1956] Van Driest, E. R. (1956). *The problem of aerodynamic heating*. Institute of the Aeronautical Sciences.
- [Wachman, 1962] Wachman, H. Y. (1962). The thermal accommodation coefficient: a critical survey. *ARS Journal*, 32(1):2–12.
- [Waswa and Hoffman, 2012] Waswa, P. M. and Hoffman, J. A. (2012). Illustrative nasa low earth orbit spacecraft subsystems design-for-demise trade-offs, analyses and limitations. *International Journal of Design Engineering*, 5(1):21–40.
- [White et al., 2018] White, C., Borg, M. K., Scanlon, T. J., Longshaw, S. M., John, B., Emerson, D., and Reese, J. M. (2018). dsmcfoam+: An openfoam based direct simulation monte carlo solver. *Computer Physics Communications*, 224:22–43.
- [White and Corfield, 2006] White, F. M. and Corfield, I. (2006). *Viscous fluid flow*, volume 3. McGraw-Hill New York.
- [Wiedmann, 1946] Wiedmann, M. L. (1946). *Thermal accommodation coefficients*. PhD thesis, Yale University.
- [Willcockson, 1999] Willcockson, W. H. (1999). Stardust sample return capsule design experience. *Journal of Spacecraft and Rockets*, 36(3).
- [Winter and Trumble, 2010] Winter, M. W. and Trumble, K. A. (2010). Spectroscopic observation of the stardust re-entry in the near uv with slit: Deduction of surface temperatures and plasma radiation.
- [Zhang, 1998] Zhang, H. (1998). Effective occlusion culling for the interactive display of arbitrary models.